Structural Reliability of Seismic Design Methodologies for Shear Walls and Distributors in RC Buildings

W.B. van der Linde

Master of Science Thesis

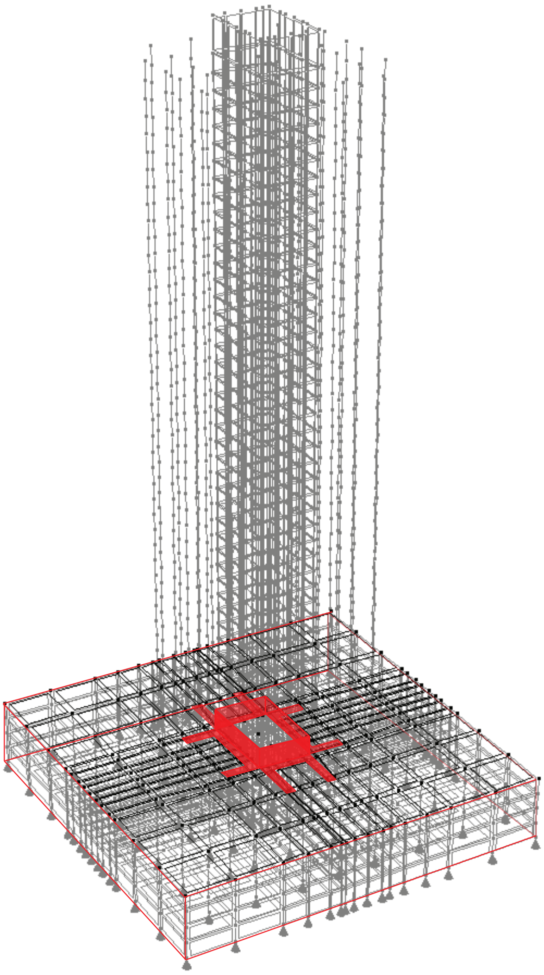

Delft University of Technology

Photo cover: ©Weber Thompson, http://www.weberthompson.com/

Structural Reliability of Seismic Design Methodologies for Shear Walls and Distributors in RC Buildings

MASTER OF SCIENCE THESIS

For the degree of Master of Science in Structural Engineering at Delft University of Technology

W.B. van der Linde

November 3, 2015

Faculty of Civil Engineering and Geosciences · Delft University of Technology

DELFT UNIVERSITY OF TECHNOLOGY
DEPARTMENT OF CIVIL ENGINEERING AND GEOSCIENCES

STRUCTURAL RELIABILITY OF SEISMIC DESIGN OF SHEAR WALLS AND DISTRIBUTORS IN RC BUILDINGS

by

W.B. VAN DER LINDE

GRADUATION COMMITTEE:

Prof. Dr. A.V. Metrikine	Delft University of Technology
Dr. ir. M.A.N. Hendriks	Delft University of Technology
Dr. ir. C van der Veen	Delft University of Technology
Prof. G.G. Deierlein	Stanford University
N.J. Mathias, PE, SE	Skidmore, Owings & Merrill
J. Zhang, SE	Skidmore, Owings & Merrill

Abstract

This study evaluated the structural reliability of seismic design methodologies for shear walls and distributors in transfer diaphragms in reinforced concrete shear wall buildings. An archetype structure was selected with typical shear walls and transfer diaphragms. The force demand and required capacity were evaluated to provide insight in the reliability of the specific force-controlled components under seismic loading.

To evaluate the response of the structure under seismic loading, the structure has been modelled in analysis program Perform 3D. The podium and basement diaphragms were modelled with elastic shell elements with modified stiffness properties. The shear walls were modelled using a fibre model. Steel and concrete fibres were modelled with nonlinear stress-strain relationships including stiffness degradation and strength deterioration. Coupling beams in the shear walls were modelled with elastic beam segments and an inelastic shear springs with a cyclic backbone curve and energy degradation factors. The basement walls were modelled with elastic wall segments and modified stiffness properties. A rigid foundation was assumed and horizontal restraints by soil below groundfloor level were neglected. Elastic gravity columns were connected to the core above groundfloor level assuming rigid diaphragms for better mass distribution and torsional behaviour. Finally, damping effects were included through a combination of hysteretic and equivalent viscous damping.

The hazard at the site was computed and corresponding target spectra were developed to calculate the design forces in the archetype structure. The seismic input for design per ASCE 7-10 [ASCE 7-10, 2010] was the design response spectrum for Modal Response Spectrum Analysis (MRSA). Design per PEER/TBI [PEER/TBI, 2010] and LATBSDC [LATBSDC, 2014] required a target spectrum to select and scale ground motions for nonlinear time history analysis (NLTHA). The Uniform Hazard Spectrum was selected as the target spectrum. The required shear capacity of the shear walls and required

capacity of the distributors in transfer diaphragms were determined for the mentioned design methodologies given the hazard at the site. The expected component capacities were derived from Building Code Requirements [ACI 318-11, 2011] and test results.

The structural reliability of the force-controlled components was verified through structural reliability analysis. An important assumption of the structural reliability analysis is that the force demand is independent of the capacity for force-controlled components. Therefore, various design methodologies could be evaluated for one set of nonlinear time history analyses. The expected force demand in the structure was determined for three intensity levels: 5% in 50 years (RP975), 2% in 50 years (RP2475), and 1% in 100 years (RP9950). Suites of 40 and 61 ground motions were selected and scaled to match the Conditional Spectrum for these three different intensity levels. The record-to-record uncertainty was calculated explicitly as the Conditional Spectrum enables the selection of ground motions matching both the target mean and target variance. The modelling uncertainty was not explicitly calculated and an assumption was made based on available literature. The required capacity of the force-controlled elements was computed for the various design methodologies. An assumption for the distribution of the capacity was made based on available literature.

The load distribution function and resistance distribution function were combined to compute the probabilities of collapse at each intensity level. Collapse fragility curves were computed to find the probability of demand exceeding capacity for each spectral acceleration. The collapse fragility curves were combined with the seismic hazard curve to find the mean annual frequency of the demand exceeding capacity and the probability of demand exceeding capacity in 50 years. The computed probabilities were compared to acceptance criteria for structural reliability of shear walls and distributors in transfer diaphragms. The acceptance criteria for critical elements, e.g. shear capacity of shear walls, were defined as less than 10% probability of demand exceeding capacity given MCE shaking and less than 1% probability of demand exceeding capacity in 50 years. For ordinary elements, e.g. distributors in transfer diaphragms, the acceptance criteria were defined as less than 25% probability of demand exceeding capacity given MCE shaking and less than 2.5% probability of demand exceeding capacity in 50 years.

The influence of stiffness variations of the diaphragms and basement walls on the structural reliability was evaluated. Furthermore, the influence of parameter estimates for the load and resistance function on the probability of demand exceeding capacity was computed for upper-bound and lower-bound cases. Moreover, the required demand to capacity ratio was computed for various target spectra.

For design of shear capacity of shear walls, it has been concluded that design per LATBSDC with UHS as target spectrum provides sufficient margin against collapse. For design with CMS as the target spectrum, the LATBSDC procedure with $\beta_{eff} = 1.50$ failed to meet the acceptance criteria for structural reliability. Therefore, the PEER/TBI procedure with $\beta_{eff} = 2.00$ is recommended for shear capacity design of shear walls with CMS as the target spectrum. Alternatively, the design criterion $\bar{V}_{CMS} \leq \beta_{eff} V_{ne}$ could be used to calculate the required capacity with $\beta_{eff} = 1.50$ and assuming $V_{ne} = 1.35V_e$. Furthermore, $\beta_{eff} = 2.00$ is recommended for design of shear walls with design codes for which use of UHS and CMS is interchangeable.

The alternative design approaches PEER/TBI and LATBSDC for design of distributors in transfer diaphragms have been found to meet the reliability intent for all cases and target spectra. On the other hand, distributor design according to ASCE 7-10 failed to meet the acceptance criteria for structural reliability for all cases and target spectra. Therefore, the PEER/TBI and LATBSDC design procedures are recommended for design of distributors in transfer diaphragms. Design of distributors in transfer diaphragms per ASCE 7-10 is discouraged. For preliminary design of distributors per ASCE 7-10, it is recommended to use unreduced shear demand in the basement walls as the expected force demand in the distributors.

This work provides insight in the reliability of current design methodologies for specific force-controlled components in reinforced concrete structures. Moreover, this work provides insight in the influence of design criteria, design decisions, and analysis assumptions on the structural reliability of force-controlled components. The proposed framework can also be used to evaluate the structural reliability of other structural components. Hence, this work sets an example for reliability analysis of structural components and is recommended for future reliability evaluations.

Contents

Preface

This thesis was written as part of the fulfillment for the Master of Science degree in Structural Engineering at Delft University of Technology. The majority of this thesis was written at Stanford University and at Skidmore, Owings & Merrill in San Francisco.

In the past year, I have learned a lot about earthquake engineering and structural reliability. Furthermore, I gained many valuable experiences through living and studying abroad for a year and I enjoyed meeting and interacting with many interesting people from different cultures. Moreover, I learned about myself by doing research for over a year. I would like to thank everyone at SOM, Stanford and TU Delft who supported me and made writing this thesis an unforgettable experience.

In particular, I would like to thank Greg Deierlein from Stanford University for his critical thinking, inspiration and guidance during the writing of this thesis. I have thoroughly enjoyed our discussions and meetings over the past year, whether we were at Stanford, in San Francisco, Amsterdam, or meeting online, and I have learned from every single one of those meetings. Furthermore, I would like to thank Neville Mathias, Joanna Zhang and all other colleagues at SOM for their encouragement and our fruitful discussions and shared moments. Also, I would like to thank my supervisors at TU Delft, Andrei Metrikine, Max Hendriks, and Cor van der Veen for supporting and challenging me throughout the whole process.

Finally, I would like to thank my mom and dad, brother, and new and old friends for their continuous support, motivation and joy, regardless of whether they were close or far away.

Delft, University of Technology
November 3, 2015

W.B. van der Linde

Chapter 1

Introduction

1-1 General

Buildings can be designed according to Code design procedures, such as ASCE 7-10 [ASCE 7-10, 2010], or alternative design procedures, such as PEER/TBI [PEER/TBI, 2010] and LATBSDC [LATBSDC, 2014]. Code design procedure generally imply modal response spectrum analyses, for which the force demand is calculated in the elastic range. To have a realistic representation of the force distribution, seismic performance factors are applied. The seismic performance factors are used to estimate the force and deformation demands on seismic-force-resisting systems that are designed using linear methods of analysis but are responding in the nonlinear range. The factors reduce the seismic force demand through ductility and inherent overstrength.

Alternative design approaches are described in PEER/TBI and LATBSDC. These alternative approaches employ nonlinear time history analyses to calculate the force demand in the structure. The structure is excited by at least 7 representative ground motions at MCE shaking level intensity. The mean calculated demand is multiplied by a factor β, which accounts for dispersion. The capacity is calculated from the nominal expected strength multiplied by a strength reduction factor ϕ.

In earthquake engineering in the US, the intent is to design structures with a probability of collapse equal or less than 1% in 50 years. The reliability intent should be achieved regardless of the structural type, building location, or design approach. Until recently, it was assumed that the reliability intent was achieved when the design requirements were met. However, it is unlikely that risk-consistency is achieved for different design approaches, as differences and discrepancies between these design approaches exist. New developments, such as the selection of ground motions matching the expected mean and variance for a given site and period, and increasing computational possibilities have paved the way for explicit calculation of the probability of collapse in a certain period for a given structure and site.

This study will use these new opportunities to develop a probabilistic framework to explicitly compute the probability of demand exceeding capacity for specific force-controlled components for which discrepancies and differences exist between various design approaches. Force-controlled components are components for which inelastic deformation capacity cannot be assured and failure poses severe consequences to the structural stability [PEER/TBI, 2010].

The reliability of shear walls loaded in shear and distributors in transfer diaphragms, designed according to current methodologies, will be evaluated and compared to the reliability intent. Both shear walls loaded in shear and distributors are classified force-controlled. The ability of various design approaches to provide sufficient safety against collapse for these components is discussed. Furthermore, this work will provide insight in required component capacities of shear walls and distributors in transfer diaphragms to achieve the reliability intent. Moreover, factors influencing the probability of collapse of these force-controlled components are discussed and evaluated. Ultimately, this work will contribute to the development of risk-consistent design of structural components between different structural configurations, building locations and design approaches.

1-2 Problem statement

Differences and discrepancies between different design methodologies for required shear capacity of shear walls and required capacity of distributors in transfer diaphragms. Therefore, risk-consistency for these elements between different design methodologies is unlikely. The discrepancies in the design of shear walls and transfer diaphragms are discussed in Sections 1-2-1 and 1-2-2.

1-2-1 Shear capacity design of shear walls

The required shear capacity of shear walls has been debated in the past few years [Wallace et al., 2013]; [PEER/TBI, 2010]; [LATBSDC, 2014]; and [ASCE 7-16, 2014]. Different design approaches require different demand-capacity ratios. Therefore, risk-consistent design of shear capacity of shear walls between design approaches is not achieved.

In PEER/TBI, the strength reduction factor ϕ is defined as 0.75, whereas in LATBSDC the strength reduction factor ϕ is set equal to 1.0. This implies that shear walls designed according to PEER/TBI require 33% more shear capacity than structures designed according to LATBSDC. PEER/TBI is the alternative guideline for San Francisco, whereas LATBSDC is used in Los Angeles. ASCE 7-16 [ASCE 7-16, 2014] also applies a ratio between the calculated demand and required capacity β_{eff}=2.0 for shear capacity design of shear walls, which is equal to the PEER/TBI approach. On the other hand, Wallace [Wallace et al., 2013] suggested that a ratio β_{eff}=1.5 should be sufficient to achieve the reliability intent without explicitly calculating the probability of failure.

Usage of ratio $\beta_{eff} = 2.00$ will result in more conservative design of shear walls. However, agreement has not yet been achieved on whether $\beta_{eff} = 2.00$ is required to achieve the reliability intent or whether $\beta_{eff} = 1.50$ suffices.

1-2-2 Design of distributors in transfer diaphragms

Transfer diaphragms are loaded by inertial force and transfer force. The Code design procedure [ASCE 7-10, 2010] calculates the required capacity of transfer diaphragms and distributors with modal response spectrum analysis using seismic performance factors and the strength reduction factor. For design of distributors, the overstrength factor Ω_o is applied to ensure sufficient margin against collapse. The overstrength factor is not applied to the design of the diaphragm as a whole. Alternative approaches PEER/TBI and LATBSDC allow response history analysis to calculate the force demand in collectors in lieu of the overstrength factor. Furthermore, variations in stiffness influence the force demand in the structure's components. As differences between ASCE 7-10 and alternative design approaches exist, it is unlikely that risk-consistency will be achieved for distributors in transfer diaphragms.

1-3 Objectives

The main objective of this study is to:

Provide insight in the reliability of current design methodologies and provide recommendations for risk-consistent design provisions of specific force-controlled components in reinforced concrete shear wall buildings.

To fulfill the main objective of this study, several sub-objectives were formulated:

- Develop a probabilistic framework to compute the reliability;
- Use the probabilistic framework to provide insight in the reliability of shear capacity of shear walls designed according to PEER/TBI and LATBSDC;
- Use the probabilistic framework to provide insight in the reliability of distributors in transfer diaphragms designed according to ASCE 7-10 and alternative design approaches;
- Provide insight in the influence of stiffness variations on the probability of demand exceeding capacity;

- Evaluate sensitivity of reliability analysis assumptions to provide insight in the influence of variations on the predicted probability of demand exceeding capacity;
- Provide recommendations for risk-consistent design of shear capacity of shear walls and distributors in transfer diaphragms for different design methodologies.

1-4 Outline of report

The outline of the report will be briefly discussed to provide the reader with some guidance. This report is subdivided into six parts.

Part I discusses selected archetype structure and structural analysis model. Furthermore, the various components of the Perform 3D analysis model are discussed. The modelling assumptions for the shear walls and coupling beams, podium and basement diaphragms, basement walls, and gravity columns and damping assumptions are discussed.

Part II defines the required input for the various earthquake analyses. The hazard at the site of the archetype structure is identified and corresponding design and target spectra are computed. Furthermore, ground motions sets selected and scaled to match the target spectra are selected for nonlinear time history analysis.

Part III validates the analysis results for the various analyses from the Perform 3D analysis model. The modal behaviour, ground motion spectra, and shear force, bending moment and interstory drift ratio over the story height are discussed. Furthermore, the computed diaphragm shear stress distributions are validated.

Part IV calculates the required capacity of the specific force-controlled components to meet the design criteria. The required distributor capacity is calculated according to ASCE 7-10 and PEER/TBI design methodologies. Furthermore, the required shear capacity of shear walls per PEER/TBI and LATBSDC design methodologies is calculated.

Part V evaluates the structural reliability of the specific force-controlled elements. The probability of demand exceeding capacity for shear walls loaded in shear and distributors in transfer diaphragms is evaluated. The effects of analysis assumptions, variations in stiffness of the diaphragms and basement walls, nonlinear behaviour and target spectra on the structural reliability of the force-controlled components is discussed. Design methodologies meeting the acceptance criteria for the specific force-controlled elements are proposed. Furthermore, the validity of the results and general applicability of the proposed framework for structural reliability analysis are discussed.

The conclusions and recommendations from this study are presented in Part VI.

Part I

Archetype structure and structural analysis model

Chapter 2

Archetype structure

2-1 Introduction

An archetype structure needs to be selected to evaluate the force-controlled components of interest. The archetype structure needs to have typical reinforced concrete shear wall and transfer diaphragms. The characteristics of the selected structure for structural reliability analysis of the force-controlled components are briefly described in Section 2-2. Section 2-3 gives an introduction on diaphragms and transfer diaphragms in particular. A brief introduction on reinforced concrete shear walls is given in Section 2-4. Furthermore, the site location of the archetype structure is given in Section 2-5.

2-2 Selected archetype structure

The selected archetype structure is a 42-story core-wall-only structure designed by the PEER Task 12 group [PEER Task 12 Group, 2011] for a location in Los Angeles. The building was designed to verify the design of alternative design procedures by PEER/TBI and LATBSDC against the Code design procedure. The designs according to Code, PEER/TBI and LATBSDC are therefore available, and the design was used to calculate the structural reliability of the specific force-controlled elements.

A schematization of the structure is given in Figures 2-1 and 2-2. The building has reinforced concrete shear walls and transfer diaphragms with distributors. Therefore, the archetype structure is fit for structural reliability analysis of the force-controlled components. The layout of the tower and basement are given in Figures 2-3 and 2-4, respectively. An introduction on transfer diaphragms and shear walls is given in Sections 2-3 and 2-4, respectively.

Figure 2-1: Archetype structure [PEER Task 12 Group, 2011]

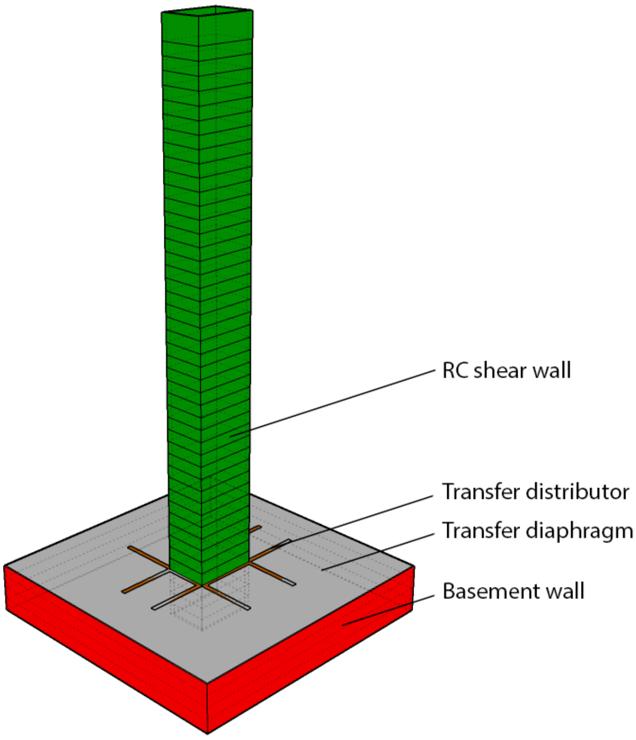

Figure 2-2: Overview of tower layout [PEER Task 12 Group, 2011]

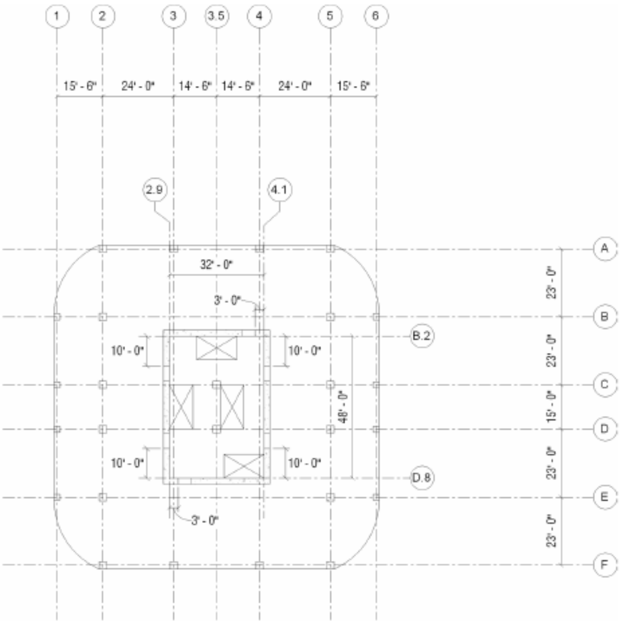

Figure 2-3: Force transfer from collector to vertical element [Moehle et al., 2010]

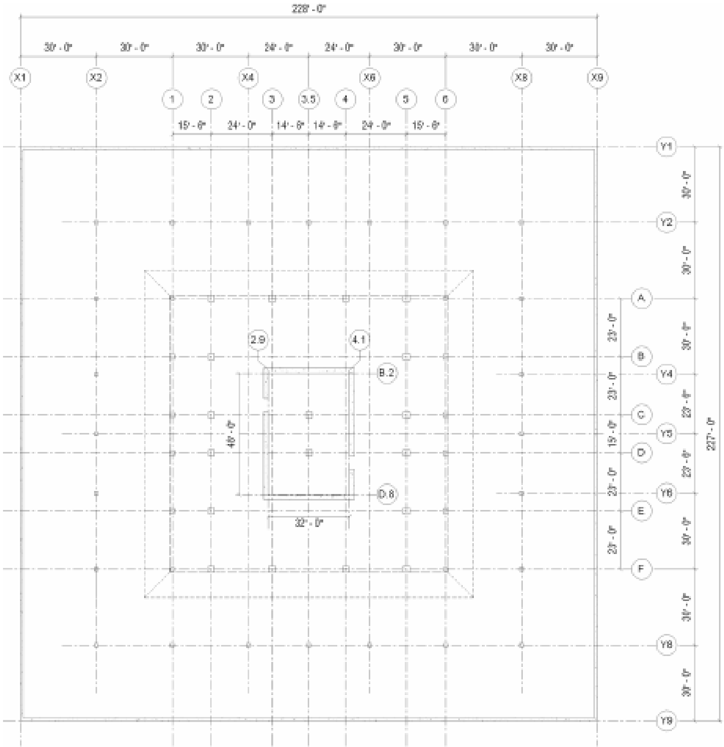

Figure 2-4: Overview of basement layout [PEER Task 12 Group, 2011]

2-3 Diaphragms

Diaphragms are typically used as the horizontal elements in seismic-force-resisting systems [Moehle et al., 2010]. The diaphragms transmit inertial forces from the floor system to the vertical elements of the lateral force-resisting system. The diaphragms may also transfer forces among vertical elements from the seismic-force-resisting system.

The diaphragms are composed of various components including the diaphragm slab, chords and collectors (or distributors) and connections to the vertical elements. The diaphragm shear is transferred to vertical elements by the collectors and by shear friction between the diaphragm and the vertical element. Collectors are compression or tension elements that are capable of transferring the seismic force originating in the diaphragm to the vertical seismic-force-resisting elements. The diaphragm shear can also be transferred into the vertical element by shear friction. Slab reinforcement perpendicular to the vertical elements is typically added to serve as shear friction reinforcement. The combination of direct and shear friction force transfer from collector to vertical element is presented in Figure 2-5.

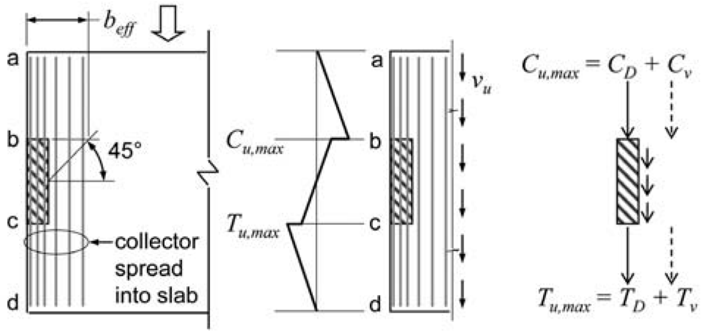

(a) Partial plan (b) Collector actions (c) Collector forces

Figure 2-5: Force transfer from collector to vertical element [Moehle et al., 2010]

The collectors are referred to as distributors when they transfer forces from the wall into the diaphragm as part of the load transfer among vertical elements, such as at podium levels. A schematization of the load transfer in a distributor and diaphragm is given in Figure 2-6.

The collector reinforcement is often located at mid-depth of the slab to minimize interference with the longitudinal reinforcement in the slab. The collectors are designed to respond linearly under axial tension and compression and the placement at mid-depth minimizes flexural yielding. Transverse confining reinforcement is recommended for buildings in regions with higher seismicity to improve the compressive capacity of the concrete and the buckling resistance of the reinforcement.

Diaphragms are generally classified as force-controlled elements. In performance-based

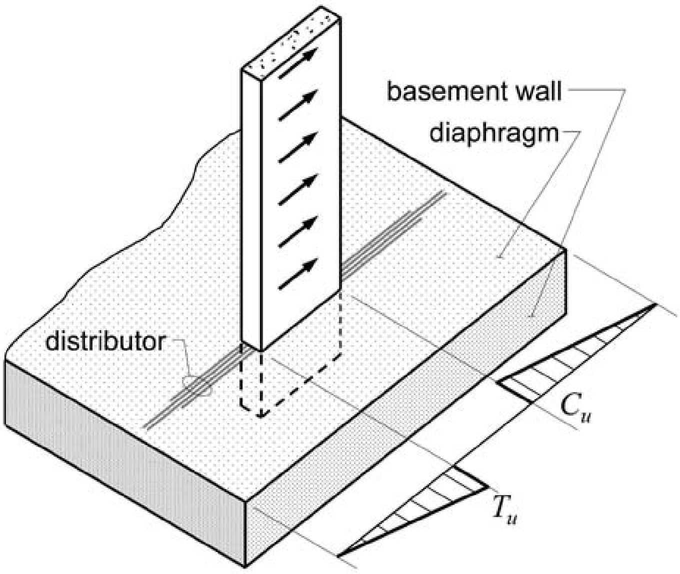

Figure 2-6: Distributor and diaphragm [Moehle et al., 2010]

design, inelastic deformations shall be restricted to deformation-controlled actions. The force-controlled diaphragms should possess sufficient strength capacity. Although diaphragms are force-controlled, cast-in-place concrete slabs are expected to have some inherent ductility provided by steel reinforcement in each direction. This inherent ductility allows redistribution of high in-place stresses through cracking, limited bond slip and yielding of reinforcement. Distributed, rather than concentrated, cracking in slabs is expected for gross reinforcement ratios greater than 0.7%-0.8% [Moehle et al., 2010].

2-3-1 Transfer forces in diaphragms in base structures

Transfer forces occur due to changes in configuration, relative stiffness and/or strength. The transfer forces are the largest at offsets or discontinuities of vertical elements of the seismic-force-resisting systems, for example at setback in the building profile or at podium level at grade. Perimeter foundation walls in base structures are orders of magnitude stiffer than high-rise shear walls [Rad and Adebar, 2006]. Lateral seismic forces are transmitted to the perimeter foundations walls through the transfer diaphragms due to displacement compatibility. For discontinuities in vertical elements, the diaphragms must be designed to resist transfer forces in addition to the inertial forces.

The lateral force resistance in the podium helps a tall building resist seismic overturning forces. he diaphragms reduce the tower wall drifts and reduce the maximum bending moment in the high-rise walls, as the bending moment at the base M_{base} is equilibrated by the sum of the bending moment $M_{foundation}$ that continues down the high-rise wall and the force couple $V_{reverse} \cdot h$. The transfer of lateral forces from the seismic-force-resisting elements in the tower to additional elements in the podium structure, typically through one or more floor diaphragms, is called the backstay effect, based on its similarity to the backspan of a cantilever beam [Moehle et al., 2010]. It is also referred to as "shear reversal" because the shear in the seismic-force-resisting elements can change direction within the podium levels. The highest shear strain is found at the first floor below the base level [Rad and Adebar, 2009]. Consequently, the maximum bending moment occurs above the base structure, which may develop into a flexural hinge. The seismic load transfer in a typical concrete shear wall building connected to a stiff base structure is shown in Figure 2-7.

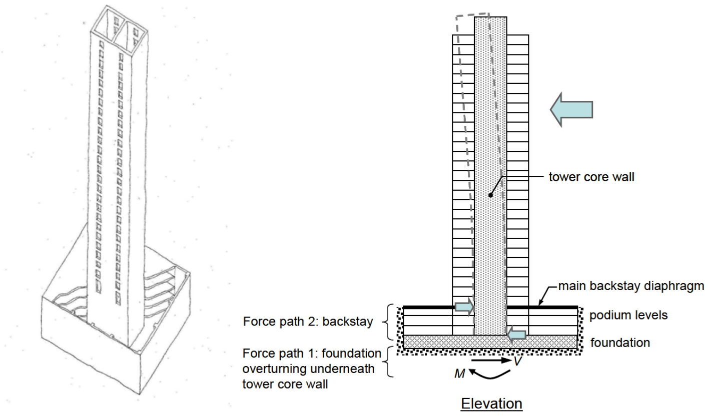

Figure 2-7: Typical concrete shear wall building connected to a stiff base structure [Moehle et al., 2010]

2-4 Shear walls

Reinforced concrete shear walls are commonly used as the primary lateral-load-resisting system for tall buildings. The structural walls effectively resist lateral loads imposed by earthquakes as they provide lateral force resistance, substantial strength and stiffness, and the deformation capacity needed to meet the demands of strong earthquake motions [Orakcal et al., 2006]. The lateral-force-resisting elements include wall segments and coupling beams. The gravity system is usually a slab-column gravity frame; the lateral and gravity system are tied together by a floor frame.

2-5 Site conditions

Since the building was designed for the expected hazard at this location, the same location must be used to evaluate the reliability of the structure. The latitude and longitude of the structure's site are given in Table 2-1.

Latitude	34.05	(West)
Longitude	-118.25	(North)

Table 2-1: Latitude and longitude site location

The structure's site is shown in Figures 2-8 and 2-9.

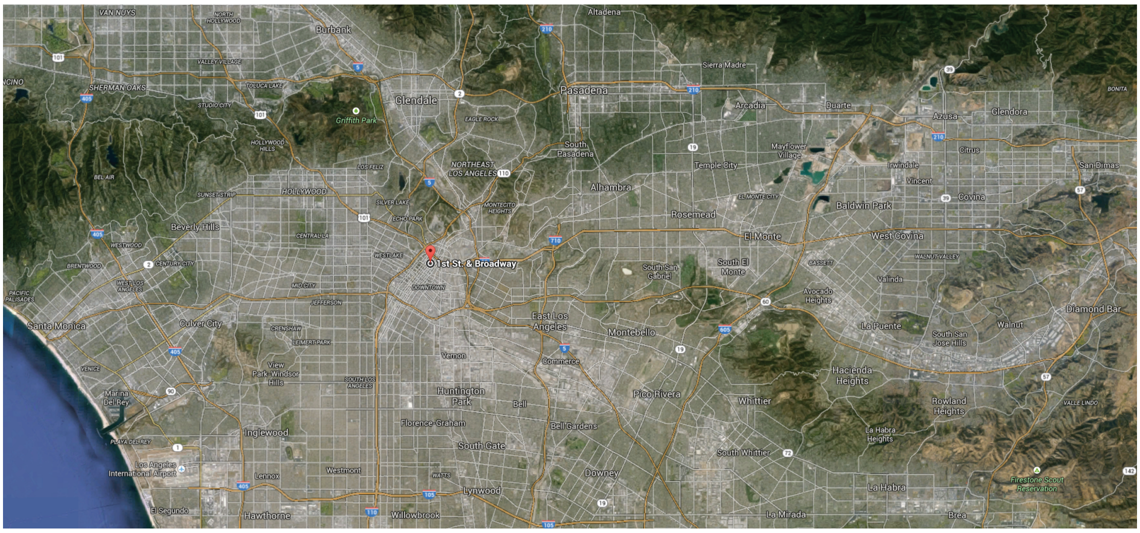

Figure 2-8: Site location

Figure 2-9: Site location - zoom 1

Chapter 3

Modelling of transfer diaphragms

3-1 Introduction

Reinforced concrete diaphragms can be idealized as rigid in an analysis model or modelled explicitly with realistic stiffness properties. First, the effect of stiffness assumptions for the diaphragms are briefly discussed in Section 3-2. Section 3-3 describes the modelling aspects of the diaphragms, including element definition, appropriate stiffness properties, and meshing assumptions.

3-2 Relative diaphragm stiffness and transfer forces

In a theoretical 2D model, the concrete floor slabs could be modelled by a horizontal spring at each floor level, representing the combined stiffness of diaphragms and foundation walls. The free-body diagram of a high-rise wall supported by a single diaphragm at the base level is shown in Figure 3-1. The ratio of the bending moment at the base M_{base} to the shear force at the base V_{base} is denoted as H'. In the shown free-body diagram, the reverse shear force $V_{reverse}$ is equal to the shear force at the foundation $V_{foundation}$.

The relative magnitudes of the bending moment $M_{foundation}$ and force couple $V_r \cdot h$ depend on the flexural rigidity and shear rigidity of the high-rise wall, stiffness of the diaphragms, and soil stiffness [Rad and Adebar, 2008]. The flexural rigidity of the wall below the base is reduced by yielding and cracking of the wall. If the flexural rigidity reduces, the bending moment transmitted down the wall is reduced and the reverse shear force is increased. The soil stiffness of the wall foundation influences the bending moment transmitted down the wall. A reduced soil stiffness reduces the bending moment $M_{foundation}$ and therefore increases the reverse shear force.

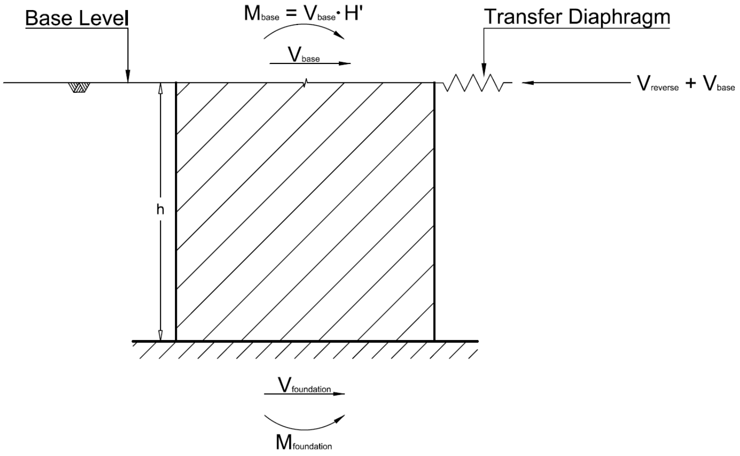

Figure 3-1: Free-body diagram of forces in high-rise shear wall

Reduction of the shear rigidity of the wall due to diagonal shear cracking reduces the reverse shear force. If the diaphragm stiffness is reduced, the maximum reverse shear force is also reduced. The diaphragm stiffness is reduced by shear cracking.

3-2-1 Rigid versus flexible diaphragms

ASCE 7-10 permits reinforced concrete diaphragms to be idealized as rigid, provided that there are no horizontal irregularities and that the span-to-depth ratio is less than or equal to three. The rigid diaphragm assumption reduces the modelling and computational effort. However, the distribution of inertial forces to and redistribution of lateral forces among the different vertical elements of the lateral system can be better estimated by including the diaphragm flexibility. This is especially true at locations where large transfer forces occur.

The podium and basement diaphragms are therefore modelled explicitly using appropriate stiffness properties. Consequently, the analysis model is able to realistically simulate the distribution of inertial forces to and transfer forces between the shear walls, diaphragms, basement walls, and foundation. The modelling aspects of transfer diaphragms, including the element definition, appropriate stiffness assumptions, and meshing, are described in Section 3-3.

3-3 Modelling aspects of transfer diaphragms

3-3-1 Element definition

The diaphragms are modelled as elastic shell elements with modified stiffness properties. The stiffness modifiers are applied to the modulus of elasticity and shear modulus when defining the material to account for stiffness reduction due to cracking, limited bond slip and yielding of reinforcement. Perform 3D only allows shell elements to be specified as elastic. This is reasonable since diaphragms are generally classified as force-controlled, as described in Section 2-3.

The shell elements are assumed to be thin, with no through-thickness shear deformations. The main difference between thin and thick shell formulation is the inclusion of transverse shear deformation in plate-bending behaviour. Inclusion affects plate-bending (out-of-plane) behaviour, but has no effect upon membrane (in-plane) behaviour. Thin-plate formulation neglects transverse shear deformation following a Kirchhoff application. Thick-plate formulation accounts for transverse shear deformation according to Mindlin/Reissner. The contribution of transverse shear deformation becomes significant when ratio between the span of plate-bending curvature and thickness is approximately 20:1 or 10:1. Furthermore, shear deformation may become significant in locations of bending-stress concentrations, for example in regions near openings or geometric discontinuities. However, thick-plate formulation is not recommended in cases where the transverse shear deformation is small, because the accuracy of thick-plate formulation is sensitive to large aspect ratios and mesh distortion.

The span-to-depth ratio is approximately 22:1 for the archetype structure and the podium diaphragms have no openings or geometric discontinuities. Therefore, the transverse shear deformation is small and use of thin shell formulation to model the podium diaphragms is justified.

3-3-2 Stiffness assumptions

The assumed in-plane stiffness properties of the diaphragm will not only affect the demand in the diaphragms, but also the force distribution among the vertical elements. For the backstay effect, an increased flexibility will reduce the force demand in the diaphragm and increase the overturning moment in the foundation. The stiffness values depend on the level of cracking. Stiffness modifiers are applied to the diaphragm in-plane gross-section stiffness properties to approximate the stiffness reduction associated with the expected diaphragm cracking. Nakaki [Nakaki, 2000] concluded that stiffness modifiers for reinforced concrete diaphragms fall in the range of 0.15 to 0.50 for design-level earthquake demands.

The selected stiffness modifiers for ground level and basement diaphragms are based on the suggested values from LATBSDC and given in Table 3-1. The selected stiffness modifiers for podium level and basement diaphragms represent mean estimates considering the level of excitation and damage of interest. The stiffness values represent the expected reduced stiffness associated with demand exceeding capacity for frequent and less frequent earthquake intensities. Hence, the same effective stiffness assumptions are used for all intensity levels.

Diaphragm	**Flexural stiffness**	**Shear stiffness**
Podium diaphragm	$0.25E_cI_g$	$0.25G_cA_g$
Basement diaphragms	$0.25E_cI_g$	$0.25G_cA_g$

Table 3-1: Stiffness assumptions of podium and basement diaphragms

3-3-3 Diaphragm mesh

An optimal diaphragm mesh finds the right balance between accuracy of the results and runtime. A preliminary study was done to find the optimal diaphragm mesh. The results and runtime for a fine diaphragm mesh were compared to a coarser diaphragm mesh. The diaphragm meshes are given in Figures 3-2 and 3-3 and a comparison of the number of elements is given in Table 3-2. It was found that the analysis runtime was reduced by 50% without impairing the shear force, transfer force or force distribution in the diaphragm. Therefore, the coarse mesh was adopted. A schematization of the selected diaphragm mesh and basement wall mesh is given in Figure 3-4.

	Fine mesh	Coarse mesh	Reduction [%]
Slab elements	1400	716	49%
Basement wall elements	624	524	15%

Table 3-2: Diaphragm mesh

3-4 Conclusion

The podium and basement diaphragms of the archetype structure will be modelled with thin elastic shell elements with modified stiffness properties. The coarse diaphragm mesh reduces analysis runtime without impairing the analysis results. The force transfer and shear stress distribution in the diaphragms is investigated and validated in Chapter 13.

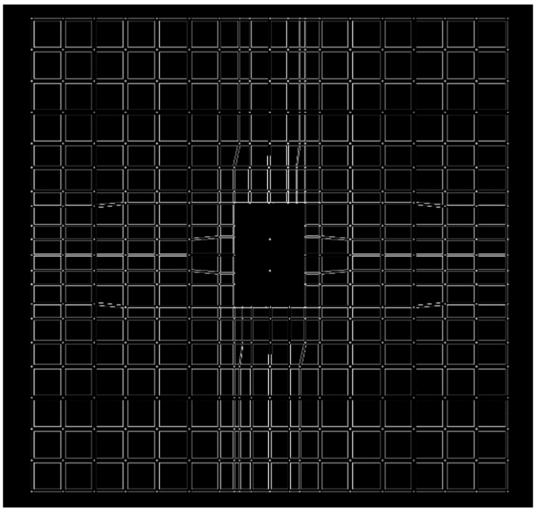

Figure 3-2: Fine diaphragm mesh in Perform 3D

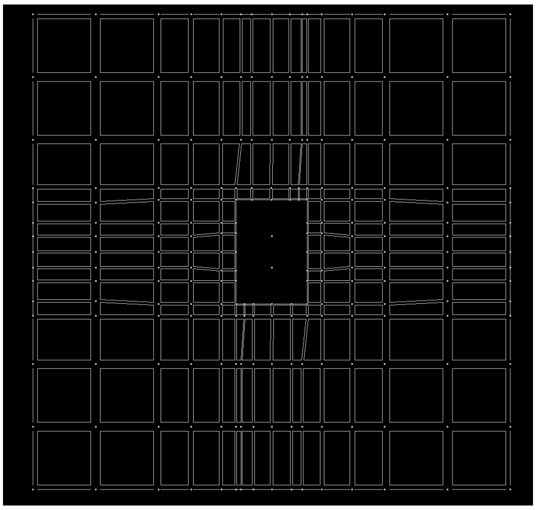

Figure 3-3: Coarse diaphragm mesh in Perform 3D

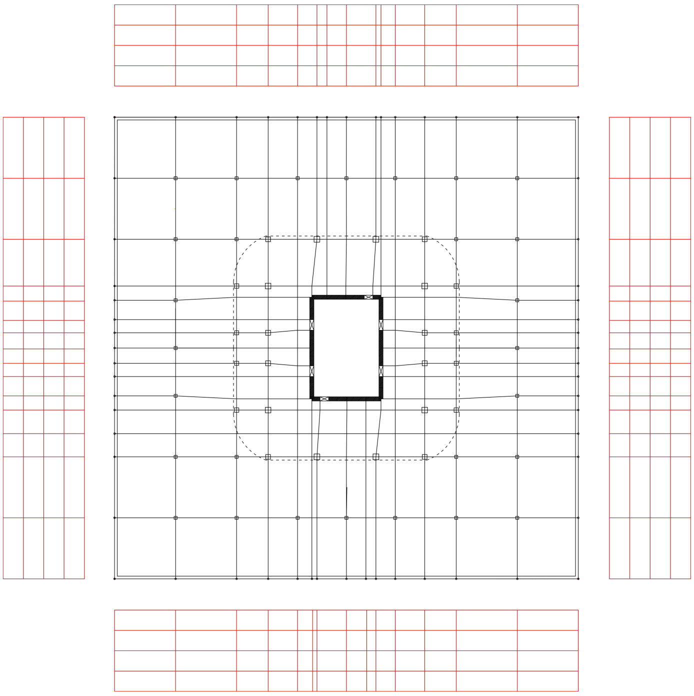

Figure 3-4: Schematization of selected diaphragm mesh and basement wall mesh

Chapter 4

Modelling of shear walls

4-1 Introduction

Modelling of the structural wall is essential to accurately predict structural response quantities from nonlinear response history analysis. The objectives when modelling concrete shear walls are to effectively capture the hysteretic response, at both local and global levels, and the interaction with other structural members. Furthermore, the model should be relatively simple to implement.

First, an overview of the shear walls in the archetype structure is given in Section 4-2. Different theoretical concrete shear wall models are discussed in Section 4-3. The Perform 3D shear wall model is discussed in Section 4-4. Furthermore, the shear wall model is validated in Section 4-5 and other modelling assumptions are discussed in Section 4-6.

4-2 Shear walls in archetype structure

An overview of the structural shear walls is given Figure 4-1. The schematization includes the floor levels, wall thickness and coupling beam configuration. The left shear wall in Figure 4-1 shows the north and south shear wall, the right shear wall shows the east and west shear wall. The thickness of the shear wall is decreases to the top of the shear wall. The largest wall thickness, 36 [in], is found in north and south wall between the foundation and level 13 have the largest wall thickness.

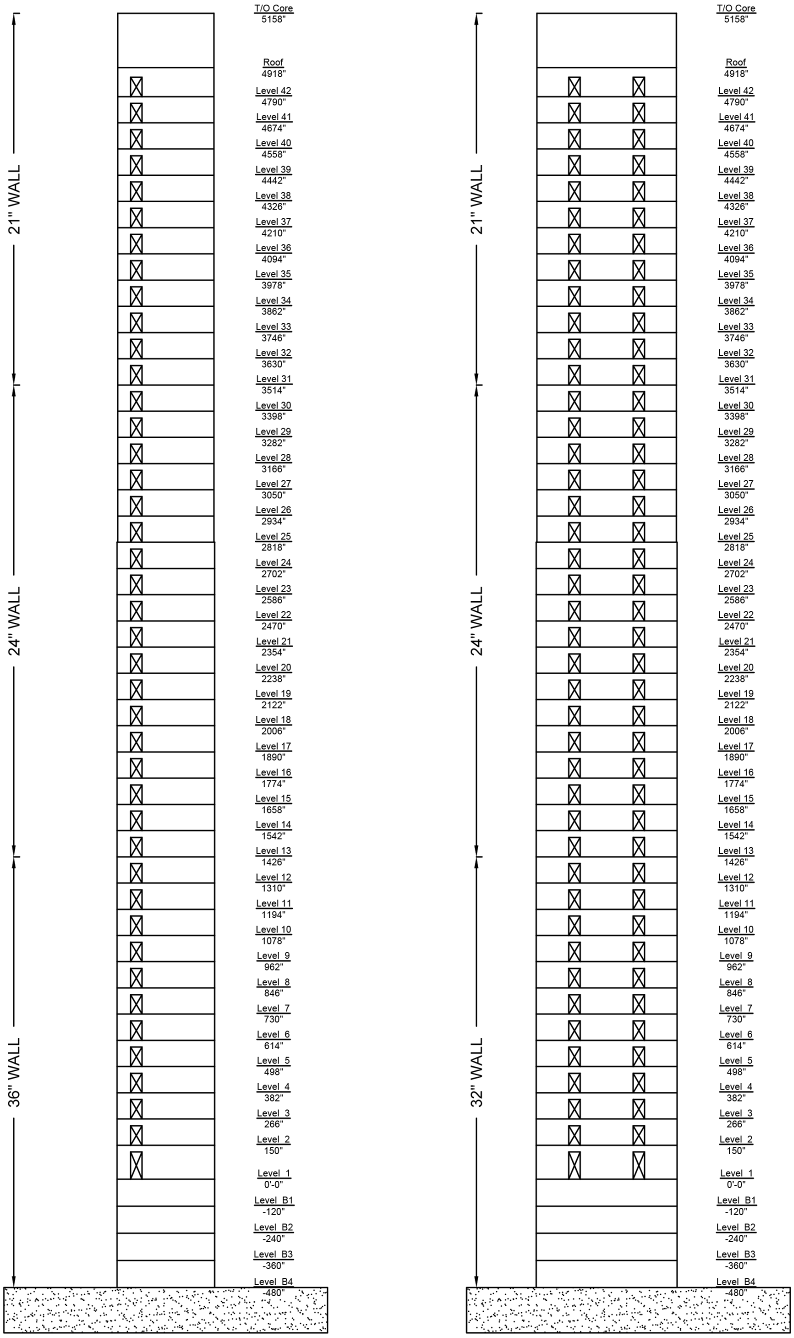

Figure 4-1: Overview shear walls in archetype structure

4-3 Theoretical concrete shear wall models

Reinforced concrete (RC) shear walls can be modelled in several ways. Two common models for analysis and design of RC shear walls, beam-column element model with rigid plastic hinges and fibre model with uniaxial material relations, are described in this section.

4-3-1 Beam-column element model

The beam-column element model with plastic hinges is simple to implement and provides reasonably accurate estimates of global and average local response [Wallace, 2012]. The beam-column element model has various drawbacks. One drawback is the inability of the model to account for migration of the neutral axis. Another drawback is that, although the effect of axial load variation on wall stiffness can be accounted for, a discrete bending stiffness is typically specified. The monitored response quantity is plastic rotation.

4-3-2 Fibre element model

Fibre element models, such as the Multiple-Vertical-Line-Element model (MVLEM), simulate the response by a series of uniaxial elements. The cross-sectional geometry of the fibre model is comprised of individually defined uniaxial concrete and reinforcing steel fibres [Orakcal and Wallace, 2004]. The primary simplification of the fibre model is the plane-section-remain-plane assumption. The fibre model has the ability to account for neutral axis migration and the effect of axial load variation on stiffness. The main drawbacks of the fibre model are the added complexity and the sensitivity of the results to the meshing [Wallace, 2012]. The monitored response quantities are average strain, curvature or rotation and the fibre model provides a good prediction of the global and local responses [Orakcal et al., 2004].

Although the fibre element model adds complexity, it has clear advantages over the beam-column element model. The MVLEM will therefore be used to model the RC shear walls.

4-3-3 Selected theoretical shear wall model

The selected MVLEM was studied extensively because it successfully balances the simplicity of a macroscopic model and the refinements of a microscopic model ([Orakcal et al., 2004]; [Orakcal et al., 2006], [Wallace, 2012]). A single MVLEM has six global degrees of freedom; two translational and one rotational degree of freedom at the centre of the rigid beams at the top and the bottom of the element, as shown in Figure 4-2. Infinitely rigid beams at the top and bottom of the element account for the primary simplification of the model: plane-sections-remain-plane when calculating the uniaxial stresses and strains in the fibre elements.

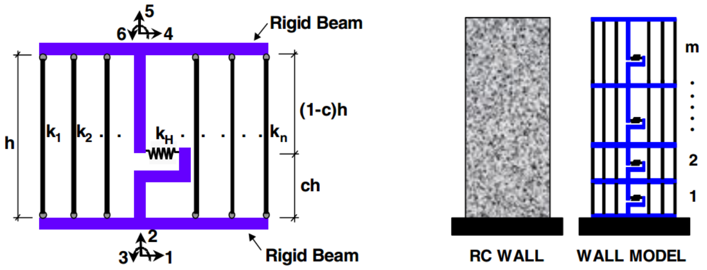

Figure 4-2: Multiple Vertical Line Element model [Orakcal et al., 2006]

The flexural response is simulated by a series of uniaxial elements connected to these rigid beams. The parameters associated with the flexural model are the number of uniaxial elements n along the length of the wall, the constitutive material relations assigned to these uniaxial elements, and the parameter c defining the location of the centre of rotation along the height of the MVLE model. The constitutive material relations assigned to the uniaxial elements and the tributary area of these uniaxial elements define the stiffness properties and force-displacement behaviour. Typically, perfect bond between the concrete and steel is assumed, i.e. the strains in concrete and steel are equal within each uniaxial element. The relative rotations between the bottom and top faces of the element occur around a point on the central axis at height ch, as shown in Figure 4-2. A suitable value of c is based on the expected curvature distribution along the element height h [Orakcal et al., 2006] and a value of c=0.4 is recommended by [Vulcano et al., 1988] based on comparison between analytical and test results.

The shear response is simulated by a horizontal shear spring placed at height ch. In the MVLEM, the flexural/axial behaviour is decoupled from the shear behaviour, which means that flexural deformations do not affect shear strength or shear deformation. The horizontal shear displacement at the top does therefore not depend on c, as shown in Figure 4-3.

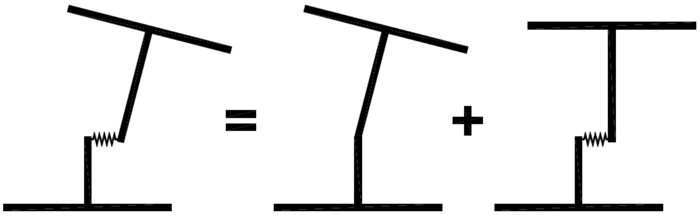

Figure 4-3: Uncoupled flexural and shear response in MVLEM [Orakcal et al., 2006]

A structural wall element is modelled as m MVLEM elements stacked on top of each other. Stacking more elements along the height, i.e. reducing the height h of the MVLE model, will improve analytic results [Fischinger et al., 1992]. The improvement is more significant in the regions where inelastic deformations is expected. A large number of MVLEM elements along the wall height will diminish the influence of parameter c on the predicted response [ATC 72-1, 2010].

Finally, it is noted that the effective stiffness is determined based on the selected material stress-strain relations, axial load and current condition of the element. Determination of an effective stiffness is therefore not required.

4-4 Perform 3D shear wall model

The fibre model employed by Perform 3D, as shown in Figure 4-4, is conceptually the same as the Multiple-Vertical-Line-Element model (MVLEM) described in Section 4-3. There are two options for modelling fibre elements in Perform 3D: 'General Wall' elements and 'Shear Wall' elements. 'General Wall' elements are substantially more complex and intended mainly for squat walls. 'Shear Wall' elements are more simple and recommended for shear walls in tall buildings [Powell, 2007]. 'Shear Wall' elements will therefore be used to model the shear walls in this study.

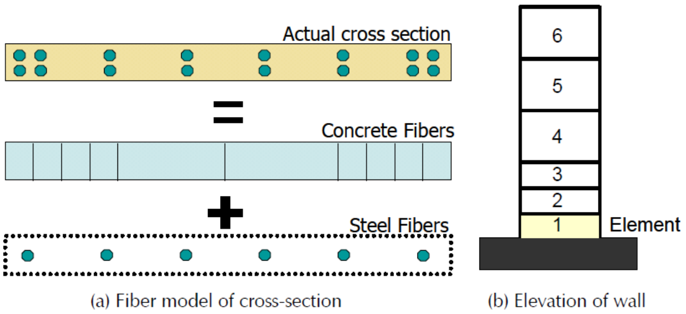

(a) Fiber model of cross-section (b) Elevation of wall

Figure 4-4: Fibre model of cross-section

The 4-node 'Shear Wall' element has 3 axes. Axis 1 is normal to the element, Axis 2 is the direction along the fibre elements, parallel to Axis IK, and Axis 3 is the transverse direction. The element orientations are shown in Figure 4-5.

The 'Shear Wall' element is an atypical element with three separate layers, namely:

1. Vertical layer used for elastic or inelastic modelling of axial/bending behaviour along Axis 2. The axial force and bending moment are constant along the length of the element. Furthermore, the cross-section is assumed to be constant along the length of the element.

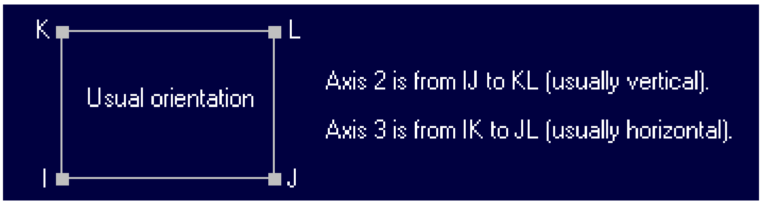

Axis 2 is from IJ to KL (usually vertical).

Axis 3 is from IK to JL (usually horizontal).

Figure 4-5: Element orientations of 'Shear Wall' element

2. Horizontal layer used for elastic modelling of axial/bending behaviour along Axis 3.
3. Shear layer to model elastic or inelastic concrete shear behaviour. A reduced shear stiffness can be assigned to the shear wall material to reflect shear cracking. In Perform 3D, the shear strength is modelled independently of the axial load effect.

The 'Shear Wall' element in Perform 3D requires only a fibre section in the vertical layer. The walls are much stiffer in-plane than out-of-plane, and the stiffness contribution of the out-of-plane bending is only a small part of the total stiffness. Therefore, the horizontal layer is assumed to be elastic. The shear layer is modelled by a single elastic or inelastic horizontal spring and therefore requires no fibre section. The vertical layer, horizontal layer and shear layer are further described in Sections 4-4-1, 4-4-2, and 4-4-3, respectively.

4-4-1 Vertical layer

4-4-1-1 Introduction

The vertical layer is used for elastic or inelastic modelling of axial/bending behaviour. The vertical layer is the only layer that requires fibre sections. Horizontal fibre sections in the vertical layer are required to model the vertical axial/bending behaviour. The fibre sections in represent the cross-sectional concrete and reinforcing steel. Constitutive material relations must be assigned to these fibre sections to define the stiffness properties and the vertical flexural/axial force-displacement behaviour of the shear wall. The response of fibre models is related directly to uniaxial material behaviour, without incorporating any additional empirical relations. The results are therefore sensitive to the chosen material parameters associated with monotonic stress-strain behaviour and the hysteretic parameters.

4-4-1-2 Fibre sections

Two types of fibre sections can be specified in Perform 3D, a Fixed Size (FS) section and an Auto Size (AS) section.

Fixed Size sections are very general and can be used for sections that have varying thickness and/or reinforcement [Powell, 2007]. This type of section requires substantial effort and care. The area and location must be specified for each fibre, the fibre locations are defined as coordinates relative to the centre of the cross-section. The specified section width should be equal to the width or height of the element in which it is used.

Auto Size sections are more restrictive, but require less effort. The section must have constant thickness and uniform reinforcement. Only the number of steel and concrete fibres needs to be specified. Perform 3D assumes equal size fibres to adjust the fibre areas and coordinates to match the width or height of the element. The steel area is specified as a percentage of the concrete area.

Powell [Powell, 2007] recommends the AS sections to set up the fibres for the basic reinforcement, and FS sections for the additional reinforcement. Powell also recommends FS sections for concrete fibres. Smaller fibres are recommended at the edges of the section to allow concrete crushing to occur. Relatively larger fibres are recommended near the centre of the section to reduce analysis time. One element is used over the entire length of the wall by Powell. In this study, the wall was subdivided into multiple elements to make a distinction between confined and unconfined concrete. The recommendation of smaller concrete fibres near the edges and larger concrete fibres near the centre of the wall was adopted. AS sections were used to specify the steel fibres and a new section was defined for every steel percentage. Furthermore, it is noted that parallel FS and AS sections are used to describe a single wall element. To avoid double-counting the shear and horizontal axial-bending the concrete fibre FS sections have the correct wall thickness and Young's modulus, whereas a very small wall thickness and Young's modulus is assigned to the steel fibre AS sections. It is recognized that avoiding double-counting of the shear is essential whereas it matters much less for horizontal axial/bending.

4-4-1-3 Constitutive stress-strain relationships

The constitutive constitutive stress-strain relationship employed by Perform 3D approximate the fairly sophisticated constitutive relations implemented by various studies [Orakcal et al., 2004]; [Orakcal and Wallace, 2004], [Orakcal et al., 2006]. These studies implement refined hysteretic stress-strain laws in the research-oriented program OpenSees. The force-deformation response of the component, i.e. the backbone curve, in Perform 3D can be elastic-perfectly-plastic (EPP) or trilinear. The loss of strength can also be modelled when appropriate. The backbone curve in Perform 3D is defined by specifying the force and deformations at up to five points: the yield point (DY), point of ultimate deformation (DU), point of onset of loss of lateral load capacity (DL), point of residual lateral load capacity (DR), and point of analysis termination (DX). The use of simplified material relations by Perform 3D does not significantly impair the ability of the fibre model to predict the overall load-displacement relations and strain distributions [ATC 72-1, 2010]. The steel and concrete stress-strain relationships will be described in the following paragraphs. The stress-strain relationships as defined in Perform 3D are given in Table 4-1.

Reinforcement steel stress-strain relationship

The modified nonlinear stress-strain relation of Menegotto and Pinto [Menegotto and Pinto, 1973] is used to define the steel stress-strain relationship in this study. The model by Menegotto and Pinto accurately describes the hysteretic behaviour of reinforcement [Orakcal et al., 2004]. The symmetric, trilinear backbone curve is defined by the yielding point, ultimate stress point and failure strain. The Menegotto-Pinto model is described in Appendix A-1-1. The trilinear backbone curve is defined for reinforcement steel type ASTM A706 Grade 60 in Appendix A-1-1 which is the reinforcement steel used in the concrete shear walls.

The expected steel stress-strain relationship in Perform 3D is defined by a symmetric, trilinear material relation and given in Figure 4-6. The definition of the Perform 3D steel stress-strain relationship, based on the modified nonlinear stress-strain relation of Menegotto and Pinto, is given in Appendix A-1-2.

Cyclic degradation of reinforcement was modelled through the specification of energy degradation factors. The energy degradation factor is the ratio between the area of the degraded hysteresis loop and the area of the undegraded loop as a function of the maximum strain in a given hysteresis loop. For small deformation cycles, the area is ratio is close to 1.0 since there is no degradation. The energy factors get progressively smaller as the maximum deformation and thus the degradation increases. The energy factors make the material backbone curve dependent on the loading history by altering the curve with each load excursion. Physically, the energy degradation factors account for the Bauschinger effect. The Bauchinger effect is a general phenomenon found in most polycrystalline metals. It includes the reduction of the yield stress after load reversal and a decrease of curvature in the transition zone between the elastic and plastic branches. The reduction of the yield stresses increases as the maximum deformation increases [Abdelnaby, 2012]. Hence, the energy factors decrease with the increase of the plastic strain component of the last load excursion. The energy factors are typically calibrated using test data. The energy degradation parameters as verified by [Orakcal et al., 2006] for a rectangular wall (RW2 test specimen) and adopted by [Ghodsi and Ruiz, 2009] are used in this study. The cyclic degradation parameters are given in Appendix A-1 Table A-2.

Concrete stress-strain relationship

The modified Mander model [Mander, J.B.; Priestley, M.J.N., Park, 1988]; [Chang and Mander, 1994b] was used for modelling cyclic stress-strain behaviour of confined concrete. The definition and calculation of the modified Mander model are given in Appendix A-2-1. The model is capable of capturing the hysteretic behaviour, progressive degradation of stiffness for increasing strain values, and the effects of confinement and tension stiffening.

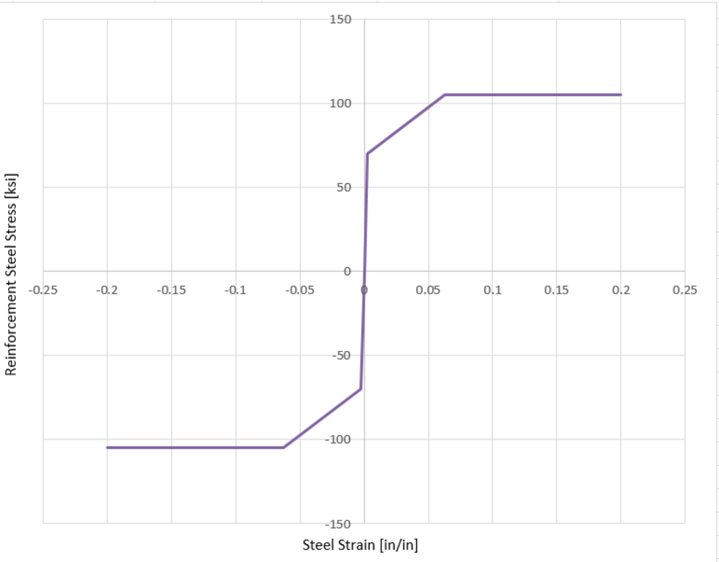

Figure 4-6: Expected steel stress-strain relationship

Furthermore, the modified Chang and Mander model succesfully simulates gradual crack closure [Orakcal et al., 2006]. The tensile strength of concrete is assumed to be zero, which is a conservative assumption.

The expected concrete stress-strain relationship in Perform 3D is defined by four linear segments. The fourth linear segment accounts for strength loss in the concrete due to concrete crushing. The multi-linear relations are derived from the modified Mander model, as described in Appendix A-2-2. The modified Mander model for confined concrete with expected compressive strength $f'_{c,exp} = 10.4$ [ksi] and the approximation in Perform 3D are given in Figure 4-7. It is shown that a close match between the multi-linear relations and modified Mander model can be obtained if the correct values are chosen.

Material	E_c	FY	FU	DU	DX	DL	DR	FR/FU
Confined Concrete (8 ksi)	5.079	10.40	13.73	0.00416	0.05	0.00572	0.0183	0.495
Steel Non-buckling	29000	70.2	105	0.0628	0.20	-	-	-

Table 4-1: Stress-strain relationships for steel and concrete fibres as defined in Perform 3D

4-4-2 Horizontal layer

The horizontal layer is used for elastic modelling of axial/bending behaviour along Axis 3. The vertical section of the horizontal layer is assumed to be elastic. The walls are

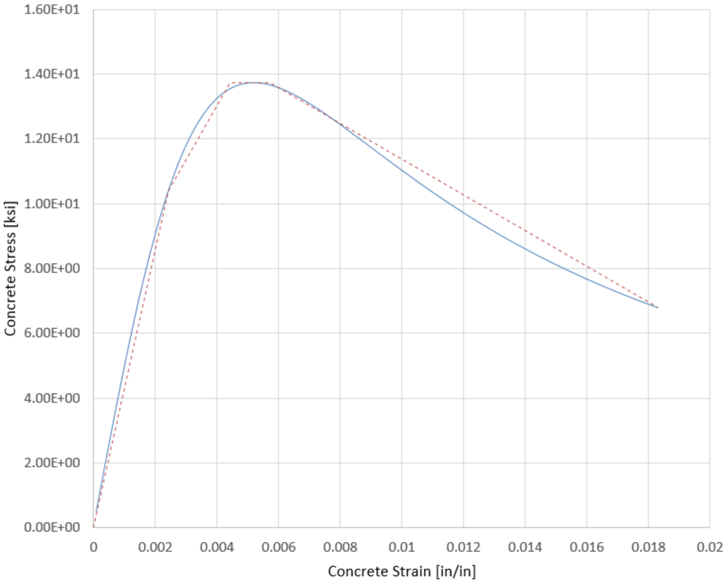

Figure 4-7: Expected stress-strain curve for confined concrete with expected concrete strength ($f'_{c,exp}$) of 10.4 [ksi]

much stiffer in-plane than out-of-plane, and the stiffness contribution of the out-of-plane bending is only a small part of the total stiffness.

The E-modulus of the horizontal layer is taken equal to the uncracked Young's modulus:

$$E_{c,hor} \quad = \quad E_c \quad = \quad 40000\sqrt{f'_{c,exp}} + 10^6 \quad = \quad 5079.216 \quad [\text{ksi}] \tag{4-1}$$

4-4-3 Shear layer

The shear layer in the 'Shear Wall' element accounts for elastic or inelastic concrete shear behaviour in the shear wall. The shear layer is modelled by a single horizontal spring. According to the model by [Wallace, 2007], the shear force-deformation relation is defined by two points, the cracking point and the point of ultimate shear stress. The definition and calculation of the cracking and ultimate shear stress-strains are given in Appendix A-3-1.

Shear and flexural/axial behaviour are uncoupled in Perform 3D. To model the wall behaviour as realistically as possible, an inelastic shear-deformation relation is adopted for the shear-deformation relation of confined concrete wall sections. Nonlinear shear deformations were observed during tests, even though the wall shear forces were only about 50% of the nominal shear capacity of the wall. To account for nonlinear shear deformations, Gogus [Gogus, 2010] suggests an initial shear spring stiffness of G_c up to the point where shear cracking occurs and a reduced post-yield stiffness of $0.1G_c$. The shear stress-strain relationship is derived from recommendations by [ACI 318-11, 2011]; [Wallace, 2007]; [ATC 72-1, 2010]; [Gogus, 2010]; and [Orakcal et al., 2006] in Appendix A-3-2. These recommendations were found to produce a good match between the overall load versus top displacement relations [Gogus, 2010]. For the archetype structure, the inelastic shear stress-strain relationship is calculated for eleven vertical sections (Floors B4-B1, B1-1, 1-4, 4-7, 7-13, 13-19, 19-25, 25-31, 31-37, 37-41, and 41-Roof), based on the horizontal reinforcement ratio, and each vertical section is subdivided into five horizontal sections (North-wall-west, North-wall-east, West-wall-north, West-wall-mid, and West-wall-south). The concrete shear stress strain relation for the walls of floors 1 to 4 is given in Figure 4-8.

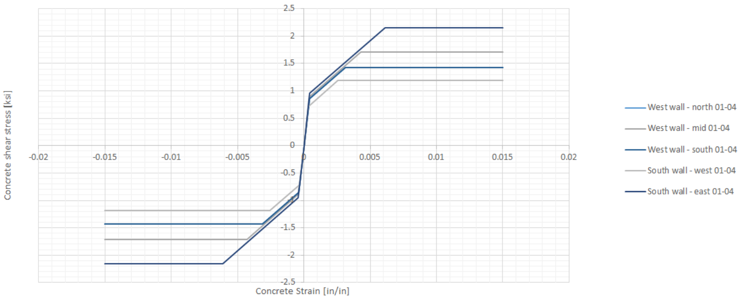

Figure 4-8: Wall shear stress-strain model for floors 1 to 4

4-5 Validation of the structural wall model

To validate the structural wall model, studies comparing test results with analytical results from a theoretical MVLE model and more simplified Perform 3D model were reviewed. It is important to validate the model to ensure that the calculated responses from the nonlinear time history analysis provide a realistic display of the responses that would be experienced in nature. Hence, a close match between test results and the analytical model is essential to obtain responses from the NLTHA that are in accordance with the actual response of the structure.

4-5-1 Comparison of analytical results from MVLE model with test results

Several studies compared results from tests on rectangular (planar) and flanged (T-shaped) RC walls to analytical results from a MVLE model to validate the theoretical MVLE model [Orakcal et al., 2004], [Orakcal and Wallace, 2004]; [Wallace, 2007]; [Gogus, 2010]; and [ATC 72-1, 2010].

Planar walls

The MVLE model provides a good prediction of the responses observed in the tests of the wall with rectangular cross-section [Orakcal et al., 2004]. The wall displacement profile of slender RC structural walls governed by flexure was well captured, including nonlinear flexural rotations and deformations experienced within the plastic hinge region of the wall. Behavioural characteristics such as shifting of the neutral axis along the wall cross-section, the effect of fluctuating axial force on strength and stiffness were also captured effectively. Furthermore, tension-stiffening, concrete confinement, lateral load capacity and nonlinear shear behaviour, and the yield point and wall stiffness both prior to and after wall yielding were captured in the analysis results. Cyclic wall response, including stiffness degradation and strength deterioration, pinching behaviour and hysteretic shape were also captured in the analysis results. Furthermore, the MVLE model was capable of capturing local responses, such as base rotation, average curvature, and average strains [Orakcal et al., 2006].

The wall tensile strains were predicted with reasonable accuracy; the wall compressive strains tended to be under-predicted by analytical models [ATC 72-1, 2010]. One reason for the discrepancy between the predicted and observed compressive strain in rectangular walls may be caused by interaction between flexural and shear behaviour [Wallace, 2007]. Larger compressive strains were predicted with the coupled model compared to the uncoupled model [Wallace, 2012]. Furthermore, the uncoupled MVLE model was found to be more accurate for wall with relatively high span-to-depth ratios [Orakcal et al., 2004]. The larger experimental compressive strains were therefore likely related to physical phenomena. Coupled shear-flexural-axial models are difficult to implement at this time [PEER/TBI, 2010]. Models that account for this interaction are not yet available in Perform-3D. For the modelled wall and loading history studied by Orakcal and Wallace [Orakcal and Wallace, 2004], the underestimation of compressive strains did not have a significant impact on the prediction of the global response.

T-shaped walls

For T-shaped walls, Orakcal and Wallace [Orakcal and Wallace, 2004] observed fairly good analytical global response prediction when the flange was in compression. The measured compressive strains along the flange were approximately uniform. The wall therefore effectively behaved like a wall with a rectangular cross-section and the same level of accuracy in the prediction of the global response was therefore observed. Meanwhile, discrepancies between the analytical model and experimental results were observed when the flange is in tension. The reason for the discrepancy is the nonlinear tensile strain distribution in the flange. This resulted in overestimation of lateral load capacity and under-prediction of inelastic lateral displacements. Similar to the rectangular walls, compressive strains tended to be underestimated, presumably due to nonlinear shear deformations within the nonlinear flexural deformation region of the wall.

From the reviewed studies it can be concluded that the analytical results from the MVLE model provide a good prediction of the responses observed in tests.

4-5-2 Comparison of simple model, complex model, and test results

The results from the simplified material models used in Perform 3D showed good agreement with test results in both the positive and negative loading direction, as shown in Figure 4-9. Furthermore, the results obtained using simplified material models were very similar to the results obtained using sophisticated research-oriented material models. Especially at smaller drift ratios, results showed good agreement between the simplified material models employed in commercial software (Perform 3D), the complex model (MVLEM) and test results. At larger drift ratios, somewhat more variations were observed between the results for different analytical models and reloading test results. Most significant discrepancies occurred in the predicted concrete compressive strains, but the results obtained using both the simple and complex model were still reasonably accurate. Therefore, it is concluded that the use of simplified material relations in Perform 3D does not significantly impair the overall performance of the MVLE model.

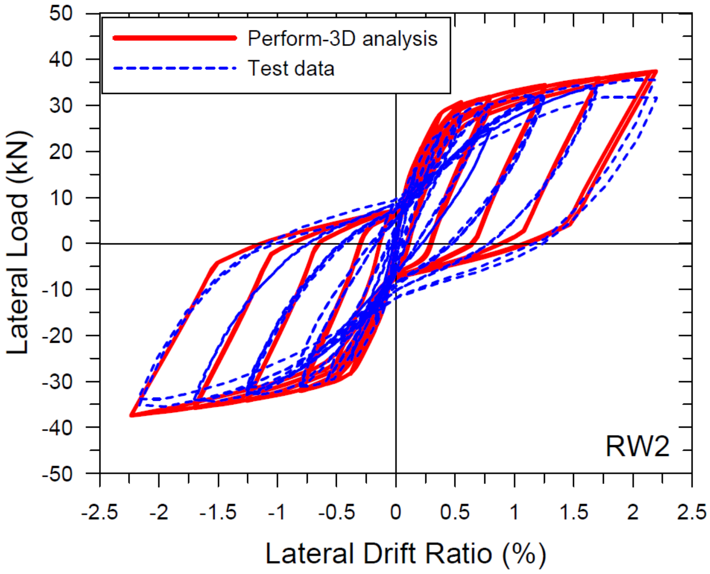

Figure 4-9: Comparison of wall versus model results generated by Perform 3D [ATC 72-1, 2010]

The Perform 3D fibre model is capable of accurate prediction of the lateral-load versus displacement behaviour of RC walls subjected to cyclic loading [Wallace, 2012]. The layout of the structural walls in the archetype structure can be schematised as I-shaped. The discrepancies between the analytical model and experimental results observed for the T-shaped wall when the flange is in tension are therefore not expected. The fibre model as modelled in Perform 3D is therefore valid to predict the structural response quantities for the archetype structure from nonlinear response history analysis.

4-6 Other modelling assumptions

4-6-1 Meshing of the shear wall

Meshing of the concrete shear wall is based on recommendations from several studies [Orakcal et al., 2006]; [Salas, 2008]; and [Wallace, 2012]. These studies found the overall results to be relatively insensitive to the number of fibres and number of elements. Increasing the number of elements, i.e. refining the mesh, can be valuable to obtain more information on local responses. As noted in Section 4-3-3, a larger number of elements also diminishes the influence of location of the horizontal shear spring placed at height ch on the predicted results. However, if a fine mesh is combined with elastic-perfectly-plastic reinforcing steel behaviour, nonlinear deformation can concentrate in a single element [Salas, 2008]. The problem of concentration of nonlinear deformations in a single element was eliminated by including a moderate post-yield hardening slope in the steel reinforcement constitutive model.

The element height in the estimated plastic hinge zone should be approximately equal to the plastic hinge zone to produce good correlation with test results [ATC 72-1, 2010]. The hinge length may be estimated by the formulas from Paulay and Priestley [Paulay and Priestley, 1992] given in Appendix A-4-1-2 Equation A-29. The plastic hinge length in the walls is limited by the story height for analysis purposes [ASCE 41-13, 2013]. The story height at the location of the critical cross section governs the finite element height for all walls, as shown in Appendix A-4-1 Table A-4. The element height outside the estimated yielding zone was chosen equal to the story height, as recommended by Powell [Powell, 2007]. As the design allows for minor flexural yielding over the full height of the wall, nonlinear elements were extended over the full height of the wall.

For a more elaborate description on the meshing assumptions and calculation of the plastic hinge length, please refer to Appendix A-4-1.

4-6-2 Geometrical approximations

Powell [Powell, 2007] provides guidelines for minor geometrical approximations in Perform 3D for shear walls. For confined concrete sections, the concrete lying outside the reinforcement, could be treated as a material with a different set of material properties. The shell concrete is unconfined, most likely less ductile and can spall off. Explicit modelling of the concrete outside the reinforcement adds complexity, and the predicted behaviour may not be warranted given the other approximations in the model [Powell, 2007]. The recommended simpler model, which ignores the shell concrete completely and uses a reduced wall thickness, was adopted in this study. The reduced wall thickness is used only for the strength calculation, not for the weight calculation.

It is also recognized that the elements overlap at the corners of the walls, as shown in Figure 4-10. For the intersection of two walls, the modelled wall area is equal to the total wall area.

Figure 4-10: Geometrical approximation of nodes and elements at web-flange junctions

4-7 Conclusion

The reinforced concrete walls of the archetype structure will be modelled by a fibre model in Perform 3D with elastic out-of-plane bending behaviour and inelastic concrete shear behaviour. The horizontal fibre section will be modelled with concrete and steel fibres with constitutive material relations. It is recognized that the fibre models are valuable design tools provided that one understands that the results obtained are not precise, i.e. the sensitivity of the results is considered. Furthermore, it is noted that local responses are more likely to be sensitive to model (e.g. mesh) and material (e.g. reinforcement, strain hardening) parameters than overall responses.

The reinforced concrete walls will be modelled according to the design of the archetype structure by PEER Task 12. The same structural wall design will be used for the performance-based and probabilistic analysis. The model in Perform 3D will be used verify the performance-based design and to evaluate the reliability of the archetype structure in the probabilistic analysis.

Chapter 5

Modelling of coupling beams

5-1 Introduction

Coupling beams are important for the behaviour of the structural wall. The coupling beams connecting structural walls can provide stiffness and are responsible for a large portion of the energy dissipation during an earthquake. When subjected to strong shaking, coupling beams act as fuses and typically undergo large inelastic rotations to dissipate energy.

The configuration of the coupling beams in the archetype structure is described in Section 5-2. The reinforcement layout of the coupling beams is described as well as the expected strength properties. Subsequently, Section 5-3 discusses theoretical coupling beam models. The implementation of the theoretical coupling beam models in Perform 3D is discussed in Section 5-4. Other modelling assumptions are discussed in Section 5-5, including geometrical approximations and extension beams.

5-2 Coupling beams in the archetype structure

5-2-1 Introduction

Coupling beams in the archetype structure connect the structural walls at every level. In the North and South (N-S) walls, one coupling beam connects two wall panels at each level. In the East and West (E-W) walls, two coupling beams connect three wall panels at every level. An example of typical coupling beam configuration is given in Appendix B Figure B-1. The coupling beam design from PEER is adopted in this study. The dimensions and reinforcement layout of the coupling beams are given in the PEER report [PEER Task 12 Group, 2011].

One of the most important characteristics of coupling beams is the length-to-depth aspect ratio. The length-to-depth aspect ratios of the coupling beams in the N-S and E-W walls are given in Table 5-1. A brief description of the reinforcement layout is given in Section 5-2-2. The strength properties are discussed in Section 5-2-3.

Coupling beam	**Aspect ratio**
Coupling beam N-S wall	1.70
Coupling beam E-W wall	2.10

Table 5-1: Aspect ratios of coupling beams

5-2-2 Reinforcement in coupling beams

Three types of reinforcement can be distinguished in the coupling beam layout given in Figure 5-1: diagonal reinforcement "a", horizontal beam reinforcement "b", and transverse full section confinement reinforcement "c".

The diagonal reinforcement "a" works as a compression and tension strut and the diagonal bars are intended to provide the entire shear and moment resistance of the beam. In compliance with ACI 318-11, diagonal bars are placed approximately symmetrically in the beam cross section, in two or more layers.

The horizontal beam reinforcement "b" is required to support the transverse confinement reinforcement. It is required per ACI 318-11 that each crosstie and each hoop leg engages a longitudinal bar of equal or larger diameter.

The transverse full section confinement reinforcement "c" is required to enhance the compressive strength and deformation capacity of the diagonal bars as well as to suppress buckling of the diagonal reinforcement. Full section reinforcement provides equivalent, if not improved, performance compared to confinement around the diagonal [Naish, 2010]. Full section confinement is provided in all coupling beams for the entire beam cross section.

Additional information on the different types of reinforcement is provided in Appendix B-1-1.

5-2-3 Expected strength properties of coupling beams

The strength properties of the coupling beams were determined according to ACI 318-11 and recommendations by PEER/TBI [PEER/TBI, 2010] and Naish [Naish et al., 2010].

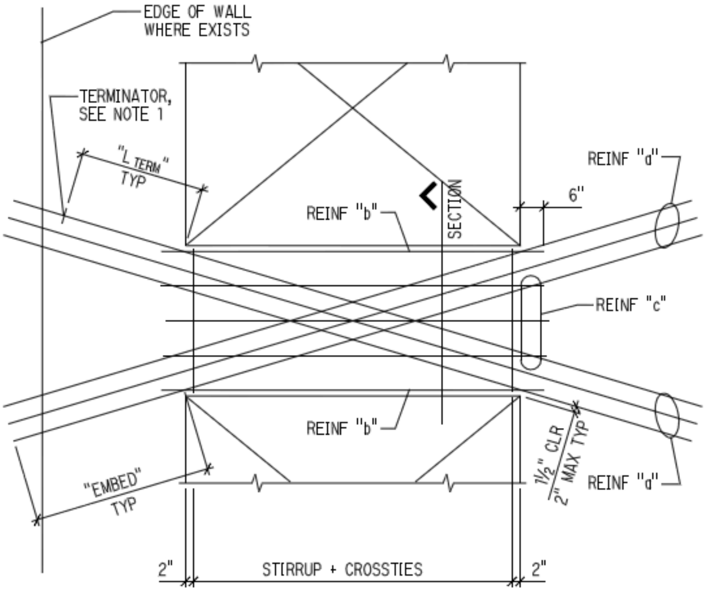

Figure 5-1: Coupling beam layout

The diagonal reinforcement is intended to provide the entire shear strength and corresponding flexural strength. The expected strength properties are calculated using the expected material properties given in Appendix B-2-1.

5-2-3-1 Expected shear strength

The expected shear strength was determined using ACI 318-11 and Naish. The expected shear strength for coupling beams reinforced with two intersecting groups of diagonally placed based symmetrical about the midspan is calculated in Appendix B-2-2. The calculation procedure is summarised in Table 5-2. The ultimate shear strength of all coupling beams is given in Appendix B Table B-3.

			Reference:
Nominal expected shear strength	$V_{n,exp}$	$= 1.33V_y$	[ACI 318-11, 2011]
Nominal expected shear strength including impact of slab	V_y	$= 1.3V_y$	[Naish, 2010]
Ultimate expected shear strength	$V_{u,exp}$	$= 2A_{vd}f_y\sin(\alpha)$	[Naish, 2010]
Residual expected shear strength	$V_{r,exp}$	$= 0.25V_{u,exp}$	[Naish, 2010]

Table 5-2: Expected shear strengths

5-2-3-2 Expected flexural strength

The expected flexural strength was determined according to ACI 318-11, as described in Appendix B-2-3. The calculated flexural strengths of the coupling beams are given in Appendix B Table B-4.

5-3 Theoretical coupling beam models

5-3-1 Coupling beam elements

Coupling beams can be modelled using either wall elements or beam elements. It is important to remember that the goal is to model the behaviour of the beam and its interaction with the walls, not to model its geometry. The beam model differs from the wall model in the following aspects:

- For the wall element model, the bending stiffness and strength depend entirely on the fibre properties and orientations. In the beam element model, the bending behaviour can be specified in a number of ways. A beam model can use shear hinges, moment hinges, elastic segments, and fibre segments.
- A beam model can be used equally well for deep and slender coupling beams. It is more difficult to model slender beams using a wall model.
- With a beam model, if horizontal imbedded beams are used, there need to be only one wall element over the height of each story. With a wall model, the adjacent walls must have at least two elements over the story height.

In general, beam elements are better because they allow better control over the modelling properties. Although it requires more initial effort to use beam elements, the beam model gives better control over the behaviour of the coupling beam than the wall model. Therefore, coupling beams will be modelled using beam elements.

5-3-2 Coupling beam hinges

The coupling beam model can be modelled with moment and/or shear hinges, depending on whether bending or shear governs. If the beam strength is clearly governed by shear, the model can have elastic beam segments and a shear hinge. If the beam is governed by bending, elastic beam segments and moment hinges can be used. The moment-hinge model (M_n-hinge model) and shear-hinge model (V_n-hinge model) are shown in Figure 5-2. Both the M_n-hinge model and the V_n-hinge model accurately capture the overall load-displacement response of the member [ATC 72-1, 2010]. Due to the fact that unloading stiffness modelling parameters are available for flexural hinges in Perform 3D, but not for shear hinges, the M_n-hinge model captures the unloading characteristics better than the V_n-hinge model.

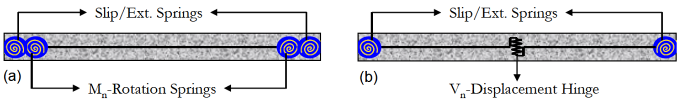

Figure 5.8 Modeling components: (a) M_n-hinge model; and (b) V_n-hinge model

Figure 5-2: Moment-hinge model and shear-hinge model

5-3-2-1 Shear-controlled coupling beams

For diagonally-reinforced coupling beams with lower aspect ratios, $1.0 < l_n/h \leq 2.0$, coupling beams are assumed to be controlled by shear. The load-deformation behaviour is much stiffer for beams with lower aspect ratios, because the slip/extension deformations and flexural deformations are smaller. The beam is therefore modelled using elastic beam elements with inelastic shear displacement-based translational spring. The shear rotation curves contain initial secant stiffness based on the effective stiffness for the elastic portion of the link beam element and a modified backbone curve to account for post-capping strength deterioration and cyclic deterioration.

The V_n-hinge model consists of an elastic beam cross-section, slip/extension hinges, and a shear force versus displacement hinge to simulate the effects of nonlinear deformations. The properties of the shear force versus displacement hinge are defined using backbone relations derived from test results.

5-3-2-2 Moment-controlled coupling beams

For diagonally-reinforced coupling beams with aspect ratios $2.0 < l_n/h \leq 4.0$, flexural deformation and slip/extension deformation account for approximately 80-85% of total deformation, shear deformations generally account for only 15-20% of total deformations. Therefore, both the flexural and shear hinges are used to represent flexural deformations, neglecting shear deformations [Naish, 2010].

The M_n-hinge model consists of an elastic beam cross-section, elastic-rotation springs (hinges) at each beam-end to simulate the effects of slip/extension deformations, and rigid plastic rotational springs (hinges) at each beam-end simulate the effects of nonlinear deformations. The rotational springs are modelled using backbone relations derived from test results.

5-4 Perform 3D Coupling beam model

5-4-1 Introduction

Shear deformations are particularly important in coupling beams with aspect ratios less than 2.25 and should therefore be considered in the analysis [Naish, 2010]. Hence, coupling beams in the N-S walls and E-W walls are modelled using the shear-hinge model with elastic beam segments.

The link beam is modelled using elastic beam segments with an inelastic shear displacement-based translation spring, denoted "Shear Hinge, Displacement Type". The slip/extension springs are not modelled explicitly, but implicitly accounted for by modified elastic stiffness values of the elastic beam segments.

5-4-2 Elastic beam segments

The elastic beam segments are modelled as rectangular reinforced concrete beam sections with cross-sectional dimensions and effective elastic stiffness properties. Slip and extension of the flexural reinforcement have a large contribution (40%-50%) to the beam deformation prior to yield. The impact of slip/extension deformations on the overall load-deformation behaviour of the member is accounted for by the effective elastic stiffness values of the elastic beam segments in accordance with test results. The effective elastic stiffness values of the elastic beam segments are determined in Appendix B-3-1-1. The effective stiffness properties of the coupling beams in the N-S and E-W wall are given in Table 5-3. The chosen strength and stiffness values of the coupling beam will have substantial impact on coupling beam rotation, but do not have a substantial impact on interstory drift, and variations do not greatly impact the core wall shear forces [Naish, 2010].

Aspect ratio	**Flexural** $[E_cI_{eff}]$	**Shear** $[G_{c,eff}A_{eff}]$	**Axial** $[E_cA_{eff}]$
$L_n/h = 1.70$ (N-S wall)	0.15 E_cI_g	0.25 E_cA_{eff}	E_cA_c
$L_n/h = 2.10$ (E-W wall)	0.15 E_cI_g	0.40 E_cA_{eff}	E_cA_c

Table 5-3: Effective stiffness properties of the coupling beams in structure

5-4-3 Displacement-based shear hinge

5-4-3-1 Cyclic backbone curve

The backbone curve characterises the force-deformation relationship, which measures strength against translational or rotational deformation. The cyclic backbone curve encloses the forces and displacements under cyclic loading [Deierlein et al., 2010]. Deterioration of strength and stiffness degrades the backbone curve. The consequence of strength and stiffness degradation is a lack of stability in the load-deformation response. The backbone curve produced by the cyclic envelope will therefore be less than the monotonic backbone curve which would result from the same structure being subjected to monotonic loading. More information on backbone curves is given in Appendix B-3-2-1.

Perform 3D employs linearized cyclic backbone curves to provide a simple, yet accurate method for estimating the overall force-deformation relationship. The linearized cyclic backbone curves were derived from tests with coupling beams closely matching the archetype structure's link beam configuration, given in Appendix B-3-2-1 Table B-7, along with suggested modelling parameters provided by Naish. The cyclic backbone curves were calibrated to the median response of the component in order to obtain the median results of the response [ATC 72-1, 2010]. Required input parameters for the linearised cyclic backbone curve are given in Appendix B-3-2-1 Equation B-7. The shear hinge cyclic backbone curve values for the coupling beams in the N-S and E-W wall are given in link beam plastic chord rotations in Table 5-4. It is noted that the shear hinge displacement is equal to the link beam plastic chord rotation multiplied by the link beam clear span l_n. Instead of measuring the link beam chord rotations directly, the shear hinge model requires shear hinge displacement as input. The properties of the displacement-based shear hinge are given in Appendix B-3-2-1 Table B-9.

Coupling beam		θU	θL	θR	θX	FU/FY	FR/FU
N-S wall ($l_n/h = 1.70$)	[Galano and Vignoli, 2010]	0.014	0.025	0.045	0.300	1.33	0.25
E-W wall $l_n/h = 2.10$	[Naish, 2010]	0.021	0.050	0.090	0.300	1.33	0.25

Table 5-4: Cyclic backbone curve properties of shear hinge (given in plastic link beam rotations)

The cyclic backbone curves in Perform 3D account implicitly for the effect of cyclic degradation on the effective strength and ductility. It does not, however, account for energy degradation in the hysteresis loop [Perform 3D User Guide, 2006]. Therefore, additional energy degradation factors need to be defined to account for energy degradation in the hysteresis loop.

5-4-3-2 Energy degradation factors

Energy degradation factors are specified to account for energy degradation in the hysteresis loop. The required input parameters are given in Appendix B-3-2-2 Equation B-8. The energy degradation factor is the ratio between the area of the degraded hysteresis loop and the area of the undegraded loop as a function of the maximum strain in a given hysteresis loop. The energy degradation factors were derived from tests on link beams closely matching the structure's link beam configuration. For consistency, the energy degradation factors were derived from the same tests as used to determine the cyclic backbone curve parameters. Hence, the energy degradation factors for the N-S walls with aspect ratio $l_n/h = 1.70$ are based on full-scale tests by Galano and Vignoli (Specimen P07, $l_n/h = 1.50$) [Galano and Vignoli, 2000]. For the link beams in the E-W walls with aspect ratio $l_n/h = 2.10$, the energy degradation factors for link beams with aspect ratios $2.00 \leq l_n/h \leq 4.00$ by Naish were used, based on full-scale tests with link beams with aspect ratio $l_n/h = 2.40$. The energy degradation factors for the link beams in the N-S and E-W walls are given in Table 5-5.

Coupling beam		Y	U	L	R	X
N-S wall ($l_n/h = 1.70$)	[Galano and Vignoli, 2010]	0.250	0.225	0.225	0.150	0.150
E-W wall ($l_n/h = 2.10$)	[Naish, 2010]	0.500	0.450	0.400	0.350	0.350

Table 5-5: Cyclic degradation parameters

5-5 Other modelling assumptions

5-5-1 Extension beams

Extension beams are additional "imbedded" beams that connect each coupling beam element to the wall elements. The use of extension beams is required, otherwise the connection between the beam element and wall element is effectively a pin connection. For slender beams, the imbedded beams that connect the beam to the walls can be horizontal, rather than vertical. This has the advantage that it reduces the number of wall elements. Coupling beams with span/depth ratios of 2.0-3.5 are not really slender, but are treated as slender beams for purposes of analysis.

The imbedded beams are stiff in bending to provide stiff connection between pier and coupling beam. The beams have small axial stiffness to avoid adding stiffness to wall elements. In an actual wall, there may be substantial local deformation where the beam connects to the pier. The degree of fixity may have an effect on the elastic stiffness of the structure, but after the coupling beam yields, in bending or shear, the amount of end fixity is likely to have little effect [Powell, 2013].

For the horizontal imbedded beam, the values given in Equation 5-1 are recommended

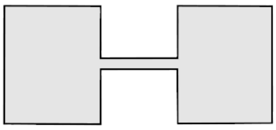

(a) Slender Beam

(b) Wall Modeled With Large Elements

(d) Simple Element for Imbedded Beam

Figure 5-3: Extension beams [Powell, 2007]

[Powell, 2007].

$$\begin{aligned} E_c I_{eff} &= 20 E_c I_g \\ G_{eff} A_s &= 3 G_c A_s \end{aligned} \tag{5-1}$$

The stiffness is based on a rectangular section that is 20 times stiffer for vertical bending than the coupling beam section. For horizontal bending, the stiffness is taken very large since there is a rigid floor diaphragm. If there were no rigid diaphragm, an appropriate value for this stiffness would be needed. To avoid stiffening of the wall, the axial and torsional stiffnesses are set very small.

A study was done by SOM for the 350 Mission Street project to compare effect of the relative flexural and shear stiffness of extension beams on the behaviour of shear wall and link beams to ensure there is no substantial artificial impact of the modelling approach on the performance. The effect of the relative flexural stiffness was studied using a link beam extension major axis flexural stiffness equal to the reduced link beam flexural stiffness and 20 times reduced link beam flexural stiffness. Also, the effect of the relative shear stiffness was studied using a link beam extension shear stiffness equal to the reduced link beam shear stiffness, 3 times reduced link beam shear stiffness, and 3 times unreduced link beam shear stiffness. The conclusion of the study was that extension beam major axis flexural stiffness and extension beam shear stiffness have a negligible effect on shear wall strains, link beam chord rotations, and core wall shears, given that the flexural and shear stiffness of the link beam extension are at least equal to the flexural and shear stiffness of the coupling beam. Based on the values recommended by Powell and the parametric study by SOM, the values given in Table 5-6 were chosen as the stiffness properties of the extension beams in the E-W and N-S walls.

5-5-2 Geometrical approximations

The beam axes are located at the floor levels, the vertical coordinates of the nodes in the model correspond to the top of the floor slab. It might be more accurate to locate the

	Extension beam stiffness properties				
	Axial area	Torsional stiffness	Flexural (in-plane)	Flexural (out-of-plane)	Shear
N-S wall	0.01	0.01	20 $E_c I_{eff}$	1.000.000	3 $G_c A_{eff}$
E-W wall	0.01	0.01	20 $E_c I_{eff}$	1.000.000	3 $G_c A_{eff}$

Table 5-6: Elastic properties of the extension beam

nodes lower, at the slab mid-thickness, but the difference is likely to be negligible (Powell - Modeling of coupling beams for shear walls).

5-6 Conclusion

The coupling beams in the archetype structure will be modelled by a shear-hinge model and elastic beam segments with modified stiffness properties. The input parameters were derived from tests on link beams with configurations similar to the archetype structure's link beams. Therefore, the modelled behaviour is in accordance with the expected behaviour of the coupling beams.

Chapter 6

Modelling of other structural components

6-1 Introduction

Modelling assumptions for other structural components of the archetype structure are discussed. The modelling of the basement walls, foundation, gravity columns, and tower diaphragms will be discussed in Section 6-2, 6-3, 6-4, and 6-5 respectively.

6-2 Modelling of basement walls

The basement walls were modelled as elastic shear wall sections with modified stiffness properties. The stiffness modifiers are applied to the E-modulus and shear modulus to account for stiffness reduction due to cracking, limited bond slip and yielding of reinforcement. In-plane and out-of-plane bending and shear are assumed to be elastic. In-plane bending behaviour was modelled with an elastic material for fibre sections. Out-of-plane bending behaviour and shear behaviour were modelled with an effective thickness $t = 16$ [in], effective elastic modulus E, and Poisson's ratio $\upsilon = 0.2$.

Similar to the stiffness assumptions for diaphragms, the selected stiffness modifiers for basement walls represent mean estimates associated with demand exceeding capacity and the same stiffness assumptions are used for all intensity levels. The selected stiffness assumptions for basement walls are based on the suggested values from LATBSDC and given in Table 6-1. The flexural stiffness is used for both in-plane and out-of-plane bending behaviour.

	Flexural stiffness	**Shear stiffness**
Basement wall	$0.8E_cI_g$	$0.8G_cA_g$

Table 6-1: Selected stiffness assumptions for basement walls

6-3 Modelling of foundation

The foundation can be modelled in several ways. One option is to account for soil-foundation-structure interaction through explicit modelling of the soil, as shown on the left of Figure 6-1. A simpler option is to model soil-structure interaction with a rigid "bathtub" with horizontal and vertical springs and parallel dashpots, as shown on the right of Figure 6-1. The third option is to neglect soil-foundation interaction effects, but include the subterranean levels of the structure, as shown in the middle of Figure 6-1.

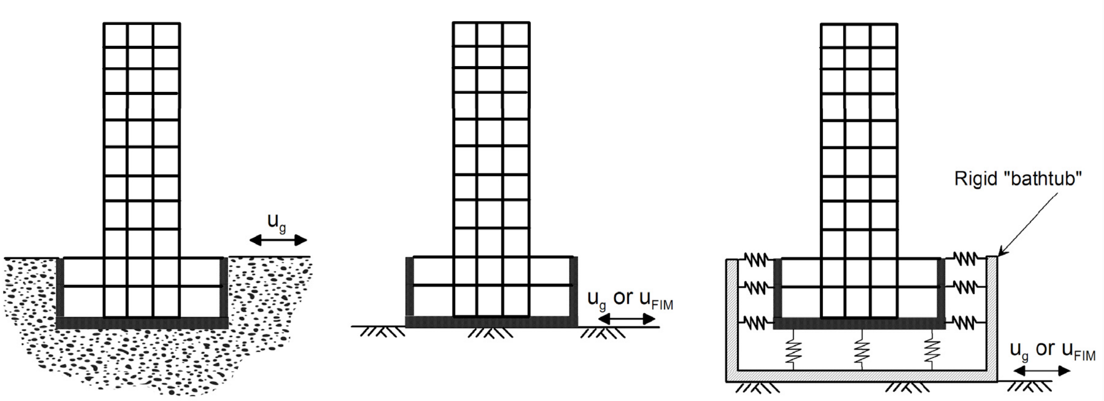

Figure 6-1: Options for modelling of foundation [PEER/TBI, 2010]

In consultation with experts at SOM, the assumption was made that the influence of the foundation on the overall response is very limited. Therefore, the PEER/TBI model in which the subterranean levels are modelled explicitly, horizontal springs and dashpots are ignored, and the foundation is assumed rigid, was used as the base model, given in Figure 6-2. For future studies, Appendix C provides additional information on how to include vertical and horizontal springs and parallel dashpots in the analysis model of the archetype structure for the site's location.

6-4 Modelling of gravity columns

The gravity columns were modelled with frame member compound components in Perform 3D. The frame member compound component consists of a reinforced concrete column

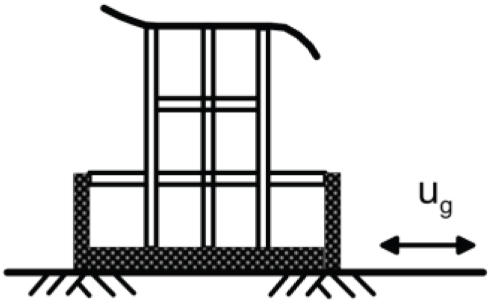

Figure 6-2: Foundation model [NEHRP Consultants Joint Venture, 2012]

section and column end releases. The shape, dimensions, section properties and material stiffnesses from the archetype structure were input for the reinforced concrete column section. The column end releases were used to ensure that all force is transferred from the shear wall into the transfer diaphragms, as further explained in Section 6-4-1. The column layout of the archetype structure is given in Figure 6-3, including tower gravity columns and basement gravity columns.

6-4-1 End zone assumption for gravity columns

In preliminary studies, by default, the column elements were connected by stiff end zones in Perform 3D. The shear stiffness of gravity columns is small compared to the shear stiffness of the walls. Therefore, plots of the shear force over the story height for stiff column end zones showed that the shear force in the columns is small in the upper levels of the tower. However, preliminary studies showed an unexpected bump in the shear force in the shear walls one level above the transfer diaphragm. Several possibilities were considered that could have caused the bump, such as the effect of time steps (noise at numerical integration over time), mass distribution. It was found that the bump in the shear force was caused by the end zone assumption for the gravity columns in combination with rigid diaphragm assumption for the tower diaphragms.

The load path of the shear force from the columns to the basement walls is relatively stiff compared to the load path of the shear force from the shear walls through the podium diaphragms to the basement walls. The stiffness of the load path from the core walls to the basement walls is increased by the modified stiffness assumptions for the podium diaphragm. Furthermore, the rigid diaphragm assumption for the tower wall increases the stiffness of the load path through the elastic columns. Both load paths are shown in Figure 6-4. The red load path gives the load path through the columns and diaphragms, the green load path gives the path through the shear walls and diaphragms to the basement walls.

The load path through the gravity columns with stiff end zones accounted for approximately

10-20% of the total transfer force. However, the gravity columns were not designed to resist large shear forces. Furthermore, the contribution of gravity columns is unrealistically large, due to rigid diaphragm assumption, infinitely stiff end zone assumption, and elastic concrete column sections, resulting in an unconservative estimate for the transfer force in the distributors in the transfer diaphragms. Therefore, the gravity columns were modelled with column end releases. This assumption eliminated the bump in the shear force one level above the podium. The column end releases are conservative, as some forces will be transferred through the gravity columns in the actual structure, reducing the transfer forces in the distributors.

6-5 Tower diaphragms

The first six stories of the tower were modelled using elastic diaphragm with an effective stiffness of $0.5E_cI_g$. Preliminary studies showed that the out-of-plane behaviour of the shear walls is better represented for flexible diaphragms, especially at the podium level. The upper stories of the tower were modelled with rigid diaphragm assumption to reduce analysis time. An overview of the model in Perform 3D including the tower diaphragms is given in Figure 6-5.

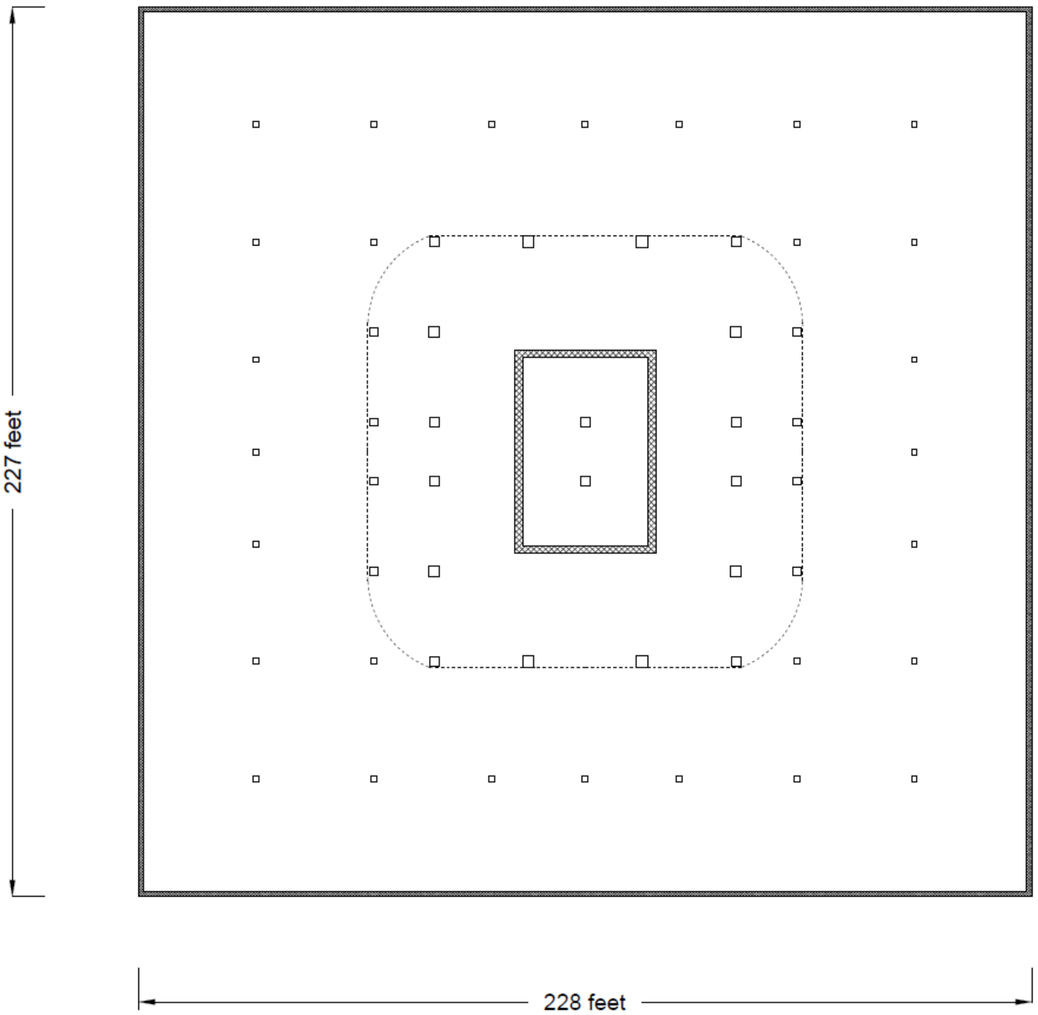

Figure 6-3: Foundation model

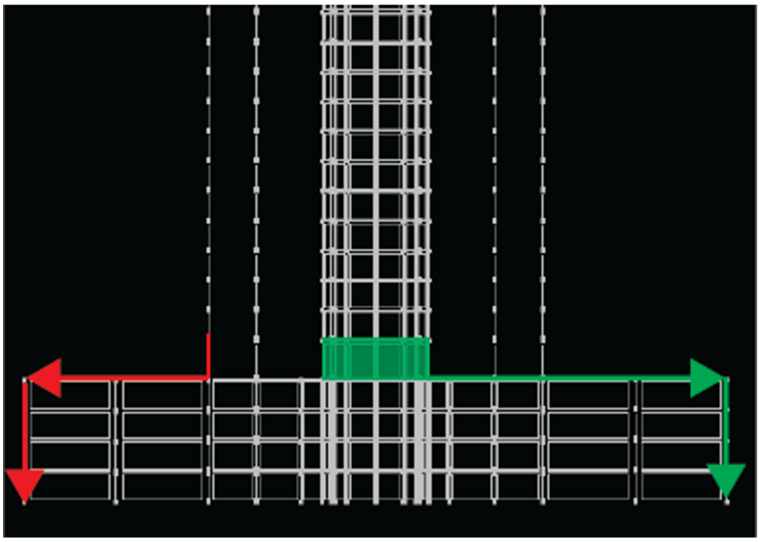

Figure 6-4: Foundation model

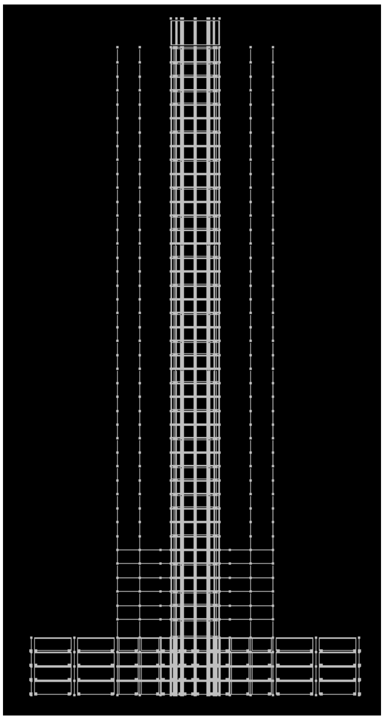

Figure 6-5: Foundation model

Chapter 7

Damping

Damping is the process in which vibration steadily diminishes in amplitude [Chopra, 2014]. Kinetic energy and strain energy are dissipated in structural and nonstructural components of the building and foundation. Damping is often modelled as equivalent viscous damping [ATC 72-1, 2010], using Rayleigh damping (i.e. linear combination of mass and stiffness matrices) and/or modal damping. However, the clear relationships of Rayleigh damping and modal damping to elastic modes do not hold for nonlinear analyses. Whereas the stiffness matrix and percentage of critical damping remain constant during elastic analyses, the stiffness reduces due to inelastic effects and the relative significance of damping can change significantly during nonlinear analyses.

In Perform 3D, damping effects are included through a combination of hysteretic and equivalent viscous damping. A distinction is made between damping from structural components and nonstructural components. Furthermore, a distinction is made between damping from explicitly modelled structural components, which are the components designed to resist earthquake motions for this project, and damping from not explicitly modelled structural components, such as the gravity system. The damping effects from the explicitly modelled structural components, the components designed to resist earthquake motions, are implicit through the hysteretic response of inelastic components, specified using energy factors for cyclic degradation in Perform 3D. Damping effects from elements that are not explicitly modelled in the analysis, such as the not explicitly modelled structural components of the gravity system, nonstructural components and the basement, are incorporated through equivalent viscous damping.

In ATC 72-1, several options to model equivalent viscous damping were explored. Modal damping was found to provide the best control of damping for elastic higher modes. Also, reasonable effective damping values were found for inelastic, elongated modes. Recommended equivalent viscous damping values range from 2% to 3% for reinforced concrete structures from laboratory tests to 1% to 5% for quasi-elastic response of buildings over 30 stories from measured data from earthquake-induced motions of actual buildings [ATC 72-1, 2010]. The recommendation for equivalent viscous damping for nonlinear response history analysis of typical buildings for all modes from ATC 72-1 is adopted in this study, as given in Equation 7-1. The recommendation holds for analyses in which most of the structure's damping is accounted for by hysteretic damping through explicitly modelled nonlinear components.

$$D \quad = \quad \alpha / N \quad = \quad 2.4\% \tag{7-1}$$

Where,

$$\begin{aligned} \alpha &= 100 \quad \text{For reinforced concrete} \\ N &= 42 \quad \text{Number of stories} \end{aligned} \tag{7-2}$$

[Perform 3D User Guide, 2006] recommends to always specify a small amount of Rayleigh damping, especially if there are masses in the V-direction. If only modal damping is specified, there can be many high frequency modes that are undamped, causing the analysis to be sensitive numerically. The recommended Rayleigh damping of 1% of the modal damping is adopted in this study, as shown in Figure 7-2. Point T_A is chosen as the point of 90% mass participation of the tower only, which is for mode 11 (Mass participation factor H1 = 0.9015; H2 = 0.9265), as shown in Figure 7-1 and $T_A = 0.3$ [sec] = 0.06 T/T_1. Point T_B is set at the expected inelastic first period at 1.4 T/T_1. The variation of damping ratio with period is given in Figure 7-2. A summary of the damping assumptions is given in Table 7-1.

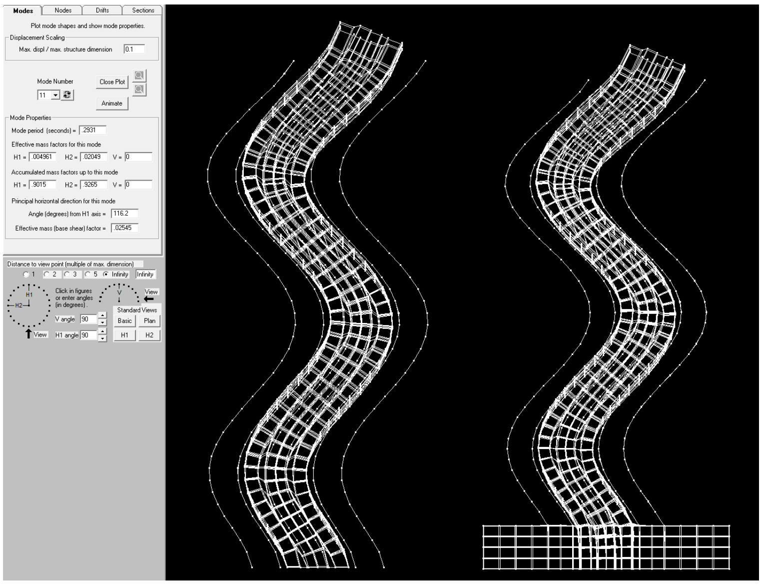

Plot mode shapes and show mode properties.

Displacement Scaling

Max. displ / max. structure dimension 0.1

Mode Number 11

Mode Properties

Mode period (seconds) = .2931

Effective mass factors for this mode

H1 = .004961 H2 = .02049 V = 0

Accumulated mass factors up to this mode

H1 = .9015 H2 = .9265 V = 0

Principal horizontal direction for this mode

Angle (degrees) from H1 axis = 116.2

Effective mass (base shear) factor = .02545

Distance to view point (multiple of max. dimension)

○ 1 ○ 2 ○ 3 ○ 5 ● Infinity Infinity

Click in figures or enter angles (in degrees).

V angle 90

H1 angle 90

Figure 7-1: Mode of 90% mass participation

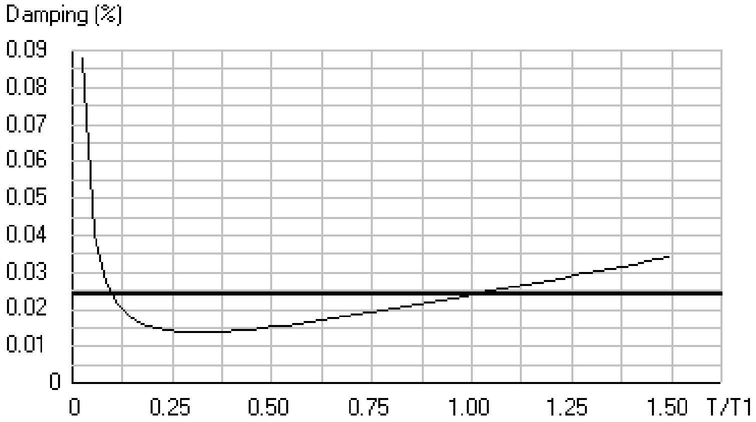

Figure 7-2: Rayleigh damping from Perform 3D, with Point $A = 0.2$ (T/T_1), Point $B = 1.4$ (T/T_1), and Rayleigh damping = 0.024%

Modal damping	Best control of damping for elastic higher modes, effective damping values for inelastic elongated modes Same damping ratio for all modes Damping ratio = 2.4 % [ATC 72-1, 2010]
Rayleigh damping	To damp high frequency modes (Accumulated mass participation factor > 0.90) $T_A = 0.06$ (T/T_1), damping ratio = 0.024 %, $T_B = 1.4$ (T/T_1), damping ratio = 0.024 %

Table 7-1: Summary of damping assumptions

Part II

Input

Chapter 8

Hazard identification, target response spectra and selecting ground motion records

8-1 Hazard Identification

To identify the hazard at a given location, all possible earthquake scenarios on contributing faults near a site must be considered. The goal of the hazard analysis is to identify a response spectrum to use for structural or geotechnical analysis.

Deterministic hazard analyses intend to identify the worst-case earthquake and worst-ground motion intensity associated with that earthquake. This choice can be difficult and subjective [REF PSHA]. Moreover, since the scatter of the log of spectral accelerations around the mean ground motion prediction is well-represented by a normal distribution, there is no theoretical upper bound limit on the amplitude of ground motion for a given earthquake scenario. Therefore, the two main issues of deterministic hazard analysis are:

- The selected ground motion intensity is never a true worst-case scenario.
- The results may be very sensitive to the chosen scenario magnitude and ground motion intensity.

Probabilistic Seismic Hazard Analyses (PSHA) addresses these issues by considering all possible earthquake events and the potential shaking intensity caused by these future earthquakes, along with their associated probability of occurrence, in order to explicitly describe the distribution of future shaking that may occur at the site. The distribution is used to identify a ground motion intensity having an acceptably small probability of being exceeded. The steps of the PSHA are described in Appendix D-1.

In practice, the PSHA is computed using the tool provided by the United States Geological Survey (USGS). Multiple Ground Motion Prediction Equations (GMPEs), formerly known as attenuation relations, are typically used for PSHA computations. Ground motion prediction equations relate earthquake-scenario information (i.e. magnitude M, distance R) and site information (i.e. average shear wave velocity in the top 30 metres $V_{s,30}$) to the ground motion intensity levels that are expected at the building site. The USGS specify three models (Boore-Atkinson 2008, Campbell-Bozorgnia 2008, and Chiou-Youngs 2008) with equal weights. The PSHA results in a hazard curve for a specified period of interest.

8-1-1 Hazard curve

As discussed in 2-5, the 42-story core-wall-only structure was designed for the expected hazard of a location in Los Angeles by the PEER Task 12 group ([PEER Task 12 Group, 2011]). Therefore, this study uses the same location to compute the hazard curve and evaluate the reliability. For completeness, the latitude and longitude of the site are repeated in Table 8-1.

Latitude	34.05	(West)
Longitude	-118.25	(North)

Table 8-1: Latitude and longitude site location

The hazard curve, given in Figure 8-1, shows the annual frequency of exceedance for different levels of spectral acceleration for the structure's site. The hazard curve is plotted for spectral period t = 5.00 [s] and site class D. The spectral period was chosen as close as possible to the first mode period of the structure (T_1 = 4.90 [sec]). Site class D was chosen based on V_{s30}, the average shear wave velocity over the top 30 metres of the site (V_{s30} = 233 [m/s]).

It is noted that longer spectral periods produce smaller spectral acceleration for a given period of exceedance. Softer soils, i.e. lower values for V_{s30}, produce larger spectral accelerations for a given probability of exceedance.

8-1-2 Disaggregation

Disaggregation is an extension of the PSHA, where the relative contribution of different earthquake sources and magnitudes to the rate of exceedance of a given ground motion intensity are calculated. The disaggregation includes a value for ε_0, the number of log standard deviations by which the predicted value exceeds the median. The controlling

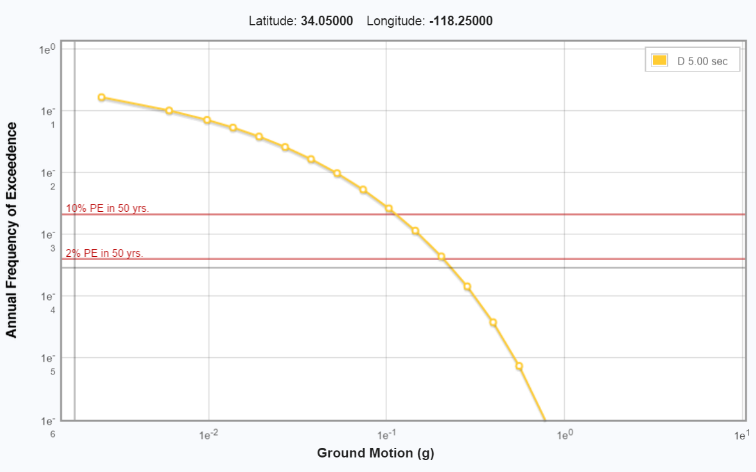

Figure 8-1: Hazard curve for spectral period t = 5.00 [s] and site class D

earthquake scenario having a certain magnitude M and distance R can be derived from the disaggregation. The geographic disaggregation of the seismic hazard at the site for a return period of 2475 years, i.e. 2% in 50 years probability of exceedance, is given in Figure 8-2. Note both the large hazard contribution of faults with small M (M≈ 6.6) near the site (small R) and the large hazard contribution of the fault further away from the site (larger R) with larger M (M≈ 8.0).

8-2 Response spectra

8-2-1 Design Response Spectrum

The code-based procedure employs smooth design spectra, representing the average of several earthquake motions, to calculate the maximum values of the displacement and member forces. Response spectra are plotted between maximum response of a single degree-of-freedom (SDOF) system subjected to specified earthquake excitation and its time period. The response spectrum represents the maximum response of a SDOF system for a given damping ratio. Seismic design parameter values are required to compute design spectra. United States Geological Survey developed a tool to retrieve seismic design parameter values for the design of buildings in the United States [Reference http://earthquake.usgs.gov/designmaps]. The 5%-damped response spectrum was developed according to ASCE 7-10 Figure 11.4-1, as shown in Figure 8-3.

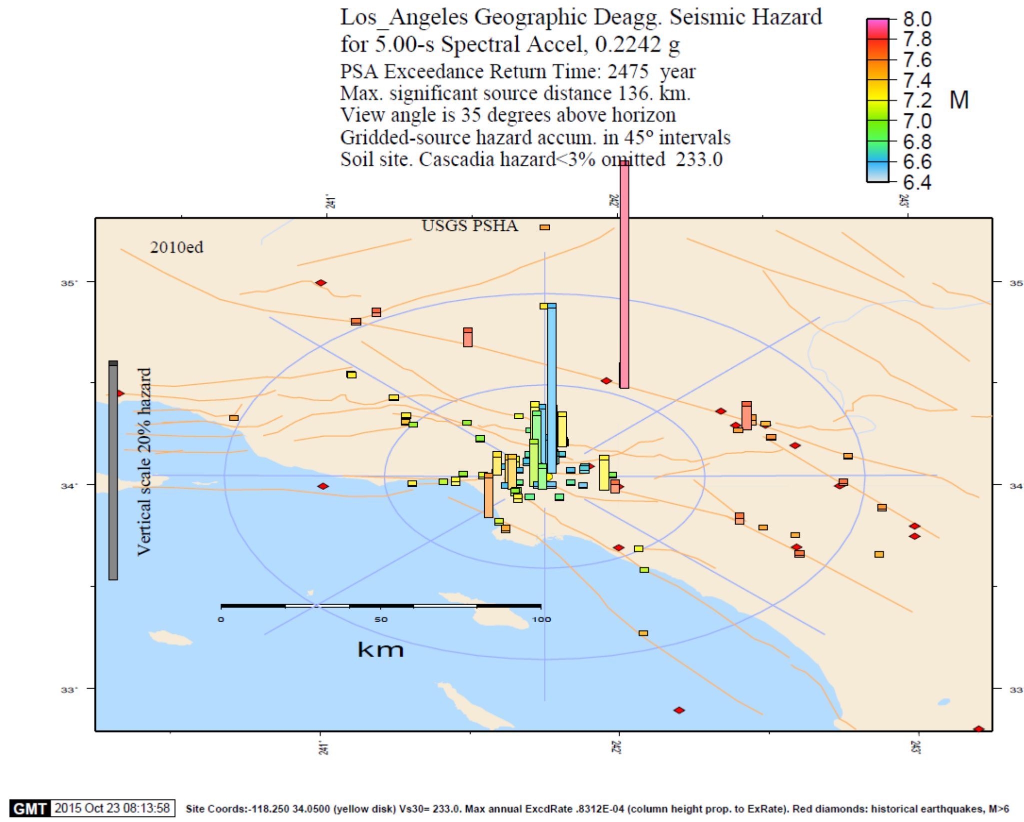

Figure 8-2: Geographical deaggregation of seismic hazard for LA site, SA period = 5.0 seconds, $V_{s,30}$ = 233 [m/s], 2% probability of exceedance in 50 years (MCE-level)

8-2-2 Target Response Spectra

The results from the probabilistic seismic hazard analysis are used to identify a design response spectrum. When the design response spectrum is used for selecting and scaling ground motions for time history analysis, it is often referred to as a target response spectrum. Several types of target response spectra exist. Three types of target response spectra and the advantages, disadvantages and challenges that these types are associated with will be discussed in this section.

8-2-2-1 Uniform Hazard Spectrum

The Uniform Hazard Spectrum (UHS) has been used as the target response spectrum in design practice for the past two decades. The UHS is constructed by computing the value of spectral acceleration using probabilistic seismic hazard analysis at many periods of interest for a given probability of exceedance. The hazard calculations are performed

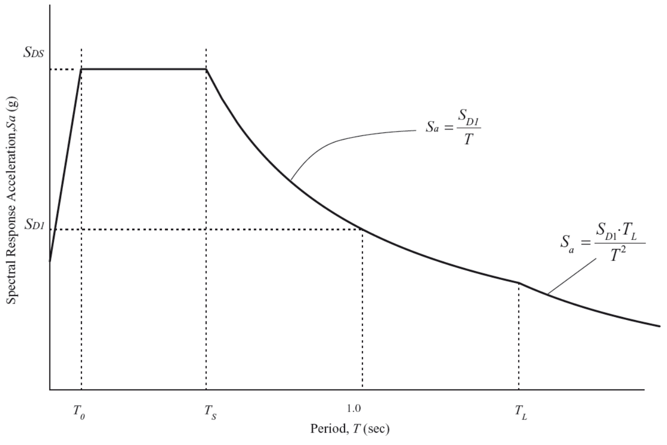

Figure 8-3: Code Design Response Spectrum (ASCE 7-10, Figure 11.4-1)

period by period, without consideration of hazard at adjacent periods. Therefore, every ordinate has an equal probability of being exceeded. Hence, the spectrum is called the uniform hazard spectrum.

It is unlikely that the spectral acceleration values at each period all occur within a single ground motion or earthquake event. This is especially true for very rare levels of ground motion, where it is most unlikely that high spectral values are observed at all periods in a single ground motion. Hence, the UHS will generally be a conservative target spectrum if used for ground motion selection and scaling.

8-2-2-2 Conditional Mean Spectrum

The Conditional Mean Spectrum (CMS) has been developed as an alternative target spectrum to the UHS. The CMS is site-specific and the input parameters require hazard disaggregation. CMS addresses the limitation of the UHS by conditioning the spectrum on spectral acceleration of a single period. This period is usually the first-mode period of the structure. The other spectral ordinates of the CMS are calculated based on the conditioning period.

The spectral ordinate of the CMS at the conditioning period is equal to the UHS, but all other spectral ordinates of the CMS are less than those of the UHS, as shown in Figure 8-5. Therefore, the structural response estimates for multi-mode or nonlinear systems obtained from a CMS are usually lower than comparable structural response estimates from a comparable UHS. Due to the omission of spectral variability, CMS will often result in unconservative structural response. If the Sa at the conditioning period is a good predictor of the EDP of interest, the unconservatism may be less significant [Lin et al., 2013].

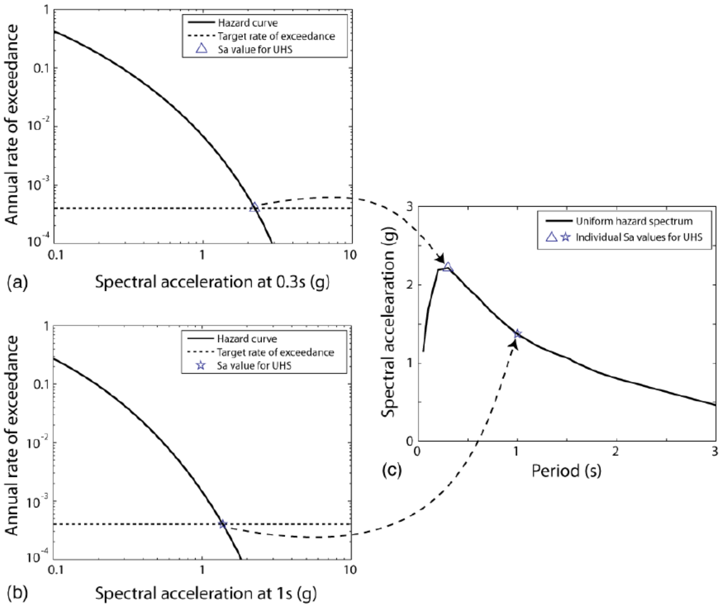

Figure 2.6: Combining hazard curves from individual periods to generate a uniform hazard spectrum with a $4*10^{-4}$ rate of exceedance for a site in Los Angeles. (a) Hazard curve for *SA*(0.3s), with UHS point identified. (b) Hazard curve for *SA*(1s), with UHS point identified. (c) Uniform hazard spectrum, based on a series of calculations like those in (a) and (b).

Figure 8-4: Target Spectrum: Uniform Hazard Spectrum

8-2-2-3 Conditional Spectrum

The Conditional Spectrum (CS) was developed to select ground motions that match both a conditional mean and conditional variability. Similar to the CMS, the CS conditions the spectrum on spectral acceleration of a single period, and then computes the spectral accelerations at all other periods. Again, the chosen period is usually the first-mode period. The CS differs from the CMS only in that it considers the variability in the response spectra at other periods than the conditioning period, which by definition has no variability.

The CS has a relative peak at the conditioning period T and tapers back towards the median spectrum at other periods. The CS shows increasing peakedness of the spectrum at the conditioning period for rarer $S_a(T)$ levels. The increasing peakedness results from the fact that high $S_a(T)$ values are larger-than-mean values for the earthquake causing the ground motion. The spectral values at other periods are therefore unlikely to be comparably high.

A tool suitable for Conditional-Spectrum-based ground motion selection was developed by Jayaram et al. [Jayaram et al., 2011]. This Matlab script selects a set of ground motions that match the target response spectrum mean and variance. The selection algorithm probabilistically generates multiple response spectra from a target distribution using Monte Carlo simulation. The generated set of response spectra has the desired mean

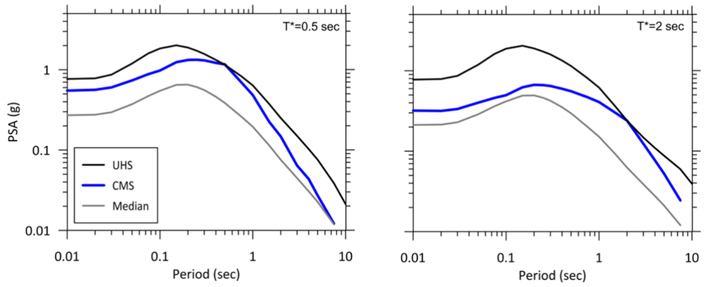

Figure 8-5: Two examples of CMS compatible with the 2% in 50-year UHS for the site in downtown Los Angeles [PEER Task 12 Group, 2011]

and variance. Then, a ground motion with a similar response spectrum is selected for each simulated response spectrum. The mean and variance of the set of ground motions therefore also correspond to the target mean and variance. Finally, a greedy optimization technique is used to replace one previously selected ground motion at a time with a record from the PEER NGA database that causes the best improvement. This technique further improves the match between the mean and variance of the set of ground motions and the mean and variance of the target spectrum.

The CS is the recommended spectrum for risk-based assessments and collapse fragility functions [Lin et al., 2013]. A comparison of the CS with the UHS is given in Figure 8-6.

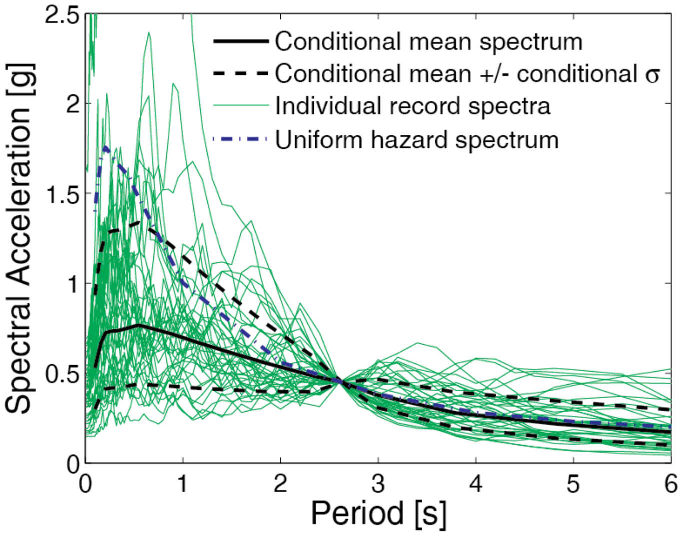

Figure 8-6: Uniform Hazard Spectrum compared to the Conditional Spectrum (ref: NIST GCR 11-917-55)

Choice of conditioning period
A conditioning period has to be chosen to compute the CMS and CS. The influence of the chosen conditioning period depends on the type of assessment. The types of assessments considered are intensity-based assessments and risk-based assessments.

- Intensity-based assessments are the most common type of assessments and involve the computation of the response of a structure at a specified intensity level. The PEER/TBI guidelines prescribe intensity-based assessments to calculate the response, including the response evaluation at MCE-level, i.e. 2475-year return period intensity level. This assessment focuses on computing the mean or average responses.
- Risk-based assessments involve a number of intensity-based assessments over the range of ground motion levels of interest. The predicted responses for each intensity-based assessment are combined with the ground motion hazard curve to calculate the annual rates of exceedance.

For intensity-based assessments, the structural response will depend to some degree on the chosen conditioning period. For risk-based assessments, the resulting structural responses are comparable regardless of the conditioning period. However, choosing a spectral acceleration-conditioning period which is a good predictor of the engineering demand parameter of interest, such as interstory drift ratio, will reduce the number of analyses required to obtain a stable result. A good conditioning period results in a small record-to-record variability in structural responses for ground motion records having the same spectral acceleration at the conditioning period.

8-3 Selecting and scaling ground motions to target spectrum

8-3-1 Ground motion selection procedure

Many ground motion intensity measures can be used to select ground motions for NLTHA. The simplest measures, such as peak ground acceleration, peak ground velocity, and peak ground displacement, provide little information on the damage potential of an earthquake ground motion of a specific building. Relatively simple but improved measures are based on the response of an elastic single-degree-of-freedom system, including spectral acceleration, velocity and displacement.

The most widely used intensity measure is 5%-damped spectral acceleration, Sa, although it has many limitations and cannot characterize the nonlinear response of a building. Three definitions of horizontal spectral acceleration are: arbitrary component (computed for analysis of single horizontal components of ground motion, could be used for planar analysis of frames), geometric mean spectral acceleration (calculated as the square root of the product of two spectral accelerations for a pair of horizontal ground motions), maximum direction spectral acceleration (greatest unidirectional acceleration value for any possible orientation of a pair of horizontal ground motions). The 5%-damped geometric mean spectral acceleration was used as the ground motion intensity measure for selection of ground motions in this study.

8-3-2 Ground motion scaling procedure

Ground motion records are selected and scaled to match the chosen target spectrum. For scaling of ground motions to the target spectrum (at distant sites), the spectral shape over the spectral range of interest is the most important factor in selecting ground motions. Secondary consideration are the earthquake magnitude M, site-to-source distance R, ϵ that dominates the hazard curve at period T, and local site conditions.

Two procedures are applied to scale ground motions to the target spectrum within the period range of scaling. First, amplitude scaling procedure applies a constant scale factor to all acceleration ordinates of the horizontal components of the selected ground motion record to match the target spectrum over the period range of interest. Different scale factors may be selected for each pair of ground motions. The second procedure is frequency-content modification. The combination of these two procedures is commonly referred to as spectrum matching. Spectrum matching consists of modification of the frequency-content of each horizontal component after the application of amplitude scaling. Spectrum matching usually results in an average SRSS spectrum that is a closer match to the target spectrum than the average SRSS spectrum obtained through the amplitude scaling procedure. However, variability in the spectral demand is lost with spectrum matching, whereas some variability is maintained with amplitude matching. Therefore, the use of spectrum-matched records will provide more accurate estimates of the mean structural response, whereas amplitude scaling methods will result in greater variability in the response.

Spectrum matching can therefore be used to match ground motions to the uniform hazard spectrum (UHS), conditional mean spectrum (CMS), or any other spectrum that intends to estimate the mean response and not the distribution of response. Ground motions selected to match the conditional spectrum (CS) are scaled through the amplitude scaling procedure and the frequency-content and inherent variability of these ground motions remains unchanged. All selected ground motions in this study were scaled according to the amplitude scaling procedure.

Chapter 9

Input Code Design

9-1 Code Design - Introduction

ASCE 7-10 prescribes that the building structure must be designed with complete lateral and vertical force-resisting systems providing sufficient strength, stiffness, and energy dissipation capacity to meet the strength and deformation requirements [ASCE 7-10, 2010]. This Code design approach intends to ensure at least minimum strength to withstand minor earthquake shaking levels (<DBE), which occur frequently, without damage, and to withstand moderate earthquake shaking (DBE) without significant damage. In addition, code provisions aim for structures to withstand major earthquake (MCE) with a low probability of collapse (less than 10%). The Maximum Considered Earthquake (MCE) is the most severe earthquake considered by the code and the MCE is defined as the intensity of ground shaking having a 2% probability of exceedance in 50 years. The DBE ground motion intensity is taken as 2/3 of the MCE.

The most recent Codes have been adopted in this study to verify the capacity and demand in the archetype structure. Hence, the response spectrum was constructed according to ASCE 7-10. For the design of the archetype structure in PEER Task 12 - Building 1, ASCE 7-05 and Site Class C were used. Based on geotechnical reports, Site Class D was selected for the site in this study.

9-2 Load combinations

ASCE 7-10 specifies two basic load combinations to account for earthquake loading, given in Equation 9-1.

$$\begin{aligned} &\text{Load combination 5:} \quad && 1.2D + 1.0E + L + 0.2S + 1.6H \\ &\text{Load combination 7:} \quad && 0.9D + 1.0E + 1.6H \end{aligned} \tag{9-1}$$

The load effects are specified in Appendix J-1. Combining the load effects given in Appendix J-1 with the basic load combinations given in Equation 9-1 gives the following load combinations for strength design of reinforced concrete diaphragms and collectors, given in Equation 9-2.

$$\begin{aligned} &\text{Load combination 5:} \quad && (1.2 + 0.2S_{ds})D + \rho \cdot Q_e + 0.2L_0 \\ &\text{Load combination 7:} \quad && (0.9 - 0.2S_{ds})D + \rho \cdot Q_e \end{aligned} \tag{9-2}$$

The seismic load combination with overstrength are also utilized for the collectors and distributors. The load combinations with overstrength factor Ω_o are given in Equation 9-3.

$$\begin{aligned} &\text{Load combination 5 with overstrength:} \quad && (1.2 + 0.2S_{ds})D + \Omega_o Q_e + L_0 \\ &\text{Load combination 7 with overstrength:} \quad && (0.9 - 0.2S_{ds})D + \Omega_o Q_e \end{aligned} \tag{9-3}$$

For Modal Response Spectrum Analyses, 100% of the effects in one primary direction are to be combined with 30% of the effects in the other direction.

9-3 Earthquake Loading

9-3-1 Introduction

The lateral seismic forces are determined using Modal Response Spectrum Analysis (MRSA). For taller buildings, the higher modes become more dominant, and as a result, the alternative Equivalent Lateral Force (ELF) procedure may underestimate the base shear. Therefore, ELF may not correctly the vertical distribution of forces.

MRSA is the most popular tool in the seismic analysis of structures [Jangid, 2014]. The calculation procedure consists of calculating the modal mass, modal participation factor, design lateral force at each floor in each mode, and the story shear in each mode calculated. For the response spectrum analysis the masses are assumed to have one degree of freedom, that of lateral displacement in the considered direction.

The response spectra calculate the response in the linear range. However, the structure is designed to respond in the nonlinear range. Current building codes apply seismic performance factors, briefly described in Section 9-3-1-1, to estimate strength and deformation demands on lateral force-resisting systems that are designed using linear methods of analysis but are responding in the nonlinear range. The calculated forces on the structure through the linear MRSA are therefore much greater than the specified design forces. The code relies upon ductility, due to inelastic material behaviour, and overstrength to account for this difference [FEMA P695, 2009].

9-3-1-1 Seismic Performance Factors

Seismic performance factors include the importance factor (I_e), the response modification factor (R-factor), the system overstrength factor (Ω_o), and deflection amplification factor (C_d). The importance factor I_e depends on the functional purpose of the building, characterized by hazardous consequences of its failure, post-earthquake functional needs, historical value or economic importance. The importance factor is intended to provide for a lower inelastic demand on a structure which should result in lower levels of structural and non-structural damage. The response modification factor R is the representation of the inherent overstrength and global ductility of the seismic-force-resisting system. A lower R-factor implies a less ductile system.

Properly detailed structures also contain elements which are not capable of safely resisting the seismic demands through inelastic behaviour. These elements must be designed with sufficient strength to resist the seismic demands in the elastic range. The overstrength factor Ω_o approximates the overstrength in typical systems to account for increased force demands in elements that are intended to remain elastic.

9-3-2 Hazard Identification

Hazard identification was done by the USGS-tool described in Section 8-2-1. The characteristics of seismic ground vibrations at any location depend on the magnitude of the earthquake and its depth of focus, the distance of the location from the epicentre and the characteristics of this path, and the soil characteristics of the site [Jangid, 2014].

9-3-3 Response Spectrum

Seismic design parameters S_s and S_1, retrieved from the hazard identification, are used to compute the site-specific design spectrum. S_s and S_1 have been calculated from probabilistic (risk-targeted) and deterministic ground motions in the direction of maximum horizontal response. The seismic design acceleration values for the site are specified in

Appendix E-1-4. The design response spectrum is given in Figure 9-1. The MCE$_R$ response spectrum is determined by multiplying the design response spectrum by 1.5 and given in Appendix E Figure E-3. MRSA employs the design response spectrum to compute the force-related and displacement-related design parameters.

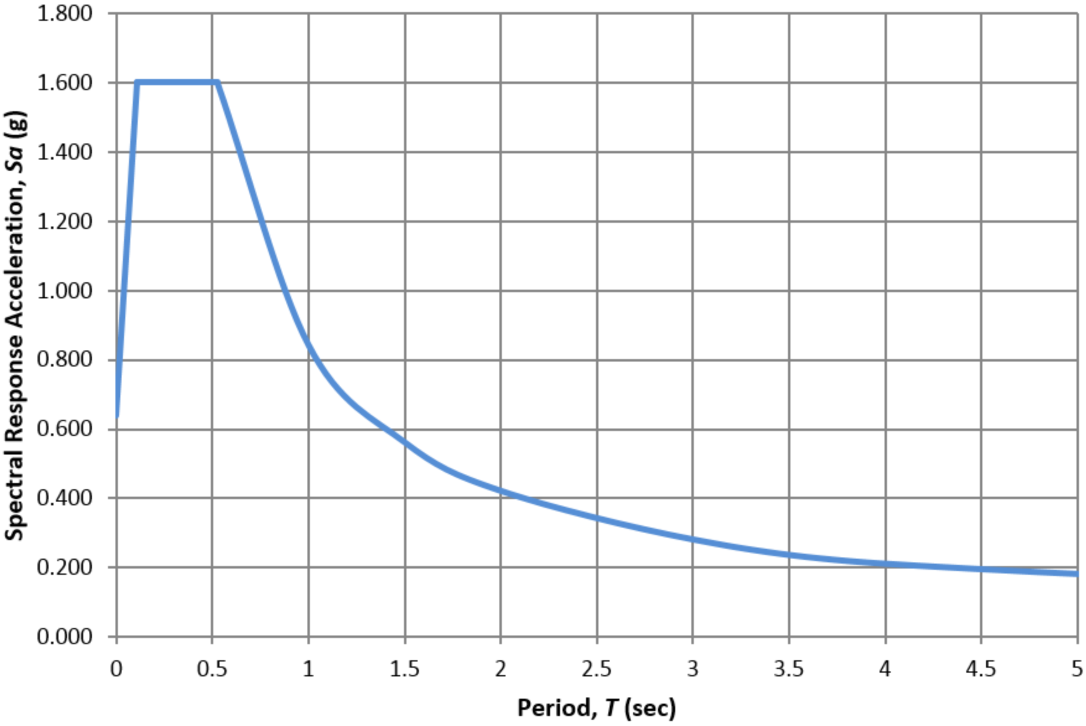

Figure 9-1: Design Response Spectrum

9-3-4 Modal Response Spectrum Analysis

Modal response spectrum analysis was conducted using Perform 3D. The natural modes of vibration of the structure were determined. Tables E-4 and E-5 give that a total of 35 modes must be included to obtain a combined modal mass participation factor of at least 90 percent of the actual mass in each of the orthogonal horizontal direction of response considered by the model, required per ASCE 7-10 Section 12.9.

Several methods can be used to obtain the total peak response quantity of a MDOF system. The commonly used square root of the sum of the squares (SRSS) method was used to obtain the total peak response quantity. The SRSS method obtains the maximum response by taking the square root of the sum of the squared peak responses in each mode. The method gives sound results where the modal frequencies are well separated and is therefore valid for the archetype structure used in this study. The maximum response is obtained by Equation 9-4.

$$r_{max} = \sqrt{\sum_{i=1}^{n} r_i^2} \tag{9-4}$$

Subsequently, the calculated maximum responses from the response spectrum analysis are subsequently multiplied by the seismic performance factors (I_e, R-factor, Ω_o, and C_d) to find the seismic demand. Force-related design parameters are divided by R/I_e. Force-related design parameters include support forces and individual member forces for each mode of response. The displacement-related design parameters are multiplied by the quantity C_d/I_e. The importance factor I_e, response modification factor R, overstrength factor Ω_o , and deflection amplification factor C_d are defined in Appendix E Table E-2 and Equation E-2.

9-4 Conclusion

The results from the modal response spectrum analysis are used to design the shear wall, podium diaphragm and collectors. Chapters 15 and 14 describe the design procedure for these elements. The code requires the nominal strength of each member to be larger than the design force demands. The nominal strengths required by code will be converted to expected strengths in the probabilistic analysis. Subsequently, the reliability of the elements will be evaluated by comparing the demands calculated by the probabilistic analysis to the expected strengths required by code.

Chapter 10

Input PEER/TBI Analysis

10-1 PEER/TBI Analysis - Introduction

As an alternative to the Code seismic design procedures described in Chapter 9, ASCE 7-10 permits non-prescriptive seismic design with inherent seismic performance levels equivalent or superior to the design in accordance with the present Building Code provisions. The Pacific Earthquake Engineering Research Center (PEER) has developed Guidelines for Performance-Based Seismic Design of Tall Buildings [PEER/TBI, 2010] as an alternative seismic design procedure. In addition, the Los Angeles Tall Building Structural Design Council (LATBSDC) provides an alternative approach for seismic design and analysis of tall building in the Los Angeles region [LATBSDC, 2014]. Similar to the Code design procedure, these alternative seismic design procedures intend to provide the buildings with the capability to withstand MCE shaking with low probability (10%) of total or partial collapse, to withstand Design Earthquake shaking (2/3 MCE) without the generation of significant hazards, and to withstand moderate-intensity earthquake shaking with limited damage.

The main difference between these alternative approaches and the Code design procedure is the verification of intended behaviour under seismic loading. The alternative approaches verify whether the structure behaves as intended under seismic loading, typically through nonlinear time history analysis. Hence, these methods are called performance-based design methods. The advantages offered by performance-based design methods include more reliable attainment of intended performance under seismic loading and the possibility to assess innovative structural systems and materials. On the other hand, the more realistic prediction of structural performance requires increased knowledge from the engineers with regard to seismic hazard analyses, nonlinear dynamic behaviour, capacity design principles and detailing of elements [PEER/TBI, 2010].

10-2 Vertical loading

The structural loading combination given in Equation 10-1 is used to determine force and deformation demands.

$$1.0D + L_{exp} + 1.0E \tag{10-1}$$

Where,

$$\begin{aligned} D &= SW + SDL + CL && \text{Expected Dead Load} \\ L &= 0.4L_0 && \text{for Live Load} \geq 100 \text{ [psf]} \\ L_{exp} &= 0.2L_0 && \text{for Live Load} \leq 100 \text{ [psf]} \\ SW &= \text{Self-Weight} \\ SDL &= \text{Superimposed Dead Load} \\ CL &= \text{Cladding Load} \end{aligned} \tag{10-2}$$

The expected live load L_{exp} is taken as 20% of the unreduced live load for live load ≤ 100 [psf], according to ATC 72-1, Section 2.1.4. The reduction factor reflects both the low probability of the full design live load occurring simultaneously throughout the building and the low probability of simultaneous occurrence of the design live load and MCE shaking.

10-3 Earthquake loading

10-3-1 Introduction

The alternative guidelines seek to satisfy seismic performance levels equivalent to present Building Code design through a two-level design approach. The guidelines require essential elastic response and limited damage under Service Level Earthquake (SLE) shaking and a low probability of collapse under Maximum Considered Earthquake (MCE) shaking. In addition, all elements are detailed for compatibility with the expected deformations.

The Service Level Earthquake is defined as the earthquake intensity having a return period of 43 years. The structure should be capable of essentially elastic response under SLE shaking. Limited damage, which may include minor cracking and limited yielding of steel members, may occur under SLE shaking. However, the structure's ability to survive MCE shaking should not be compromised.

The Maximum Considered Earthquake shaking is defined by a 5%-damped acceleration response spectrum having a return period of 2475 years, which is equal to a 2% probability of exceedance in 50 years. The structure will experience significant inelastic deformation during MCE shaking and the evaluation aims to provide adequate safety against collapse. The target conditional probability of collapse is 10% or less.

10-3-2 Analysis methods

The structure's response under SLE shaking is evaluated using linear response spectrum analysis, without the application of response modification or overstrength factors and scaling to minimum base-shear criteria, i.e. assuming elastic response. Acceptable performance implies that the deformations are less than those that result in damage requiring repair and that the force-controlled, i.e. linear, actions do not exceed the expected strengths.

A nonlinear time history analysis is typically used in performance-based earthquake engineering to evaluate the structure's behaviour under MCE shaking. Nonlinear analysis provides the means to determine the behaviour beyond the elastic range, including strength and stiffness deterioration. The nonlinear time history analysis is used to confirm that the expected portions of the structure undergo inelastic deformations and to characterize the deformation demands on yielding elements and force demands on non-yielding elements [Deierlein et al., 2010].

10-3-3 Ground motion selection procedure

The alternative guidelines require a suite of seven ground motion records for nonlinear time history analysis. Ground motion selection requires the definition of a period of scaling and target response spectrum [ASCE 7-10, 2010]. The intent is to scale records such that the maximum responses are, on average, about equal, but not less than, the design spectrum over the period range.

Ground motions in two horizontal directions are considered. Vertical ground motions should only be considered if significant, for example in large spans where differential settlements are not allowed. Vertical ground motions are not significant for the archetype structure and therefore neglected in this study.

10-3-3-1 Period range of scaling

To capture higher mode responses and period elongation in each principal direction, the period range of scaling should be taken as 1.5 times the greater first mode period and 0.2 times the smaller first mode period. The upper limit of $1.5T_1$ is chosen to account for period elongation due to inelastic response, the lower limit of $0.2T_1$ is intended to correctly capture higher mode periods of the response.

10-3-3-2 Target spectrum

To evaluate the structure's behaviour under MCE shaking, the suite of seven ground motion records is selected and scaled to match a target reponse spectrum corresponding to a 2475-year return period earthquake intensity for the site. For performance-based earthquake engineering, the Uniform Hazard Spectrum, described in Section 8-2-2-1, is typically taken as the target spectrum. The UHS is generally a conservative target spectrum if used for ground motion selection and scaling and will therefore be used for the performance-based analysis in this study.

10-3-4 Uniform Hazard Spectrum

The site-specific Uniform Hazard Spectrum was computed by PEER NGA-West2 Spectrum. The input parameters used to compute the UHS were obtained from USGS hazard disaggregation as described in Section 8-1-2 and Section 11-3-2-1. The input parameters are given in Appendix F Table F-2. The computed UHS for the site is given in Figure 10-1.

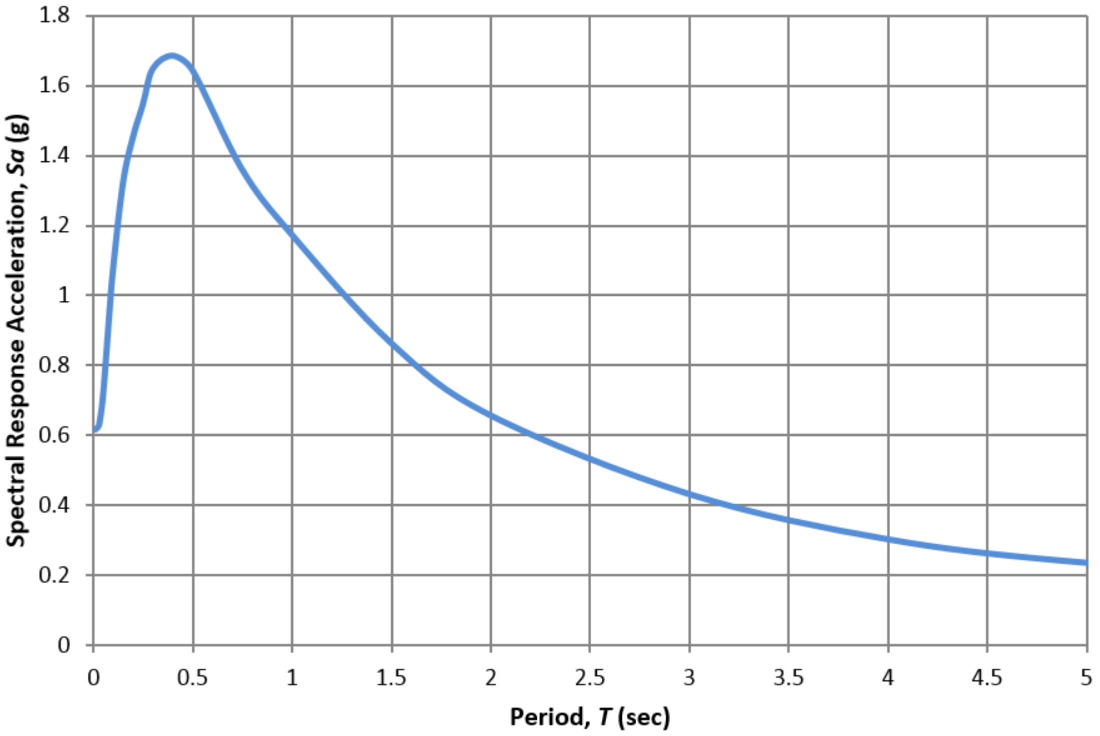

Figure 10-1: Uniform Hazard Spectrum for site

10-3-5 Ground motions for performance-based analysis

A suite of seven ground motion records for performance-based analysis was selected and scaled by PEER NGA-West2 Spectrum to match the UHS. Furthermore, secondary ground motion selection parameters magnitude M, distance R and local site conditions, such as $V_{s,30}$, were defined to select and scale the records. The secondary selection parameters are given in Appendix F Table F-3. Other search parameters, such as the initial scale factor, spectral ordinate, suite average, scaling method and weight function, were defined in Appendix F Tables F-4, F-5, F-6, and F-7.

The selected suite of seven ground motion records for performance-based analysis is given in Appendix F Table F-8. The Uniform Hazard Spectrum, response spectra of the selected ground motion records and suite mean are given in Figure 10-2.

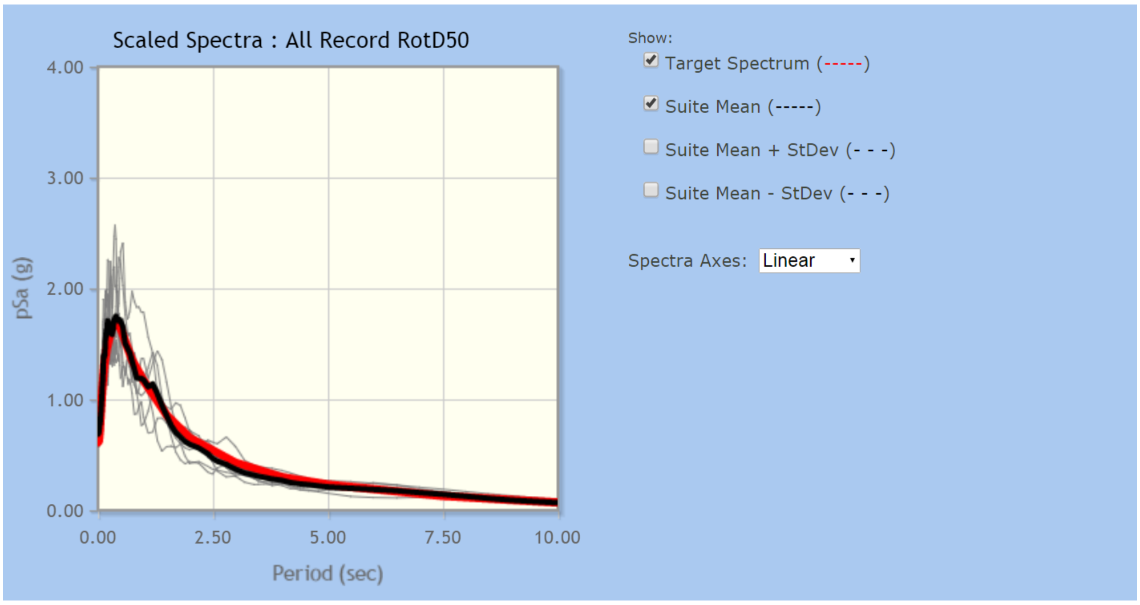

Show:
☑ Target Spectrum (-----)
☑ Suite Mean (-----)
☐ Suite Mean + StDev (- - -)
☐ Suite Mean - StDev (- - -)

Spectra Axes: Linear

Figure 10-2: Uniform Hazard Spectrum, frequency content ground motion records ands suite mean

The suite mean compares very well to the target spectrum for all spectral periods and Figure 10-2 shows no bias. The selected ground motions are input for the NLTHA. Seismic performance factors are not used in performance-based analysis. The maximum responses from each ground motion record can be extracted directly from the model. For design, the average value (arithmetic mean) of seven responses is compared to an acceptance level, and the component passes if the demand is less than the capacity.

10-4 Conclusion

The results from the nonlinear time history analysis with seven ground motions are used to design the shear wall, podium diaphragm and collectors. The design procedure is described in Chapters 14 and 15.

The alternative guidelines require the nominal strength as computed from applicable building codes but based on expected material properties to be larger than the demand obtained from statistical evaluation of nonlinear time history analysis for critical actions. The nominal strengths required by the alternative guidelines will be converted to expected strengths and compared to the demands from the probabilistic analysis to evaluate the reliability of the elements.

Chapter 11

Input Structural Reliability Analysis

11-1 Structural Reliability Analysis - Introduction

The Code seismic design procedure and alternative guidelines intent to design buildings that have less than 1 percent probability of collapse within a 50-year period. The Code and alternative guidelines expect to achieve this performance goal without explicit calculation of the collapse probability. The Code design procedure described in ASCE 7-10 indirectly evaluates the performance goal. Seismic performance factors are used to compute design forces for a given framing system. The alternative guidelines employ simple acceptance criteria to ensure stable, predictable response of the framing system under MCE shaking. However, many more than the seven sets of ground motions used for performance-based analysis must be generated and analysed to calculate the distribution of responses and to compute the reliability of a structure with reasonable confidence. Furthermore, if distributions of responses are required, the ground motions scaling methods must not only match the suite mean to the target spectrum but must also address and account for record-to-record variability.

The structural reliability analysis intents to explicitly calculate the distribution of responses and to compute the reliability of the structure with reasonable confidence. The reliability is defined as the probability of the demand exceeding the capacity in a specified period of time. A larger suite of ground motion records matching both the target spectrum mean and standard deviation will be selected for nonlinear time history analysis to calculate the distribution of responses. Also, the response of the structure will be evaluated at multiple intensity levels. The probability of demand exceeding the capacity for a lower intensity level earthquake may be smaller than for a higher intensity earthquake. However, the lower intensity level earthquake is probably more common than the higher intensity earthquake and can therefore contribute significantly to the probability of the demand exceeding capacity in a specified period of time. The probabilistic analysis provides insight in the reliability of the various elements of the structure designed by the Code seismic design procedure and alternative guidelines. Therefore, the probabilistic analysis is the means to evaluate whether the Code and alternative guidelines reach their intent to design buildings that have less than 1 percent probability of collapse within a 50-year period.

11-2 Vertical loading

The same vertical loading combination is applied to the structure for the probabilistic analysis as for the performance-based analysis as described in Section 10-2.

11-3 Earthquake loading

11-3-1 Introduction

The response of the structure will be evaluated at multiple intensity levels, as discussed in Section 11-1. Three intensity levels were selected. The chosen intensity levels have a probability of exceedance of 5% and 2% in 50 years and 1% in 100 years, i.e. 975-, 2475-, and 9950-year return periods, respectively. Nonlinear time history analysis is used to evaluate the structure's behaviour under the earthquake loading.

This section will elaborate on the ground motion selection procedure for the intensity level with a 2% probability of exceedance in 50 years, i.e. 2475-year return period. The ground motion selection procedure includes hazard identification and selecting the target spectrum. The same procedure was used to select ground motions at the other two intensity levels. The selected suite of ground motions consists of 61 records for the 2475-year return period. Suites of 40 ground motions were selected for the 975-year and 9950-year return period intensity level. A suite of 40 ground motions is recommended to obtain the distribution of the responses at a given intensity level [**REF**]. The suite for the 2475-year return period is larger to investigate the sensitivity of the results and distributions to the number of ground motions.

11-3-2 Ground Motion Selection procedure

Selection of a suite of ground motions for probabilistic analysis requires hazard identification, disaggregation and selection of a target spectrum.

Ground motions in two horizontal directions are considered. Similar to the performance-based analysis, vertical ground motions are not taken into account, as the structure does not have long spans, vertical discontinuities or other features that could lead to significant contributions to response by vertical ground motions.

11-3-2-1 Hazard Identification and Disaggregation

Probabilistic seismic hazard analysis (PSHA) is required for hazard identification at the site. The USGS tool described in Section 8-2-1 was used. The tool specifies three ground motion prediction equations (Boore-Atkinson 2008, Campbell-Bozorgnia 2008, and Chiou-Youngs 2008) with equal weights. The percentage contribution of each GMPE for the 2475-year return period intensity level is given in Appendix G-1-1 Table G-2.

Hazard disaggregation, discussed in Section 8-1-2, is required to compute the target spectrum. The hazard disaggregation calculates the controlling earthquake scenario, which includes the SA amplitude that is exceeded for a given intensity level. This SA amplitude, denoted as $sa*$, will be the target value for computation of the target spectrum. The mean distance, magnitude and ε_0 values associated with the hazard disaggregation are also used for target spectrum computation. The hazard disaggregation procedure and results are given in Appendix G-1-1. The results from the hazard disaggregation for the 2475-year return period intensity level for the building site are shown in Figure 11-1.

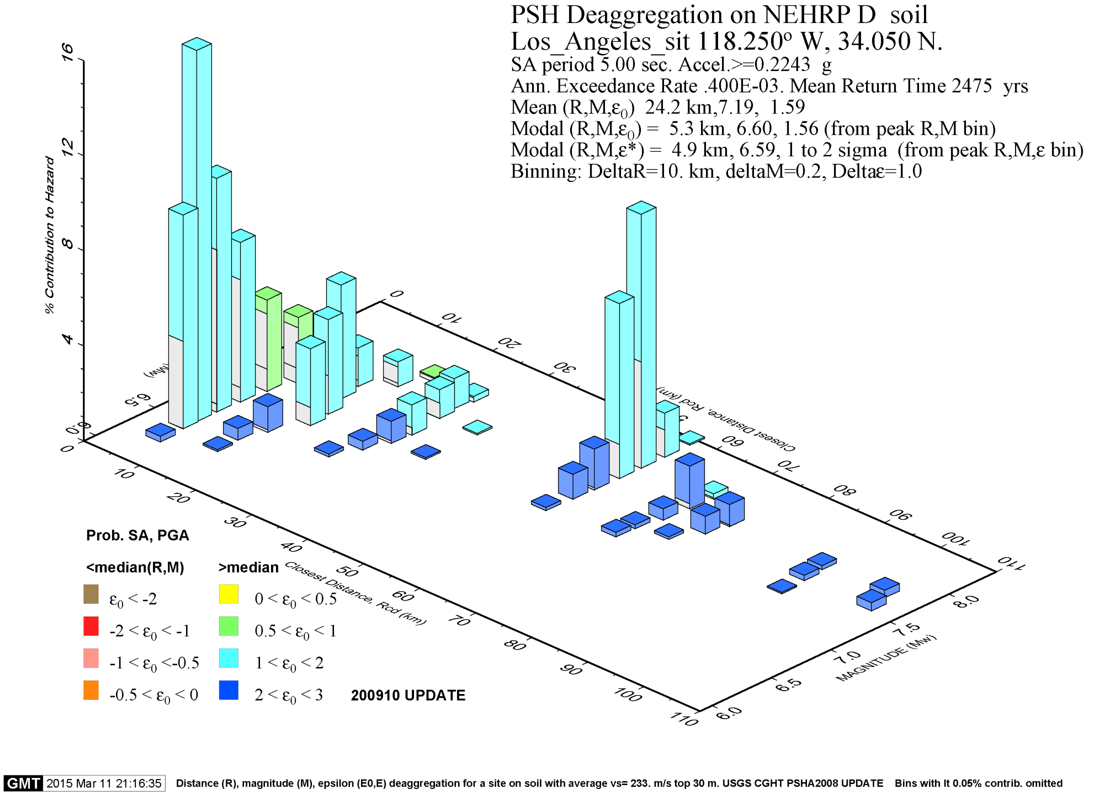

Figure 11-1: Disaggregation results for LA site, 2% probability of exceedance in 50 years (MCE-level)

Figure 11-1 shows that for a spectral acceleration period of 5.0 seconds, $V_{s,30} = 233$ [m/s], and a return period of 2475 years, the spectral acceleration amplitude exceeded with this return period is 0.2243 [g]. The mean distance R_{mean} is 24.2 [km], the mean magnitude M_{mean} is 7.19. It is important to note that the ε_0 given by the hazard disaggregation is not the same as the ε used for computation of the target spectrum [Lin et al., 2012]. The ε-values were back-calculated based on M, R, and S_a inputs from USGS disaggregation results, according to Equation G-1. The value ε indicates how many standard deviations the considered mean magnitude $\ln M_{mean}$ differs from the average $\ln M$ produced by the source. The sa^* amplitude will be used as the target value, where the conditional distribution of M, R and ε are good predictors of spectral shape.

11-3-2-2 Target Spectrum

Probabilistic analysis require selection of a set of ground motions that matches bot the target response spectrum mean and variance. Therefore, the Conditional Spectrum (CS), discussed in Section 8-2-2-3, was chosen as the target spectrum to select and scale ground motions for time-history analysis.

11-3-3 Conditional Spectrum

The site-specific Conditional Spectrum for each intensity level was computed by the Matlab tool developed by Jayaram et al. [Jayaram et al., 2011]. The input parameters for computation of the CS are given in Appendix G-2 Table G-5. The computed median, 2.5 and 97.5 percentile target conditional spectra for the 2475-year return period intensity level are given in Figure 11-2. The target logarithmic standard deviation is given in Figure 11-3. It is worth noting that the standard deviation is zero at spectral period T = 4.90 [sec], since the target spectrum is conditioned at this period.

11-3-4 Ground motions for probabilistic analysis

The Matlab script by Jayaram et al. (2011) was used to select and scale a suite of ground motion records to match the conditional spectrum for each intensity. Input parameters for ground motion selection for the 2475-year return period intensity level are given in Appendix G-2 Table G-6. The response spectra of the selected ground motions and the median, 2.5 and 97.5 percentile conditional response spectra are given in Figure 11-4. The spectra are conditioned on spectral acceleration of 0.2243 [g] at spectral period T = 4.90 [sec], corresponding to the 2475-year return period intensity level. A comparison of the target and sample exponential logarithmic means is given in Figure 11-5. Figure 11-5 shows that the logarithmic mean of the selected and scaled ground motions compares very well to the target spectrum for all spectral periods and has no bias. A comparison of the target and sample logarithmic standard deviations is given in Figure 11-6. Figure 11-6 shows that the sample standard deviations of S_a of the selected and scaled ground motions match well with the target standard deviation, especially at the spectral periods

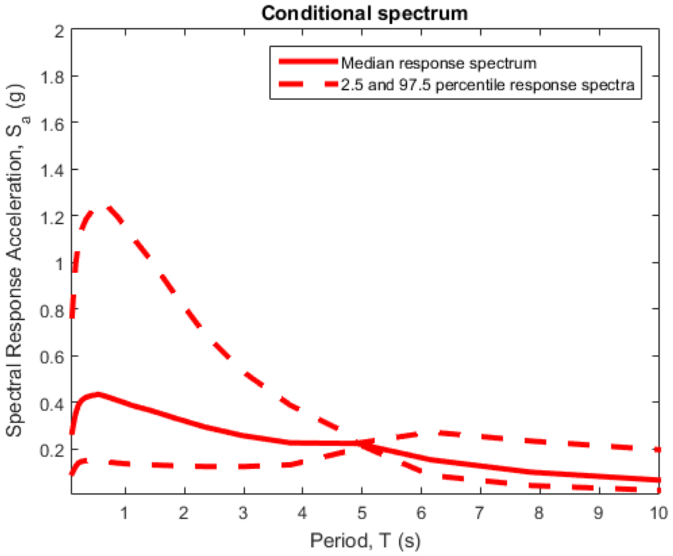

Figure 11-2: Median, 2.5 and 97.5 percentile conditional response spectra for 2475-year return period intensity level

of interest between $0.2T_1 \approxeq 1.0$ [sec] and $1.5T_1 \approxeq 7.5$ [sec]. The periods of interest are specified by ASCE 7-10, where the upper limit of $1.5T_1$ is chosen to account for period elongation due to inelastic response and the lower limit of $0.2T_1$ is intended to correctly capture higher mode response periods.

From Figures 11-4, 11-5, and 11-6, it can be concluded that the log mean and standard deviation values of Sa of the set of ground motions match well with the target spectrum. Therefore, the suite of 61 ground motion records is suitable for the probabilistic analysis.

The NGA record sequence number, scale factor, number of time steps and total number of steps of the selected ground motion records are given in Appendix G-3 Tables G-7, G-8, and G-9.

11-4 Conclusion

The expected capacity of the members designed by Code and alternative seismic design procedure will be compared to the demands calculated by the probabilistic analysis. Therefore, the results from the probabilistic analysis are used to gain insight in the reliability of the archetype structure.

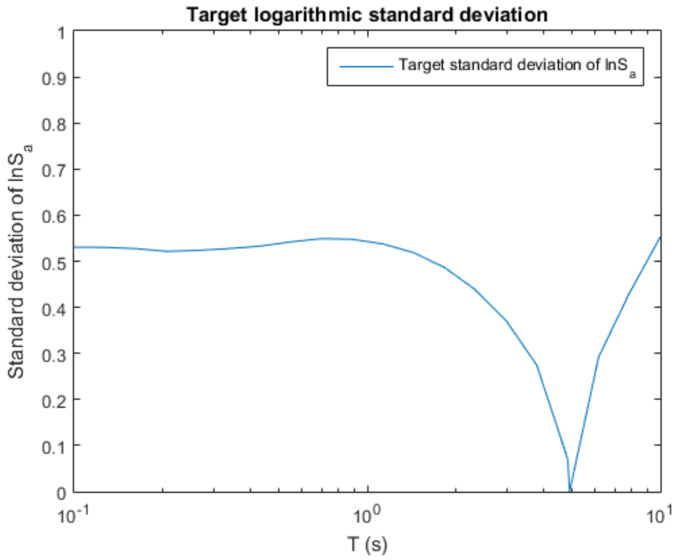

Figure 11-3: Target logarithmic standard deviation for 2475-year return period intensity level

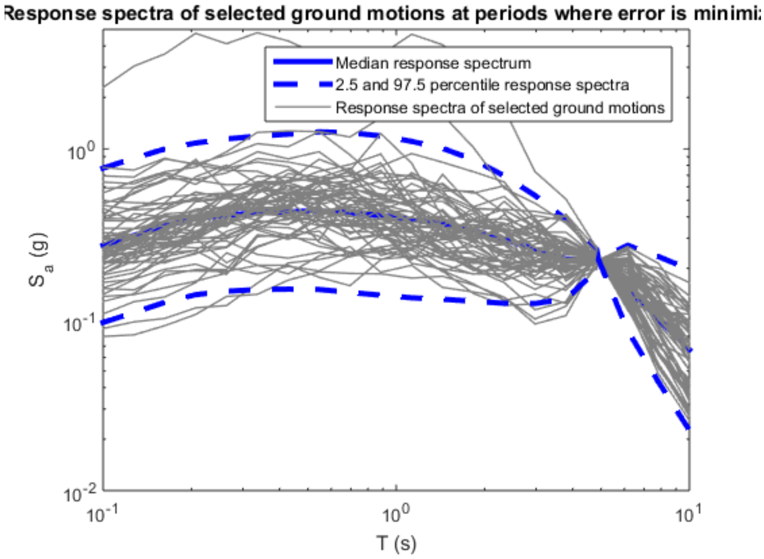

Figure 11-4: Response spectra of selected ground motions and median, 2.5 and 97.5 percentile conditional response spectra

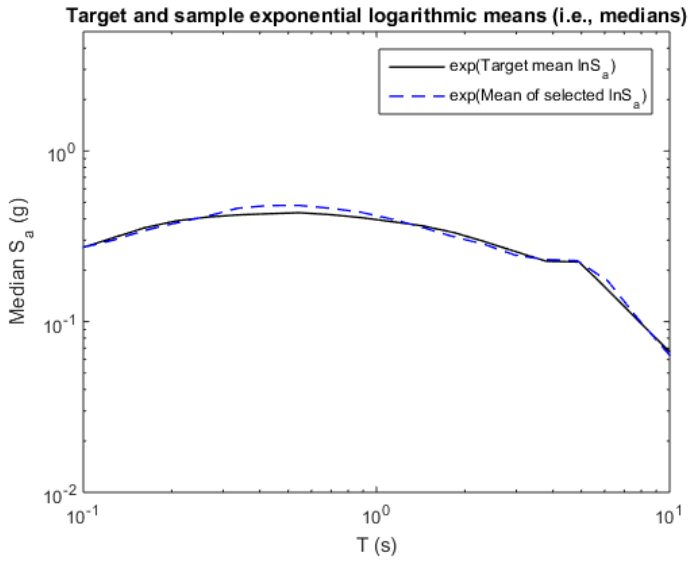

Figure 11-5: Comparison of target and sample exponential logarithmic means

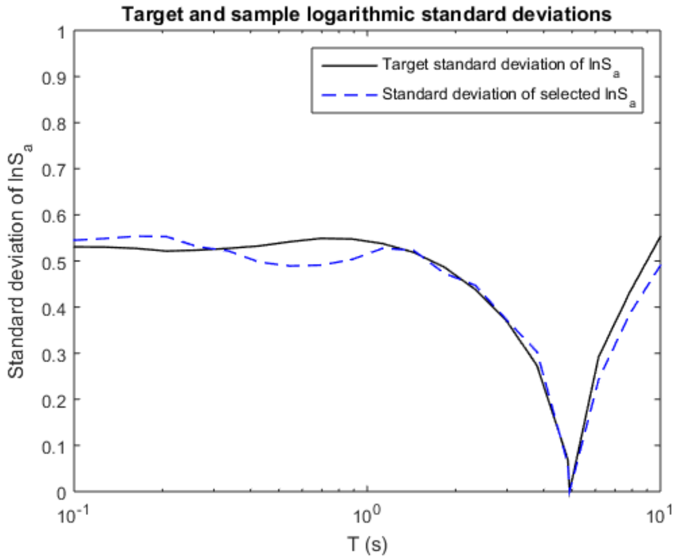

Figure 11-6: Comparison of target and sample logarithmic standard deviations

Part III

Validation of analysis results

Chapter 12

Overall structural behaviour

12-1 Introduction

The goal of this chapter is to evaluate the results of the nonlinear time history analyses in Perform 3D and to decide whether the results are valid for structural reliability analysis. First, the modal behaviour of the structure is evaluated in Section 12-2. Then, the target spectra are compared in Section 12-3. Subsequently, the shear force over the story height, bending moment over the story height and interstory drift ratios are evaluated in Section 12-4. Finally, Section 12-5 elaborates on the results of the NLTHAs in Perform 3D and the validity of the results.

12-2 Modal behaviour

To evaluate the validity of the structure, the modal behaviour is discussed. The first 12 modes are given in Figures 12-1 to 12-12. As expected, the first mode is in the weaker direction H1, the second mode is in direction H2, and angular vibration is observed for the third mode. Two hinges occur for modes 4 and 5 in direction H1 and H2, respectively. Mode 11 and 12 clearly show four hinges in direction H2 and H1, respectively. It is concluded that the modal behaviour of the structure in Perform 3D is as expected.

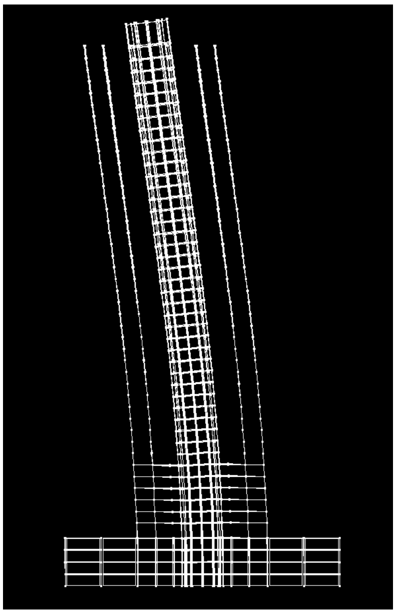

Figure 12-1: First mode T_1= 4.90 [sec]

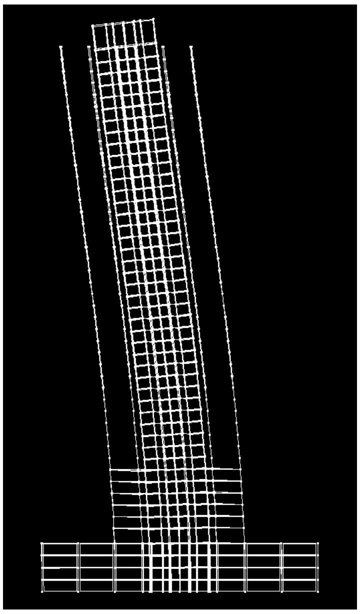

Figure 12-2: Second mode T_2= 3.44 [sec]

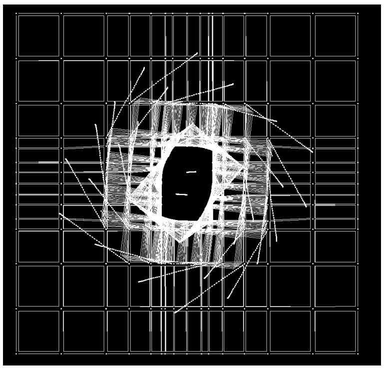

Figure 12-3: Third mode T_3= 2.42 [sec]

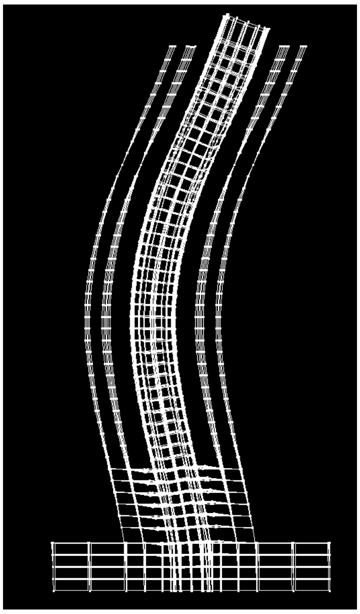

Figure 12-4: Fourth mode T_4= 0.95 [sec]

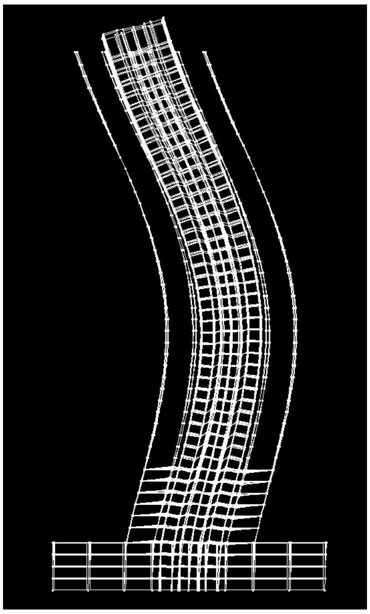

Figure 12-5: Fifth mode T_5= 0.88 [sec]

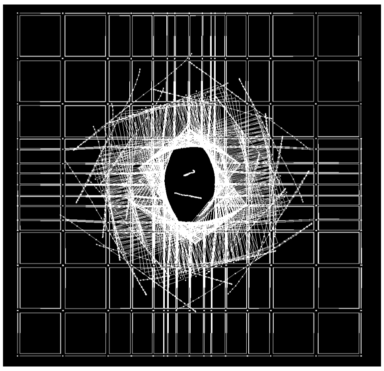

Figure 12-6: Sixth mode T_6= 0.80 [sec]

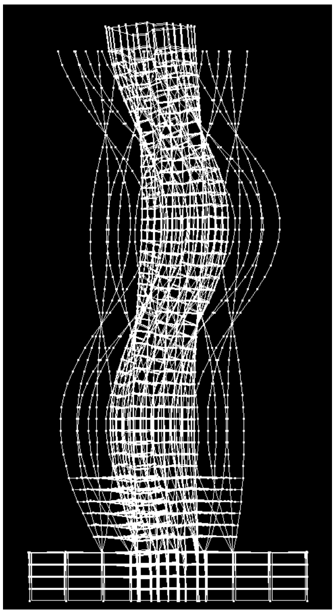

Figure 12-7: Seventh mode T_7= 0.47 [sec]

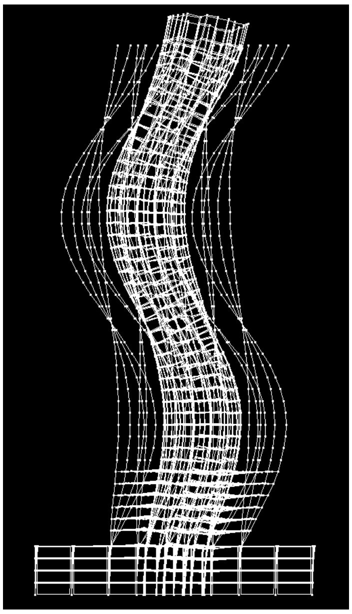

Figure 12-8: Eighth mode T_8= 0.44 [sec]

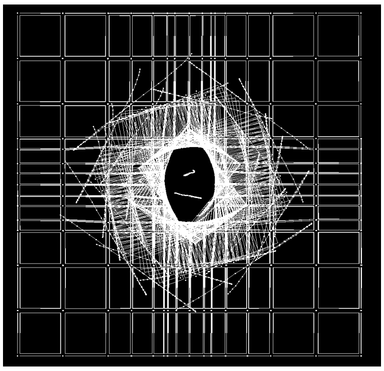

Figure 12-9: Ninth mode T_9= 0.41 [sec]

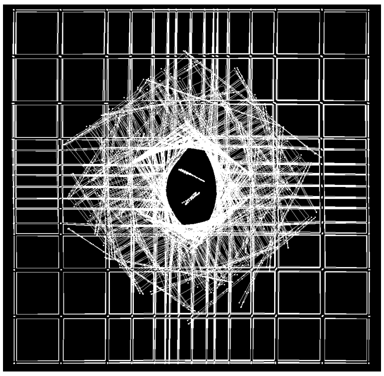

Figure 12-10: Tenth mode T_{10}= 0.29 [sec]

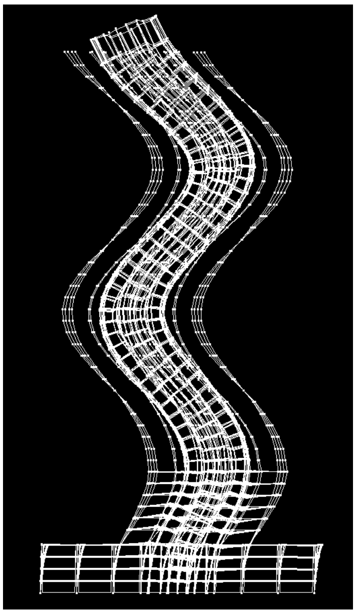

Figure 12-11: Eleventh mode T_{11}= 0.28 [sec]

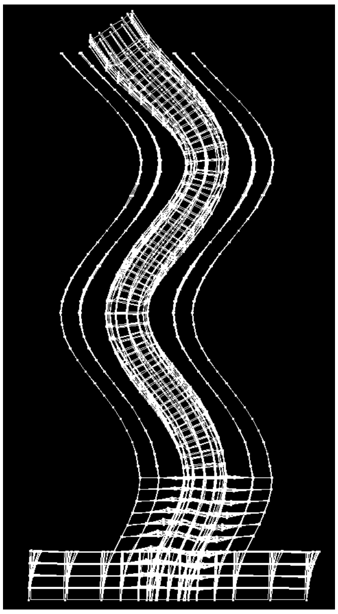

Figure 12-12: Twelfth mode T_{12}= 0.25 [sec]

12-3 Comparison of Ground motion spectra

12-3-1 Uniform Hazard Spectrum

The site-specific 2%-in-50-years Uniform Hazard Spectrum is given in Figures 12-13 in normal scale and 12-14 in log-log scale. The figures on the left give the UHS target spectrum, the response spectra of 14 single ground motions, selected for PEER/TBI analysis, and the mean response spectrum of the 14 single ground motions. These 14 GMs form 7 pairs of ground motions for PEER/TBI analysis. The response spectra of the single ground motions in direction H1, the corresponding mean response spectrum and UHS target spectrum are given in the middle figure. The same is done for GMs in H2 direction in the right figure.

The combined mean response spectrum and the mean response spectra in H1 and H2 direction match fairlywell with the target spectrum. The mean response in direction H1 matches slightly better with the UHS than the mean response spectrum in Direction H2. The mean response spectrum of the GMs in Direction H2 is slightly less than the UHS for some periods. Evaluation of the ratio between the results from NLTHAs with ground motions scaled to the Conditional Spectrum (the reliability analysis) and the results from NLTHAs with ground motions scaled to the UHS (PEER/TBI analysis) might therefore result in a lower ratio in direction H2. These results include bending moments, shear forces and interstory drift ratios.

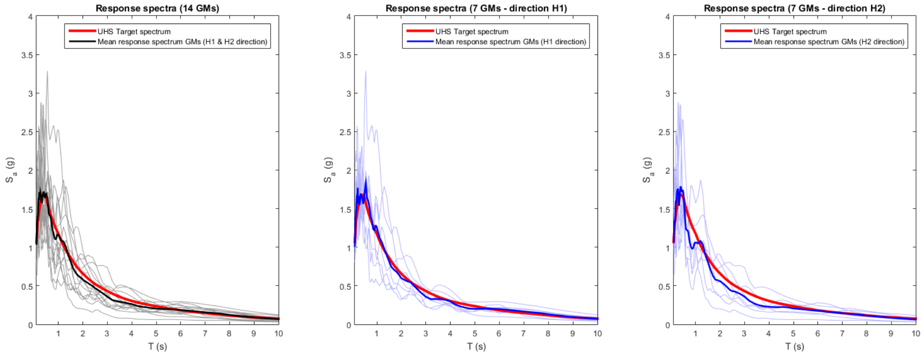

Figure 12-13: UHS Target spectrum compared to mean response spectra selected GMs

12-3-2 Conditional Spectra

The 5%-in-50-years, 2%-in-50-years ,and 1%-in-100-years Conditional Spectra are given in Figure 12-15. The median response spectra and the 2.5% and 97.5% percentile response spectra are given in the left figure. Furthermore, the response spectra of the selected ground motions are given in the right figure of Figure 12-15. It is noted that the target

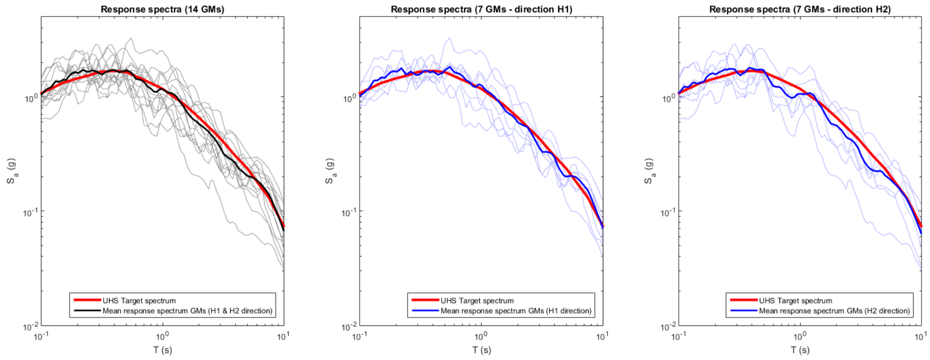

Figure 12-14: UHS Target spectrum compared to mean response spectra selected GMs in log-log scale

spectral acceleration increases for less frequent ground motion intensities. Furthermore, the target spectrum shows increasing peakedness at the conditioning period for rarer $S_a(T)$ levels, as discussed in Section 8-2-2-3.

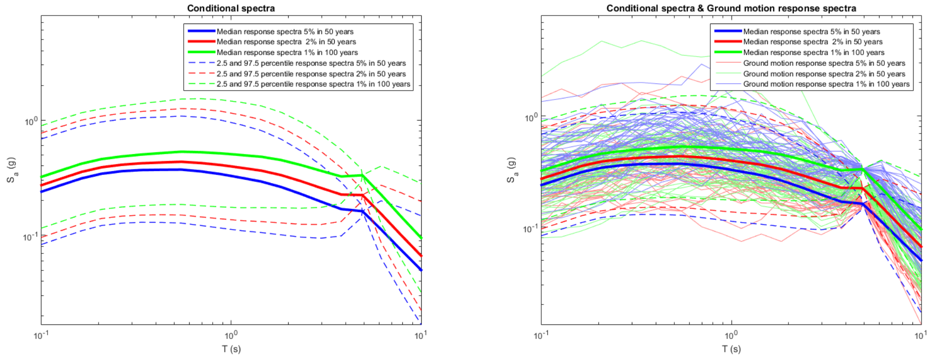

Figure 12-15: Conditional spectra for 5% in 50 years, 2% in 50 years, 1% in 100 years ground motion intensities

12-3-3 Conditional Mean Spectrum versus Uniform Hazard Spectrum

The Conditional Mean Spectra, which is effectively the Conditional Spectrum without variance, and the 2%-in-50-years UHS are compared in Figure 12-16. It is noted that the CMS is equal to the UHS at the target period, and tapers back towards to median response spectrum. Therefore, the response spectra of the selected GMs for 2%-in-50-years UHS and 2%-in-50-years CS are comparable around the target period. Furthermore, the difference between the response spectra increases for spectral periods further away from the target period, as the CMS target spectrum tapers back towards the median response spectrum.

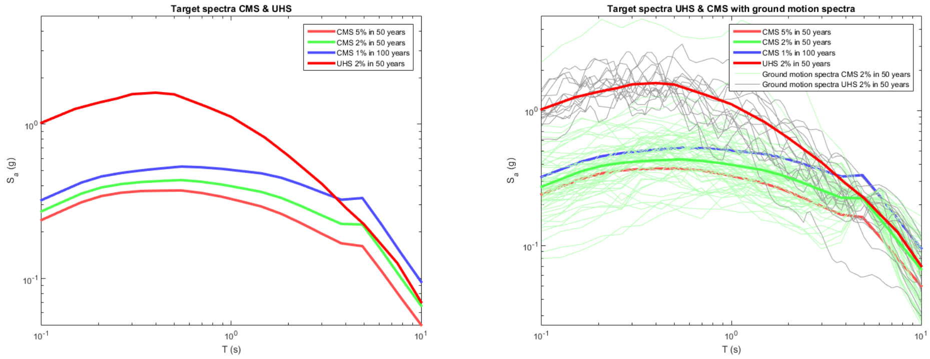

Figure 12-16: UHS and CMS target spectra and ground motion spectra

12-4 Structural behaviour

12-4-1 Shear force over story height

The mean shear forces over the story height for different intensity levels in direction H1 and H2, normalized to the seismic weight W=91000 [kips], are given in Figure 12-17. As expected, the shear force is close to zero at the top of the structure and is largest at the base. Furthermore, the mean shear force increases for increasing ground motion intensity levels for every story. The same shape of shear forces over the story height is observed for all intensity levels, which is another indicator of valid results for each intensity level.

The shear force in the shear walls below base level is less than the base shear. The larger relative stiffness of the shear walls in Direction H2 results in larger below-ground shear forces and larger transfer forces compared to shear forces in Direction H1.

The individual results for shear force over the story height for RP975, RP2475, and RP9950 are given in Appendix H Figures H-1, H-2, and H-3, respectively.

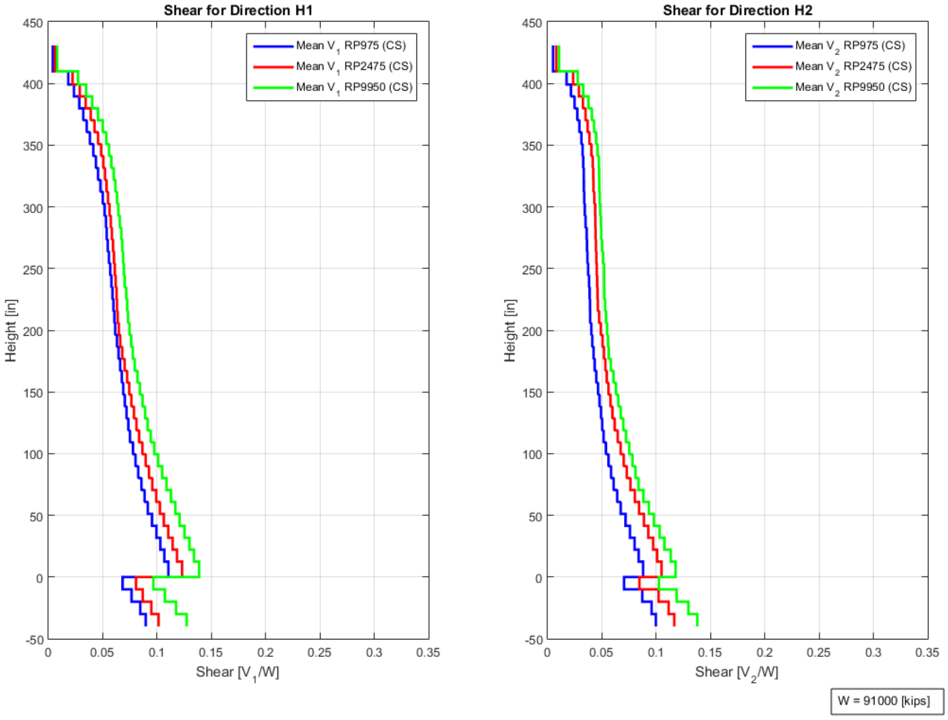

Figure 12-17: Mean shear force over story height for intensity levels RP975, RP2475, and RP9950

12-4-2 Bending moment over story height

The mean bending moments over the story height for different intensity levels in direction H1 and H2 are given in Figure 12-18. The bending moments are normalized to the mean base bending moment M_0=2.1097·10^7 [kip-inches] in Direction H2 for RP2475. The mean bending moment is close to zero at the top of the structure and largest at the base. The reversed shear force reduces the bending moment below the podium diaphragm. Similar to the shear force, the mean bending moment increases for increasing intensity levels at every story and the shape of the bending moment is similar for different intensity levels.

It is noted that the bending moment in direction H2 is almost twice as large as the bending moment in direction H1. The larger moment of inertia in Direction H2 is expected to cause the different in bending moment in direction H1 and H2.

The individual results for bending moment over the story height for RP975, RP2475, and RP9950 are given in Appendix H Figures H-4, H-5, and H-6, respectively.

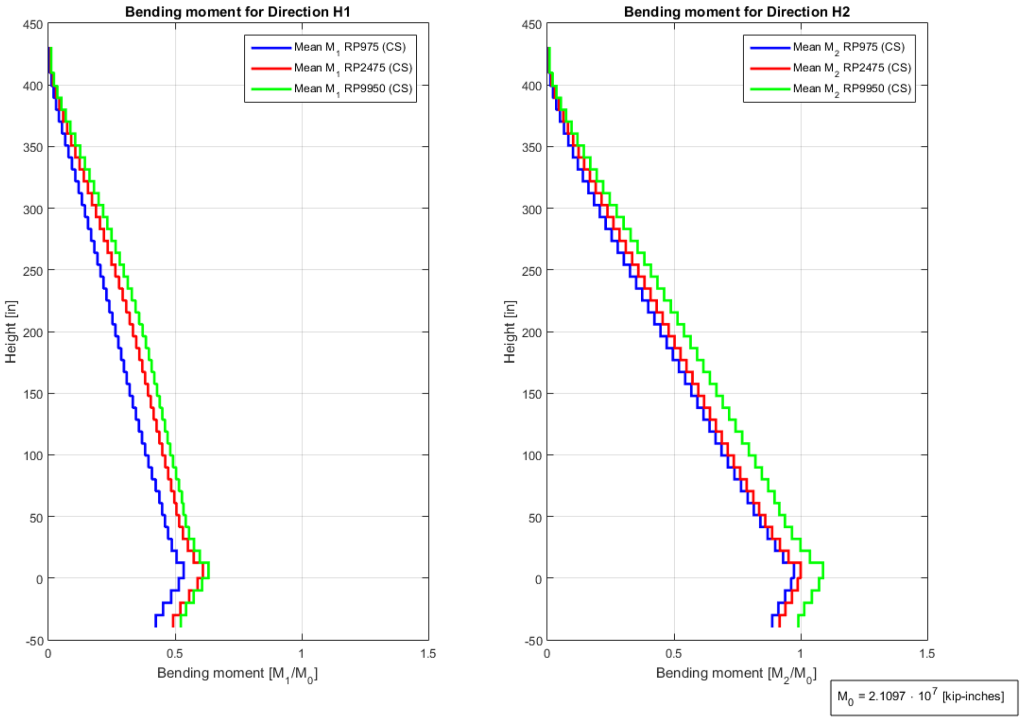

Figure 12-18: Mean bending moment over story height for intensity levels RP975, RP2475, and RP9950

12-4-3 Interstory drift ratio over story height

The mean interstory drift ratios (IDR) over story height for different intensity levels in direction H1 and H2 are given in Figure 12-19. The drift ratio is measured in the North-East corner of the core and given as a percentage. THe IDR increases towards the top of the structure. Furthermore, the IDR increases for increasing intensity levels and the shape of the drift ratios over story height is similar for every intensity level.

The IDR in direction H1 are larger than the IDR in direction H2. This is expected, as the moment of inertia of the core is smaller in direction H1. The individual IDR over the story height for RP975, RP2475, and RP9950 are given in Appendix H Figures H-4, H-5, and H-6, respectively.

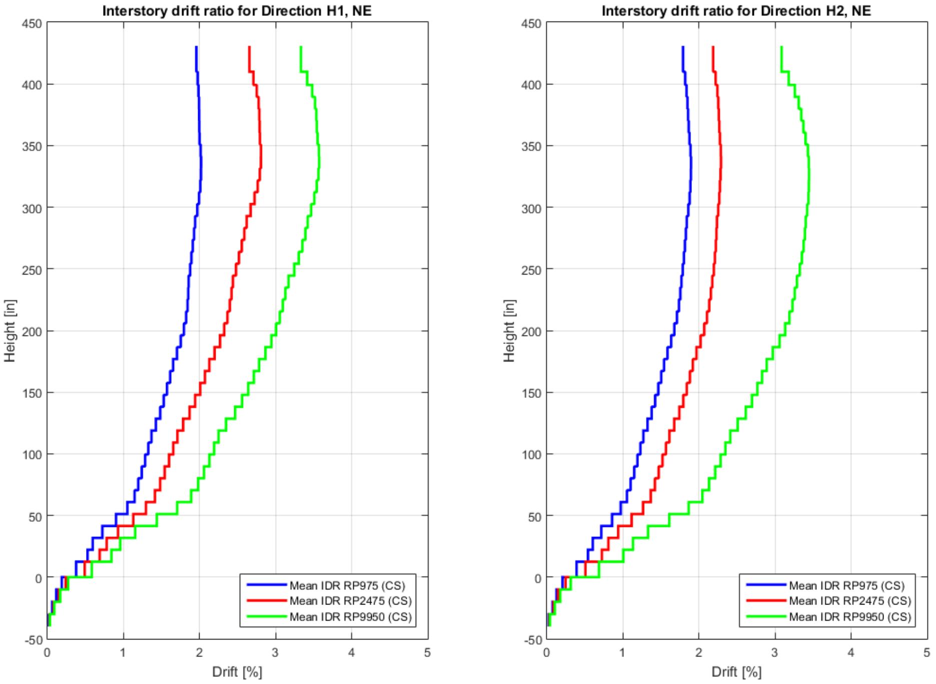

Figure 12-19: Mean interstory drift ratio over story height for intensity levels RP975, RP2475, and RP9950

12-5 Conclusion

Evaluation of modal behaviour and comparison of target spectra in two directions gave expected results. Furthermore, evaluation of the shear force over the story height, bending moment over the story height en interstory drift ratios over the story height showed expected results. The EDPs increased for increasing intensity levels and the shape was similar for different intensity levels. Furthermore, differences in the results in direction H1 and H2 could be explained by the structural properties in both directions. Therefore, it is concluded that the overall structural behaviour is logical and analysis results from NLTHAs in Perform 3D are valid for the structural reliability analysis.

Chapter 13

Diaphragm shear stress distribution

13-1 Introduction

The goal of this chapter is to investigate and validate the force transfer and shear stress distribution in the podium diaphragm found from NLTHA in Perform 3D. First, the static shear stress distribution from transfer forces in the shear walls as computed by Scia Engineer 15.1 is discussed in Section 13-2. In Section 13-3, the static shear stress distribution in the basement walls computed with Scia Engineer 15.1 is compared to the shear distribution of a thin-walled box section. Section 13-4 discusses the differences between the static and dynamic load case. In Section 13-5, the usage ratio plots from nonlinear time history analysis (NLTHA) in Perform 3D are deduced to a combination of individual load cases. Finally, Section 13-6 elaborates on the accuracy of the results found by Perform 3D for force transfer through the basement diaphragms.

13-2 Static shear stress distribution in diaphragms

This section elaborates on the static shear stress distribution in the diaphragm resulting from static transfer forces introduced from the shear walls into the diaphragm. The shear stress was computed using Scia Engineer 15.1. Nine load combinations investigate the effect of different ratios of transfer force V_1 and V_2. The shear stress distribution was computed for V_1 only; V_1 & $0.25V_2$; V_1 & $0.50V_2$; V_1 & $0.75V_2$; V_1 & V_2; $0.75V_1$ & V_2; $0.50V_1$ & V_2; $0.25V_1$ & V_2; and V_2 only. The results are given in Figures 13-2, 13-3, 13-4, 13-5, 13-6, 13-7, 13-8, and 13-9.

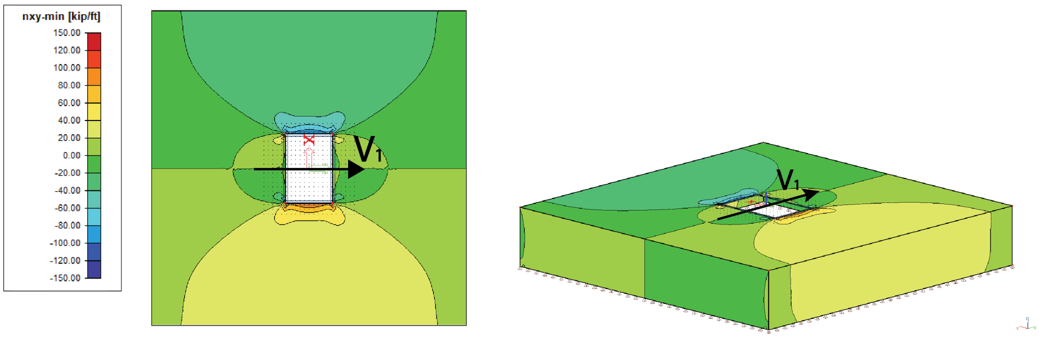

Figure 13-1: Shear stress distribution; Shear force V_1 only

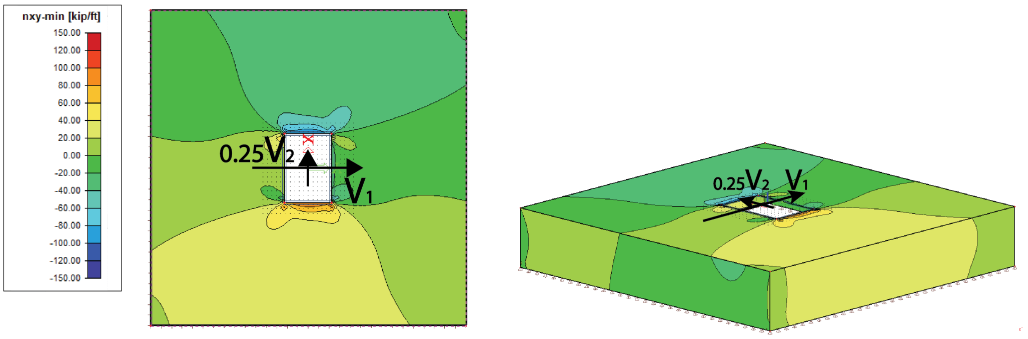

Figure 13-2: Shear stress distribution; Shear force V_1 & $0.25V_2$

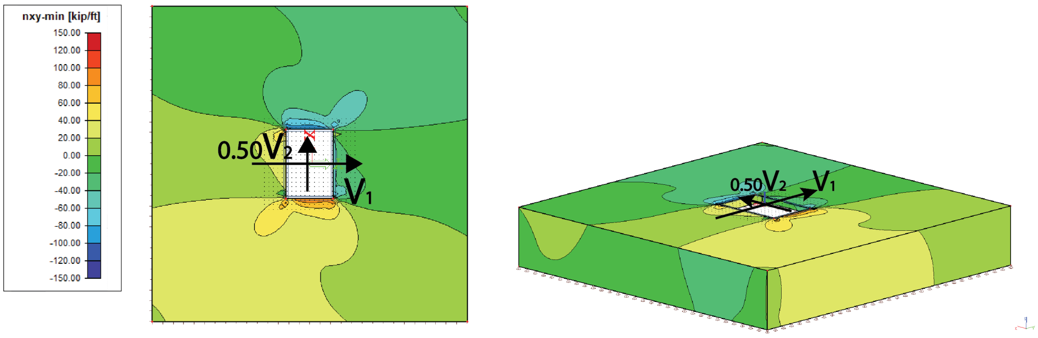

Figure 13-3: Shear stress distribution; Shear force V_1 & $0.50V_2$

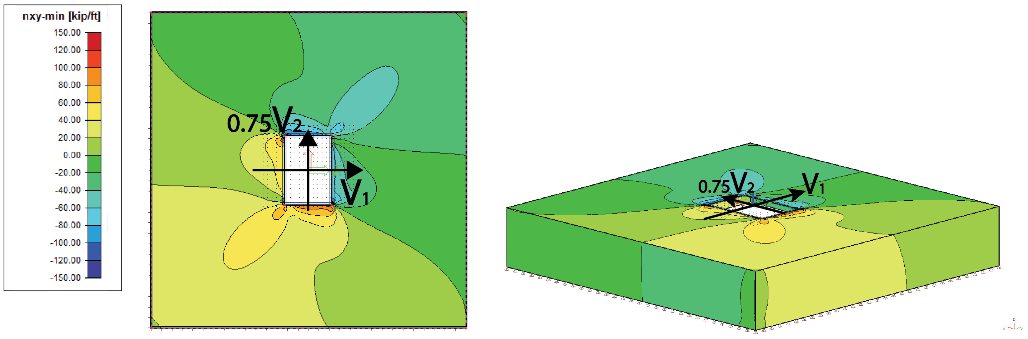

Figure 13-4: Shear stress distribution; Shear force V_1 & $0.75V_2$

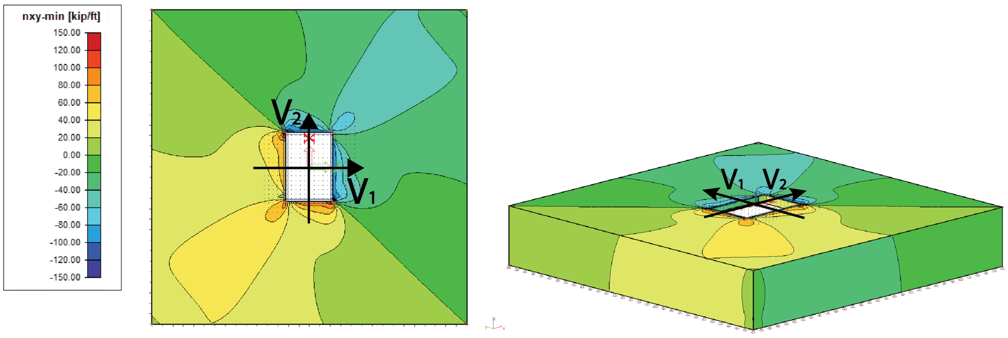

Figure 13-5: Shear stress distribution; Shear force V_1 & V_2

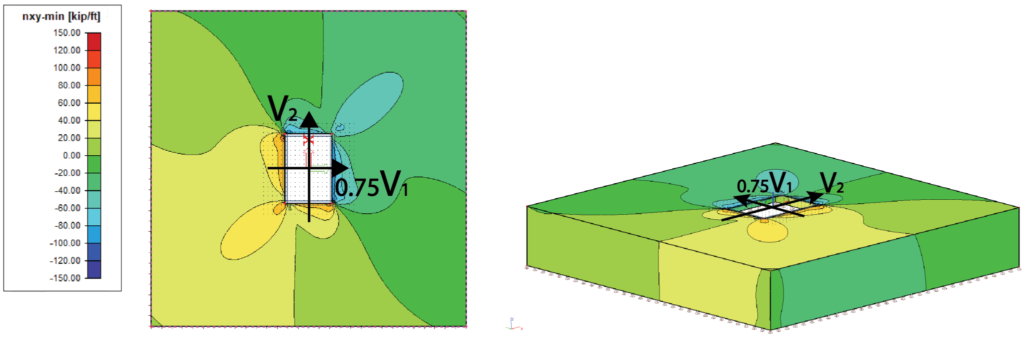

Figure 13-6: Shear stress distribution; Shear force $0.75V_1$ & V_2

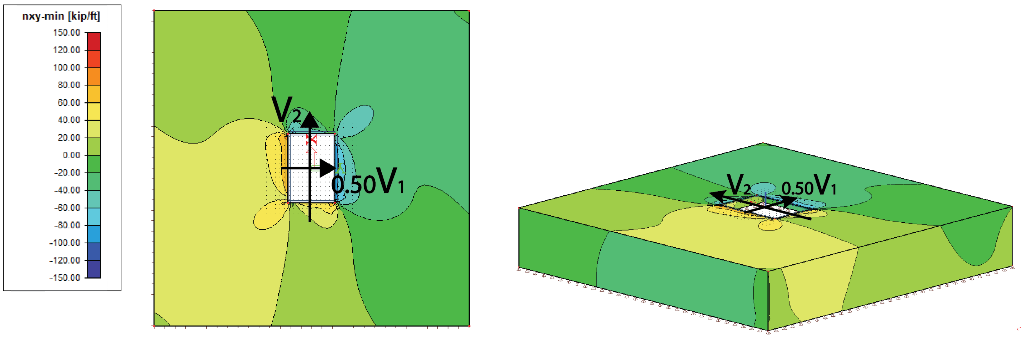

Figure 13-7: Shear stress distribution; Shear force $0.50V_1$ & V_2

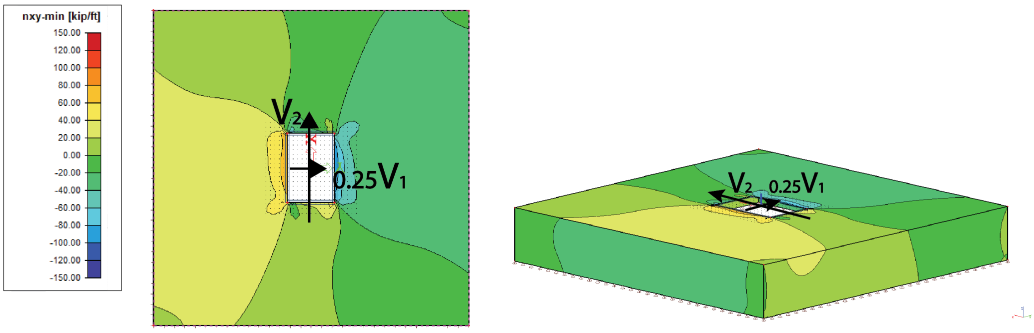

Figure 13-8: Shear stress distribution; Shear force $0.25V_1$ & V_2

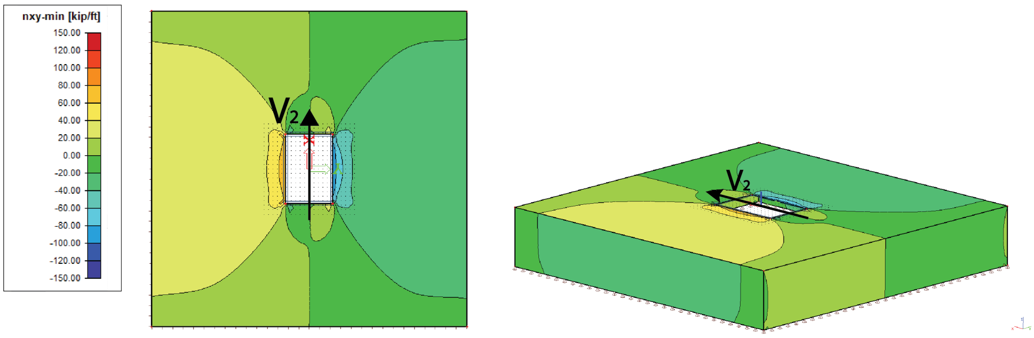

Figure 13-9: Shear stress distribution; Shear force V_2 only

13-3 Static shear stress distribution in basement walls

The shear stress distribution of a thin-walled box section for five different load combinations was compared to the shear stress distribution found by Scia Engineer 15.1 for these load combinations to get better understanding of the calculated shear stress distribution. The shear stress distribution from Scia Engineer 15.1 and the theoretical shear stress distribution of a box section for load combinations V_1 only; V_1 & $0.5V_2$; V_1 & V_2; $0.5V_1$ & V_2; and V_2 only are shown in Figures 13-10, 13-11, 13-12, 13-13, and 13-14, respectively. The results show good comparison between the theoretical and computer model. Therefore, the static shear stress distribution in the basement walls can be schematized by a thin-walled box section.

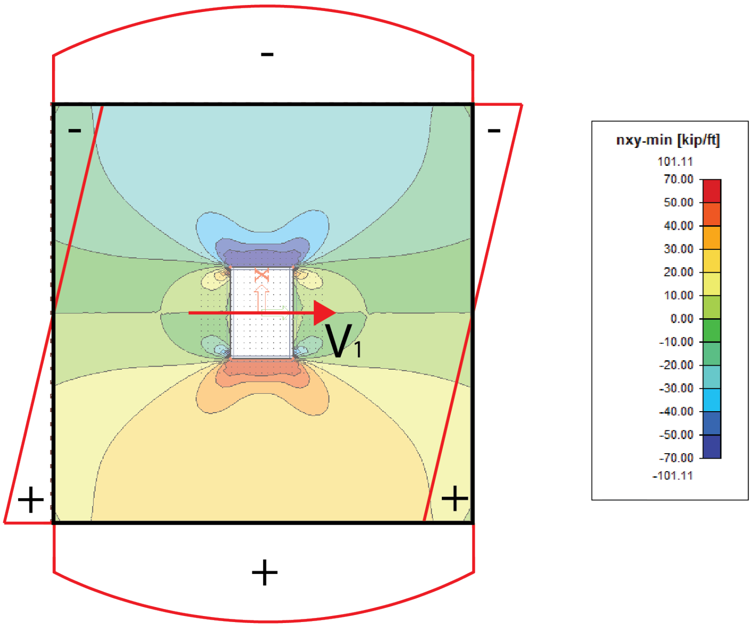

Figure 13-10: Case 1: Shear force V_1 only

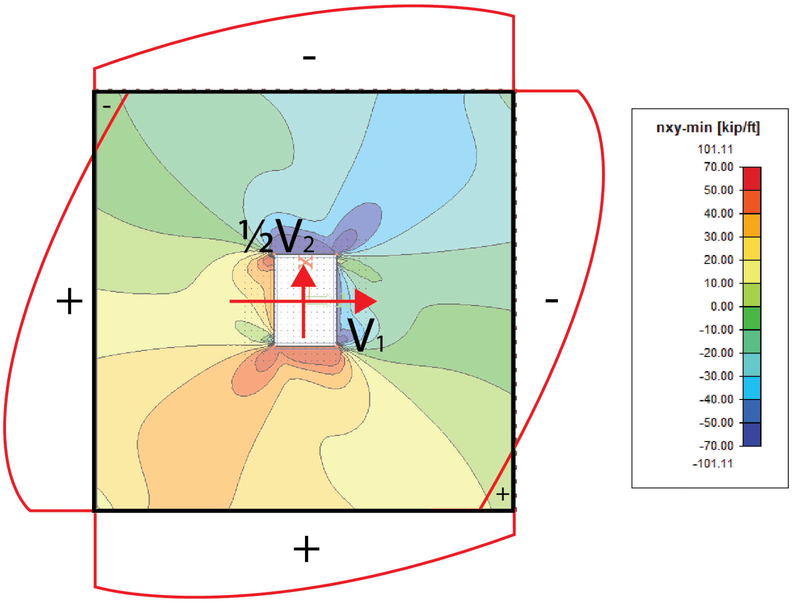

Figure 13-11: Case 2: Shear force V_1 & $0.50V_2$

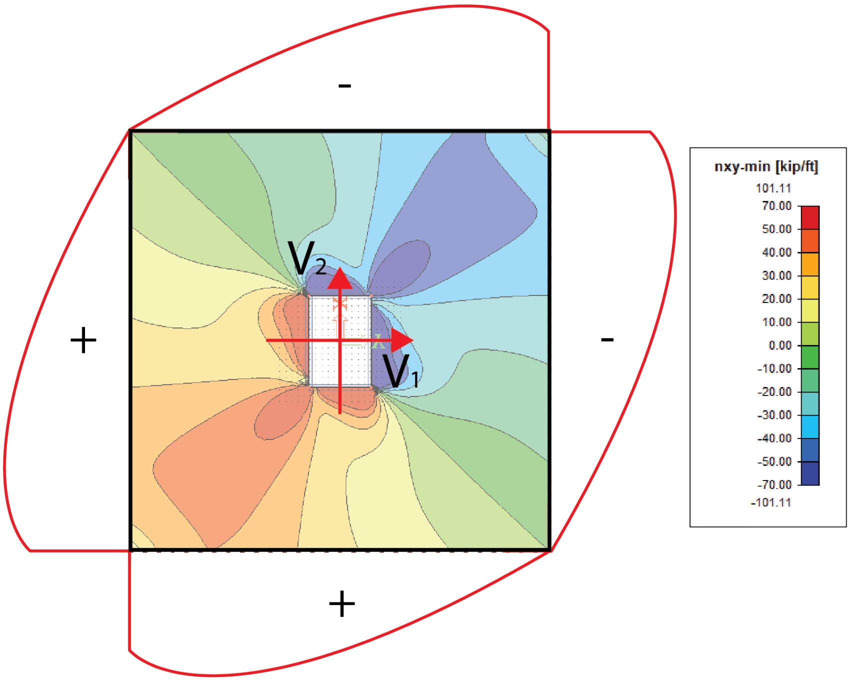

Figure 13-12: Case 3: Shear force V_1 & V_2

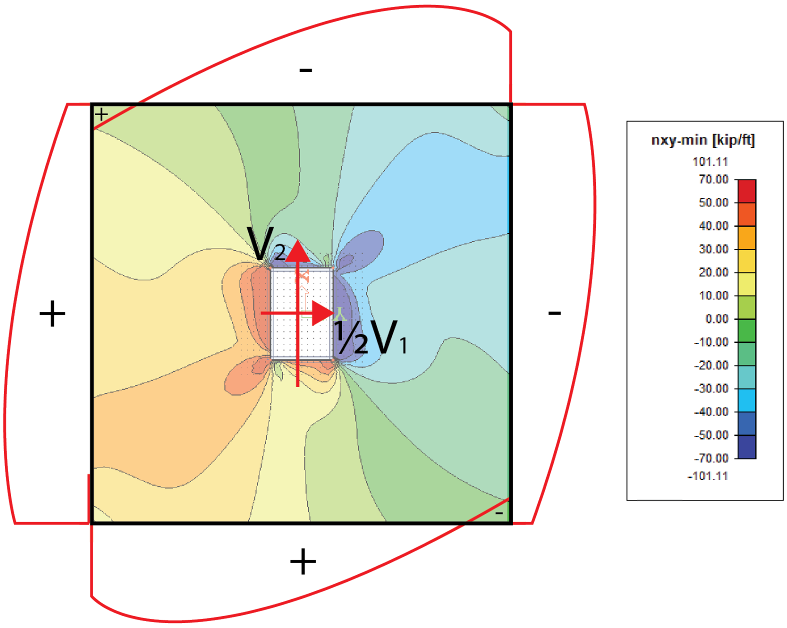

Figure 13-13: Case 4: Shear force $0.50V_1$ & V_2

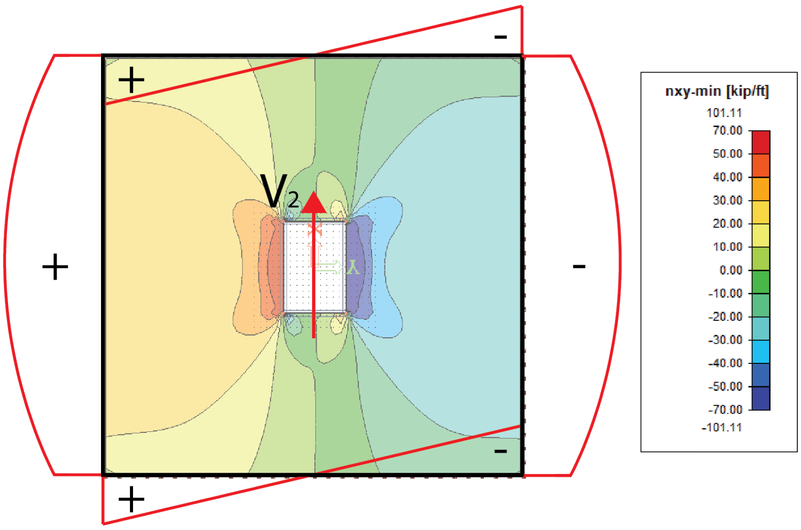

Figure 13-14: Case 5: Shear force V_2 only

13-4 Static versus dynamic load case

13-4-1 Theoretical load cases versus Earthquake loading

In Section 13-2, nine theoretical static load combinations were evaluated to understand the influence of different combinations of V_1 and V_2 on the force transfer and shear stress distribution. The dynamic earthquake loading causes many more combinations of V_1 and V_2. Transfer forces V_1 and V_2 can be both positive, both negative and of different signs for different time t during the earthquake loading. Furthermore, torsion may results in different forces occurring in the individual shear walls for the same time t. The shear stress distribution found from the earthquake loading will therefore always differ from the theoretical load combinations from the static model. However, the theoretical load combinations are useful to identify the principal load combination or combinations resulting from the earthquake loading.

13-4-1-1 Torsion

The archetype structure is symmetric in two directions. Therefore, large torsion of the structure due to earthquake loading is not expected. To evaluate torsion, the shear force was evaluated above the ground floor diaphragm in level L01. Torsion in the structure results in differences in the shear forces in the opposite walls or shear forces of opposite sign. Therefore, shear force in the north wall is compared to the south wall, and the shear force in the east wall is compared to the west wall for two ground motions. Figures 13-15 and 13-16 give the shear forces found for ground motion 6 of PEER/TBI analysis (UHS-GM6). Figures 13-18 and 13-17 show the shear force over time for GM20 of RP9950 from the probabilistic analysis (RP9950-GM20). The figures indicate that torsion forces are small, as expected for the symmetric archetype structure.

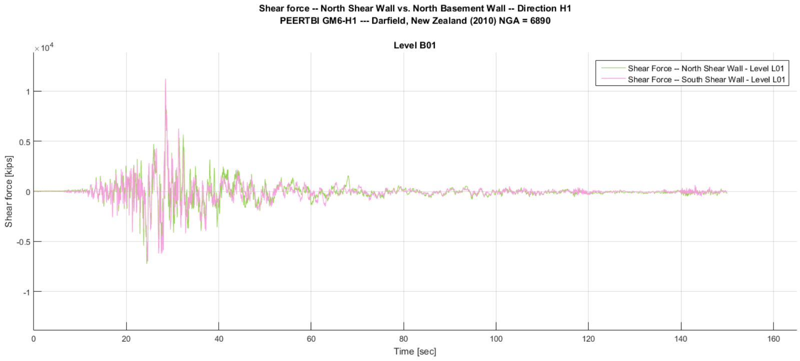

Figure 13-15: UHS-GM6: Shear wall level L01 - North wall & South wall

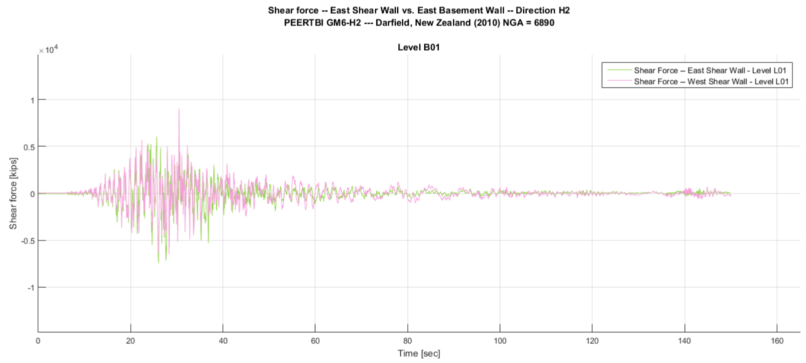

Figure 13-16: UHS-GM6: Shear wall level L01 - East wall & West wall

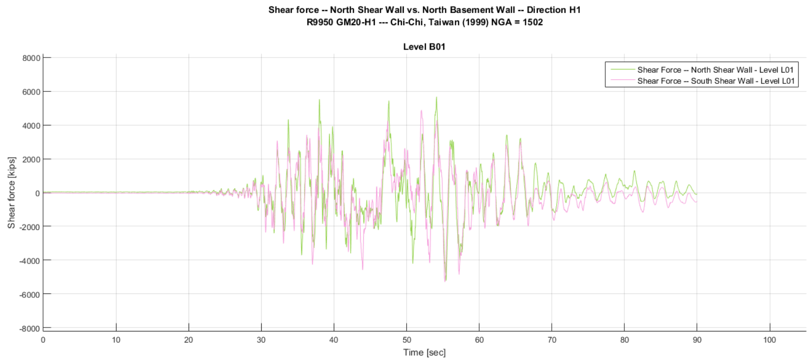

Figure 13-17: RP9950-GM20: Shear wall level L01 - North wall & South wall

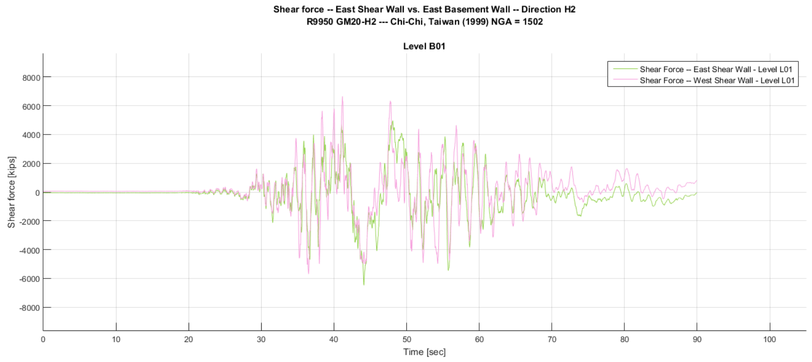

Figure 13-18: RP9950-GM20: Shear wall level L01 - East wall & West wall

13-4-2 Transfer forces versus inertial forces

The theoretical load combinations only account for the shear stress distribution resulting from the transfer force. The total transfer force is therefore equal to the total force in the basement walls. The shear stress in the diaphragm during earthquake loading results from a combination of transfer force and inertial force from the mass of the diaphragm. The total transfer force is therefore not equal to the total force in the basement walls. Depending on the orientation of the transfer force and inertial force, the total force in the basement walls can be smaller or larger than the transfer force. The magnitude of the inertial force can be calculated from the difference between the transfer force and the force in the basement walls. Figures 13-19, 13-20, 13-21, and 13-22 give the transfer force versus the basement wall force over time in the groundfloor diaphragm in Directions H1 and H2 for UHS-GM6 and RP9950-GM20. These figures show that the difference between force in the basement walls and total transfer force is relatively small. Therefore, it is concluded that the inertial force is relatively small compared to the transfer force in the groundfloor diaphragm. From Figure 13-23 for UHS-GM6 and Figure 13-24 for RP950-GM20 it can be concluded that the same holds for the other basement levels.

However, when the usage ratio plots from the NLTHAs were evaluated, it was concluded that the inertial effects can not be neglected. Magnified plots at various time steps t show that the inertial force can cause the peak usage in certain elements, as shown in Figure 13-25. Moreover, the combination of inertial force and transfer force can increase or decrease the total shear stress and deformation in the diaphragm, as shown in Figures 13-26 and 13-27. The elements most affected by inertial force are the elements adjacent to the basement wall, as the inertial shear force increases linearly towards the sides of the slab. Shear stresses due to inertial forces were observed near the highest earthquake intensity, whereas the peak transfer force tended to occur after the peak ground motion intensity. This can be explained by the fact that the inertial forces result from peak acceleration whereas the transfer forces occur due displacement of the tower and displacement compatibility between the shear walls and basement walls. Due to the longer period of the tower, it takes some time before the tower reaches maximum displacement. Therefore, the peak transfer force occurs some time after the peak ground motion intensity.

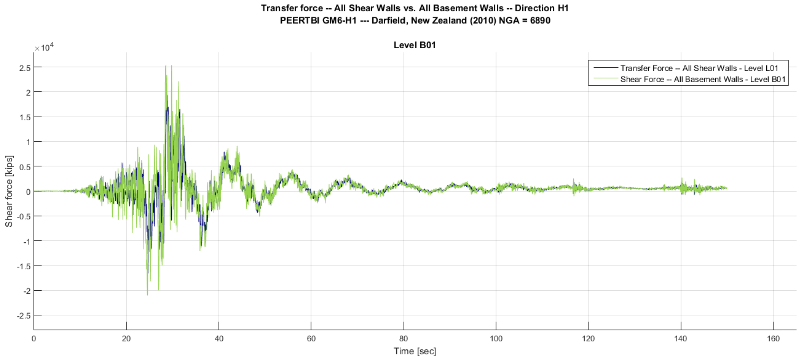

Figure 13-19: UHS-GM6: Transfer force versus Basement wall force - Groundfloor diaphragm Direction H1

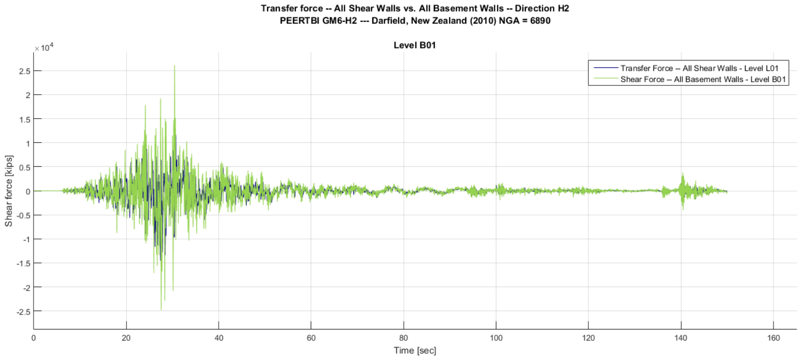

Figure 13-20: UHS-GM6: Transfer force versus Basement wall force - Groundfloor diaphragm Direction H2

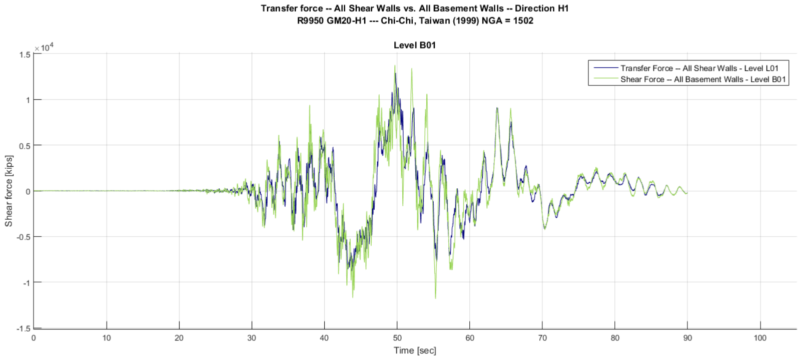

Figure 13-21: RP9950-GM20: Transfer force versus Basement wall force - Groundfloor diaphragm Direction H1

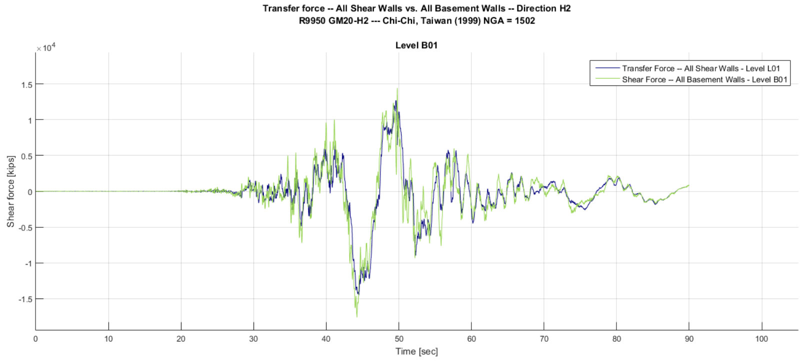

Figure 13-22: RP9950-GM20: Transfer force versus Basement wall force - Groundfloor diaphragm Direction H2

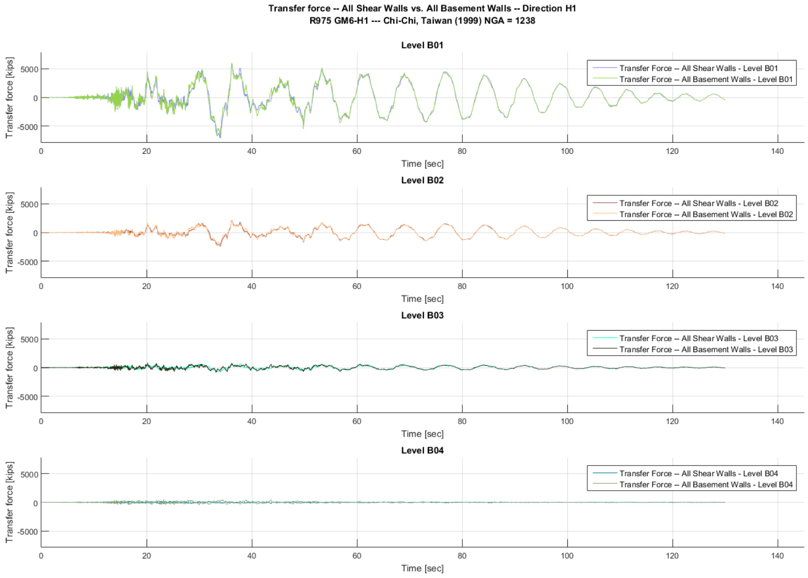

Figure 13-23: UHS-GM6: Transfer force versus Basement wall force - All basement diaphragms Direction H1

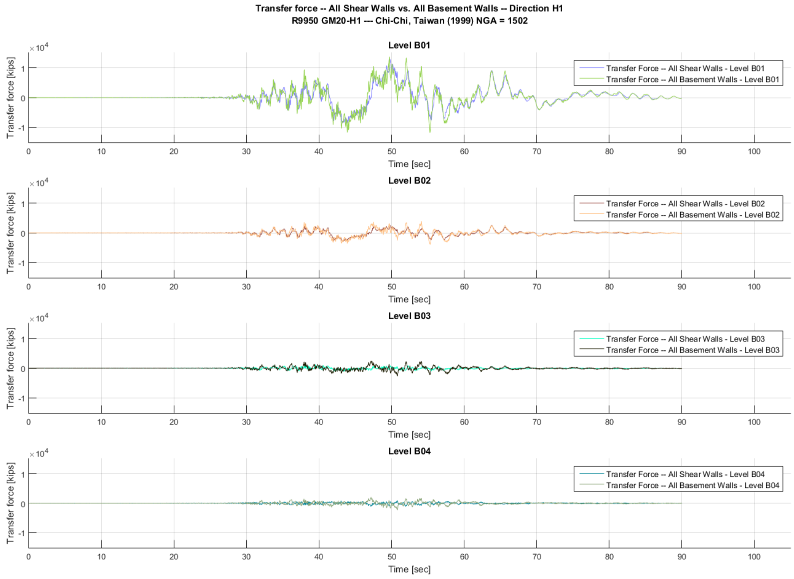

Figure 13-24: RP9950-GM20: Transfer force versus Basement wall force - All basement diaphragms Direction H1

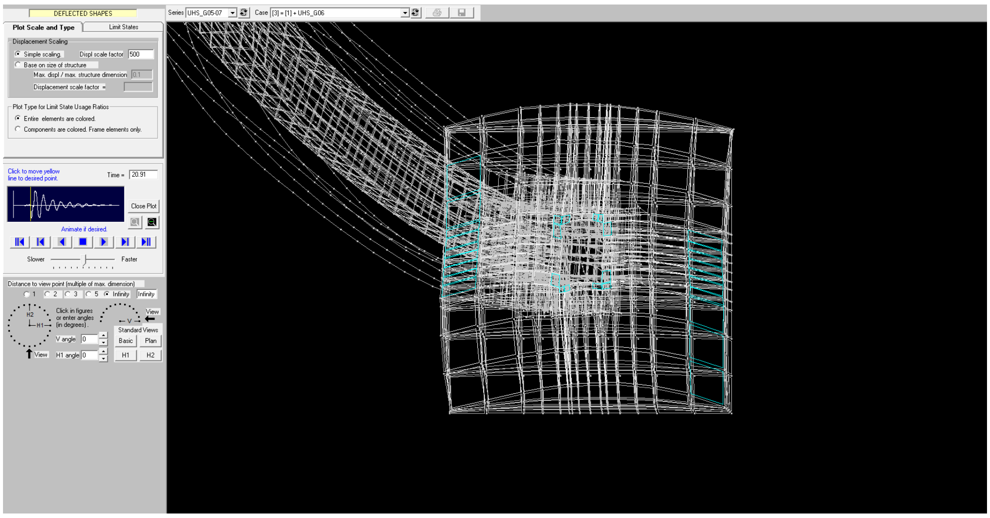
Series UHS_G05-07

Case [3] = [1] + UHS_G06

Displacement Scaling

● Simple scaling. Displ scale factor 500

○ Base on size of structure

Max. displ / max. structure dimension 0.1

Displacement scale factor =

Plot Type for Limit State Usage Ratios

● Entire elements are colored.

○ Components are colored. Frame elements only.

Click to move yellow line to desired point.

Time = 20.91

Animate if desired.

Distance to view point (multiple of max. dimension)

○ 1 ○ 2 ○ 3 ○ 5 ● Infinity Infinity

Click in figures or enter angles (in degrees).

V angle 0

H1 angle 0

Figure 13-25: UHS-GM6 - 20.9 [sec] - Deformation magnified 500x - Shear stress due to inertial force

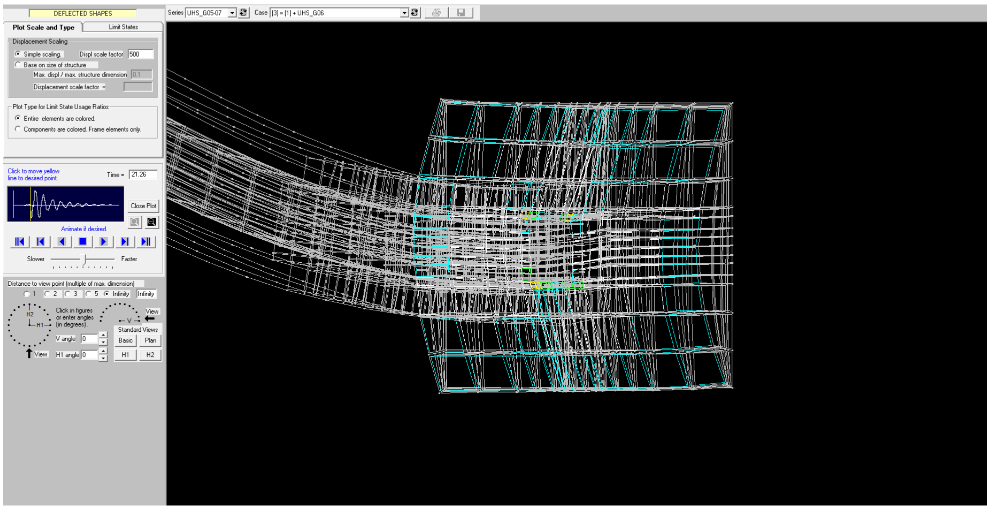

Series UHS_G05-07
Case [3] = [1] + UHS_G06
● Simple scaling. Displ scale factor 500
● Entire elements are colored.
Time = 21.26
● Infinity
V angle 0
H1 angle 0

Figure 13-26: UHS-GM6 - 21.3 [sec] - Deformation magnified 500x - Shear stress and deformation due to transfer force plus inertial force

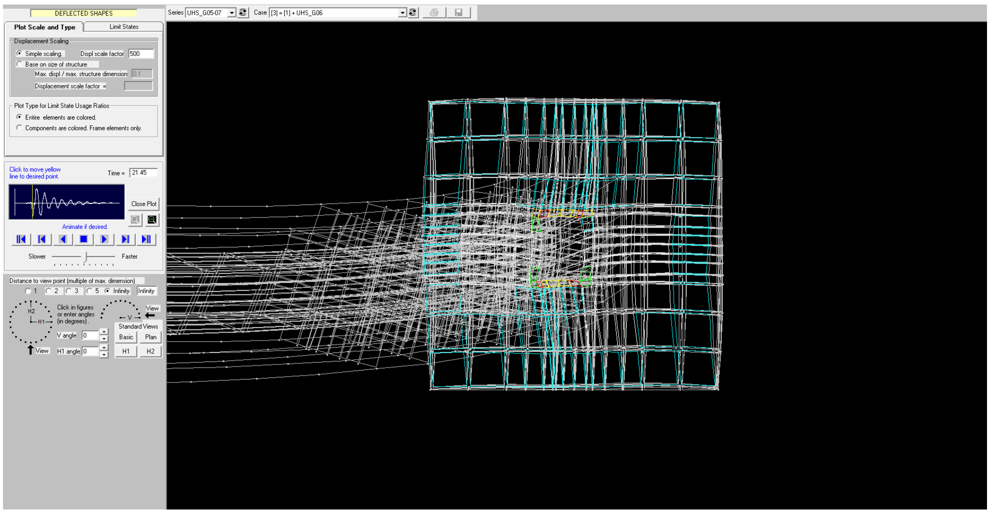

Series UHS_G05-07
Case [3] = [1] + UHS_G06
● Simple scaling. Displ scale factor 500
● Entire elements are colored.
Time = 21.45
● Infinity
V angle 0
H1 angle 0

Figure 13-27: UHS-GM6 - 21.5 [sec] - Deformation magnified 500x - Shear stress and deformation due to transfer force minus inertial force

13-5 Usage ratio plots from NLTHA

13-5-1 NLTHAs with results similar to Case 2, 3, and 4

The usage ratio plots from various ground motion records result compare well to theoretical load combinations 2, 3, and 4, as given in Figures 13-11, 13-12, and 13-13, respectively. RP9950-GM20 is an example. Six usage ratios at different time *t* are shown in Figures 13-28, 13-29, 13-30, 13-31, 13-32, and 13-33. It is noted that Perform 3D shows the maximum usage ratio up until the displayed time *t*, and not the instantaneous usage ratios. Magnified deformation plots are given in Appendix I Section I-1-1-1. Other examples of ground motions records with the principal load combination similar to cases 2, 3, and 4 are given in Appendix I Section I-1-1-2.

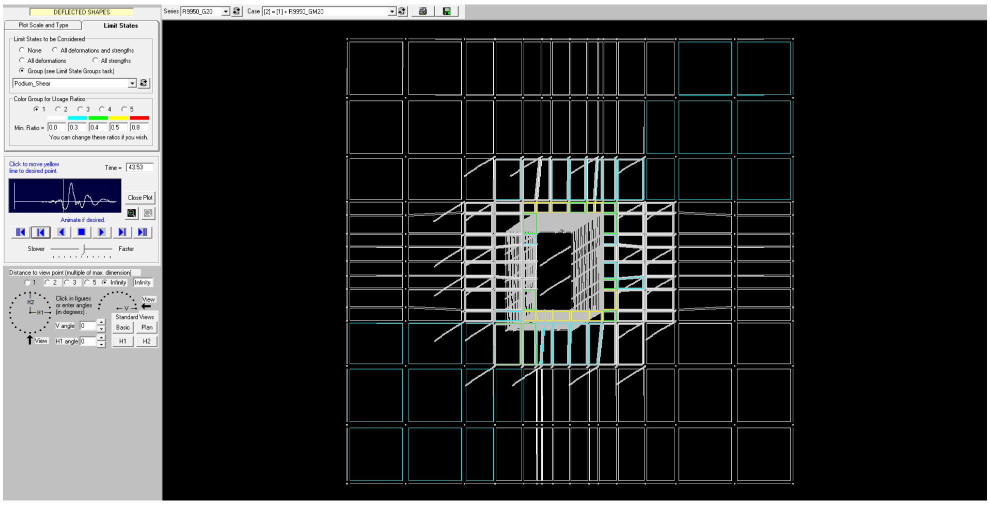

Series R9950_G20

Case [2] = [1] + R9950_GM20

● Group (see Limit State Groups task)

Podium_Shear

● 1

Min. Ratio = 0.0 | 0.3 | 0.4 | 0.5 | 0.8

Time = 43.53

● Infinity

Infinity

V angle 0

H1 angle 0

Figure 13-28: RP9950 - GM20 - 43.5 [sec] - Start of GM record

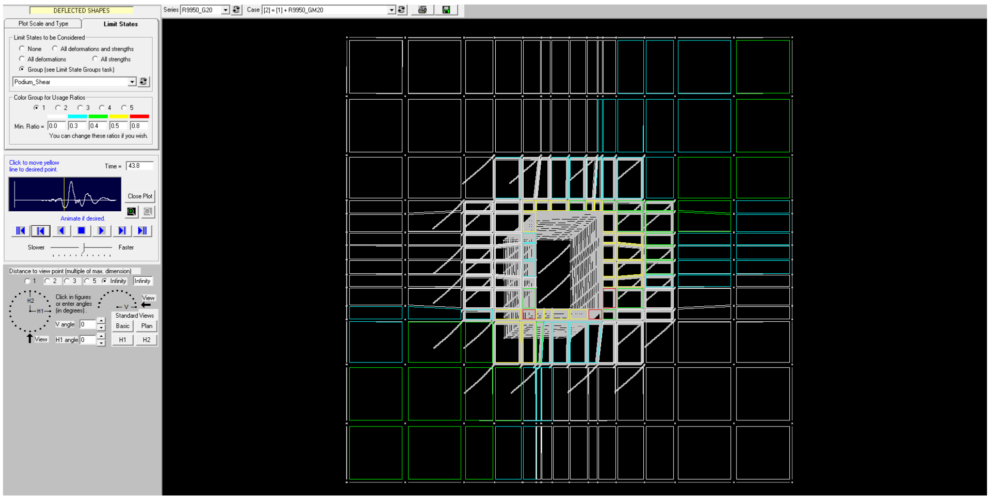

Series R9950_G20

Case [2] = [1] + R9950_GM20

Limit States to be Considered

○ None ○ All deformations and strengths

○ All deformations ○ All strengths

● Group (see Limit State Groups task)

Podium_Shear

Color Group for Usage Ratios

● 1 ○ 2 ○ 3 ○ 4 ○ 5

Min. Ratio = 0.0 | 0.3 | 0.4 | 0.5 | 0.8

You can change these ratios if you wish.

Click to move yellow line to desired point.

Time = 43.8

Distance to view point (multiple of max. dimension)

○ 1 ○ 2 ○ 3 ○ 5 ● Infinity Infinity

Click in figures or enter angles (in degrees).

V angle 0

H1 angle 0

Figure 13-29: RP9950 - GM20 - 43.8 [sec] - Case 2 (V_1 & $0.5V_2$) and Case 3 (V_1 & V_2)

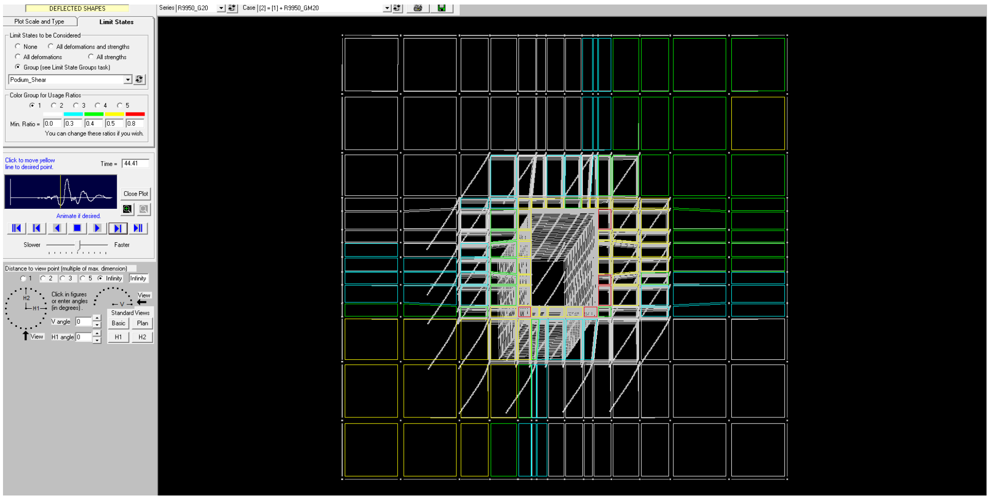

Series R9950_G20

Case [2] = [1] + R9950_GM20

Limit States to be Considered

○ None ○ All deformations and strengths

○ All deformations ○ All strengths

● Group (see Limit State Groups task)

Podium_Shear

Color Group for Usage Ratios

● 1 ○ 2 ○ 3 ○ 4 ○ 5

Min. Ratio = 0.0 | 0.3 | 0.4 | 0.5 | 0.8

You can change these ratios if you wish.

Click to move yellow line to desired point.

Time = 44.41

Distance to view point (multiple of max. dimension)

○ 1 ○ 2 ○ 3 ○ 5 ● Infinity Infinity

Click in figures or enter angles (in degrees).

V angle 0

H1 angle 0

Figure 13-30: RP9950 - GM20 - 44.4 [sec] - Case 3 (V_1 & V_2)

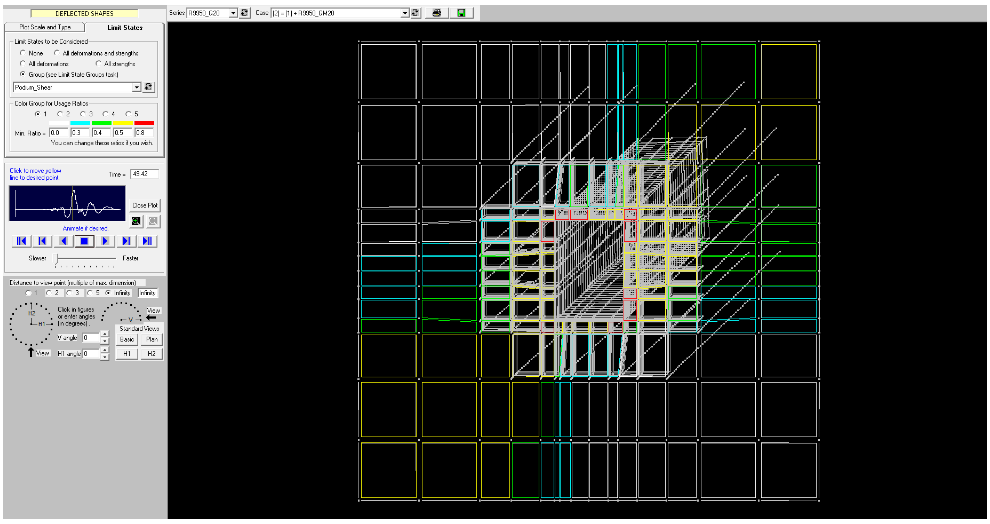

Series R9950_G20
Case [2] = [1] + R9950_GM20

Limit States to be Considered
○ None ○ All deformations and strengths
○ All deformations ○ All strengths
● Group (see Limit State Groups task)
Podium_Shear

Color Group for Usage Ratios
● 1 ○ 2 ○ 3 ○ 4 ○ 5
Min. Ratio = 0.0 0.3 0.4 0.5 0.8
You can change these ratios if you wish.

Click to move yellow line to desired point.
Time = 49.42

Distance to view point (multiple of max. dimension)
○ 1 ○ 2 ○ 3 ○ 5 ● Infinity Infinity
V angle 0
H1 angle 0

Figure 13-31: RP9950 - GM20 - 49.4 [sec] - Case 2 (V_1 & $0.5V_2$)

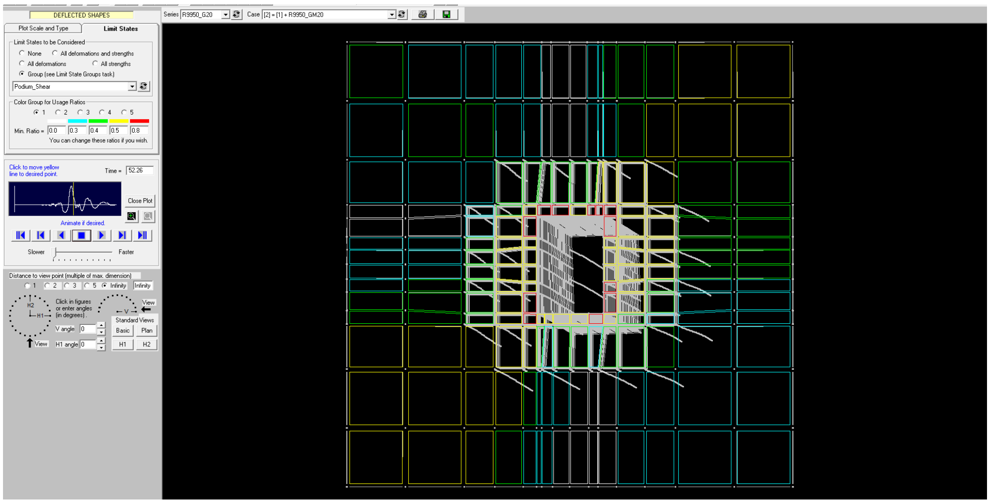

Series R9950_G20
Case [2] = [1] + R9950_GM20

Limit States to be Considered
○ None ○ All deformations and strengths
○ All deformations ○ All strengths
● Group (see Limit State Groups task)
Podium_Shear

Color Group for Usage Ratios
● 1 ○ 2 ○ 3 ○ 4 ○ 5
Min. Ratio = 0.0 0.3 0.4 0.5 0.8
You can change these ratios if you wish.

Click to move yellow line to desired point.
Time = 52.26

Distance to view point (multiple of max. dimension)
○ 1 ○ 2 ○ 3 ○ 5 ● Infinity Infinity
V angle 0
H1 angle 0

Figure 13-32: RP9950 - GM20 - 52.3 [sec] - Case 2 (V_1 & $0.5V_2$) and Case 3 (V_1 & V_2)

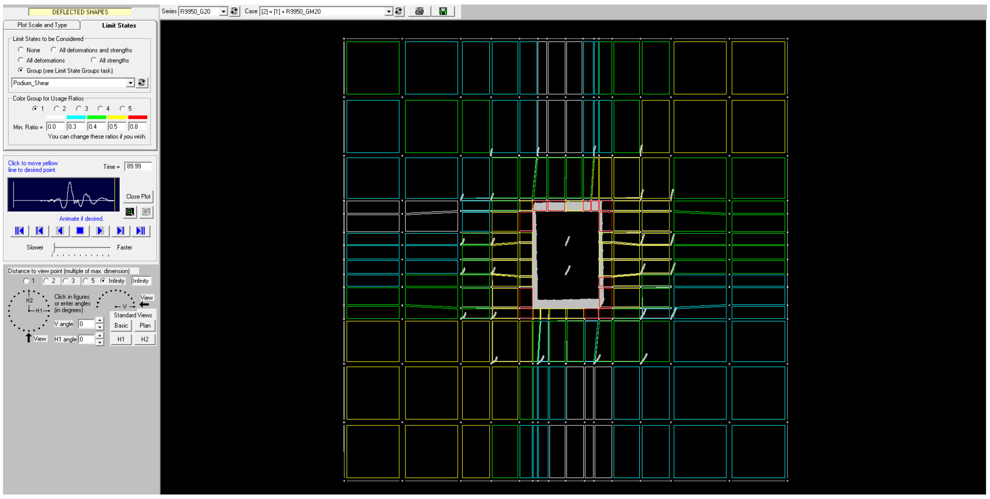

Series R9950_G20

Case [2] = [1] + R9950_GM20

Limit States to be Considered: ● Group (see Limit State Groups task)

Podium_Shear

Color Group for Usage Ratios: ● 1

Min. Ratio = 0.0 0.3 0.4 0.5 0.8

You can change these ratios if you wish.

Click to move yellow line to desired point.

Time = 89.99

Animate if desired.

Distance to view point (multiple of max. dimension): ● Infinity

Click in figures or enter angles (in degrees).

V angle 0

H1 angle 0

Figure 13-33: RP9950 - GM20 - 90.0 [sec] - End of GM record

13-5-2 NLTHAs with results similar to Case 1 and 5

Other NLTHAs result in usage ratio plots comparable to theoretical load cases 1 and 5. In these cases, there is mainly load transfer in one direction. UHS-GM6 is an example. In UHS-GM6 the main transfer force is in Direction H1. Six usage ratios at different times t are shown. The final usage ratio plot is compared to the stress distribution in Figures 13-34, 13-35, 13-36, 13-37, and 13-38.

The stress distribution in Scia shows that the shear force in the diaphragm changes sign in the middle of the slab for Case 1. This would not be expected for a concentrated shear force V. However, the change of sign of the shear force is observed because the transfer force is introduced into the diaphragm from two walls at a certain distance from each other. Where the two forces meet, the shear force changes sign and follows the shear stress distribution found for a concentrated transfer force in the diaphragm. The distance from the shear walls is dependent on the distance between the two walls. The sign change will appear further away from the shear walls as the walls ar further, which is also observed when comparing Case 1 and Case 5. The usage ratio plot shows from Perform 3D a few white elements, where the usage ratio does not exceed 0.4. The white-colored elements in the usage ratio plot from UHS-GM6 indicate that the phenomenon of sign-change of the shear force is also captured by Perform 3D.

Magnified deformation plots are given in Appendix I Section I-1-1-3. Other examples of ground motions records with the principal load combination similar to cases 1 and 5 are given in Appendix I Section I-1-1-4.

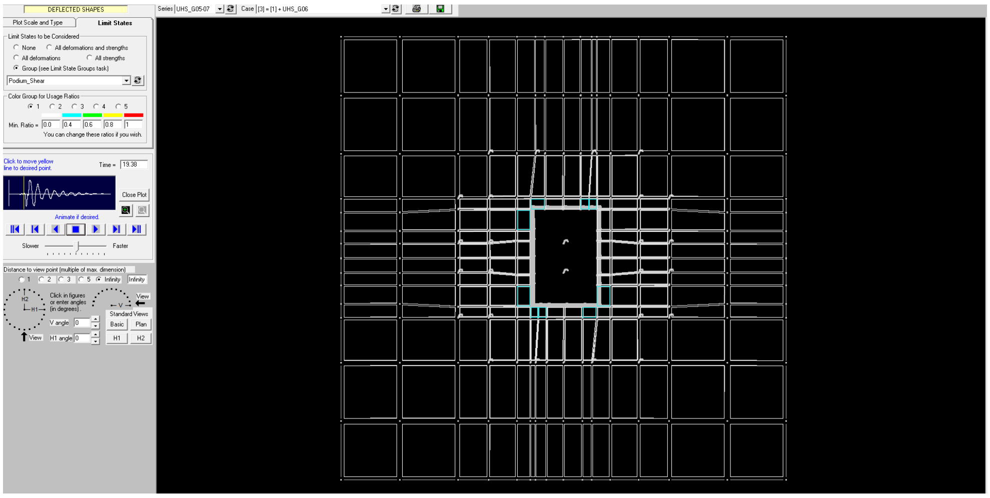

Series UHS_G05-07

Case [3] = [1] + UHS_G06

● Group (see Limit State Groups task)

Podium_Shear

● 1

Min. Ratio = 0.0 0.4 0.6 0.8 1

Time = 19.38

● Infinity Infinity

V angle 0

H1 angle 0

Figure 13-34: UHS - GM6 - 19.4 [sec] - Start of GM record

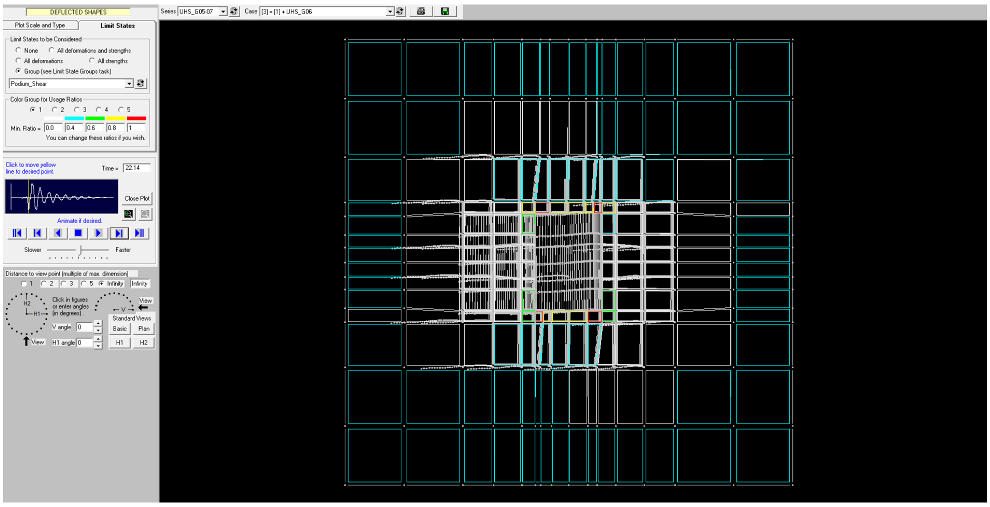

Series UHS_G05-07

Case [3] = [1] + UHS_G06

○ None ○ All deformations and strengths

○ All deformations ○ All strengths

● Group (see Limit State Groups task)

Podium_Shear

● 1 ○ 2 ○ 3 ○ 4 ○ 5

Min. Ratio = 0.0 0.4 0.6 0.8 1

Time = 22.14

○ 1 ○ 2 ○ 3 ○ 5 ● Infinity Infinity

V angle 0

H1 angle 0

Figure 13-35: UHS - GM6 - 22.1 [sec] - Case 1 (V_1 only)

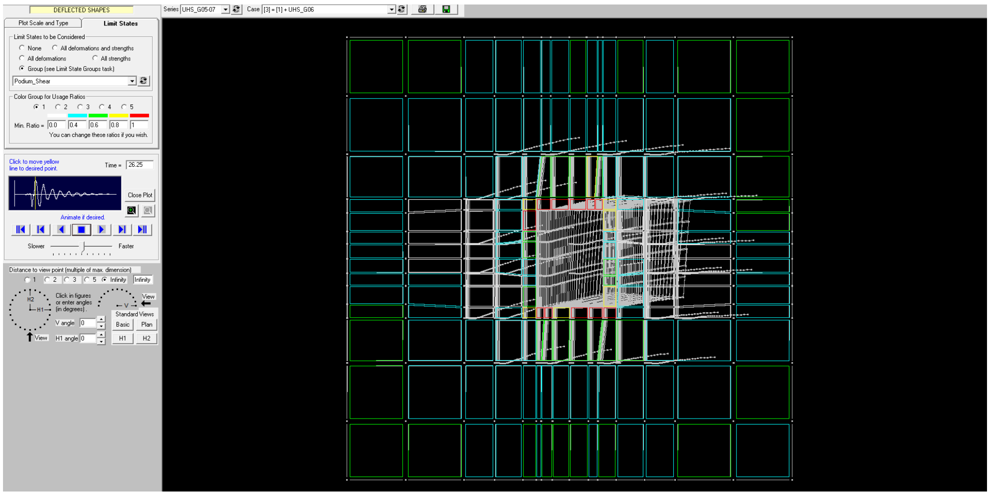

Series UHS_G05-07

Case [3] = [1] + UHS_G06

○ None ○ All deformations and strengths

○ All deformations ○ All strengths

● Group (see Limit State Groups task)

Podium_Shear

● 1 ○ 2 ○ 3 ○ 4 ○ 5

Min. Ratio = 0.0 0.4 0.6 0.8 1

Time = 26.25

○ 1 ○ 2 ○ 3 ○ 5 ● Infinity Infinity

V angle 0

H1 angle 0

Figure 13-36: UHS - GM6 - 26.3 [sec] - Case 1 (V_1 only) and Case 2 (V_1 & $0.5V_2$)

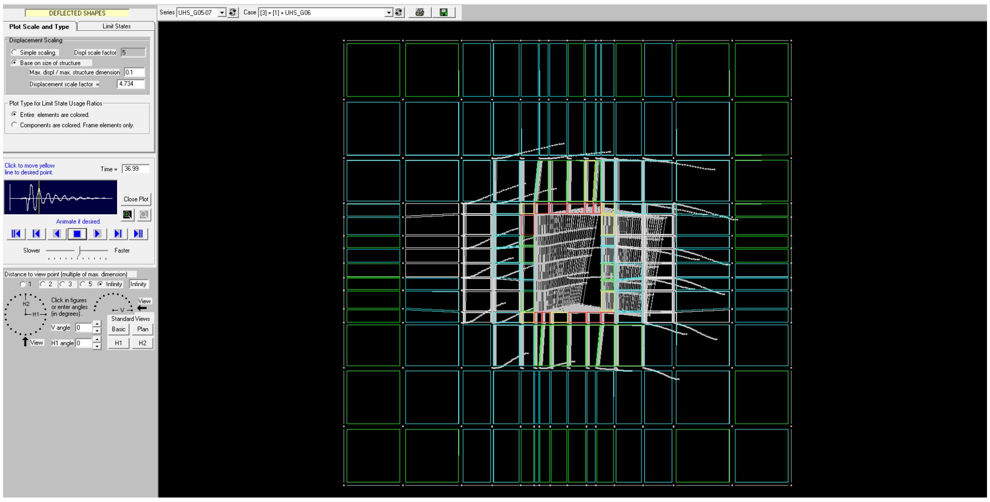

Series UHS_G05-07

Case [3] = [1] + UHS_G06

○ Simple scaling. Displ scale factor 5

● Base on size of structure

Max. displ / max. structure dimension 0.1

Displacement scale factor = 4.734

● Entire elements are colored.

○ Components are colored. Frame elements only.

Time = 36.99

○ 1 ○ 2 ○ 3 ○ 5 ● Infinity Infinity

V angle 0

H1 angle 0

Figure 13-37: UHS - GM6 - 37.0 [sec] - Case 1 (V_1 only) and Case 2 (V_1 & $0.5V_2$)

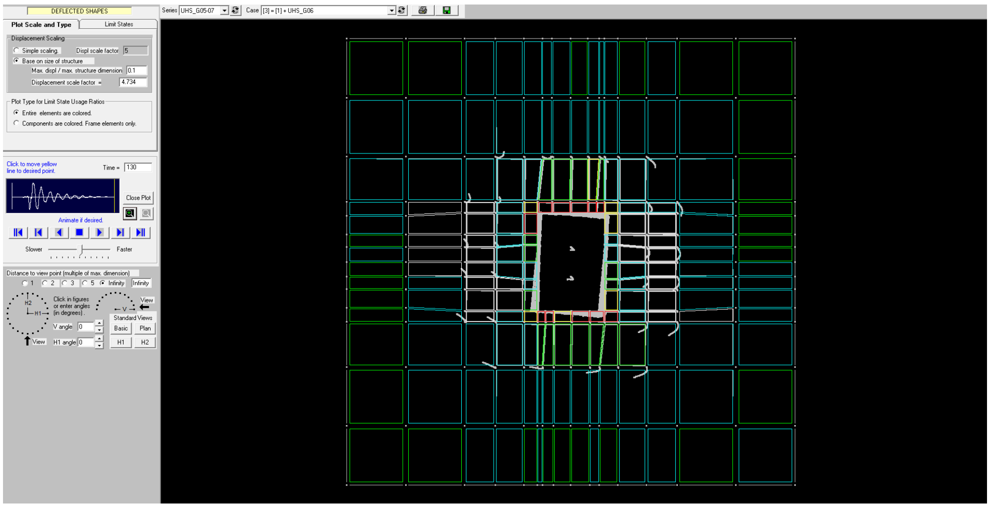

Series UHS_G05-07

Case [3] = [1] + UHS_G06

○ Simple scaling. Displ scale factor 5

● Base on size of structure

Max. displ / max. structure dimension 0.1

Displacement scale factor = 4.734

● Entire elements are colored.

○ Components are colored. Frame elements only.

Time = 130

○ 1 ○ 2 ○ 3 ○ 5 ● Infinity Infinity

V angle 0

H1 angle 0

Figure 13-38: UHS - GM6 - 130.0 [sec] - End of GM record

13-5-3 NLTHAs with results similar to combination of all load cases

Usage ratios from NLTHAs were also found to resemble a combination of all load cases, including inertial forces. Examples are shown in Figures 13-39 for UHS-GM2, 13-40 for UHS-GM5, and 13-41 for RP9950-GM9.

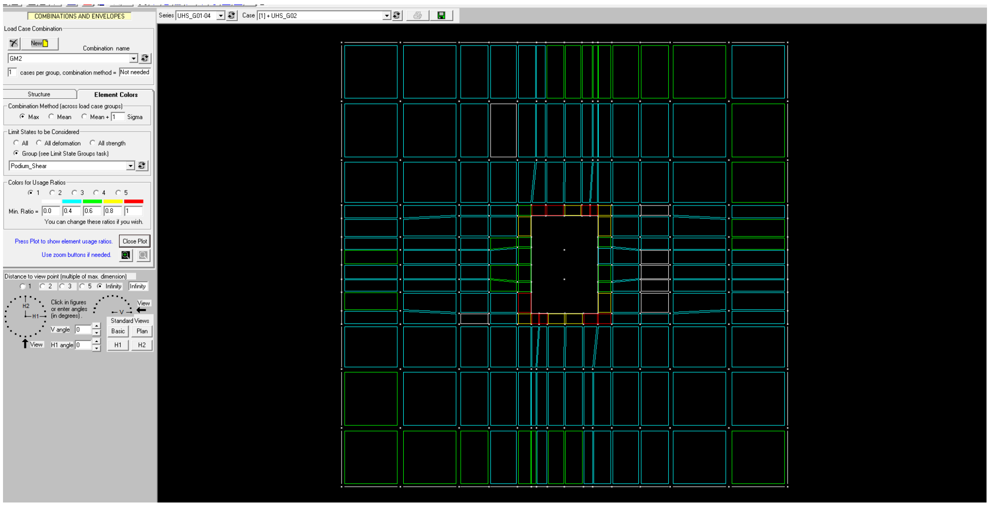

Series UHS_G01-04
Case [1] + UHS_G02
Combination name GM2
1 cases per group, combination method = Not needed
● Max
● Group (see Limit State Groups task)
Podium_Shear
● 1
Min. Ratio = 0.0 0.4 0.6 0.8 1
● Infinity Infinity
V angle 0
H1 angle 0

Figure 13-39: UHS - GM2 - Case 1 (V_1 only), Case 5 (V_2 only) and inertial force in Direction H1/H2

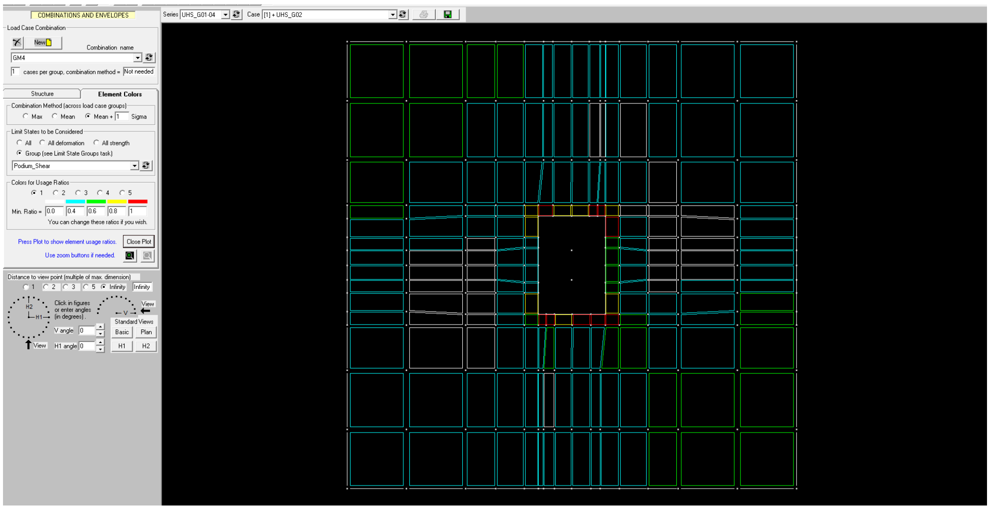

Series UHS_G01-04
Case [1] + UHS_G02
Combination name GM4
1 cases per group, combination method = Not needed
● Mean + 1 Sigma
● Group (see Limit State Groups task)
Podium_Shear
● 1
Min. Ratio = 0.0 0.4 0.6 0.8 1
● Infinity Infinity
V angle 0
H1 angle 0

Figure 13-40: UHS - GM4 - Case 1 (V_1 only) and Case 3 (V_1 & V_2)

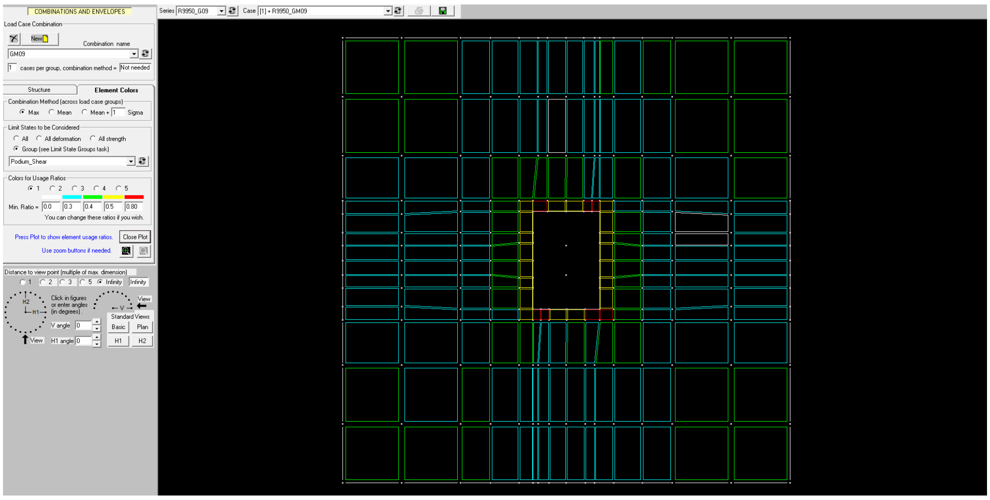

COMBINATIONS AND ENVELOPES

Series R9950_G09

Case [1] + R9950_GM09

Load Case Combination

Combination name GM09

1 cases per group, combination method = Not needed

Combination Method (across load case groups)

● Max ○ Mean ○ Mean + 1 Sigma

Limit States to be Considered

○ All ○ All deformation ○ All strength

● Group (see Limit State Groups task)

Podium_Shear

Colors for Usage Ratios

● 1 ○ 2 ○ 3 ○ 4 ○ 5

Min. Ratio = 0.0 0.3 0.4 0.5 0.80

You can change these ratios if you wish.

Press Plot to show element usage ratios.

Use zoom buttons if needed.

Distance to view point (multiple of max. dimension)

○ 1 ○ 2 ○ 3 ○ 5 ● Infinity Infinity

Click in figures or enter angles (in degrees).

V angle 0

H1 angle 0

Figure 13-41: RP9950 - GM9 - Case 1 (V_1 only), Case 3 (V_1 & V_2), and Case 5 (V_2 only)

13-6 Conclusion

It is concluded that the force transfer is accurately captured by Perform 3D. Comparison of theoretical static load cases with results from NLTHAs showed that the results from the NLTHAs can be derived from the theoretical static load cases. Furthermore, it was shown that the effect of inertial forces is relatively small compared to the transfer forces in the podium and basement diaphragms, but can not be neglected.

Usage ratio plots provide fairly accurate force distributions in the diaphragm. More accurate results could be obtained for a finer mesh size. However, earlier research has shown that refining the mesh significantly increases the analysis time. Comparison between the forces in the basement wall and transfer force has shown that the force is transferred correctly for the chosen mesh size and that the results are therefore reliable.

Part IV

Design

Chapter 14

Diaphragm design

14-1 Introduction

Transfer diaphragms can be designed according to the Code seismic design procedure specified in ASCE 7-10 or according to alternative guidelines such as PEER/TBI. ASCE 7-10 employs linear elastic modal response spectrum analysis to calculate the force demand and required capacity. The PEER/TBI seismic design procedure calculates the force demand and required capacity through nonlinear time history analysis.

The diaphragms and collectors are force-controlled and modelled using elastic elements. Therefore, it is assumed that the response is independent of the design methodology. One set of calculations was done for the structural reliability analysis to evaluate the reliability of the distributors and diaphragms designed according to the different design methodologies.

This chapter describes the design of diaphragms and distributors according to the ASCE 7-10 and PEER/TBI. First, the diaphragm force demand is calculated. Subsequently, the capacity of distributors and the diaphragm is determined per ACI 318-11. Finally, the diaphragms and distributors are designed as required per ASCE 7-10 and PEER/TBI and the design from the two design methodologies are compared.

14-2 Diaphragm force demand

14-2-1 Building Code demand

Building Code provisions prescribe that the design of diaphragms must consider inertial seismic forces F_x, diaphragm design forces F_{px}, and transfer forces. The forces were calculated by a Modal Response Spectrum Analysis (MRSA). The Building Code requires the diaphragm design forces to be larger than the required strength calculated by MRSA.

The inertial lateral seismic forces F_x are calculated by the floor accelerations times tributary mass. The inertial seismic forces F_x are applied to the design of the vertical elements of the seismic-force-resisting system. The diaphragm design forces F_{px} are applied to the design of diaphragms and correspond to the peak responses for that floor. It would be overly conservative to design the vertical elements for the sum of the individual peaks in each diaphragms, as these forces will occur at different times during the dynamic response. The individual diaphragms, however, must be designed for these peak responses. Transfer forces occur due to changes in relative stiffness above and below the podium diaphragm. The transfer force is calculated by the difference between the shear force in the shear wall above and below the podium diaphragm. Where transfer forces occur, these transfer forces must be added to the diaphragm design forces F_{px} for diaphragm design.

14-2-1-1 Diaphragm demand

The diaphragm forces were calculated for each vibration mode and then combined using the SRSS method, given in Appendix E-4-3 Equation E-32. The cumulative diaphragm design forces and transfer forces for the main contributing modes in Direction H1 and H2, as measured at the top of the basement wall, are given in Table 14-1 and 14-2, respectively. The calculation of inertial seismic force, diaphragm design force, and transfer force is further described in Appendices E-4-2, E-4-2-1, and E-4-3.

14-2-1-2 Collector demand

Collector elements are designed to resist the seismic forces amplified by an overstrength factor Ω_o. The overstrength factor $\Omega_o = 2.5 - 3.0$ for most common systems. The rationale for applying an overstrength factor is that the seismic forces in the building are estimated to be approximately Ω_o times the code design forces when walls or frames of a building respond inelastically. Failure of some connections between diaphragms and walls in the 1994 Northridge earthquake induced the introduction of the overstrength factor. The overstrength requirement is applied to collector elements, splices, and connections to vertical elements of the seismic-force-resisting system, but not to the diaphragm as a whole.

The forces in the diaphragm, given in Tables 14-1 and 14-2, result from the combined effect of transfer force from the shear walls to the basement walls through the diaphragm and the inertial force from the podium diaphragms. It is noted that the transfer force has a large contribution to the total basement wall force for lower modes of vibration, and that the inertial force from the diaphragm has a larger contribution for higher modes. The transfer force is introduced into the diaphragm through concentrated collectors and transverse reinforcement, whereas the inertial force is activated by the distributed mass of the diaphragm.

One design approach is to calculate the transfer force from the difference in shear in the shear wall above and below the diaphragm for each mode. The inertial force is then calculated from the difference between the shear force in the basement walls and the transfer force. The transfer force was calculated up to mode 12, where almost full shear force in the wall was reached (20306 of 21239 [kips] for 50 modes in H1-direction, 20622 of 21290 [kips] in H2-direction). For the first approach, collectors and transverse reinforcement are designed to resist the transfer force only. The cumulative transfer forces in two directions are given in Tables 14-1 and 14-2.

The second approach assumed zero inertial force in the diaphragm. The shear force in the basement walls is therefore equal to the transfer force. Hence, this approach is an upper-bound estimate. The upper-bound estimate is given in Table E-15.

	Total force	Cumulative diaphragm design force (SRSS)	Cumulative transfer force (SRSS)	Contribution combination component (SRSS)
Mode 1-3	5843	69	5774	894
Mode 1-6	7179	468	6862	2058
Mode 1-9	7792	1255	7111	2929
Mode 1-12	8200	2475	7123	3220

Table 14-1: Total diaphragm design force and transfer force component - Direction H1

	Total force	Cumulative diaphragm design force (SRSS)	Cumulative transfer force (SRSS)	Contribution combination component (SRSS)
Mode 1-3	6837	10	6828	362
Mode 1-6	8232	384	8017	1831
Mode 1-9	8964	1451	8300	3061
Mode 1-12	9580	3598	8300	3153

Table 14-2: Total diaphragm design force and transfer force component - Direction H2

14-2-2 PEER/TBI demand

PEER/TBI design provisions employ nonlinear time history analysis to determine forces in diaphragms, collectors and their connections, as an alternative to Code provisions using

Ω_o-amplified forces F_x and F_{px}. A suite of seven representative ground motions is input for the analysis, as described in Chapter 10. The diaphragm is designed to resist axial forces in X and Y direction and shear XY, as shown in Figure 14-1. The core walls, basement walls, and diaphragms are modelled explicitly and the force demands in the diaphragms and collectors are extracted directly from the analysis program Perform 3D. Unreduced forces from the nonlinear time history analysis can be used in lieu of the application of overstrength factor Ω_o.

It is noted that the distribution of forces is sensitive to the stiffness assumptions of the diaphragm and collectors. Therefore, the alternative PEER/TBI design requires a realistic stiffness representation. Exact stiffness predictions are difficult due to stiffness reductions in concrete associated with diaphragm cracking. Analysis with upper and lower bound stiffnesses can therefore be useful to determine the sensitivity of the behaviour to variability in diaphragm stiffness.

14-2-2-1 Diaphragm demand

The diaphragm demands were determined through nonlinear time history analysis. The axial forces in X and Y direction and shear XY were evaluated. The peak demands in the elastic diaphragm elements are expressed in usage ratios. The usage ratios are allowed to be averaged over seven ground motions [FEMA 356, 2000]. There are several combination options to analyse the results from the suite of seven ground motions, summarized in Table 14-3. The Max-Max method is most conservative and the Max-Mean method is least conservative. The Max-(Mean+N sigma) method is recommended for strength-based limit states when capacity design is used [Perform 3D User Guide, 2006]. In this case, diaphragm strength based on the Max-Mean method may not be sufficiently large to ensure essentially elastic behaviour. The recommended Max-(Mean+N sigma) method with N=1 was therefore used to calculate the diaphragm demands.

Method	*Description*
Max-Max	Maximum over all load cases and the maximum over all elements
Mean-Max	Maximum over all load cases and the mean over all elements
Max-Mean	Mean over all load cases and the maximum over all elements
Max-(Mean+N sigma)	Mean + N times the standard deviation over all load cases, the maximum over all elements

Table 14-3: Combination options for calculation of diaphragm demand

14-2-2-2 Collector demand

Collector demands were also determined through nonlinear time history analysis. The transfer force was calculated as the difference between the shear force in the shear wall just above and below the considered diaphragm. In compliance with PEER/TBI, the design force demands are equal to 1.5 times the arithmetic mean value of seven responses. The required collector reinforcement and transverse shear reinforcement are required to be equal or larger than the transfer design force demands.

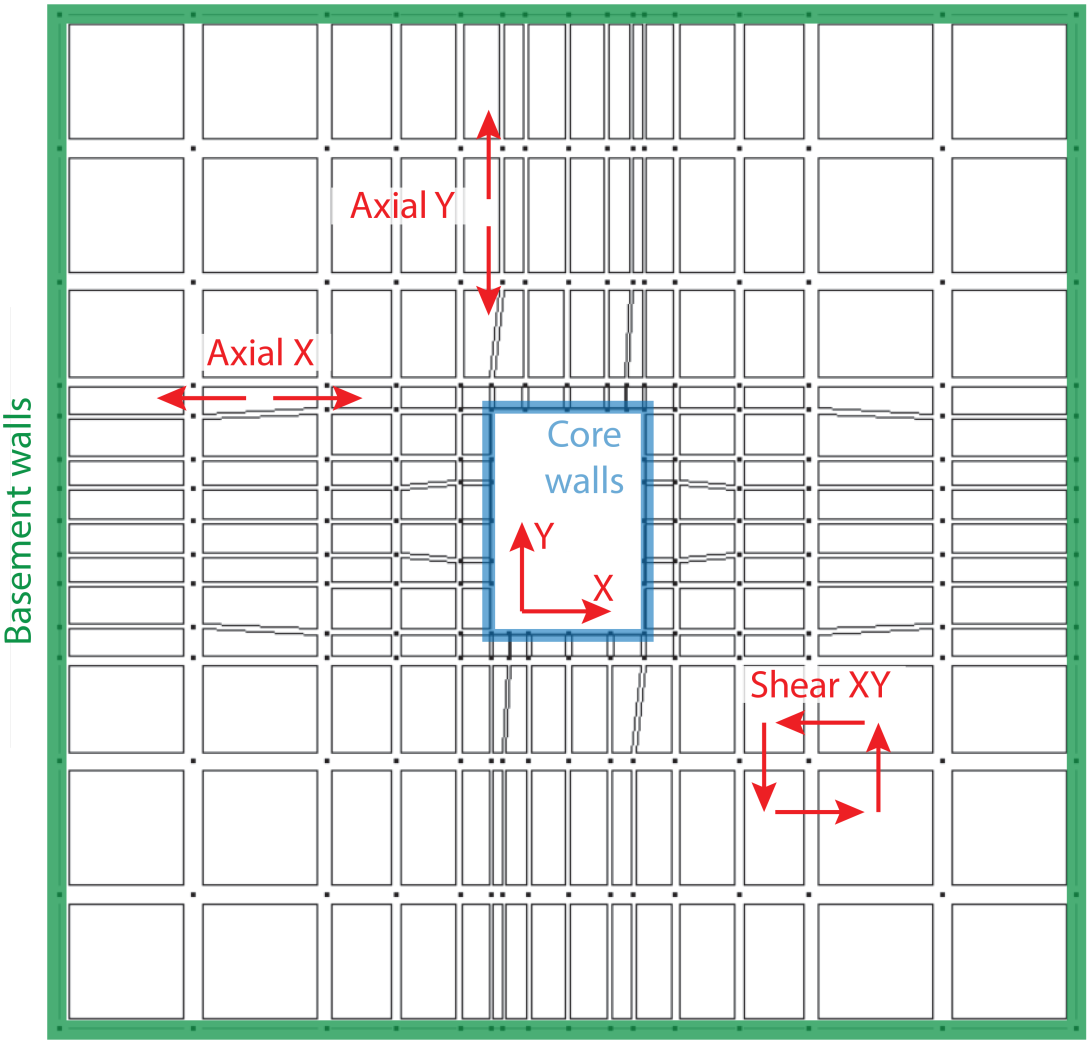

Figure 14-1: Diaphragm forces from Perform 3D

14-3 Diaphragm capacity

The calculation procedure for shear capacity of the diaphragm and transfer capacity of the distributors is described in the following sections. The diaphragm thicknesses are given in Table 14-4.

	Thickness
Podium diaphragm thickness	12 [in]
Basement diaphragm thickness	10 [in]

Table 14-4: Basic diaphragm dimensions

14-3-1 Shear capacity

The nominal and nominal expected in-plane shear capacity of reinforced concrete diaphragms were calculated according to ACI 318-11. The in-plane shear capacity V is calculated as the sum of the concrete shear capacity V_c and shear reinforcement capacity V_s. The shear strength provided by concrete for nonprestressed members is calculated in Appendix K-3-1. The shear strength provided by the shear reinforcement and the design requirements for shear reinforcement are described in Appendix K-3-2.

14-3-1-1 Nominal shear capacity

The nominal shear strength is calculated by Equation 14-1.

$$V_n = A_{cv}(2\sqrt{f'_c} + \rho_n f_y) \leq 8\sqrt{f'_c}A_{cv} \tag{14-1}$$

The net area of the concrete section A_{cv} is bounded by the slab thickness and length in the direction of the shear force considered. The nominal shear strength of the concrete section is represented by $2\sqrt{f'_c}$, the reinforcement ratio ρ_n accounts for reinforcing steel parallel to the direction of the shear force considered. The nominal shear capacity is used for the diaphragm design according to the Building Code. The maximum value of shear V_n may not exceed $8\sqrt{f'_c}A_{cv}$ [ACI 318-11, 2011].

14-3-1-2 Nominal expected shear capacity

The nominal expected shear capacity for the alternative PEER/TBI design is calculated by Equation 14-2. The nominal expected shear capacity is calculated using expected material properties.

$$V_{n,exp} = A_{cv}(2\sqrt{f'_{c,exp}} + \rho_n f_{y,exp}) \leq 8\sqrt{f'_{c,exp}}A_{cv} \tag{14-2}$$

No further test data was available for shear capacity of diaphragms, it was assumed that the expected capacity V_e is equal to the nominal expected capacity calculated with Equation 14-2.

14-3-2 Transfer force capacity

14-3-2-1 Introduction

Transfer force capacity is provided by a combination of shear friction action and distributor action. The recommended design approach is to choose a reasonable distribution of forces that satisfies equilibrium and does not exceed the capacities of the collector elements and shear transfer mechanism provided [Moehle et al., 2010]. The recommended design approach is adopted in this study.

The expected transfer force capacity was assumed equal to the nominal expected capacity using expected material properties as no further information on the transfer force capacity from test data was available.

14-3-2-2 Shear-friction capacity

Virtually all shear provisions are intended to prevent diagonal tension failures rather than direct shear transfer failures [ACI 318-11, 2011]. However, direct shear transfer is to be considered for an interface between two dissimilar elements, such as the interface between a structural wall and diaphragm.

Although uncracked concrete is relatively strong in direct shear, a crack can always occur. The shear-friction capacity is calculated based on this principle. Once a crack occurs, the shear-friction resistance is provided by dowel action of the shear-friction reinforcement crossing the crack, friction between the crack faces, and by resistance to shearing off of concrete protrusions. The shear-friction capacity is calculated in accordance with ACI 318-11 Section 11.6. Both a conservative relationship between shear-transfer capacity and reinforcement crossing the shear plane and a closer estimate of shear-transfer capacity are provided by ACI 318-11. Furthermore, ACI 318-11 provides upper limits on the shear-friction capacity.

The conservative prediction of the shear-friction capacity is given in Equation 14-3. Equation 14-3 assumes that the full shear-friction capacity is provided by shear reinforcement and neglects the resistance provided by friction between crack faces and shearing off of protrusions. The shear resistance is calculated as a function of the area of shear reinforcement A_{vf}, tensile strength f_y and coefficient of friction μ. The coefficient of friction for concrete placed against hardened concrete with surface intentionally roughened $\mu = 1.0\lambda$, and $\lambda = 1.0$ for normalweight concrete.

$$V_n = A_{vf} f_y \mu \tag{14-3}$$

Equation 14-4 gives a closer estimate of shear-transfer capacity for shear reinforcement perpendicular to the shear plane. The first term in Equation 14-4 represents the contribution of friction to shear-friction resistance, where 0.8 represents the coefficient of friction. The second term accounts for the combined resistance provided by shearing off of protrusions and dowel action of the reinforcement, as a function of area of concrete section resisting shear A_c and $K_1 = 400$ [psi] for normalweight concrete.

$$V_n = 0.8 A_{vf} f_y + A_c K_1 \tag{14-4}$$

Upper limits on the shear-friction strength V_n are given in Equation 14-5. The upper limits are necessary as Equations 14-3 and 14-4 may become unconservative in some cases.

$$\begin{aligned} V_n &\leq 0.2 f'_c A_c \\ &\leq (480 + 0.08 f'_c) A_c \\ &\leq 1600 A_c \end{aligned} \tag{14-5}$$

The calculation of the shear-friction capacity can be found in Appendix K-3-3. Nominal material values were used to calculate the nominal shear-friction capacity used in Code design. Expected material values were used to calculate expected shear-friction capacity for the alternative PEER/TBI design.

14-3-2-3 Collector/distributor capacity

Collector/distributor capacity must be sufficient to transfer forces originating in other portions of the structure to the element providing the resistance to those forces. Collectors are designed for tension and compression. Therefore, force transfer occurs in the collectors at both wall ends.

Collector reinforcement provides compressive force transfer capacity, which is limited by the maximum compressive stress in the concrete section. The concrete section A_c is taken equal to the width of the wall multiplied by the depth of the diaphragm. Collector elements with compressive stresses exceeding $0.2 f'_c$ at any section shall have transverse reinforcement over the length of the element. The collector compressive capacity is calculated by Equation 14-6.

$$C_u = f_{y,exp} \cdot A_s \leq f'_{c,exp} \cdot A_c \tag{14-6}$$

Upon load reversal, the tensile capacity is provided by the same reinforcement as the compressive capacity. The tensile capacity of the collector is therefore equal to the compressive capacity and calculated by Equation 14-7.

$$T_u = C_u = f_{y,exp} \cdot A_s \tag{14-7}$$

The calculation of the collector/distributor is given in Appendix K-6. The Code design employs nominal material parameters to calculate the collector/distributor capacity, whereas the alternative PEER/TBI design employs expected material properties.

14-4 Diaphragm design

The structural designer can choose the optimal distribution between the force transferred through shear friction and force transferred through the collectors. One boundary solution is to maximize the shear friction capacity and to transfer the remaining force through the collectors. The shear friction strength is limited by the maximum shear force in the diaphragm and the maximum shear friction force in the connection between the shear wall and diaphragm. The other boundary solution is to use the full collector force capacity and transfer the remaining force through shear friction. The collector capacity is limited by the maximum compressive force in the diaphragm. Both boundary solutions were calculated in Appendix K-6 for the Building Code and PEER/TBI design.

14-4-1 Building Code design

The transfer forces were determined through MRSA. The design transfer forces were found through multiplication by seismic performance factors I_e and Ω_o and division by response modification factor R. The total strength is the sum of the shear friction strength and the collector strength. The design strength was determined using the nominal material strengths. The total transfer strength multiplied by the strength reduction factor ϕ must be larger than the design transfer force, as given in Equation 14-8.

$$\begin{aligned} \text{Design transfer force} &\leq \text{Design transfer strength} \\ V_{transfer} \cdot \left(\frac{\Omega_o I_e}{R}\right) &\leq \phi \cdot (\text{Collector strength} + \text{Shear friction strength}) \end{aligned} \tag{14-8}$$

Where,

$$\phi = 0.60 \quad [\text{-}] \tag{14-9}$$

Wall, Direction	Required strength		Required strength (upper-bound)	
N-S wall, H1	2718	[kips]	6445	[kips]
E-W wall, H2	3255	[kips]	5763	[kips]

Table 14-5: Code design - required transfer capacity of distributors per wall

Wall, Direction	Shear friction reinforcement	Collector reinforcement
N-S wall, H1	#7 - 12	Not required
E-W wall, H2	#6 - 12	Not required

Table 14-6: Code design - Boundary solution 1 - maximum shear friction strength

Wall, Direction	Shear friction reinforcement	Collector reinforcement
N-S wall, H1	Not required	14 #11
E-W wall, H2	Not required	16 #11

Table 14-7: Code design - Boundary solution 2 - maximum collector strength

Wall, Direction	Shear friction reinforcement	Collector reinforcement
N-S wall, H1	#10 - 12	13 #12
E-W wall, H2	#10 - 12	6 #12

Table 14-8: Upper-bound Code design

14-4-2 PEER/TBI design

Transfer forces were determined through NLTHA for the suite of seven ground motions scaled to the UHS. The design transfer force is the mean of the maximum transfer forces from each ground motion multiplied by the dispersion factor β_u. The design transfer strength is equal to the sum of the shear friction strength and the collector strength. The design strength was determined using expected material strengths. The design transfer strength must be larger than the design transfer force, as given in Equation 14-10.

$$\begin{aligned} \text{Design transfer force} &\leq \text{Design transfer strength} \\ \bar{V}_{transfer} \cdot \beta_u &\leq \text{Collector strength} + \text{Shear friction strength} \end{aligned} \tag{14-10}$$

Where,

$$\beta_u = 1.50 \quad [\text{-}] \tag{14-11}$$

Wall, Direction	Required strength
N-S wall, H1	13475 [kips]
E-W wall, H2	11295 [kips]

Table 14-9: PEER/TBI design - required strength per wall

The required strength is larger than the sum of the maximum shear friction and maximum collector strength. Therefore, additional measures need to be taken to resist the transfer force. The total thickness of the diaphragm can be increased or additional beams can be provided to accommodate the collector reinforcement [Moehle et al., 2010]. It was chosen to provide additional beams, as this solution affects the properties of the diaphragm only locally. The overall self-weight and stiffness of the diaphragm remain unchanged and the used analysis model is still valid.

Furthermore, it is noted that the total mean transfer force in Direction H1 is larger than the transfer force in the individual N-S walls, due to the out-of-plane shear stiffness in the E-W walls. For design, it was assumed that the total force is transferred trough shear friction and collector action. Therefore, the total mean transfer force was governing for transfer capacity design in Direction H1. The transfer force in the individual walls was governing for transfer capacity design in Direction H2.

Wall, Direction	Shear friction reinforcement	Collector reinforcement	Collector beam depth (including diaphragm depth)
N-S wall, H1	#10 - 12	42 #12	18 [in]
E-W wall, H2	#10 - 12	29 #12	18 [in]

Table 14-10: PEER/TBI design - reinforcement

14-4-3 Comparison Code and PEER/TBI design

The required strength for the Code design-transfer force is approximately 25% of the required strength for the PEER/TBI design. If the upper bound is taken, for which it is assumed that the transfer force accounts for the total shear force in the basement walls, the required strength is approximately 55% of the required PEER/TBI transfer capacity. An overview is given in Table 14-11.

The design methodologies are schematized in Figure 14-2. It is noted that the unreduced upper-bound force demand from MRSA is close to the mean demand from NLTHA. However, the combination seismic performance factors and strength reduction factor reduces the required capacity per ASCE 7-10 design procedure, whereas the PEER/TBI procedure requires the capacity to be β_u times the mean demand.

	Expected capacity $V_{e,transfer}$		
Wall, Direction	Code design - transfer force	Code design - upper bound	PEER/TBI design
N-S wall, H1	2718 [kips]	6445 [kips]	13640 [kips]
E-W wall, H2	3255 [kips]	5763 [kips]	11470 [kips]

Table 14-11: Comparison Code and PEER/TBI design - expected capacity

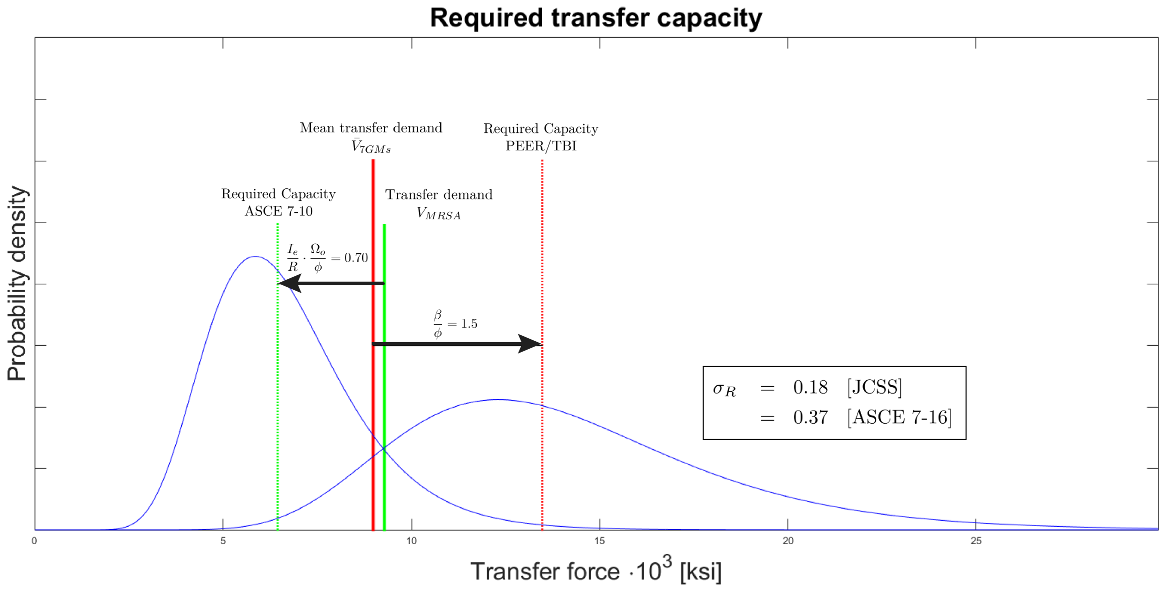

Figure 14-2: Diaphragm design procedure

Chapter 15

Shear wall design

15-1 Introduction

Shear walls can be designed according to Code seismic design procedure specified in ASCE 7-10 or according to alternative guidelines such as PEER/TBI and LATBSDC. As discussed in Section 1-2-1, shear walls designed according to PEER/TBI are required to have 33% more shear capacity than structures designed according to LATBSDC. This study evaluates the alternative seismic design procedures and the Code seismic design procedure for shear walls is not taken into consideration.

The shear behaviour of shear walls is force-controlled. Therefore, the shear response in the shear walls is assumed to be independent of the design methodology. Hence, the shear demand found for different intensity levels in the structural reliability analysis for the archetype structure can be used to evaluate the reliability of shear walls designed according to the different alternative design methodologies.

This chapter describes the shear capacity design of shear walls according to PEER/TBI and LATBSDC. First, the diaphragm force demand is calculated, which is assumed to be equal for both design methodologies. Subsequently, the capacity is calculated per ACI 318-11. Finally, the required shear capacity of the shear walls per PEER/TBI and LATBSDC is calculated and compared to the shear capacity of the archetype structure.

15-2 Shear wall shear demand

The alternative seismic design procedure employ nonlinear time history analysis to determine the shear wall shear demand. The demand is calculated for seven ground motion pairs selected and scaled to match the Uniform Hazard Spectrum, as described in Section 10. The resulting peak shear demands are given in Table L-1 and L-2. The mean shear force demands in the shear walls are given in Table 15-1.

Wall, Direction	$\bar{V}_{7GMs}$	
N-S wall, H1	11901	[kips]
E-W wall, H2	8618	[kips]

Table 15-1: Mean shear force demand from 7 NLTHAs

15-3 Shear wall shear capacity

The nominal expected shear capacity of the shear wall for PEER/TBI and LATBSDC design is calculated by Equation 15-1. The nominal expected shear capacity is calculated using expected material properties. The parameters to determine the nominal expected shear strength are further described in Appendix L-2-1.

$$V_{n,e} = A_{cv}\left(\alpha_c\lambda\sqrt{f'_{c,exp}} + \rho_t f_{y,exp}\right) \leq 8\cdot A_{cv}\sqrt{f'_{c,exp}} \tag{15-1}$$

Wallace, Hamburger et al. [Wallace et al., 2013] tested 37 walls to verify the ratio of expected shear capacity to nominal expected shear capacity $V_e/V_{n,e}$. Ratio $V_e/V_{n,e} = 1.35$ is recommended for expected material strengths $f'_{c,exp} = 1.3f'_c$ and $f_{y,exp} = 1.17f_y$, as given in Equation 15-2.

$$V_e = 1.35V_{n,e} = 1.35\cdot A_{cv}\left(\alpha_c\lambda\sqrt{f'_{c,exp}} + \rho_t f_{y,exp}\right) \tag{15-2}$$

The nominal expected shear capacity and expected shear capacity of the archetype structure at the base, calculated according to Equations 15-1 and 15-2, are given in Table 15-2.

Wall, Direction	$V_{n,e}$		V_e	
N-S wall, H1	12637	[kips]	17060	[kips]
E-W wall, H2	12381	[kips]	16715	[kips]

Table 15-2: Nominal expected and expected shear capacity of the archetype structure

15-4 Shear wall shear design

The shear capacity of the shear wall must be larger than the design shear force demand. The mean shear force demand was calculated through NLTHA of 7 ground motions selected and scaled to match the UHS, given in Table 15-1. The mean shear force demand $\bar{V}_{7GMs}$ was multiplied by dispersion factor β_u and divided by strength reduction factor ϕ to find the design shear force demand, as given in Equation 15-3.

$$\begin{aligned} \text{Design shear force} &\leq \text{Design shear strength} \\ \bar{V}_{7GMs} \cdot \beta_u &\leq \phi \cdot \text{Expected shear strength} \end{aligned} \tag{15-3}$$

PEER/TBI defines dispersion factor $\beta_u = 1.50$ and strength reduction factor $\phi = 0.75$. LATBSDC prescribes dispersion factor $\beta_u = 1.50$ and strength reduction factor $\phi = 1.00$. Effectively, the mean shear force demand $\bar{V}_{7GMs}$ is multiplied by $\beta = 2.00$ for PEER/TBI and by $\beta = 1.50$ for LATBSDC.

15-4-1 PEER/TBI design

The archetype structure was designed by according to PEER/TBI design requirements. The nominal expected shear capacity of the archetype structure is compared to the required shear capacity per PEER/TBI in Table 15-3. Furthermore, the expected shear capacity of the archetype structure is compared to the required shear capacity per PEER/TBI in Table 15-4. Tables 15-3 and 15-4 give that the nominal expected shear capacity provides insufficient shear capacity and the expected shear capacity of the archetype structure provides sufficient shear capacity in direction H1 but just fails to meet the criteria in direction H2, which is unexpected as the structure was designed according to PEER/TBI design requirements. However, the ground motions used to design the archetype structure were not given, and it is likely that a different set of ground motions produces different results. Therefore, the archetype structure does not meet the criteria for shear capacity of shear walls, but gives a capacity close to the required capacity per PEER/TBI. Furthermore, it is concluded that the shear walls were designed using expected shear capacity, as the nominal expected shear capacity fails to meet the design criteria.

Wall, Direction	$V_{n,e}$	Required capacity PEER/TBI	Unity check (≤ 1.0)
N-S wall, H1	12637 [kips]	15868 [kips]	1.26
E-W wall, H2	12381 [kips]	17236 [kips]	1.39

Table 15-3: Nominal expected shear capacity archetype structure [PEER Task 12 Group, 2011] and required capacity per PEER/TBI

Wall, Direction	$V_{n,e}$		Required capacity PEER/TBI		Unity check (≤ 1.0)
N-S wall, H1	17060	[kips]	15868	[kips]	0.93
E-W wall, H2	16715	[kips]	17236	[kips]	1.03

Table 15-4: Expected shear capacity archetype structure [PEER Task 12 Group, 2011] and required capacity per PEER/TBI

15-4-2 LATBSDC design

LATBSDC provides less conservative design criteria for shear capacity of shear walls. The nominal expected shear capacity and expected shear capacity of the archetype structure are compared to the required shear capacity per LATBSDC in Tables 15-5 and 15-6, respectively. As expected, the archetype structure's expected shear capacity meets the design criteria in both directions, since the archetype structure was designed using more conservative design criteria.

Wall, Direction	$V_{n,e}$		Required capacity PEER/TBI		Unity check (≤ 1.0)
N-S wall, H1	12637	[kips]	11901	[kips]	0.94
E-W wall, H2	12381	[kips]	12927	[kips]	1.04

Table 15-5: Nominal expected shear capacity archetype structure [PEER Task 12 Group, 2011] and required capacity per LATBSDC

Wall, Direction	V_e		Required capacity PEER/TBI		Unity check (≤ 1.0)
N-S wall, H1	17060	[kips]	11901	[kips]	0.70
E-W wall, H2	16715	[kips]	12927	[kips]	0.77

Table 15-6: Expected shear capacity archetype structure [PEER Task 12 Group, 2011] and required capacity per LATBSDC

15-4-3 Comparison PEER/TBI and LATBSDC design

An overview of the expected shear capacity of the archetype structure, and required shear capacity per LATBSDC and PEER/TBI is given in Table 15-7. The design methodologies are schematized in Figure 15-1. The mean shear demand is equal for both design methodologies, and the required shear strength per LATBSDC is 75% of the required shear capacity per PEER/TBI.

Wall, Direction	$V_{e,shear}$		Required capacity LATBSDC		Required capacity PEER/TBI	
N-S wall, H1	17060	[kips]	11901	[kips]	15868	[kips]
E-W wall, H2	16715	[kips]	12927	[kips]	17236	[kips]

Table 15-7: Expected shear capacity archetype structure [PEER Task 12 Group, 2011] and required capacity per LATBSDC and PEER/TBI

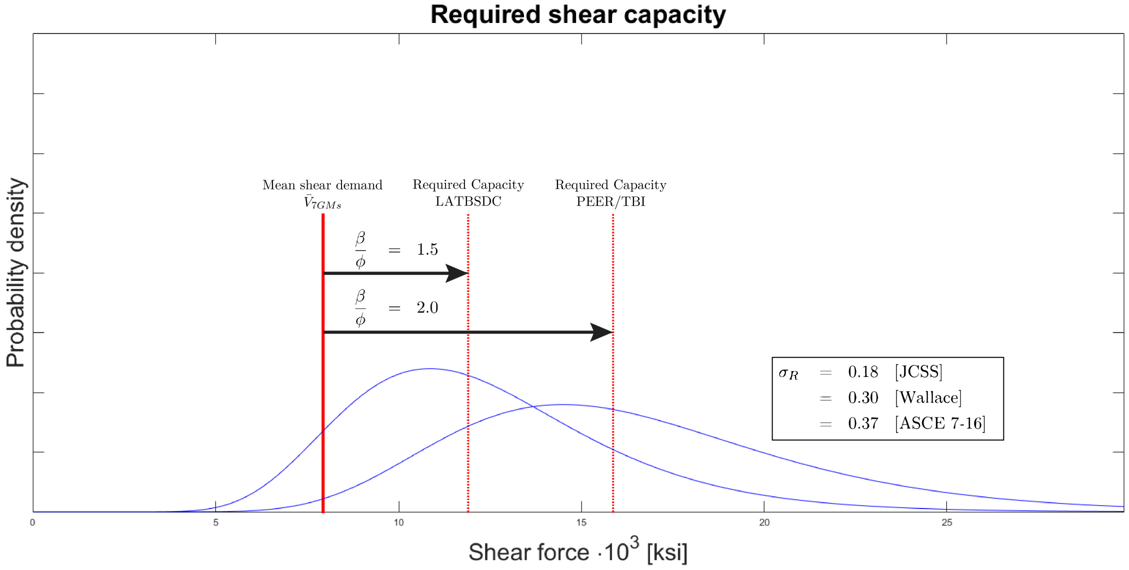

Figure 15-1: Shear wall design procedure

Part V

Structural reliability

Chapter 16

Structural reliability

16-1 Introduction

This goal of this study is to evaluate the structural reliability of shear walls in shear and distributors in transfer diaphragms. The structural reliability is the ability of the structure to withstand the load experienced during its lifespan and is defined as the demand not exceeding the capacity. The capacity of the structural components is described by the resistance function R in Section 16-2. The demand in the considered components is described by the load function S, defined in Section 16-3.

Failure is the complement of the reliability and therefore defined as demand exceeding capacity. The limit state is the state just before failure occurs and described by the limit state function Z. The probability of the demand exceeding capacity at a given intensity level is computed in Section 16-4 using numerical integration. The probability of demand exceeding capacity as a function of the intensity level is specified by collapse fragility curves fitted to the data from NLTHA using the maximum likelihood estimate in Section 16-5. The collapse fragility curves is combined with the ground motion hazard curve to compute the mean annual frequency of demand exceeding capacity λ_c in Section 16-6 and probability of demand exceeding capacity P(D>C in 50 years) in Section 16-7.

16-1-1 Acceptance criteria

The structural reliability will be compared to acceptance criteria specified in the considered design codes ASCE 7-10, ASCE 7-16, PEER/TBI and LATBSDC. A distinction is made between critical, ordinary, and non-critical elements. Critical elements are elements for which failure will result in total or partial collapse of the structure. Ordinary elements are elements for which failure could result in endangerment of individual lives.

ASCE 7-10 specifies a 1% probability of collapse within a 50-year period as the acceptance level. In ASCE 7-16, the acceptance level for critical elements is set at 10% probability of collapse conditioned on the occurrence of Maximum Considered Earthquake shaking. Furthermore, 25% probability of collapse is acceptable for ordinary elements given MCE shaking. No acceptance criteria for a 50-year period is specified in ASCE 7-10. For comparison, a 2.5% probability of collapse in within a 50-year period is specified for ordinary elements in this study. PEER/TBI and LATBSDC apply the 10% probability of collapse given MCE shaking acceptance criteria.

The shear capacity of shear walls is considered a key element, and must therefore satisfy the acceptance levels specified for critical elements. The distributors in transfer diaphragms are defined as ordinary elements, for which failure could result in endangerment of individual lives. The acceptance criteria are summarized in Table 16-1. The considered cases for structural reliability analysis are described in Section 16-1-2.

Element	Element category	Acceptance criteria	
		P(D>C|MCE)	P(D>C in 50 years)
Shear capacity shear walls	Critical	≤10%	≤1.0%
Transfer capacity distributors	Ordinary	≤25%	≤2.5%

Table 16-1: Acceptance criteria for considered components

It can be noted that the design codes considered probabilities of collapse instead of probabilities of demand exceeding capacity. For the reliability analysis, it was assumed that collapse always occurs when the demand exceeds the capacity, i.e. P(Collapse|D>C)=1. A short discussion on the probability of collapse in relation to the probability of demand exceeding capacity is provided in Section 18-1-1.

16-1-2 Considered cases

The shear forces just above the podium diaphragm and the transfer forces into the podium diaphragm are evaluated. The core has four shear walls. The shear forces in the individual walls and in the combined walls in each direction are evaluated. Furthermore, transfer forces into the podium diaphragm from the individual walls and from the combined walls in each direction are evaluated. Therefore, the probability of demand exceeding capacity is evaluated for twelve different combinations. The considered cases are summarized in Table 16-2.

Direction	Walls	Action	
		Shear force	Transfer force
H1-direction	All walls	Combined shear force in North and South wall just above podium diaphragm	Combined transfer force from North and South wall into podium diaphragm
	North wall/ South wall	Shear force in individual wall just above podium diaphragm	Transfer force from individual wall into diaphragm
H2-direction	All walls	Combined shear force in East and West wall just above podium diaphragm	Combined transfer force from East and West wall into podium diaphragm
	East wall/ West wall	Shear force in individual wall just above podium diaphragm	Transfer force from individual wall into diaphragm

Table 16-2: Considered load cases for shear force and transfer force

16-2 Resistance function R

The capacity of the elements is described by resistance function R. The resistance function R is a lognormal distribution function. The central limit theorem states that the product of a large number of independent basic random variables results in a variable with a lognormal distribution. Furthermore, the lognormal distribution is used for variables that physically cannot have a negative value. Hence, the strength parameters for steel and concrete and the resistance function are best described using the lognormal distribution [Cur-instituut, 2000].

16-2-1 Mean expected strength $V_{e,i}$

The mean expected strength $V_{e,i}$ was determined from ACI 318-11 in Chapters 14 and 15 for the diaphragm and shear wall, respectively. The mean expected strengths $V_{e,transfer}$ and $V_{e,shear}$ of the archetype structure are given in Table 16-3.

Direction	Walls	Expected shear capacity shear wall $V_{e,shear}$		Expected transfer capacity $V_{e,transfer}$	
H1-direction	All walls	34120	[kips]	27280	[kips]
	North wall	17060	[kips]	13640	[kips]
	South wall	17060	[kips]	13640	[kips]
H2-direction	All walls	33430	[kips]	22939	[kips]
	East wall	16715	[kips]	11470	[kips]
	West wall	16715	[kips]	11470	[kips]

Table 16-3: Mean expected shear and transfer strengths capacities $V_{e,i}$

The mean $\mu_{R,i}$ of the lognormal resistance function R was calculated using the definition of the lognormal distribution as given in Equation 16-1.

$$\mu_{R,i} = \ln\left(V_{e,i} - \frac{1}{2}\beta_R^2\right) \tag{16-1}$$

16-2-2 Resistance function standard deviation β_R

The standard deviation β_R was determined for shear capacity and transfer capacity. The standard deviation β_R of the resistance function R is equal to the capacity uncertainty β_{cap}.

For shear capacity, a dispersion value $\beta_{cap} = 0.20$ was found from 37 tests by Wallace, Hamburger et al. [Wallace et al., 2013]. However, the dispersion value of 0.20 is relatively low for brittle failure modes of reinforced concrete. Therefore, capacity uncertainty $\beta_{cap} = 0.30$ was assumed for this study, as recommended by Wallace, Hamburger et al.

For transfer force, capacity uncertainty $\beta_{cap} = 0.37$ recommended by ASCE 7-16 was adopted. The capacity uncertainty accounts for the typical variability in the strength equation from available test data, typical uncertainty in strength equation from extrapolation beyond available data and uncertainty in as-built strength due to construction quality and possible errors. The variation coefficients V for shear capacity of shear walls and transfer capacity of distributors are given in Table 16-4.

Element	Standard deviation β_R
Shear capacity shear walls	0.30
Transfer capacity distributors	0.37

Table 16-4: Resistance function standard deviation β_R

16-2-3 Computed resistance function R

The resistance function R is independent of the loading function and therefore equal for all S_a. The resistance function R for $S_a = 0.2243$ [%g] and the resistance function R for all S_a for transfer force in East wall are given in Figures 16-1 and 16-2, respectively.

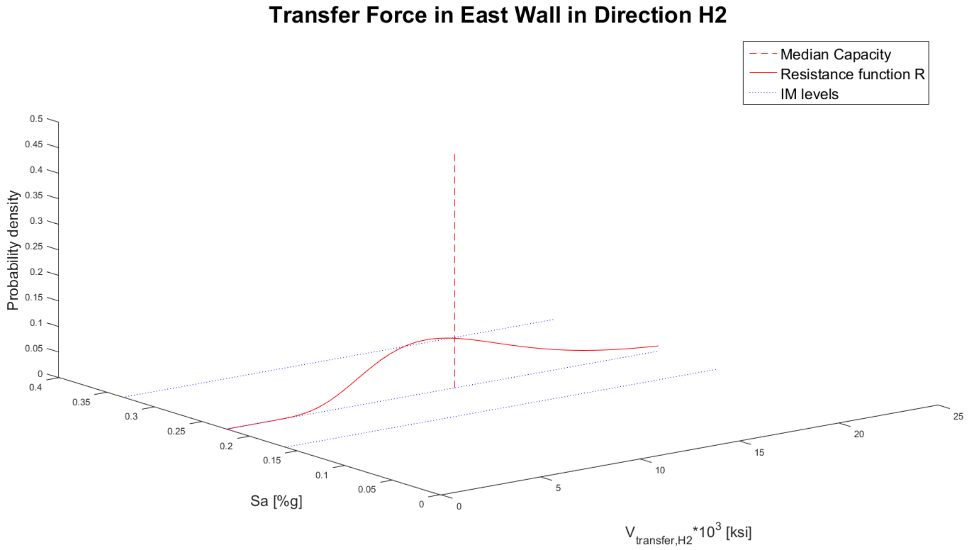

Figure 16-1: Transfer force capacity; East wall for $S_a = 0.2243$ [%g]

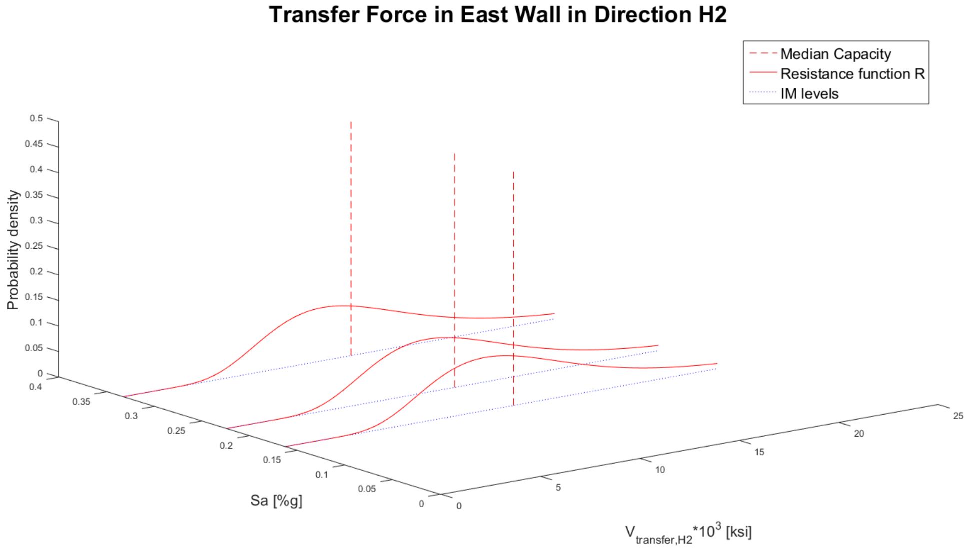

Figure 16-2: Transfer force capacity; East wall for all S_a

16-3 Load function S

The force demands in the considered elements are described by the load function S. The load function S is a probability distribution function fitted to data obtained from NLTHAs. The data consists of values for maximum forces in the considered elements. For intensity levels RP975 and RP9950, the distribution function is fitted to 40 data points. For intensity level RP2475, the distribution function is fitted to 61 data points.

The probability distribution function that gives the best fit with the data is defined in Section 16-3-1 using Anderson-Darling test. The lognormal distribution function produced the best fit with the data, and the mean θ_S and record-to-record variability of the load function were derived from the fitted lognormal distribution functions in Sections 16-3-2 and 16-3-3. The standard deviation β_S of the load function S is the combined standard deviation from record-to-record variability β_{RTR} found from NLTHA and modelling uncertainties β_{MDL}. The standard deviation β_S of the load function S is derived in Section 16-3-4. The computed load function parameters are given in Figure 16-3-5.

16-3-1 Probability distribution function

Various statistical tests can be applied to verify whether a given sample of data is drawn from a given probability distribution function. Empirical distribution function (EDF) statistics measure the distance between empirical cumulative distribution function of the dataset F_n and the hypothesized distribution F. The tests calculate the probability of obtaining data which have a still larger distance between the empirical and hypothesized distribution. This probability is called the confidence level and a small probability (e.g. < 0.01) indicates a poor fit.

The Kolmogorov-Smirnov (KS) test and Anderson-Darling (AD) test are EDF procedures to determine the goodness of fit. The AD procedure gives more weight to the tails of the distribution than the KS test. Since the tails of the load distribution function are most important for the limit state function, the AD procedure was adopted to determine the distribution function.

The AD procedure is a quadratic test to determine the goodness of fit, based on the squared difference between the empirical and hypothesized distribution. Various hypothesized distributions were tested on the datasets. It is noted that the AD test probabilities are wrong if the model was derived from the dataset. The theory underlying the EDF procedures requires independence between the curves under consideration. Therefore, the AD test probabilities are computed by bootstrap resamples of the original dataset. The goodness of fit of the normal distribution, exponential distribution, extreme value distribution, lognormal distribution, and Weibull distribution function were evaluated by the Anderson-Darling procedure. The results are given in Appendix M.

16-3-1-1 Lognormal distribution function

From the results in Appendix M, it was concluded that the lognormal distribution produced the best fit, and the lognormal distribution was therefore used to define the load function. The Matlab function *lognfit* was used to determine the maximum likelihood estimates of parameters of the lognormal distribution fitting the dataset. The distribution functions fitting the data were derived for two actions, transfer force in the diaphragm and shear force in the wall, three intensity levels and six element combinations. The parameter estimates $\hat{\theta}$ and $\hat{\beta}$ fitting the shear force in the shear wall and transfer force in the distributors are given in Tables 16-5 and 16-6, respectively.

Direction	Walls	RP975		RP2475		RP9950	
		$\hat{\theta}$	$\hat{\beta}$	$\hat{\theta}$	$\hat{\beta}$	$\hat{\theta}$	$\hat{\beta}$
H1 direction	All walls	8163	0.342	9173	0.277	10425	0.243
	North wall	4423	0.326	5144	0.259	5806	0.221
	South wall	4171	0.354	4762	0.265	5565	0.247
H2 direction	All walls	9743	0.233	10872	0.231	12389	0.193
	East wall	5144	0.225	5832	0.201	6674	0.194
	West wall	5367	0.232	6073	0.199	6670	0.187

Table 16-5: Parameter estimates shear force

Direction	Walls	RP975		RP2475		RP9950	
		$\hat{\theta}$	$\hat{\beta}$	$\hat{\theta}$	$\hat{\beta}$	$\hat{\theta}$	$\hat{\beta}$
H1 direction	All walls	8728	0.408	9963	0.332	11098	0.314
	North wall	3879	0.376	4381	0.327	4853	0.272
	South wall	3809	0.369	4274	0.303	4810	0.277
H2 direction	All walls	8912	0.182	9867	0.213	11651	0.206
	East wall	5429	0.159	6066	0.176	7195	0.158
	West wall	5528	0.176	6084	0.166	6976	0.197

Table 16-6: Parameter estimates transfer force

16-3-2 Load function median θ_S

The load function median θ_S is equal to the parameter estimate $\hat{\theta}$ for the lognormal distribution function fitted to the data from NLTHAs at different intensity levels, given in Tables 16-5 and 16-6. From Table 16-5 follows that the median shear force increases for increasing S_a-values for the considered cases. The same holds for the transfer force, as follows from Table 16-6.

16-3-3 Record-to-record variability β_{RTR}

Record-to-record uncertainty β_{RTR} is the uncertainty due to variablity in the response to different ground motion records scaled to a given intensity level [FEMA P695, 2009]. The record-to-record uncertainty β_{RTR} is equal to the parameter estimate $\hat{\beta}$ for the lognormal distribution function fitted to the data from NLTHAs at different intensity levels.

From Table 16-5 and 16-6 follows that in direction H1 the standard deviation σ_Y decreases for increasing IM-values. A decrease in standard deviation σ_Y indicates that the maximum values are more closely spaced. The median force increases for increasing IM-levels, and the extreme values decreasingly increase for increasing S_a. Hence the standard deviation σ_Y decreases for increasing S_a.

In H2-direction, the standard deviation σ_Y of the shear force load function decreased slightly for increasing IM-values. No decrease was found for the transfer force in H2 direction.

16-3-3-1 Record-to-record variability estimates

It is expected that the probability of demand exceeding capacity P(D>C|IM) increases with increasing IM values. However, the probability of demand exceeding capacity did not increase for increasing S_a-values for the shear force and transfer force in direction H1, despite the increase in the median shear force. The resistance function R is constant for all intensity levels. Therefore, the decrease of P(D>C|IM) for increasing IM is caused by the decreasing record-to-record variability β_{RTR} of the load function for increasing IM.

Unexpected decrease in probability of demand exceeding capacity for increasing S_a produced unrealistic parameter estimates for the collapse fragility curves for shear force in direction H1 and H2 direction and transfer force in direction H1. Therefore, an approximation of the RTR-uncertainty $\sigma_{RTR,est}$ for each combination was required to compute the load function S.

Most conservative estimate
The conservative estimate of the probability of demand exceeding capacity and collapse

fragility curves is found by taking the maximum RTR-variability $\sigma_{RTR,max}$ for each combination and applying the RTR-variability to all load functions S in combination with the median force found from the NLTHAs at each S_a. This approach results in the largest probability of collapse and neglects the saturation of forces for larger intensity levels due to nonlinear behaviour, as described in Section 18-3.

Least conservative estimate

The least conservative estimate of the probability of demand exceeding capacity and collapse fragility curve is found by taking the minimum RTR-uncertainty $\sigma_{RTR,min}$ and applying $\sigma_{RTR,min}$ to all load functions S for each case. This would imply that the parameter estimate $\hat{\beta}$ of the maximum S_a value is used to compute the load functions S. Although this approach results in the least conservative estimate of CFC, it is not necessarily unconservative, since the parameter estimate $\hat{\beta}$ at $S_{a,max}$ might give the most accurate estimate of the force distribution near the limit state.

Estimate for record-to-record variability β_{RTR}

The load function estimate for $IM = RP2475$ is expected to give the better estimate of the RTR-uncertainty β_{RTR}. It is assumed that $\hat{\beta}$ for $IM = RP2475$ gives a closer estimate of the record-to-record variability near the limit state than $\hat{\beta}$ for $IM = RP975$. Furthermore, the estimate for $\hat{\beta}$ at $IM = RP2475$ is more conservative than the estimate for the maximum IM-level. Moreover, the dataset for $IM = RP2475$ consists of 61 points, whereas the other sets contain 40 data points. Hence, the standard deviation estimate $\hat{\beta}$ for $IM = RP2475$ was selected as the record-to-record uncertainty β_{RTR} for all load functions S. The record-to-record uncertainties β_{RTR} are given in Table 16-7.

The record-to-record variability reduces for increasing ground motion intensities due to increased nonlinear behaviour of the structure. A discussion on the record-to-record variability in relation to nonlinear behaviuor is provided in Section 18-3.

Direction	Walls	Shear force	Transfer force
		β_{RTR}	β_{RTR}
H1 direction	All walls	0.277	0.332
	North wall	0.259	0.327
	South wall	0.265	0.303
H2 direction	All walls	0.231	0.213
	East wall	0.201	0.176
	West wall	0.199	0.166

Table 16-7: Record-to-record variability β_{RTR}

16-3-4 Load function standard deviation β_S

The standard deviation β_S of the load function S must be determined by combining the record-to-record variability β_{RTR} with modelling uncertainty β_{MDL}. The modelling uncertainty is the uncertainty resulting from estimating force demand using the structural model. It accounts for how well the archetype structure represents the full range of responses and how well the analysis model captures structural collapse behaviour [FEMA P695, 2009]. Neglecting the modelling uncertainty is unconservative [Liel et al., 2007]. This study adopts the modelling uncertainty suggested by ASCE 7-16 β_{MDL}=0.20.

Since the record-to-record variability β_{RTR} and modelling uncertainty β_{MDL} are assumed to be statistically independent, the total standard deviation β_S of the load function S can be calculated using the SRSS method, given in Equation 16-2. The standard deviation β_S of the load function S for the considered cases is given in Table 16-8.

$$\beta_S = \sqrt{\beta_{RTR}^2 + \beta_{MDL}^2} \tag{16-2}$$

Direction	Walls	Shear force			Transfer force		
		β_{RTR}	β_{MDL}	β_S	β_{RTR}	β_{MDL}	β_S
H1 direction	All walls	0.277	0.200	0.342	0.332	0.200	0.388
	North wall	0.259	0.200	0.327	0.327	0.200	0.383
	South wall	0.265	0.200	0.332	0.303	0.200	0.363
H2 direction	All walls	0.231	0.200	0.306	0.213	0.200	0.292
	East wall	0.201	0.200	0.284	0.176	0.200	0.266
	West wall	0.199	0.200	0.282	0.166	0.200	0.260

Table 16-8: Load function standard deviation β_S

16-3-5 Computed load function S

The load function parameters median θ_S and standard deviation β_S for the considered cases are given in Tables 16-9 and 16-10 for the shear force and transfer force, respectively.

The computed load function S, the individual results from NLTHA, and the resistance function R for $S_a = 0.2243$ [%g] are given for transfer force in the East wall in Figure 16-3. The load functions S, individual results from NTLHA and resistance function R for all IM are given in Figure 16-4.

Direction	Walls	RP975		RP2475		RP9950	
		Median	β_S	Median	β_S	Median	β_S
H1 direction	All walls	8163	0.342	9173	0.342	10425	0.342
	North wall	4423	0.327	5144	0.327	5806	0.327
	South wall	4171	0.332	4762	0.332	5565	0.332
H2 direction	All walls	9743	0.306	10872	0.306	12389	0.306
	East wall	5144	0.284	5832	0.284	6674	0.284
	West wall	5367	0.282	6073	0.282	6670	0.282

Table 16-9: Shear force load function parameters

Direction	Walls	RP975		RP2475		RP9950	
		Median	β_S	Median	β_S	Median	β_S
H1 direction	All walls	8728	0.388	9963	0.388	11098	0.388
	North wall	3879	0.383	4381	0.383	4853	0.383
	South wall	3809	0.363	4274	0.363	4810	0.363
H2 direction	All walls	8912	0.292	9867	0.292	11651	0.292
	East wall	5429	0.266	6066	0.266	7195	0.266
	West wall	5528	0.260	6084	0.260	6976	0.260

Table 16-10: Transfer force load function parameters

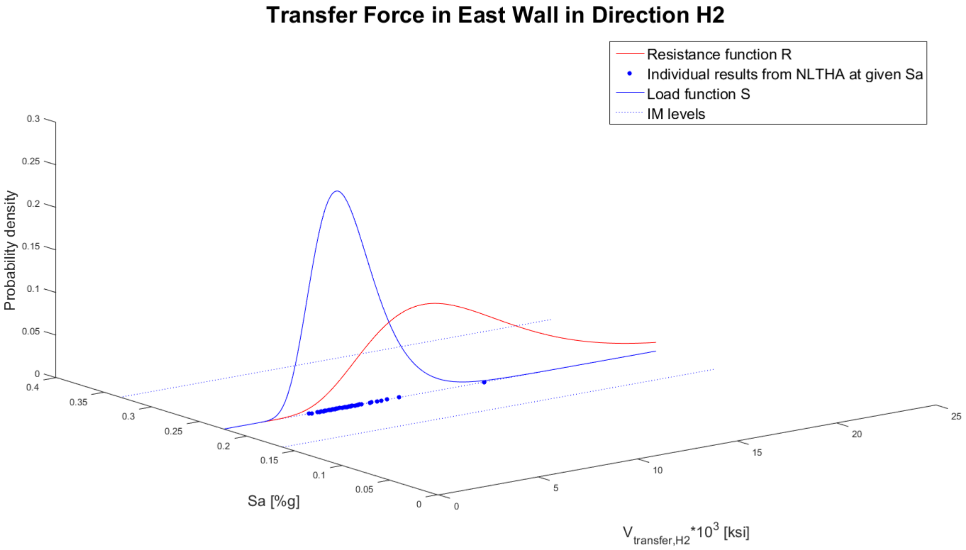

Figure 16-3: Transfer force capacity and demand; East wall for $IM = 0.2243$ [%g]

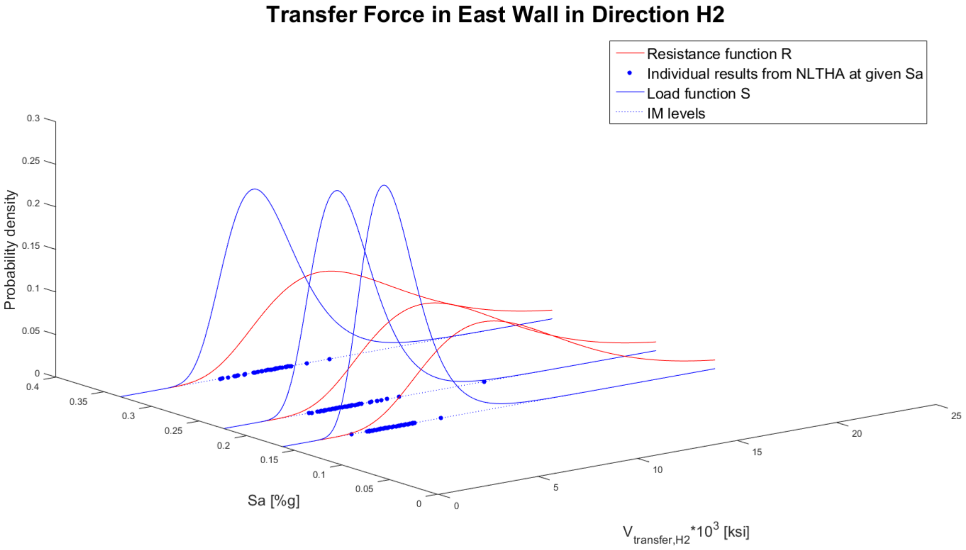

Figure 16-4: Transfer force capacity and demand; East wall for all IM

16-4 Probability of demand exceeding capacity given IM

The probability of demand exceeding capacity given an IM level P(D>C|IM) was evaluated using the limit state function Z. The limit state function is defined in Section 16-4-1. The probability of demand exceeding capacity for all cases and intensity levels IM is computed in Section 16-4-2. The computed probabilities of demand exceeding capacity are evaluated in Section 16-4-3.

16-4-1 Limit state function Z

The limit state is the state just before demand exceeds capacity. The capacity of the structure is described by the resistance function $R(\vec{X_R})$, which is defined by the basic random variables $\vec{X_R}$ and derived in Section 16-2. The demand on the structure is described by means of basic random variables $\vec{X_S}$ in the load function $S(\vec{X_S})$, deduced in Section 16-3. The limit state function Z is defined by Equation 16-3.

$$Z(\vec{X_R}, \vec{X_S}) \quad = \quad R(\vec{X_R}) - S(\vec{X_S}) \quad = \quad 0 \tag{16-3}$$

The numerical value of the limit state function $Z(\vec{X})$ depends on the stochastic values of the basic random variables $\vec{X}$. The joint probability density function $f_{\vec{X}}(\vec{X})$ describes the likelihood of the basic random variables $\vec{X}$ having a certain value $\vec{X}$, as given in Equation 16-4.

$$f_{\vec{X}}(\vec{X}) \quad = \quad f_{X_1,X_2,\ldots,X_n}(X_1, X_2, \ldots, X_n) \tag{16-4}$$

The reliability of the structure $P_{reliable}$ is equal to the probability that the limit state is not exceeded. The failure probability $P_{D>C}$ is defined as the probability of demand exceeding capacity given IM P(D>C|IM). The failure probability $P_{D>C}$ is described by the subset of the sample space where the basic random variables $\vec{X}$ take on values such that the limit state function is less than or equal to zero, as given in Equation 16-5.

$$\begin{aligned} P_{D>C} &= P(Z(\vec{X}) \leq 0) \\ &= \iint \cdots \int_{Z\leq 0} f_{X_1,X_2,\ldots,X_n}(X_1, X_2, \ldots, X_n)\mathrm{d}X_1\mathrm{d}X_2 \ldots \mathrm{d}X_n \end{aligned} \tag{16-5}$$

In case the variable $X_1, X_2, \ldots, X_n$ are stochastically independent, Equation 16-5 simplifies to Equation 16-6.

$$\begin{aligned} P_{D>C} &= P(Z(\vec{X}) \leq 0) \\ &= \iint \cdots \int_{Z\leq 0} f_{X_1}(X_1)f_{X_2}(X_2) \ldots f_{X_n}(X_n)\mathrm{d}X_1\mathrm{d}X_2 \ldots \mathrm{d}X_n \end{aligned} \tag{16-6}$$

16-4-1-1 Fundamental solution for two basic random variables

In case the resistance function R and load function S can both be described by one basic variable, the limit state function from Equation 16-3 can be simplified to Equation 16-7.

$$Z(R,S) \quad = \quad R - S \tag{16-7}$$

According to Equation 16-5, the probability of failure can then be calculated by Equation 16-8.

$$P_{D>C} \quad = \quad \iint\limits_{Z\leq 0} f_{\mathrm{R,S}}(R,S)\mathrm{d}R\mathrm{d}S \tag{16-8}$$

Since $Z < 0$ if $R < S$, Equation 16-9 holds.

$$P_{D>C} = \int_{-\infty}^{\infty}\int_{-\infty}^{S} f_{\mathrm{R,S}}(R,S)\mathrm{d}R\mathrm{d}S \tag{16-9}$$

Assuming that the resistance and load are independent, Equation 16-9 simplifies to Equation 16-10 using the definition of cumulative distribution function.

$$\begin{aligned} P_{D>C} \quad &= \quad \int_{-\infty}^{\infty}\int_{-\infty}^{S} f_R(\mathrm{R})f_S(\mathrm{S})\mathrm{d}R\mathrm{d}S \\ &= \quad \int_{-\infty}^{\infty} F_R(\mathrm{S})f_S(\mathrm{S})\mathrm{d}S \end{aligned} \tag{16-10}$$

In the same manner, the convolution integral can be determined, as given in Equation 16-11.

$$P_{D>C} \quad = \quad P(S > R) \quad = \quad \int_{0}^{\infty} (1 - F_{\mathrm{S}}(R))\, f_{\mathrm{R}}(R)\mathrm{d}R \tag{16-11}$$

16-4-2 Computed probability of demand exceeding capacity given IM

The probability of failure $P_{D>C}$ for the structural reliability analysis was defined as the probability of demand exceeding capacity given IM $P(\mathrm{D{>}C|IM})$. $P(\mathrm{D{>}C|IM})$ was computed through numerical integration using the Matlab function *cumtrapz*. This function computes an approximation of the cumulative intregral via the trapezoidal method with unit spacing.

The probability of failure $P(\mathrm{D{>}C|IM})$ was calculated for all cases defined in Section 16-1-2 and all considered intensity levels IM. The results for all cases and intensity levels are given in Tables 16-11 and 16-12.

Deaggregation of the probability of failure for $S_a = 0.2243$ [%g] for transfer force in the east wall is given in Figure 16-5, in combination with the load function S and resistance function R. The probabilities of demand exceeding capacity $P(\mathrm{D{>}C|IM})$ for computed S_a are given in Figure 16-6.

Direction	Walls	Intensity level IM		
		RP975	RP2475	RP9950
H1 direction	All walls	0.0008	0.0018	0.0043
	North wall	0.0011	0.0032	0.0072
	South wall	0.0008	0.0020	0.0058
H2 direction	All walls	0.0018	0.0040	0.0096
	East wall	0.0020	0.0050	0.0124
	West wall	0.0027	0.0066	0.0123

Table 16-11: Shear force P(D>C|IM)

Direction	Walls	Intensity level IM		
		RP975	RP2475	RP9950
H1 direction	All walls	0.0155	0.0284	0.0445
	North wall	0.0085	0.0155	0.0249
	South wall	0.0063	0.0117	0.0209
H2 direction	All walls	0.0207	0.0344	0.0722
	East wall	0.0482	0.0787	0.1510
	West wall	0.0508	0.0777	0.1332

Table 16-12: Transfer force P(D>C|IM)

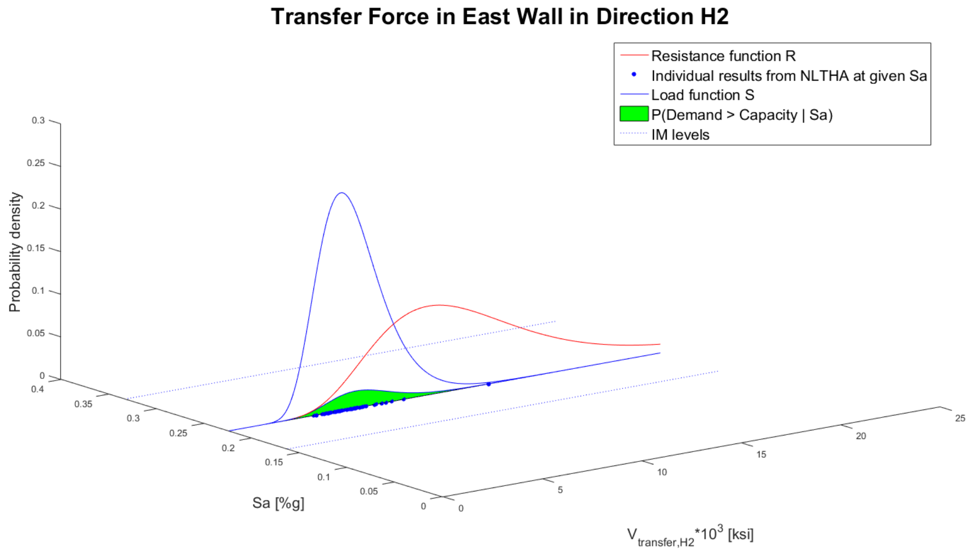

Figure 16-5: Transfer force capacity, demand, and deaggregation of P(D>C|IM=im); East wall for $S_a = 0.2243$ [%g]

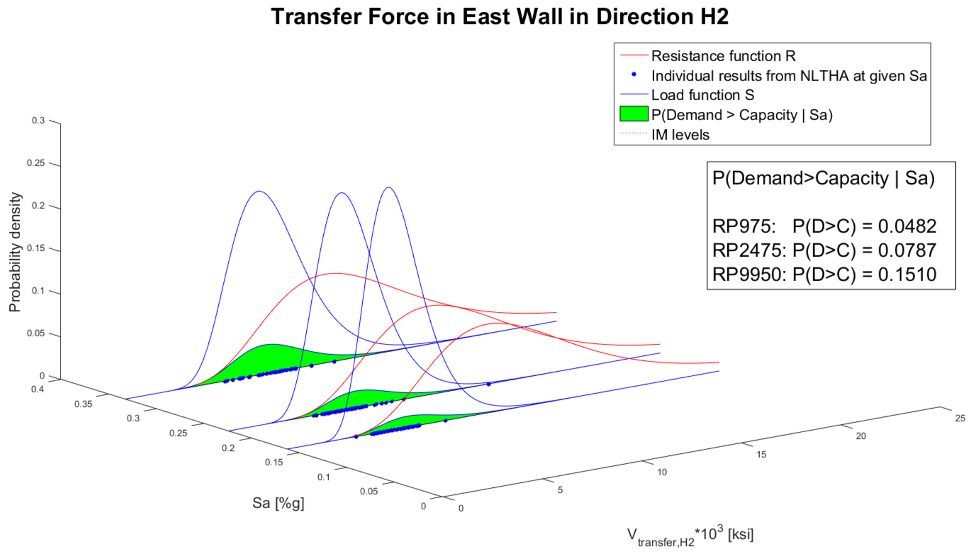

Figure 16-6: Probability of failure; Transfer force east wall for all S_a

16-4-3 Evaluation of computed probability of demand exceeding capacity given IM

The probability of demand exceeding capacity given IM is calculated with the limit state function Z, which consists of the load function S and resistance function R. It is expected that the probability of failure increases with increasing IM values. However, a larger probability of collapse may not always be observed for increasing IM because a different, finite set of GMs is selected at each IM level.

The resistance function is constant for all intensity levels, so the difference in $P(\text{D>C}|\text{IM})$ between different intensity levels results from the load function S. From Table 16-9 follows that the median shear force always increases for increasing S_a-values for the considered cases. The same holds for the transfer force, which follows from Table 16-10. As the standard deviation of the load function S was taken equal for all IM, see Section 16-3-3, the probability of demand exceeding capacity increases for increasing IM.

The results from Tables 19-6 and 19-9 show that the probability of demand exceeding capacity is larger for the transfer force than for the shear force. Furthermore, the probability of shear demand exceeding shear capacity is larger in H1 direction. The probability of transfer demand exceeding transfer capacity is larger in H2 direction.

16-5 Collapse fragility curves

Collapse fragility curves specify the probability of collapse of a structure as a function of the ground motion intensity measure, IM. The ground motion intensity measure IM was chosen as the spectral acceleration S_a at the first mode period of the structure T_1 and 5% damping ratio. Multiple stripe analysis was used to collect data for the fragility function. NLTHAs were done at multiple intensity levels, the "stripes", for which each intensity level has a unique set of ground motions. The ground motions at each IM were selected using the Conditional Spectrum for the given site in Los Angeles.

The IM values of ground motions causing collapse are assumed lognormally distributed [Eads et al., 2013]; [Baker, 2014]. A lognormal cumulative distribution function was therefore used to define the fragility function, as given in Equation 16-12, where $P(C|IM = im)$ is the probability of collapse at a given intensity level $IM = im$. The function is defined by the median of the fragility function θ_c and the standard deviation β_c of $\ln(IM)$. The estimates of the median θ_c and standard deviation β_c were denoted $\hat{\theta}_c$ and $\hat{\beta}_c$, respectively.

$$P(D > C|IM = x) \quad = \quad \Phi\left(\frac{\ln(x/\theta_c)}{\beta_c}\right) \tag{16-12}$$

The maximum likelihood estimate (MLE) is the most appropriate method to fit a collapse fragility curve to the observed data [Baker, 2014]. It performs better than alternatives such as minimizing the sum of squared errors (SSE). SSE ignores that the variance of the observations is non-constant. If zero collapses are observed, this is a strong indicator of a very small probability of collapse. However, SSE does not recognize that the error of observing zero collapses at a given S_a value and a fitted probability of collapse of 0.1 is larger than the error of a fitted probability of collapse of 0.6 for 50% observed collapses at another S_a level. The MLE takes better advantage of this knowledge. This is especially important when computing the mean annual frequency of collapse, since ground motions with a lower IM value occur more frequently than ground motions with higher IM values. Therefore, errors in the lower part of the collapse fragility function may have a significant effect on the computed mean annual frequency of collapse.

16-5-1 MLE approach

The maximum likelihood estimate approach is used to identify the collapse fragility curve that gives the highest probability of having observed the collapse data that was obtained from the NLTHAs at multiple intensity levels.

For a given intensity level $IM = im$, the probability, or likelihood, of observing a given number of collapses z_j out of a total number of ground motions n_j is given by the binomial distribution from Equation 16-13.

$$P(z_j \text{ collapses in } n_j \text{ ground motions}) \quad = \quad \binom{n_j}{z_j} p_j^{z_j} \left(1 - p_j\right)^{n_j - z_j} \tag{16-13}$$

For multiple intensity levels m, the likelihood is given by the product of the binomial probabilities at each IM, as given in Equation 16-14.

$$\text{Likelihood} \quad = \quad \prod_{m}^{j=1} \binom{n_j}{z_j} p_j^{z_j} \left(1 - p_j\right)^{n_j - z_j} \tag{16-14}$$

When the lognormal cumulative distribution from Equation 16-12 is used to define the fragility function, the fragility parameters θ_c and β_c are explicit in the likelihood function, see Equation 16-15. The median θ_c determines the location of the fragility function, whereas the standard deviation β_c determines the steepness of the function. The estimates of the fragility function $\hat{\theta}_c$ and $\hat{\beta}_c$ are obtained by maximizing the fragility function.

$$\text{Likelihood} \quad = \quad \prod_{m}^{j=1} \binom{n_j}{z_j} \Phi\left(\frac{\ln(x/\theta_c)}{\beta_c}\right)^{z_j} \left(1 - \Phi\left(\frac{\ln(x/\theta_c)}{\beta_c}\right)\right)^{n_j - z_j} \tag{16-15}$$

A Matlab tool developed by Baker [Baker, 2014] uses the equivalent logarithm of the likelihood function to find the parameter estimates $\hat{\theta}_c$ and $\hat{\beta}_c$, given in Equation 16-16.

$$\begin{aligned} \left\{\hat{\theta}_c, \hat{\beta}_c\right\} \quad = \quad \arg\max_{\theta_c, \beta_c} \sum_{m}^{j=1} \Bigg[\ln \binom{n_j}{z_j} + z_j \Phi\left(\frac{\ln(x/\theta_c)}{\beta_c}\right) + \\ (n_j - z_j)\left(1 - \Phi\left(\frac{\ln(x/\theta_c)}{\beta_c}\right)\right) \Bigg] \end{aligned} \tag{16-16}$$

The binomial distribution requires that the structural analyses produce integers for the number of collapses z_j at each $IM = im$. However, the probability of collapse computed in Section 16-4-2 multiplied by the number of ground motions n_j is not necessarily an integer. To evaluate the fragility curves for a non-integer number of collapses out of a total number of collapses, a numerically equivalent alternative to Equation 16-16 must be used which allows non-integer number of collapses. Baker implemented another function in the Matlab tool which uses general linear regression with a Probit link function to predict the probability of collapse as a function of $\ln(IM)$. This function is numerically equivalent to Equation 16-16 and allows non-integer number of collapses. The alternative function was therefore used to identify the maximum likelihood collapse fragility curves.

16-5-2 Computed collapse fragility curves

Collapse fragility curves were computed for the shear force and transfer force in for all cases described in Section 16-1-2. The collapse fragility curves were calculated using the computed P(D>C|IM) for different IM given in Tables 19-6 and 19-9. The collapse fragility curve for transfer force in east wall is given in Figure 16-7.

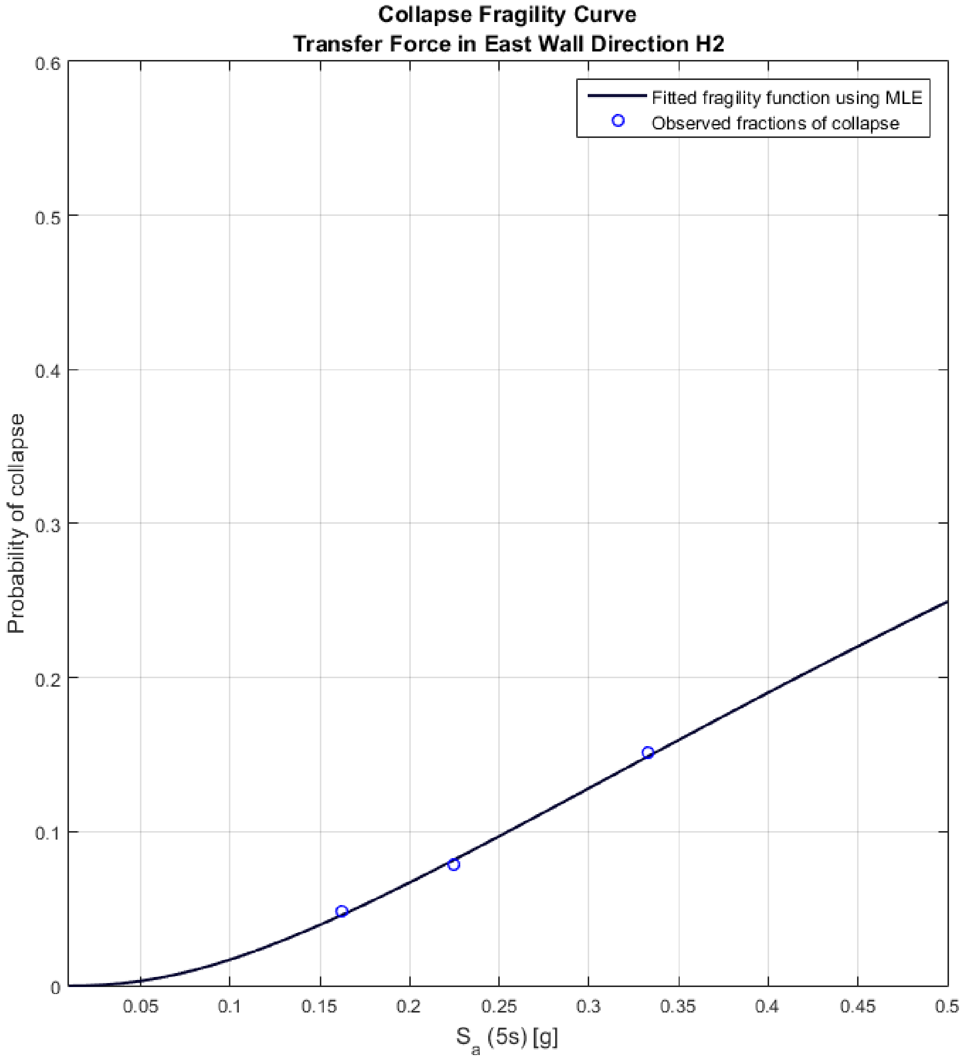

Figure 16-7: Collapse fragility curve; Transfer force east wall for all S_a

16-5-3 Evaluation of computed collapse fragility curve

The collapse fragility curves are described by two parameter estimates, the median S_a-value of the fragility function $\hat{\theta}_c$ and standard deviation $\hat{\beta}_c$. The parameter estimates are given in Table 16-13 for the considered cases.

A larger estimated mean $\hat{\theta}_c$ gives a larger margin against collapse. Furthermore, a small standard deviation $\hat{\beta}_c$ improves the reliability of the element, as the probability of failure is lower for S_a-values less than median $\hat{\theta}_c$ than for CFCs with larger standard deviation $\hat{\beta}_c$. From the median $\hat{\theta}_c$ follows that transfer force in H2 direction has the largest probability of collapse, as was also found for the computed probability of collapse.

Direction	Walls	Shear force		Transfer force	
		$\hat{\theta}_c$	$\hat{\beta}_c$	$\hat{\theta}_c$	$\hat{\beta}_c$
H1 direction	All walls	11.41	1.35	5.32	1.64
	North wall	7.02	1.25	10.12	1.75
	South wall	5.50	1.11	8.55	1.60
H2 direction	All walls	6.50	1.27	1.95	1.20
	East wall	4.37	1.15	1.06	1.11
	West wall	8.38	1.44	1.50	1.35

Table 16-13: Parameter estimates of collapse fragility curves

16-6 Mean annual rate of demand exceeding capacity

The fragility curves can be combined with a ground motion hazard curve to compute the mean annual frequency of demand exceeding capacity, given in Equation 16-17 [Haselton and Deierlein, 2007]; [Liel and Deierlein, 2008].

$$\lambda_c(y) = \int P(D > C|im) \cdot \left|\frac{d\lambda_{\mathrm{IM}}(im)}{d(im)}\right| d(im) \tag{16-17}$$

In order to compute Equation 16-17, numerical integration is used. Thus, the continuous case is transformed into a discrete case. It is noted that for smaller ΔIM, more accurate results are obtained. The numerical calculation of the mean annual frequency of collapse is given by Equation 16-18.

$$\lambda_c(y) = \sum P(D > C|im) \cdot \left|\frac{d\lambda_{IM}(im)}{d(im)}\right| \Delta IM \tag{16-18}$$

In Equation 16-18, $P(D > C|im)$ is given by the collapse fragility curve and $\left|\frac{d\lambda_{IM}(im)}{d(im)}\right|$ is given by the slope of the hazard curve. The collapse fragility curves are discussed in Section 16-5. The hazard curve is discussed in Section 8-1-1.

16-6-1 Slope of the hazard curve

To compute the slope of the hazard curve for numerical integration, the fourth degree polynomial was used to obtain a polynomial fit for the hazard curve. The fourth polynomial fit is given by Equation 16-19. The polynomial fit was obtained through Matlab calculations and given in Figure 16-8. The coefficient of determination R^2 was calculated to measure the fit to the original data points. The coefficient of determination R^2 is calculated by Equation 16-20 and is given in Figure 16-8. As can be seen in Figure 16-8, the coefficient of determination R^2 is close to 1, which indicates that the fourth degree polynomial gives a good fit.

$$\begin{aligned}\ln[MAF(IM)] = {} & a_0 + a_1 \ln(IM) + a_2[\ln(IM)]^2 + \\ & a_3[\ln(IM)]^3 + a_4[\ln(IM)]^4\end{aligned} \tag{16-19}$$

$$\begin{aligned} R^2 &= 1 - \frac{SS_{res}}{SS_{tot}} \\ SS_{res} &= \sum_i (y_i - f_i)^2 \\ SS_{tot} &= \sum_i (y_i - \bar{y})^2 \end{aligned} \tag{16-20}$$

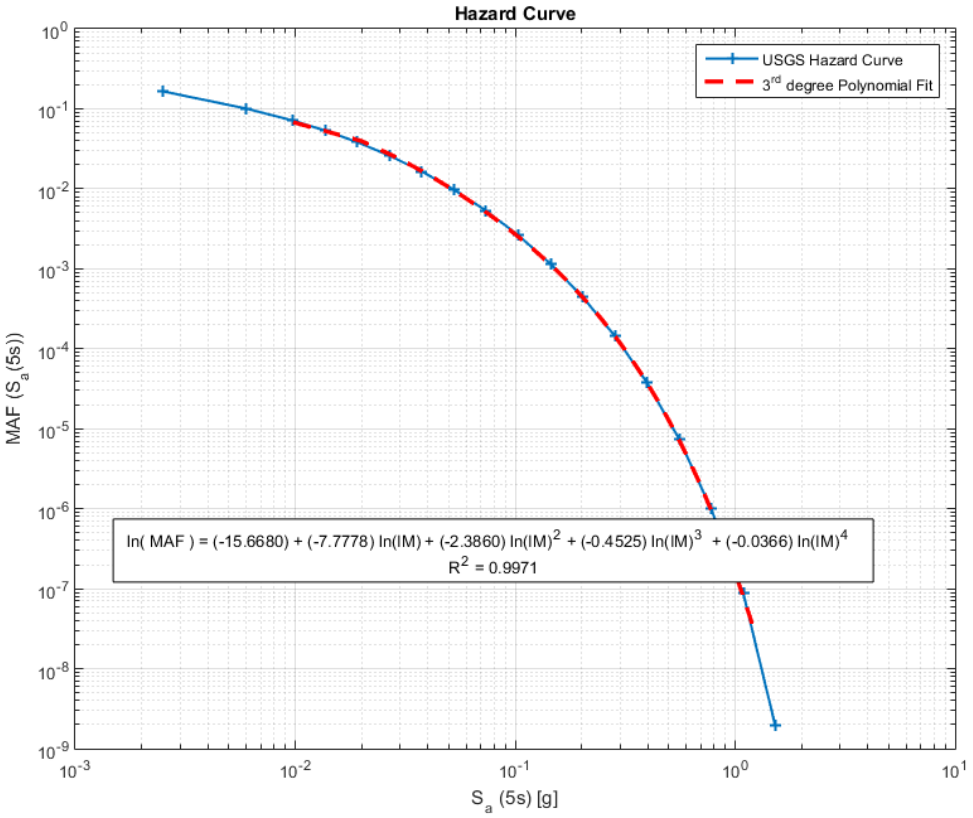

Figure 16-8: Hazard curve and fourth-order polynomial fit

16-6-2 Computed mean annual rate of demand exceeding capacity λ_c

The mean annual frequency of demand exceeding capacity λ_c was computed for the shear force and transfer force in for all cases. The deaggregation of the mean annual frequency of demand exceeding capacity for transfer force in east wall is given in Figure 16-9. Estimated mean annual rates of demand exceeding capacity for all cases are given in Table 16-14.

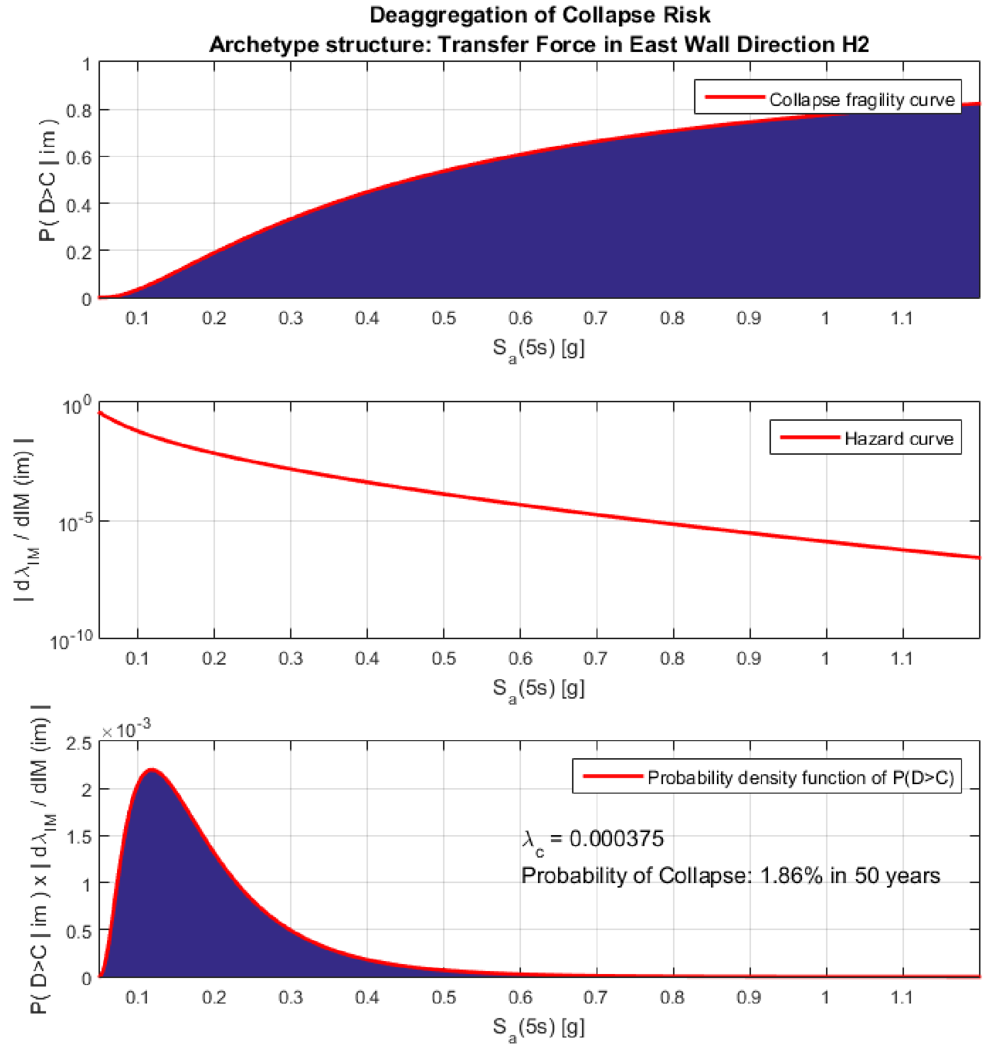

Figure 16-9: Deaggregation of mean annual frequency of demand exceeding capacity; Transfer force in east wall

Direction	Walls	Mean annual rate of demand exceeding capacity λ_c	
		Shear force	Transfer force
H1 direction	All walls	1.203E-05	1.293E-04
	North wall	2.044E-05	7.235E-05
	South wall	1.740E-05	5.751E-05
H2 direction	All walls	2.610E-05	1.795E-04
	East wall	3.407E-05	3.750E-04
	West wall	3.360E-05	3.644E-04

Table 16-14: Mean annual rate of demand exceeding capacity λ_c

16-7 Probability of demand exceeding capacity in 50 years

The probability of demand exceeding capacity in 50 years is calculated using Equation 16-21 [Luco et al., 2007].

$$P(\text{D>C in Y years}) \quad = \quad 1 - (1 - \lambda_c)^Y \tag{16-21}$$

The probability of demand exceeding capacity in 50 years is given for all combinations in Table 16-15.

Direction	Walls	Probability of collapse $P_{C,50}$	
		Shear force	Transfer force
H1 direction	All walls	0.060%	0.644%
	North wall	0.102%	0.361%
	South wall	0.087%	0.287%
H2 direction	All walls	0.130%	0.894%
	East wall	0.170%	1.858%
	West wall	0.168%	1.806%

Table 16-15: Probability of collapse $P_{C,50}$

Chapter 17

Sensitivity Analysis

17-1 Introduction

For the given archetype structure, only record-to-record variability β_{RTR} was explicitly computed in the structural reliability analysis. An assumption based on literature was made to account for modelling uncertainty. Modelling uncertainty accounts for how well the archetype structure represents the full range of responses [FEMA P695, 2009]. The force demand in the shear walls and stiffness properties is also a function of the modified stiffness properties of the diaphragm, basement walls, rotational stiffness of the foundation and horizontal stiffness of the soil below basement level [ATC 72-1, 2010]. Therefore, the influence of variation in diaphragm stiffness and stiffness of the basement walls on the force demand and probability of shear failure in the shear walls and distributor failure in the podium diaphragm will be studied. The influence of the rotational and horizontal stiffness is outside the scope of this research.

17-2 Sensitivity analysis: Diaphragm stiffness

17-2-1 Stiffness variation

The force demand in the structure was evaluated for three diaphragm stiffness configurations. The force demand for the median diaphragm stiffness was already evaluated in the reliability analysis. For the sensitivity analysis, the force demand for the median diaphragm stiffness minus one standard deviation, i.e. lower bound stiffness, and median diaphragm stiffness plus one standard deviation, i.e. upper bound stiffness, was evaluated for a set of 20 ground motions selected and scaled to match the Conditional Spectrum for $IM = RP2475$.

The modified diaphragm stiffness for the lower bound, median and upper bound evaluation are given in Table 17-1.

Diaphragm	Lower bound stiffness	Median stiffness	Upper bound stiffness
Podium (t = 12 [in])	$0.20E_cI_g$; $0.10G_cA_g$	$0.25E_cI_g$; $0.25G_cA_g$	$0.50E_cI_g$; $0.50G_cA_g$
Basement (t = 10 [in])	$0.20E_cI_g$; $0.10G_cA_g$	$0.25E_cI_g$; $0.25G_cA_g$	$0.50E_cI_g$; $0.50G_cA_g$

Table 17-1: Stiffness assumptions for podium and basement diaphragms

17-2-2 Resistance function R

The resistance function R is described by a lognormal distribution function, mean expected strength capacity θ_R, and variation coefficient V. The resistance function is independent of the diaphragm stiffness SD and intensity level IM, and therefore independent of the load function S. The resistance functions R for the sensitivity analysis are therefore the same as the resistance functions from the reliability analysis, given in Section 16-2.

17-2-3 Load function S

The Matlab function $lognfit$ was used to determine the maximum likelihood estimates of parameters for a lognormal distribution fitting the dataset. For the lower bound $(\mu - \sigma)$ and upper bound $(\mu + \sigma)$ stiffness, the distribution function is fitted to 15 data points obtained through NLTHA. The load function for the median stiffness (μ) is obtained from 61 data points. The load functions were derived for every load combination and each diaphragm stiffness configuration. The load functions S are given in Table 17-2 and 17-3 for the shear force and transfer force, respectively.

17-2-3-1 Evaluation of computed load function S

The shear force load functions S yield similar results for the upper and lower bound diaphragm stiffness. The shear force in the wall slightly reduces for increasing diaphragm stiffness. However, the mean and standard deviation are almost equal, which indicates that the diaphragm stiffness has little influence on the shear force in the shear wall.

The difference between the load functions for mean stiffness μ on one hand and the lower-bound and upper-bound stiffness on the other hand is attained by the difference

Direction	Walls	Lower-bound stiffness ($\mu - \sigma$)		Mean stiffness (μ)		Upper-bound stiffness ($\mu + \sigma$)	
		Median	$\sigma_{RTR,SD}$	Median	σ_{RTR}	Median	$\sigma_{RTR,SD}$
H1 direction	All walls	9672	0.234	9173	0.277	9521	0.234
	North wall	5442	0.251	5144	0.259	5297	0.270
	South wall	4961	0.228	4762	0.265	4716	0.220
H2 direction	All walls	10787	0.173	10872	0.231	10611	0.184
	East wall	5640	0.208	5832	0.201	5378	0.226
	West wall	6173	0.143	6073	0.199	6119	0.138

Table 17-2: Shear force load functions S for variation in Diaphragm stiffness

Direction	Walls	Lower-bound stiffness ($\mu - \sigma$)		Mean stiffness (μ)		Upper-bound stiffness ($\mu + \sigma$)	
		Median	σ_Y	Median	σ_{RTR}	Median	σ_Y
H1 direction	All walls	7860	0.289	9963	0.332	13872	0.238
	North wall	3200	0.244	4381	0.327	6123	0.196
	South wall	3265	0.292	4274	0.303	6315	0.248
H2 direction	All walls	7582	0.207	9867	0.213	13391	0.123
	East wall	5749	0.182	6066	0.176	7241	0.119
	West wall	5584	0.149	6084	0.166	7465	0.123

Table 17-3: Transfer force load functions S for variation in Diaphragm stiffness

in set of ground motions. A set of 61 ground motions was used to evaluate the mean stiffness, whereas a set of 10 ground motions was used to evaluate the effect of lower- and upper-bound diaphragm stiffness.

The load functions S for transfer force in H1 and H2 direction are affected by the diaphragm stiffness. The mean of the load functions increases significantly for an increasing diaphragm stiffness. In H1 direction, the transfer force almost doubles from the lower-bound to upper-bound case. A significant increase is also observed in H2 direction. A slight decrease in standard deviation is noted for increasing diaphragm stiffness, which may indicate a capping mechanism for increasing diaphragm stiffness.

It can be concluded from the load functions S in Table 17-2 and 17-3 that the diaphragm stiffness significantly influences the transfer force in the diaphragm but does not affect shear force in the shear wall just above the podium. It can also be noted that the shear force in the shear wall below the podium will change, as the transfer force is equal to the difference between the shear force just above and below the diaphragm.

17-2-4 Probability of demand exceeding capacity given IM and SD

The probability of demand exceeding capacity given an earthquake intensity level IM and diaphragm stiffness SD $P(\mathrm{D{>}C|IM,SD})$ was evaluated according to Level III structural reliability analysis, discussed in Section 16-4. Under the assumption that resistance function R and load function S are independent, the probability of failure is given by Equation 17-1, as derived in Section 16-4-1-1. The convolution integral is given in Equation 17-2.

$$P_{failure} = \int_{-\infty}^{\infty} F_R(\mathrm{S}) f_S(\mathrm{S}) \mathrm{d}S \tag{17-1}$$

$$P_{failure} = P(S > R) = \int_{-\infty}^{\infty} \left(1 - F_{\mathrm{S}}(R)\right) f_{\mathrm{R}}(R) \mathrm{d}R \tag{17-2}$$

The probability of failure $P_{failure}$ for the structural reliability analysis was defined as the probability of demand exceeding capacity given IM and SD $P(\mathrm{D{>}C|IM,SD})$. $P(\mathrm{D{>}C|IM,SD})$ was computed through numerical integration.

17-2-4-1 Computed probability of demand exceeding capacity given IM and SD

The probabilities of failure given IM and SD were computed for RP2475 and three diaphragm stiffness configurations SD, given in Table 17-4 and 17-5.

Direction	Walls	Stiffness diaphragm		
		$\mu - \sigma$	μ	$\mu + \sigma$
H1 direction	All walls	0.0005	0.0010	0.0004
	North wall	0.0029	0.0020	0.0034
	South wall	0.0006	0.0011	0.0002
H2 direction	All walls	0.0000	0.0000	0.0000
	East wall	0.0000	0.0000	0.0000
	West wall	0.0000	0.0001	0.0000

Table 17-4: Probability of failure $P(\mathrm{D{>}C|SD,IM{=}RP2475})$: Shear force

Direction	Walls	Stiffness diaphragm		
		$\mu - \sigma$	μ	$\mu + \sigma$
H1 direction	All walls	0.0001	0.0038	0.0115
	North wall	0.0000	0.0012	0.0013
	South wall	0.0000	0.0005	0.0060
H2 direction	All walls	0.0000	0.0012	0.0066
	East wall	0.0035	0.0056	0.0163
	West wall	0.0010	0.0047	0.0242

Table 17-5: Probability of failure P(D>C|SD,IM=RP2475): Transfer force

17-2-4-2 Evaluation of computed probability of demand exceeding capacity given IM and SD

The probability of demand exceeding capacity given IM and SD is calculated for three diaphragm stiffnesses, given in Table 17-1. The resistance function R is equal for all diaphragm stiffnesses. The load function S may vary for every SD.

In line with the conclusions for the load function S in Section 17-2-3, the probability of demand exceeding capacity given $IM = RP2475$ for shear force in the shear wall is not significantly affected by the diaphragm stiffness. Differences between the bounding stiffnesses and mean stiffness are attributed to the difference in sets of ground motions.

P(D>C|IM=RP2475,SD) increases for increasing SD, as the median transfer force of the load function S increases for increasing SD. The diaphragm stiffness has a large influence on P(D>C|IM=RP2475,SD). P(D>C|IM=RP2475,SD) is up to 100 times larger for the upper bound case compared to the lower bound case.

17-2-5 Joint probability of demand exceeding capacity given IM

The joint probability of demand exceeding capacity given IM and including the diaphragm stiffness variation, P(D>C|IM), was calculated by the weighted sum of the probabilities of demand exceeding capacity given IM and SD, given in Equation 17-3. P(D>C|SD,IM) was calculated with NLTHAs for three discrete diaphragm stiffnesses, as described in Section 17-2-4; the weight of each P(D>C|SD,IM) is given by the cumulative probability of occurrence of the diaphragm stiffness P(SD).

$$P(D > C|\text{IM}) \quad = \quad \sum_{j=1}^{m} P(D > C|\text{SD,IM}) \cdot P(\text{SD}) \tag{17-3}$$

17-2-5-1 Calculation of cumulative probability of occurrence P(SD)

The diaphragm stiffness was defined by three discrete values: the mean stiffness (μ), the lower-bound stiffness ($\mu - \sigma$), and the upper-bound stiffness ($\mu + \sigma$). The corresponding cumulative probabilities of occurrence of each stiffness are given in Figure 17-1 and Table 17-6.

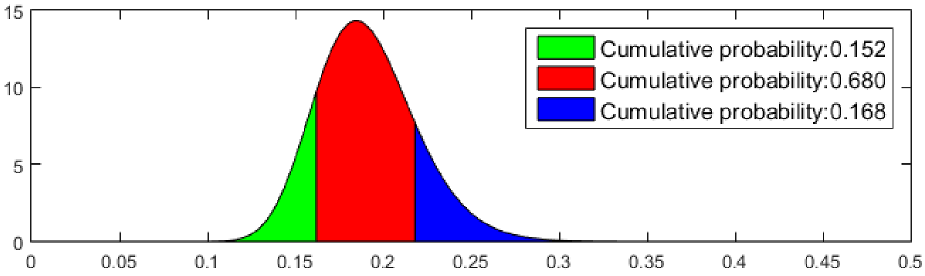

Figure 17-1: Distribution of lognormal distribution function with V=0.15

Stiffness diaphragm	P(SD)
$\mu - \sigma$	0.152
μ	0.680
$\mu + \sigma$	0.168

Table 17-6: Shear force load functions S for variation in Diaphragm stiffness

17-2-5-2 Joint load function S(IM=RP2475)

As the resistance function R is constant for all diaphragm stiffnesses, the joint probability of demand exceeding capacity P(D>C|IM) depends on variations of the load function S for varying SD. The joint load function S(IM=RP2475) is calculated by Equation 17-4.

$$S(IM) = \sum_{j=1}^{m} S(IM, SD) \cdot P(\mathrm{SD}) \tag{17-4}$$

The perimeter estimates of the joint load functions S(IM=RP2475) are given in Tables 17-7 and 17-8.

Evaluation joint load function S(IM=RP2475)

The joint load function S(IM=RP2475) for shear force demand does not change significantly when diaphragm stiffness variation is included; no significant decrease or increase

Direction	Walls	Joint load function, including SD		Load function, no SD	
		Median	$\sigma_{RTR,SD}$	Median	σ_{RTR}
H1 direction	All walls	9304	0.265	9173	0.277
	North wall	5219	0.255	5144	0.259
	South wall	4828	0.261	4762	0.265
H2 direction	All walls	10834	0.224	10872	0.231
	East wall	5781	0.207	5832	0.201
	West wall	6120	0.189	6073	0.199

Table 17-7: Joint load functions S: Shear force

Direction	Walls	Joint load function, including SD		Load function, no SD	
		Median	$\sigma_{RTR,SD}$	Median	σ_{RTR}
H1 direction	All walls	10688	0.355	9963	0.332
	North wall	4654	0.362	4381	0.327
	South wall	4587	0.351	4274	0.303
H2 direction	All walls	10635	0.265	9867	0.213
	East wall	6572	0.180	6066	0.176
	West wall	6572	0.188	6084	0.166

Table 17-8: Joint load functions S: Transfer force

is observed in the the median or standard deviation σ_Y of the load function. Therefore, only small differences in the joint probability of demand exceeding capacity P(D>C|IM) of the shear force are expected.

The joint load function S(IM=RP2475) for transfer force changes when diaphragm stiffness variation is included. The median of the load function increases, and the standard deviation $\sigma_{RTR,SD}$ also increases. Both the increase of the median and standard deviation are expected to increase the probability of demand exceeding capacity P(D>C|IM).

17-2-5-3 Computed probability of demand exceeding capacity given IM

The probabilities of demand exceeding capacity for $IM = RP2475$ computed with Equation 17-3 are given in Tables 17-9 and 17-10.

The load functions S for lower-bound, median, and upper bound diaphragm strength and the joint load function S_j and corresponding probabilities of demand exceeding capacity for $IM = RP2475$ for transfer force in East wall are given in Figure 17-2.

Direction	Walls	P(D>C|IM) including SD	P(D>C|IM) no SD
H1 direction	All walls	0.0009	0.0010
	North wall	0.0020	0.0020
	South wall	0.0014	0.0011
H2 direction	All walls	0.0000	0.0000
	East wall	0.0000	0.0000
	West wall	0.0000	0.0000

Table 17-9: Estimate P(D>C|IM) - Shear force direction

Direction	Walls	P(D>C|IM) including SD	P(D>C|IM) no SD
H1 direction	All walls	0.0051	0.0038
	North wall	0.0015	0.0012
	South wall	0.0015	0.0005
H2 direction	All walls	0.0025	0.0012
	East wall	0.0062	0.0056
	West wall	0.0109	0.0047

Table 17-10: Estimate P(D>C|IM) - Transfer force direction

17-2-5-4 Evaluation of computed probability of demand exceeding capacity given IM

For comparison, the probability of demand exceeding capacity was computed for $\beta_S = 0.18$ from JCSS [JCSS, 2000], and with $\beta_R = \beta_{RTR}$ for P(D>C|IM) no SD, and with $\beta_R = \beta_{RTR,SD}$ for P(D>C|IM) including SD. Therefore, much lower values are found compared to the structural reliability analysis, which includes modelling uncertainty β_{MDL}. Therefore, it can be concluded that the increased variability from including SD does not exceed the modelling uncertainty, and $\beta_{MDL} = 0.20$ is still valid for structural reliability analysis.

From Table 17-9 it can be concluded that the probability of demand exceeding capacity given $IM = RP2475$ for shear force is not affected by including diaphragm stiffness variation.

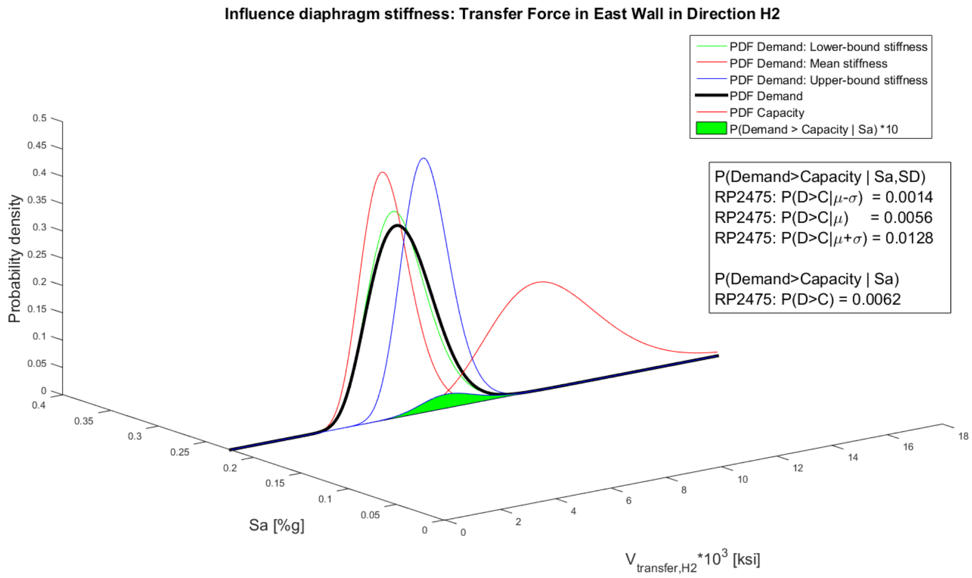

Figure 17-2: Individual load functions for diaphragm stiffness configurations and joint load function S for Transfer force in H2 direction in East wall

From Table 17-10, it can be found that the probability of demand exceeding capacity given $IM = RP2475$ increases by including diaphragm stiffness variation. As noted in Section 17-2-5-2, the median and standard deviation of the joint transfer load function increase when diaphragm stiffness variation is taken into account, and the increase in computed probability of demand exceeding capacity given $IM = RP2475$ was therefore expected.

17-3 Sensitivity analysis: Basement wall stiffness

17-3-1 Stiffness variation

The force demand in the shear wall and distributors was evaluated for three basement wall stiffness configurations. The force demand for the median basement wall stiffness was evaluated as part of the reliability analysis. The force demand was evaluated for the lower-bound basement wall stiffness, i.e. median stiffness minus one standard deviation, and upper-bound basement wall stiffness, i.e. median stiffness plus one standard deviation. Three ground motions from $IM = RP2475$ were selected that yielded median transfer force demand in H1 and H2 direction for the median basement wall stiffness configuration.

The lower-bound, median, and upper-bound basement wall stiffness configurations are given in Table 17-11.

	Lower bound stiffness	Median stiffness	Upper bound stiffness
Basement walls	$0.50E_cI_g$; $0.50G_cA_g$	$0.80E_cI_g$; $0.80G_cA_g$	$1.00E_cI_g$; $1.00G_cA_g$

Table 17-11: Stiffness assumptions for basement walls - CONTROLEREN

17-3-2 Evaluation of influence stiffness variation

As three ground motions are evaluated, only the mean of these three ground motions is compared for the three basement wall configurations.

The difference between the mean of the lower-bound and upper-bound configuration is approximately 1%, for both the shear force in the shear wall and the transfer force in the diaphragm. For most cases, a small increase was measured for increasing basement wall stiffness. It is concluded that the stiffness of the basement wall has no significant influence on the shear force and transfer force.

It can be noted that only three ground motions are evaluated. Although it is believed that these ground motions are a strong indicator of the limited influence of the basement wall stiffness on the shear force in the wall and transfer force in the diaphragm, more ground motions need to be evaluated to verify this assumption.

Direction	Walls	Stiffness basement wall					
		$\mu - \sigma$		μ		$\mu + \sigma$	
H1 direction	All walls	9833	[kips]	9895	[kips]	9920	[kips]
	North wall	4663	[kips]	4699	[kips]	4663	[kips]
	South wall	5161	[kips]	5189	[kips]	5218	[kips]
H2 direction	All walls	12183	[kips]	12210	[kips]	12193	[kips]
	East wall	6430	[kips]	6403	[kips]	6390	[kips]
	West wall	6086	[kips]	6115	[kips]	6095	[kips]

Table 17-12: Probability of failure P(D>C|SD,IM=RP2475): Shear force

Direction	Walls	Stiffness basement wall					
		$\mu - \sigma$		μ		$\mu + \sigma$	
H1 direction	All walls	10185	[kips]	10308	[kips]	10321	[kips]
	North wall	4507	[kips]	4510	[kips]	4557	[kips]
	South wall	4150	[kips]	4205	[kips]	4226	[kips]
H2 direction	All walls	10083	[kips]	10146	[kips]	10134	[kips]
	East wall	6622	[kips]	6706	[kips]	6699	[kips]
	West wall	5618	[kips]	5560	[kips]	5560	[kips]

Table 17-13: Probability of failure P(D>C|SD,IM=RP2475): Transfer force

Chapter 18

Evaluation of structural reliability analysis

The results from the structural reliability analysis in Chapter 16 will be evaluated in this chapter. The reliability of the shear capacity of shear walls is evaluated in Section 18-1. The reliability of distributors in transfer diaphragms is evaluated in Section 18-2.

18-1 Reliability of shear capacity of shear walls

The reliability of shear walls as designed for the archetype structure and reliability of shear capacity design according to LATBSDC and PEER/TBI will be compared to the acceptance criteria. As discussed in Section 16-1-1, shear capacity of shear walls is considered a key element, and must therefore satisfy the acceptance levels specified for critical elements. The acceptance criteria for critical elements were set at a probability of collapse less than 10% given MCE shaking and less than 1% in 50 years.

First, some notes on structural reliability analysis for shear walls loaded in shear are given in Section 18-1-1. Subsequently, the reliability of the shear walls in the archetype structure is evaluated in Section 18-1-2. Then, the reliability of shear walls designed according to LATBSDC and PEER/TBI will be computed in Section 18-1-3. Finally, the reliability of shear walls designed according to different design metholodogies will be compared in Section 18-1-4.

18-1-1 Notes on structural reliability analysis of shear walls in shear

For comparison of the results from the structural reliability analysis to the acceptance criteria for probability of collapse collapse, it has been assumed that collapse always occurs when the shear force demand exceeds the capacity, i.e. P(Collapse|D>C)=1. However, the probability is most likely not equal to 1. The reliability of the shear capacity of the shear wall increases when the probability of collapse given demand exceeding capacity P(Collapse|D>C) becomes less than 1. Comparison of the probability of demand exceeding capacity to the acceptance criteria assuming P(Collapse|D>C)=1 is therefore an upper-bound, conservative estimate.

18-1-2 Reliability of shear walls archetype structure

The probability of demand exceeding capacity in 50 years and given MCE shaking for the archetype structure was computed in Section 16. The results are given in Table 18-1. The probability of demand exceeding capacity given MCE is largest in the west wall in H2 direction. The probability of demand exceeding capacity in 50 years is largest in the east wall in H2 direction. The shear walls in the archetype structure, designed according to PEER/TBI design procedure and assuming $\theta_R = V_e = 1.35V_{ne}$, $\beta_R = 0.30$ and $\beta_{RTR} = \hat{\beta}_{RP2475}$, $\beta_{MDL} = 0.20$, $\beta_S = \sqrt{\beta_{RTR}^2 + \beta_{MDL}^2}$ and $\theta_S = \hat{\theta}_{CS}$, meet the acceptance criteria.

Given the analysis assumptions, the shear wall design of the archetype structure seems conservative. The maximum ratio between P(D>C|MCE) and P(C|MCE, acceptance) is 0.06, the maximum ratio between P(D>C in 50 years) and P(C in 50 years, acceptance) is 0.17. The influence of the analysis assumptions will be discussed in Chapter 19.

Direction	Walls	Acceptance criteria	
		P(D>C|MCE)	P(D>C in 50 years)
H1 direction	All walls	0.179%	0.060%
	North wall	0.324%	0.102%
	South wall	0.202%	0.087%
H2 direction	All walls	0.405%	0.130%
	East wall	0.501%	0.170%
	West wall	0.659%	0.168%

Table 18-1: Reliability shear walls archetype structure

18-1-3 Reliability of shear walls designed according to LATBSDC and PEER/TBI

An overview of the expected shear capacity of the archetype structure, and the required expected shear capacity per LATBSDC and PEER/TBI was given in Table 15-7. To calculate the required shear capacity per LATBSDC and PEER/TBI, the force demand was calculated using a suite of 7 ground motions selected and scaled to match the UHS. The ratio between the calculated force demand and required capacity is denoted β_{eff}. LATBSDC requires β_{eff}=1.50, whereas PEER/TBI is more conservative for shear capacity design of shear walls and requires β_{eff}=2.00. Therefore, LATBSDC design requires a smaller shear capacity than design according to PEER/TBI.

The design methodologies were schematized in Figure 15-1. The median of the resistance function R of the archetype structure, PEER/TBI and LATBSDC varies. Lognormal distribution and $\beta_R = 0.30$ have been assumed for the resistance function. Furthermore, load function S was assumed independent of the design approach.

18-1-3-1 Probability of demand exceeding capacity for various design methodologies

The probability of demand exceeding capacity given MCE and in 50 years for the PEER/TBI and LATBSDC design methodology were computed. The results are given in Tables 18-2 and 18-3. The shear walls designed according to PEER/TBI and LATBSDC meet the acceptance criteria for probability of collapse given MCE and probability of collapse in 50 years.

PEER/TBI design gave the smallest probabilities of demand exceeding capacity. In H2 direction, the probability of demand exceeding capacity was smaller than the probability of demand exceeding capacity of the archetype structure. The reliability analysis for PEER/TBI gave maximum a P(D>C|MCE)=0.531% for the west wall in H2 direction, and maximum P(D>C in 50 years)=0.155% for the north wall in H1 direction.

From Table 18-2 and 18-3 follows that LATBSDC design gives the largest probability of shear demand exceeding shear capacity. Furthermore, the probability of demand exceeding capacity was larger than the probability of demand exceeding capacity of the archetype structure. The reliability analysis for LATBSDC gave a maximum P(D>C|MCE)=3.241% for east wall in H2 direction, and maximum P(D>C in 50 years)=0.728% for west wall in H2 direction. Although the probabilities of demand exceeding capacity are larger for LATBSDC design and $\beta_{eff} = 1.50$, the results still meet the acceptance criteria.

18-1-4 Comparison reliability for different design approaches

The reliability of the archetype structure, PEER/TBI design procedure and LATBSDC design procedure are compared in Table 18-4. Furthermore, the ratio between the calculated force demand from 7 ground motion pairs scaled to UHS and the capacity

Direction	Walls	P(D>C|MCE) for shear force		
		Archetype	PEER/TBI	LATBSDC
H1 direction	All walls	0.179%	0.296%	1.732%
	North wall	0.324%	0.527%	2.868%
	South wall	0.202%	0.336%	1.974%
H2 direction	All walls	0.405%	0.326%	2.063%
	East wall	0.501%	0.402%	2.600%
	West wall	0.659%	0.531%	3.241%

Table 18-2: P(D>C|MCE) for shear capacity of shear walls for various design methodologies

Direction	Walls	P(D>C in 50 years) for shear force		
		Archetype	PEER/TBI	LATBSDC
H1 direction	All walls	0.060%	0.093%	0.440%
	North wall	0.102%	0.155%	0.679%
	South wall	0.087%	0.130%	0.551%
H2 direction	All walls	0.130%	0.108%	0.533%
	East wall	0.170%	0.142%	0.673%
	West wall	0.168%	0.138%	0.728%

Table 18-3: P(D>C in 50 years) for shear capacity of shear walls for various design methodologies

β_{eff} is given in Table 18-4. It was found that the reliability of the shear walls loaded in shear increases for an increasing ratio β_{eff}. Moreover, it can be concluded that shear wall design according to LATBSDC with $\beta_{eff} = 1.50$ meets the acceptance criteria for structural reliability.

Direction	Walls	β_{eff}	Max P(D>C|MCE)	Max P(D>C in 50 years)
H1 direction	Archetype	2.15	0.324%	0.102%
	PEER/TBI	2.00	0.527%	0.155%
	LATBSDC	1.50	2.868%	0.679%
H2 direction	Archetype	1.94	0.659%	0.170%
	PEER/TBI	2.00	0.531%	0.142%
	LATBSDC	1.50	3.241%	0.728%

Table 18-4: Reliability of different design methodology

18-2 Reliability of distributors in transfer diaphragms

The reliability of the distributors in transfer diaphragms in the archetype structure, designed according to PEER/TBI and ASCE 7-10, will be compared to the acceptance criteria. As discussed in Section 16-1-1, the distributors are considered ordinary elements, for which failure could results in endangerment of individual lives. Failure of the distributors does most likely not result in failure of the structure, as the loads could be redistributed to other transfer diaphragms or resisted by the overturning moment in the foundation. The acceptance criteria for ordinary elements were set at a probability of collapse less than 25% given MCE shaking and less than 2.5% in 50 years.

First, notes on the structural reliability results for distributors will be given in Section 18-2-1. Secondly, the reliability of the distributors designed according to PEER/TBI and ASCE 7-10 will ne evaluated in Section 18-2-2. The reliability of the distributors designed according to the different methodologies will be compared in Section 18-2-3.

18-2-1 Notes on structural reliability analysis of distributors in transfer diaphragms

This section provides notes on the structural reliability analysis of distributors in transfer diaphragms. The ratio between test results and nominal expected capacity, nonlinear behaviour of diaphragms and the influence of other load-transferring mechanisms will be discussed.

18-2-1-1 Test results versus nominal expected transfer capacity

The median of the resistance function R was calculated assuming that the ratio between the median test strength, the expected strength, and nominal expected strength from ACI 318-11 is equal to 1.00. This is a conservative estimate. No test results were available to determine whether the ratio $V_{test}/V_{n,ACI}$ is larger than 1.00. In construction, Type II couplers are common to connect shear friction reinforcement to the shear walls. These couplers guarantee shear capacity up to $1.25f_y$, whereas the expected steel strength is equal to $1.17f_y$. Consequently, it is not expected that the ratio $V_{test}/V_{n,ACI}$ is much larger than 1.00. Therefore, a more accurate prediction of ratio $V_e/V_{n,e}$ is not expected to significantly increase the calculated reliability of the distributors.

18-2-1-2 Nonlinear behaviour of distributors

Perform 3D only has elastic shell elements. Subsequently, elastic stress-strain behaviour was assumed. The diaphragms were modelled with elastic shell elements with modified stiffness properties. However, it is expected that the diaphragm, collectors and shear friction reinforcement have some yielding capacity. Yielding of the distributors will result in redistribution of the forces to below-grade diaphragms and the tower foundation. Therefore, it is expected that allowance of nonlinear capacity of distributors will cap the maximum forces, reduce the record-to-record variability β_S for the load function S and hence increase the reliability of the distributors.

18-2-1-3 Other load-transferring mechanisms

To calculate the probability of demand exceeding capacity of the distributors, the conservative assumption was made that the full transfer load is transferred by the distributors. However, several other load-transferring mechanisms, for example gravity columns, can transfer load from the tower into the diaphragm. These load-transferring mechanisms will reduce the demand in the distributors, decrease the median θ_S of the load function S, and therefore increase the reliability of the distributors. Other load-transferring mechanisms will be briefly discussed in the following paragraphs.

Gravity columns

In preliminary models, it was found that gravity columns with rigid connections, in combination with rigid diaphragms, can provide a stiff load path transferring from the shear wall through the podium diaphragm to the basement walls. The gravity columns with rigid moment connections accounted for approximately 10-15% of the total load transfer. In the probabilistic model, the gravity columns were assumed to have pinned connections. The gravity columns were therefore unable to transfer load to the diaphragm.

In the actual structure, load transfer through gravity columns will be expected, although to a lesser degree than observed in the preliminary model. Load transfer through gravity columns reduces the force demand in the diaphragms and thus increases the reliability of the distributors.

Dual system

Code design requires structures over 160 feet to have a dual horizontal-load-resisting system. The second system must be capable of resisting at least 25% of the design seismic forces. The second system, e.g. a concrete moment-frame, would also transfer load into the diaphragm. Therefore, the force demand in the distributors is further reduced and the reliability of the distributors increases.

Out-of-plane shear stiffness

If it is assumed that the walls are also capable to transfer force out-of-plane, the probability of failure in H1-direction is further reduced. Especially thick walls will have some out-of-plane shear stiffness. Governing transfer demand was found for all walls in H1-direction due to out-of-plane shear demand in the E-W walls. Using the out-of-plane transfer capacity of thick walls when calculating the transfer demand in the distributors will therefore reduce the distributor demand and consequently increase the reliability of the distributors.

18-2-2 Reliability of distributors designed according to ASCE 7-10 and PEER/TBI

The reliability of the distributors of the archetype structure, designed according to PEER/TBI, is compared to the reliability of distributors designed by Code (ASCE 7-10). The median θ_R of the resistance function R varies for ASCE 7-10 and PEER/TBI design. Other assumptions for structural reliability analysis of analysis, $\theta_R = V_e = 1.00V_{ne}$, $\beta_R = 0.37$ and $\beta_{RTR} = \hat{\beta}_{RP2475}$, $\beta_{MDL} = 0.20$, $\beta_S = \sqrt{\beta^2_{RTR} + \beta^2_{MDL}}$ and $\theta_S = \hat{\theta}_{CS}$, have been assumed constant for different design methodologies, as the diaphragm stiffness and thickness of the archetype structure were independent of the design methodology.

The expected distributor capacities for ASCE 7-10 and PEER/TBI design were given in Table 14-11. The required capacity of the distributors was determined given the diaphragm thickness of the archetype structure. The required distributor capacity for the Code design was calculated using MRSA, seismic performance factors $R = 6$, $I_e = 1.0$ and $\Omega_o = 2.5$, and strength reduction factor ϕ=0.60. The upper-bound force demand was taken to design the distributors for Code design, equal to the maximum shear force in the basement walls. The required PEER/TBI distributor capacity was calculated by multiplying $\beta_{eff} = 1.50$ with the mean of a suite of seven ground motions selected and scaled to UHS. As discussed in Section 14-4-3, the upper-bound strength of Code-designed distributors is approximately 55% of the required PEER/TBI transfer capacity. The design procedures are schematized in Figure 14-2.

The probability of demand exceeding capacity given MCE and in 50 years are given Tables 18-2 and 18-3, respectively. PEER/TBI design meets the acceptance criteria. However, ASCE 7-10 design fails to meet the acceptance criteria.

PEER/TBI gave the acceptable probabilities of demand exceeding capacity. The largest probability of demand exceeding capacity given MCE for PEER/TBI design was found in the east distributor P(D>C|MCE)=7.866%, the largest probability in 50 years P(D>C in 50 years)=1.858% was found in the west distributor in H2 direction.

The reliability of the upper-bound Code-designed distributors is insufficient. The probability of demand exceeding capacity given MCE, given in Table 18-5, is larger than 25% for 4-out-of-6 cases, the probability of demand exceeding capacity in 50 years, given in Table 18-6, is larger than 2.5% for all cases. The large probabilities of demand exceeding capacity show that the Code design procedure, using MRSA, seismic performance factors, including the overstrength factor Ω_o, and strength reduction factors, is unable to adequately predict the transfer force demand. Therefore, the current Code procedure is unsuitable to design distributors in transfer diaphragms.

Direction	Walls	P(D>C|MCE) for transfer force	
		PEER/TBI	ASCE 7-10 (upper-bound)
H1 direction	All walls	2.839%	31.588%
	North wall	1.555%	23.669%
	South wall	1.171%	21.591%
H2 direction	All walls	3.445%	37.289%
	East wall	7.866%	55.546%
	West wall	7.769%	55.852%

Table 18-5: P(D>C|MCE) for distributors in transfer diaphragms for PEER/TBI and ASCE 7-10

Direction	Walls	P(D>C in 50 years) for transfer force	
		PEER/TBI	ASCE 7-10 (upper-bound)
H1 direction	All walls	0.644%	7.547%
	North wall	0.361%	5.678%
	South wall	0.287%	5.048%
H2 direction	All walls	0.894%	8.460%
	East wall	1.858%	12.758%
	West wall	1.806%	14.074%

Table 18-6: P(D>C in 50 years) for distributors in transfer diaphragms for PEER/TBI and ASCE 7-10

18-2-3 Comparison reliability for different design approaches

The reliability of the distributors in the archetype structure, designed according to PEER/TBI and ASCE 7-10 design procedures, was computed in Section 18-2-2. It was concluded that distributors designed according to ASCE 7-10 have unacceptable probabilities of failure. Therefore, it is concluded that the current ASCE 7-10 design procedure is unfit to design distributors in transfer diaphragms. Hence, design of distributors according to ASCE 7-10 should be discouraged. More research is required to establish adequate guidelines to design diaphragms according to the ASCE 7-10.

Distributors designed according to PEER/TBI meet the acceptance criteria for structural reliability. Therefore, it is recommended to establish the alternative PEER/TBI and LATBSDC design procedures as the recommended method to design distributors and transfer diaphragms.

18-3 Influence of nonlinear stress-strain behaviour on β_{RTR}

In Section 16-3-3, smaller record-to-record variability was observed for higher intensity level earthquakes. The larger record-to-record variability for lower intensity earthquakes resulted in larger probabilities of shear failure for higher intensity earthquakes, although the mean shear force was larger for the higher intensity earthquakes.

This section will investigate whether nonlinear behaviour of the structure reduces the record-to-record variability for increasing ground motion intensities. The model captures yielding of the coupling beams, yielding of the wall reinforcement, concrete strength degradation and shear cracking. In Section 18-3-1, it will be investigated whether nonlinear shear stress-strain behaviour results in more closely spaced extreme force demands. Other nonlinear behaviour of the structure will be discussed in Section 18-3-2. In Section 18-3-3, it will be concluded whether it is reasonable to assume that nonlinear behaviour of the structure reduces the record-to-record variability for higher earthquakes intensities.

18-3-1 Nonlinear shear stress-strain behaviour

First, it has been investigated whether nonlinear modelling of shear stress-strain behaviour affects the variance of maximum forces. The shear stress-strain behaviour was modelled with a trilinear material relationship, defined by the cracking strength $V_{cr,exp}$. ultimate shear strength $V_{cu,exp}$, pre-crack stiffness G_c, post-crack stiffness $G_{c,y}$, and ultimate shear strain γ_c. When the shear force exceeds the cracking strength $V_{cr,exp}$, the tangent shear stiffness $G_{c,y}$ decreases to 10% of the uncracked shear stiffness G_c. Therefore, the post-cracked deformation needs to be ten times larger than the pre-cracked shear deformation to achieve the same shear force increase. Therefore, the shear force would increase less rapidly for increasing shear deformations.

If shear is governing, it would be expected that the shear force reaches $V_{cr,exp}$ more often for larger S_a, resulting in more closely spaced extreme values of the shear force. Figure 18-1 shows that the expected cracking strength is not exceeded for all but one ground motion for the highest $IM = RP9950$. Therefore, it is concluded that the nonlinear shear behaviour does not cause the reduced β_{RTR} for larger S_a.

18-3-2 Other nonlinear behaviour

Subsequently, it has been investigated whether other nonlinear behaviour caps the maximum shear force in the shear wall and transfer force in the diaphragm. To investigate the development of maximum bending moments, shear forces, interstory drift ratios and

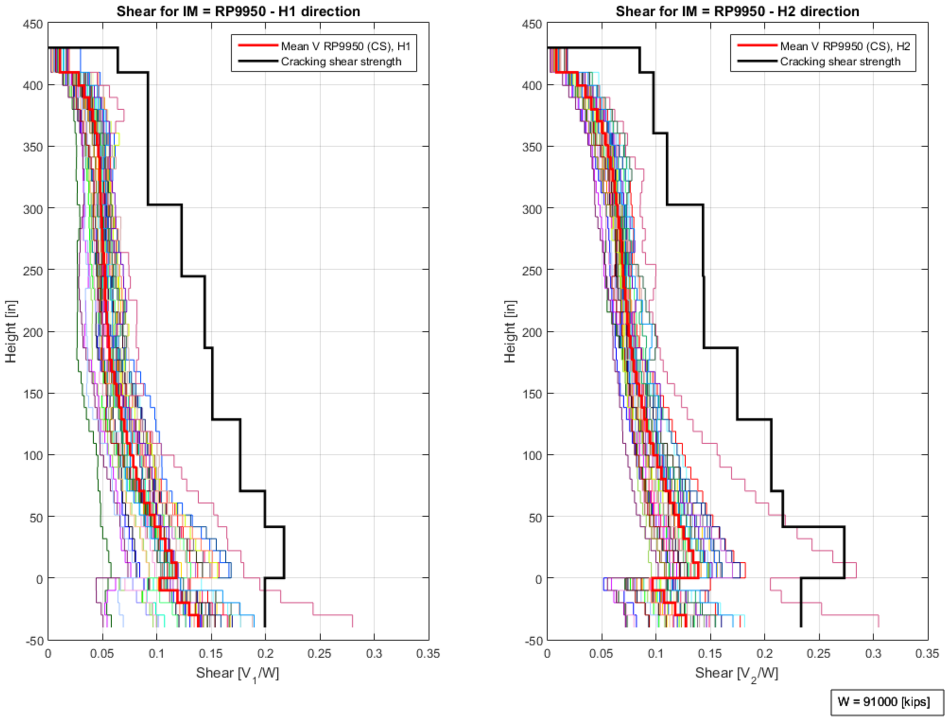

Figure 18-1: Shear force versus expected cracking strength $V_{cr,exp}$ for $IM = RP9950$

transfer forces saturate for increasing S_a, these actions were evaluated at three levels in the structure, at level 1, level 14, and level 31. The demands were normalized to the demand at the lowest intensity level $S_a = 0.1625$ [%g]. The results are given in Figures 18-2, 18-3, and 18-4.

Figures 18-2, 18-3, and 18-4 show saturation of the mean bending moment. For direction H1, the increase in bending moment is relatively small for increasing S_a, in the range of 10%-30% for an increase of IDR up to 70%. For H2 direction, the increase in bending moment is larger, but saturation of the bending moment is observed for all considered levels, and the largest saturation is observed at level 1. It is concluded that nonlinear behaviour is largest in H1 direction.

Rad and Adebar [Rad and Adebar, 2009] showed that flexural yielding over the height of the shear wall has a significant influence on capping of the corresponding shear force envelopes. The relative shear force reduction is larger for increasing flexural yielding. Nonlinear behaviour is largest in H1 direction. Therefore, the largest decrease in record-to-record variability β_{RTR} was observed in H1 direction. Hence, it was concluded that the reduction of the RTR variability for increasing S_a is caused by nonlinear behaviour of the structure.

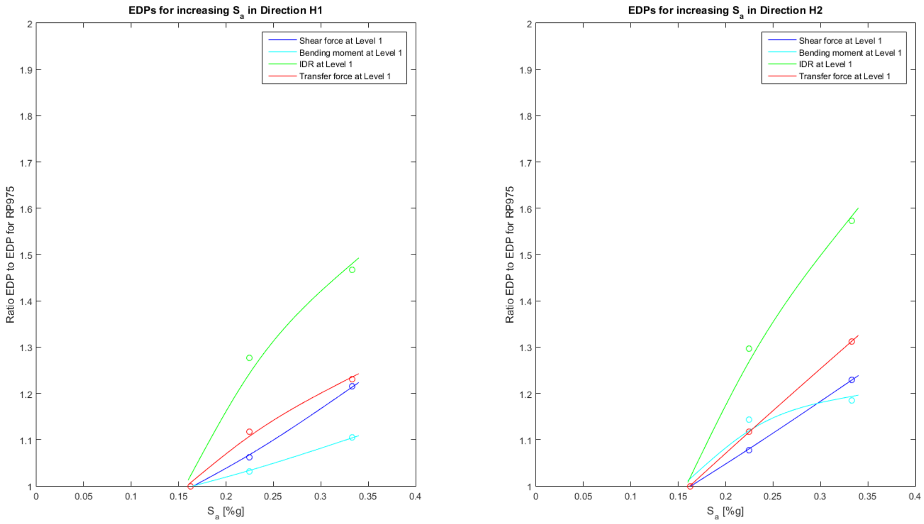

Figure 18-2: Transfer force capacity; East wall for $S_a = 0.2243$ [%g]

18-3-3 Conclusion effect nonlinear behaviour of β_{RTR}

From the previous section, it can be concluded that it is reasonable to assume that nonlinear behaviour reduces the record-to-record variability. Nonlinear behaviour was observed in the structure at all evaluated levels, and nonlinear behaviour of the structure saturated force demand. Therefore, more closely spaced extreme force demands were observed for increased nonlinear behaviour. More nonlinear behaviour of the structure was observed for higher intensity level earthquakes. Therefore, smaller record-to-record variability was observed for higher intensity level earthquakes than for lower intensity level earthquakes.

Furthermore, it is noted that allowance of nonlinear stress-strain behaviour increases the reliability of the structure. Moreover, disregard of nonlinear stress-strain behaviour and capping of maximum shear forces in the analysis model may result in overestimation of the probability of demand exceeding capacity.

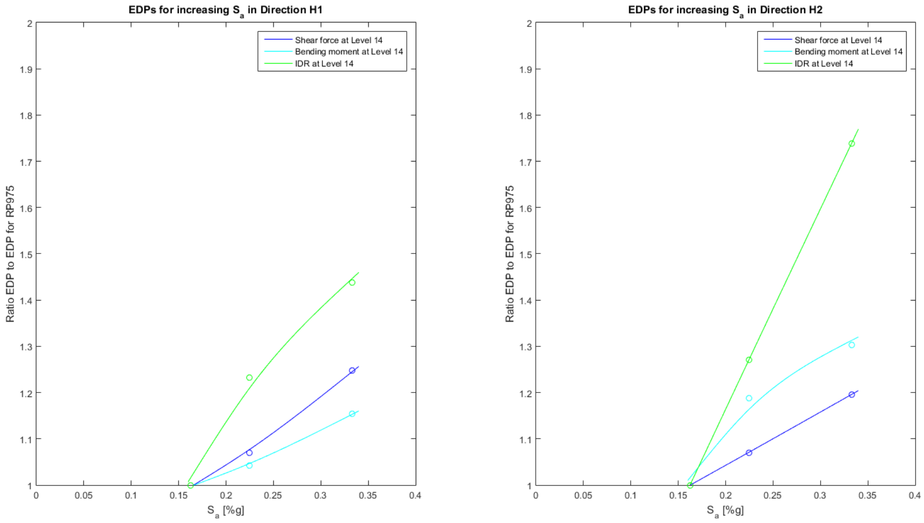

Figure 18-3: Transfer force capacity; East wall for $S_a = 0.2243$ [%g]

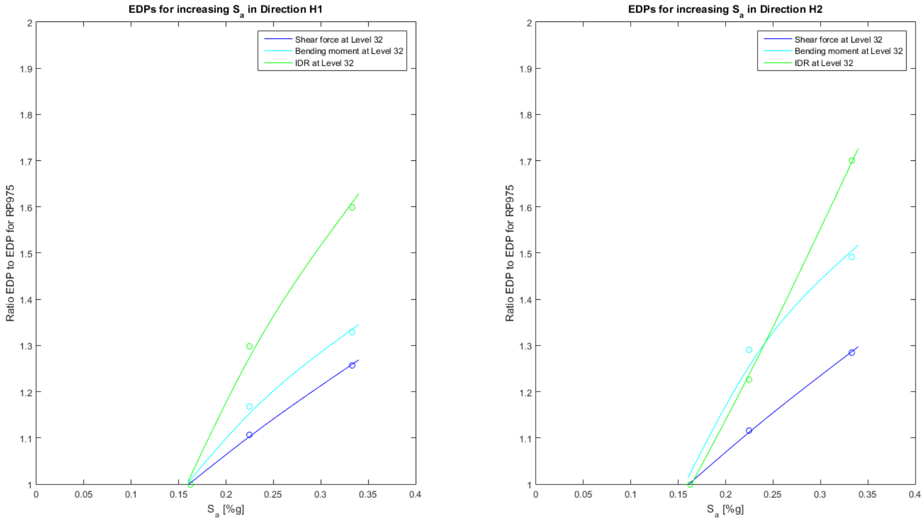

Figure 18-4: Transfer force capacity; East wall for $S_a = 0.2243$ [%g]

Chapter 19

Evaluation of reliability analysis assumptions

In Chapters 16 and 18, the reliability of shear in shear walls and distributors in transfer diaphragms was calculated. To compute the reliability, a limit state function Z was computed with the load function S and resistance function R. Assumptions were made to define the median θ_S and standard deviation β_S of the load function S, and median θ_R and standard deviation β_R of the resistance function R. The influence of the assumptions for the reliability analysis will be evaluated in this chapter.

First, the selected parameter estimates for the structural reliability analysis in Chapter 16 and 18 will be briefly discussed in Section 19-1. In Section 19-2, various cases will be defined to evaluate the assumptions for load function S and resistance function R. In Section 19-3, the probability of demand exceeding capacity for the different cases is evaluated. Finally, the probability of demand exceeding capacity given MCE and in 50 years will be evaluated for the various load function S and resistance function R assumptions in Section 19-4.

19-1 Parameter estimates for reliability analysis

Assumptions for the load function S and resistance function R were described in Chapter 16 to calculate the reliability of the shear walls in shear and distributors in transfer diaphragms. The assumptions for the reliability analysis will be briefly discussed in Sections 19-1-1 and 19-1-2.

19-1-1 Assumptions for reliability analysis of shear walls in shear

The mean demand θ_S for each intensity level was calculated from the shear demand found from NLTHA in Perform 3D. The standard deviation of the load function β_S was calculated by combining the record-to-record variability found from the NLTHA for 2% in 50 years and modelling uncertainty according to ASCE 7-16.

The mean resistance θ_R is equal to the nominal expected strength calculated according to ACI 318-11, using expected material properties, multiplied by a factor $Ve/V_{n,e} = 1.35$ which accounts for the difference between nominal expected capacity and expected capacity, validated by test results. The standard deviation of the resistance function was taken equal to $\beta_R = 0.30$ [Wallace et al., 2013]. Case 3 in Section 19-2 is the reference case for the reliability analysis of shear walls in shear.

19-1-2 Assumptions for reliability analysis of distributors in transfer diaphragms

The parameter estimates θ_S and β_S for the load function were calculated in the same way as the parameter estimates for the load function S for shear force. The median of resistance function θ_R was taken equal to the nominal expected strength calculated according to ACI 318-11 with expected material properties. The standard deviation was taken equal to the demand uncertainty recommended by ASCE 7-16, $\beta_R = 0.37$. Case 4 in Section 19-2 is the reference case for the reliability analysis of distributors in transfer diaphragms.

19-2 Cases to evaluate reliability analysis assumptions

Various cases have been defined to evaluate the influence of assumptions for θ_S, β_S, θ_R, and β_R. The values for β_S and β_R were taken from literature [JCSS, 2000]; [Wallace et al., 2013]; and [ASCE 7-16, 2014].

In Case 1, the capacity uncertainty for concrete in shear $\beta_R = 0.18$ from JCSS [JCSS, 2000] was adopted as a lower-bound value. To evaluate the influence of θ_R, it was assumed that $V_{n,e}/V_e = 1.00$ for shear force in Case 2. Cases 3 and 4 are the initial cases for structural reliability analysis. Case 4 uses the upper-bound value for capacity uncertainty $\beta_R = 0.37$ from ASCE 7-16 [ASCE 7-16, 2014]. The mean transfer demand $\theta_S = 0.80\bar{V}_{CS}$ for lower-bound diaphragm stiffness was assumed in Case 5, to evaluate the reliability of the distributors for reduced diaphragm stiffness and force demand. The demand uncertainty recommendations from ASCE 7-16 for well-defined mechanism (β_S=0.29) and general mechanism ($\beta_S = 0.46$) were adopted in Cases 6 and 7 to evaluate the influence of assumptions for standard deviations β_S.

	Load function S	**Resistance function R**
Case 1 (JCSS Capacity)	$\theta_S = \bar{V}_{CS}$ (Mean θ_S of load function from NLTHA results)	$\theta_R = (1.35/1.00)\ V_{ne}$ (Expected shear capacity is $1.35 V_{ne}$, expected transfer capacity is $1.00 V_{ne}$)
	$\beta_S = \sqrt{\beta_{RTR}^2 + \beta_{MDL,ASCE}^2}$ (Modelling uncertainty according to ASCE 7-16 $\beta_{MDL,ASCE}$=0.20)	$\beta_R = 0.18$ (Capacity uncertainty in shear (JCSS))
Case 2 ($V_{test}/V_{ne} = 1$)	$\theta_S = \bar{V}_{CS}$	$\theta_R = (1.00/1.00)\ V_{ne}$
	$\beta_S = \sqrt{\beta_{RTR}^2 + \beta_{MDL,ASCE}^2}$	$\beta_R = 0.30$
Case 3 - shear only [Wallace et al, 2013]	$\theta_S = \bar{V}_{CS}$	$\theta_R = 1.35\ V_{ne}$; From 37 test on walls, for $f'_{ce} = 1.3 f'_c$; $f_{ye} = 1.17\ f_y$
	$\beta_S = \sqrt{\beta_{RTR}^2 + \beta_{MDL,ASCE}^2}$	$\beta_R = 0.30$; The dispersion value of 0.20 is relatively low for brittle failure modes of reinforced concrete; therefore, for this preliminary study, dispersion values are assumed to be 0.30
Case 4 (ASCE 7-16 Capacity)	$\theta_S = \bar{V}_{CS}$	$\theta_R = (1.35/1.00)\ V_{ne}$
	$\beta_S = \sqrt{\beta_{RTR}^2 + \beta_{MDL,ASCE}^2}$	$\beta_R = 0.37$ (Capacity uncertainty (ASCE 7-16))
Case 5 - transfer only (Reduced diaphragm stiffness)	$\theta_S = 0.80\ \bar{V}_{CS}$ (Mean transfer demand for lower-bound diaphragm stiffness was assumed for distributors and diaphragms designed according to ASCE 7-10)	$\theta_R = 1.00\ V_{ne}$
	$\beta_S = \sqrt{\beta_{RTR}^2 + \beta_{MDL,ASCE}^2}$	$\beta_R = 0.37$ (Capacity uncertainty (ASCE 7-16))
Case 6 (ASCE 7-16 - Well-defined)	$\theta_S = \bar{V}_{CS}$	$\theta_R = (1.35/1.00)\ V_{ne}$
	$\beta_S = 0.29$ (Demand uncertainty for well-defined mechanism (ASCE 7-16))	$\beta_R = 0.37$
Case 7 (ASCE 7-16 - General)	$\theta_S = \bar{V}_{CS}$	$\theta_R = (1.35/1.00)\ V_{ne}$
	$\beta_S = 0.46$ (Demand uncertainty for general mechanism (ASCE 7-16))	$\beta_R = 0.37$

Table 19-1: Cases to investigate the effect of load function and resistance function parameter estimates

19-3 Influence of parameter estimates

The influence of assumptions for median θ_S and standard deviation β_S of the load function S and median θ_R and standard deviation β_R of the resistance function R will be evaluated based on the cases defined in Section 19-2.

The influence of assumptions for β_S will be evaluated through comparison of Cases 4, 6, and 7. The affect of variation in β_R will be evaluated through comparison of Cases 1, 3, and 4. Furthermore, Cases 2 and 3 will be compared to investigate the influence of the mean of the resistance function θ_R. The influence of mean of the load function θ_S will be investigated by comparing Cases 4 and 5.

19-3-1 Median θ_S of load function S

The median of the load function was determined through NLTHA in Perform 3D. The ground motions were selected and scaled to match the Conditional Spectrum, with the target spectral acceleration at T_1=4.90 [sec]. Each time history analysis gives a maximum base shear force, maximum transfer force, and so forth. The maxima from the sets of ground motions were used to calculate the median of the load function S.

The sensitivity analysis showed that variation in the diaphragm stiffness or basement wall stiffness does not affect the mean shear demand in the shear walls. However, decreasing diaphragm stiffness reduces the transfer force demand in the distributors. It was found that the transfer force demand for the lower-bound diaphragm stiffness is approximately 80% of the transfer force demand for median diaphragm stiffness.

The influence of the median θ_S of load function S on the structural reliability of the distributors will be calculated in Case 5. All other parameter estimates are equal to Case 4 for transfer diaphragms. The resulting probabilities of demand exceeding capacity given MCE and in 50 years for the ASCE 7-10 and PEER/TBI design methodology are given in Table 19-2. The resulting collapse fragility curves are given in Figure 19-1.

Reducing the median of the load function changes the probability of demand exceeding capacity. It is noted how a 20%-reduction of the loads drastically reduces P(D>C). The absolute reduction is largest for ASCE 7-10 design methodology, the relative reduction is largest for the PEER/TBI design methodology.

Design Method	Case	P(D>C|MCE)	P(D>C in 50 years)
ASCE 7-10 (Transfer force)	(4) $\theta_S = \bar{V}_{CMS}$	55.852%	14.074%
	(5) $\theta_S = 0.80\ \bar{V}_{CMS}$	36.062%	8.448%
PEER/TBI (Transfer force)	(4) $\theta_S = \bar{V}_{CMS}$	7.866%	1.858%
	(5) $\theta_S = 0.80\ \bar{V}_{CMS}$	2.781%	0.765%

Table 19-2: Influence of mean θ_S of load function S on probability of demand exceeding capacity

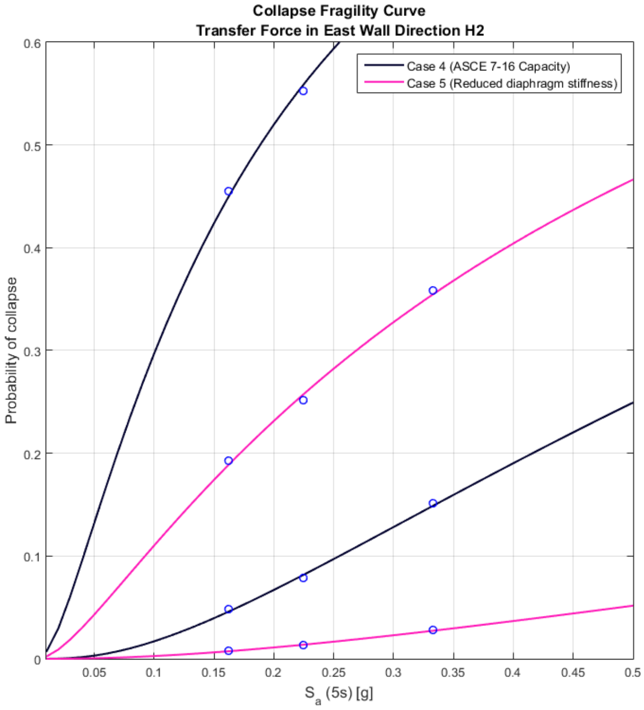

Figure 19-1: Collapse Fragility Function, Transfer force East wall

19-3-2 Standard deviation of load function S

The standard deviation β_S has been determined by combining the record-to-record variability determined from NLTHA in Perform 3D and modelling uncertainty according to ASCE 7-16 through SRSS. Neglecting the modelling uncertainty is unconservative [Liel et al., 2007]. ASCE 7-16 also specifies values for demand uncertainty for well-defined and general mechanisms. The influence of varying the standard deviation β_S of the load function is evaluated by comparing Case 4, 6, and 7. The standard deviation β_S is increased from $\beta_S = 0.28$ to $\beta_S = 0.46$ for Case 4 to Case 7. Increasing the standard deviation β_S increases the probability of demand exceeding capacity. The results are given in Table 19-3 and Figures 19-2 and 19-3. The relative increase of the shear force is the largest. An increase of the standard deviation of two-thirds results in an increase of P(D>C|MCE) of more than 3 times. The relative increase is therefore larger for the shear force, the absolute increase is largest for the transfer force.

Design Method	Case	P(D>C|MCE)	P(D>C in 50)
PEER/TBI (Shear Force)	(4) $\beta_S = \sqrt{\beta_{RTR}^2 + \beta_{MDL}^2} = 0.28$	1.134%	0.266%
	(6) $\beta_S = 0.29$	1.205%	0.282%
	(7) $\beta_S = 0.46$	3.729%	0.864%
PEER/TBI (Transfer Force)	(4) $\beta_S = \sqrt{\beta_{RTR}^2 + \beta_{MDL}^2} = 0.27$	7.866%	1.858%
	(6) $\beta_S = 0.29$	8.632%	2.003%
	(7) $\beta_S = 0.46$	14.045%	3.471%

Table 19-3: Influence of standard deviation β_S of load function S on probability of demand exceeding capacity

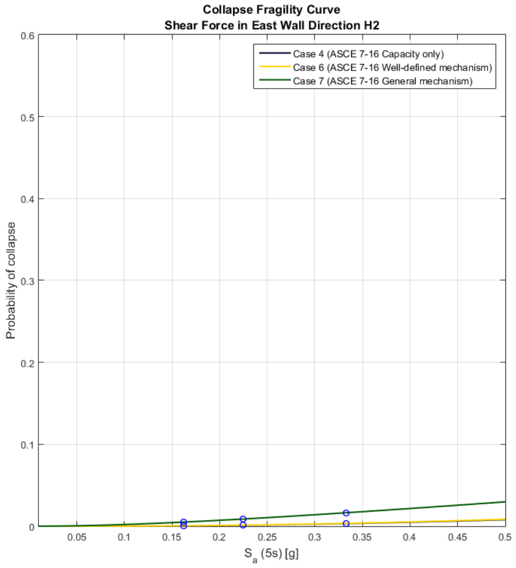

Figure 19-2: Collapse Fragility Function, Shear force East wall

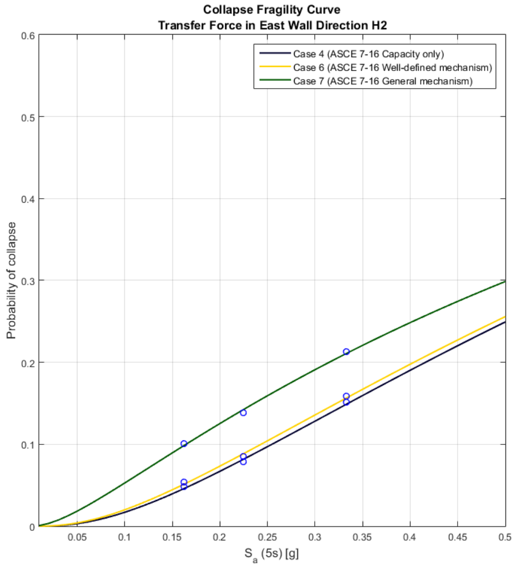

Figure 19-3: Collapse Fragility Function, Transfer force East wall

19-3-3 Median of resistance function R

The median θ_R of the resistance function R was calculated as the required capacity multiplied by a test-based factor accounting for the difference between nominal expected capacity and expected capacity. For the structural reliability analysis, it was assumed that $V_e/V_{n,e} = 1.35$. The reliability of the shear walls of the archetype structure is evaluated for Case 2 with $V_e/V_{n,e} = 1.00$ and compared to Case 3 with $V_e/V_{n,e} = 1.35$. The resulting probabilities of demand exceeding capacity and collapse fragility curves are given in Table 19-4 and 19-5.

Increasing the median of the resistance function increases the reliability of the element. For smaller probabilities of demand exceeding capacity ($\beta_{eff} = 1.94$), the relative increase is largest.

Design Method	Case	P(D>C|MCE)	P(D>C in 50)
Archetype (H1, $\beta_{eff} = 2.15$)	(2) $\theta_R = V_{n,e}$	2.078%	0.511%
	(3) $\theta_R = 1.35V_{n,e}$	0.324%	0.102%
Archetype (H2, $\beta_{eff} = 1.94$)	(2) $\theta_R = V_{n,e}$	4.091%	0.907%
	(3) $\theta_R = 1.35V_{n,e}$	0.659%	0.170%

Table 19-4: Influence of mean θ_S of resistance function R on probability of demand exceeding capacity

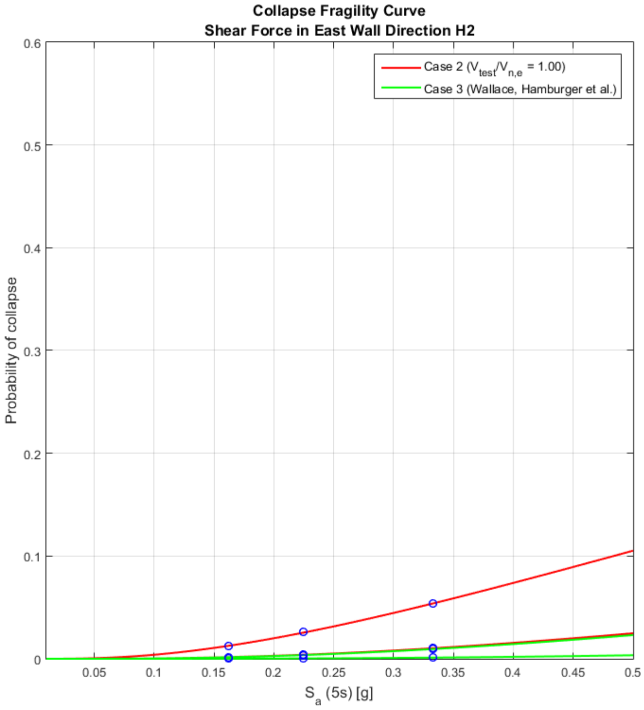

Figure 19-4: Collapse Fragility Function, Transfer force East wall

19-3-4 Standard deviation of resistance function R

The standard deviation β_R of the resistance function was taken from literature. The Joint Committee of Structural Safety [JCSS, 2000] recommends a relatively low value of $\beta_R = 0.18$. Wallace et al. [Wallace et al., 2013] recommend β_R=0.30, although test results gave a dispersion value of 0.20, which was thought relatively low for brittle failure modes of reinforced concrete. The capacity uncertainty recommended by ASCE 7-16 is β_R=0.37. Case 1, 3, and 4 investigate the influence of dispersion value of the resistance function. The results are given in Table 19-5 and Figures 19-5 and 19-6.

It was found that doubling the assumptions for standard deviation β_R of the resistance function R increases the probability of shear failure by a factor of almost seven. In accordance with previous findings, the largest absolute increase was found for transfer force.

Design Method	Case	P(D>C|MCE)	P(D>C in 50)
Shear force PEER/TBI	(1) $\beta_R = 0.18$ [JCSS]	0.126%	0.058%
	(3) $\beta_R = 0.30$ [Wallace]	0.531%	0.155%
	(4) $\beta_R = 0.37$ [ASCE 7-16]	1.134%	0.266%
Transfer force PEER/TBI	(1) $\beta_R = 0.18$ [JCSS]	2.378%	0.888%
	(4) $\beta_R = 0.37$ [ASCE 7-16]	7.866%	1.858%

Table 19-5: Influence of mean β_S of resistance function R on probability of demand exceeding capacity

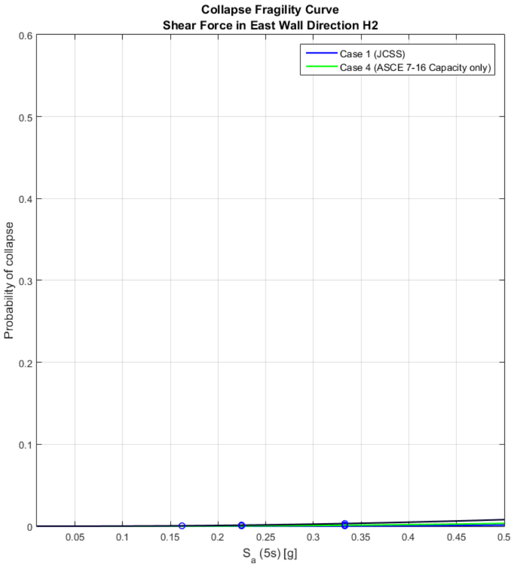

Figure 19-5: Collapse Fragility Function, Shear force East wall

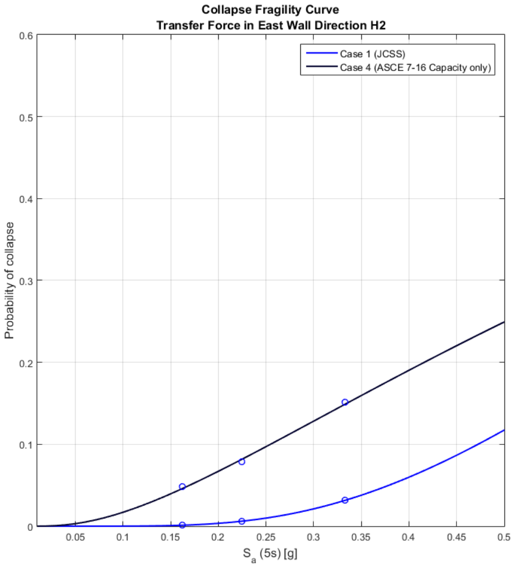

Figure 19-6: Collapse Fragility Function, Transfer force East wall

19-4 Conclusion cases

The structural reliability of the shear walls and distributors was evaluated for seven different cases. These cases gave insight in the effect of parameter assumptions for θ_S, β_S, θ_R, and β_R on the structural reliability. In general, it was found that the largest absolute increase was found for larger probabilities of failure, and the largest relative increase was found for smaller probabilities of failure.

In Section 19-4-1, the reliability of the shear walls in shear for different cases will be evaluated for the given archetype structure, PEER/TBI design and LATBSDC design. In Section 19-4-2, the reliability of distributors for different cases will be evaluated for PEER/TBI design and ASCE 7-10 design.

19-4-1 Reliability of shear walls in shear

The probabilities of demand exceeding capacity given MCE shaking for three designs and seven cases are displayed in Figure 19-7 and Table 19-7. The acceptance criterion for critical elements is less than 10% given MCE shaking. For the archetype structure, PEER/TBI design, and LATBSDC design, the acceptance criterion for MCE shaking is met. The largest probabilities were found for Case 7, with $\beta_S = 0.46$ and $\beta_R = 0.37$. The lowest probabilities were found for Case 1, with $\beta_S = 0.28$ and $\beta = 0.18$. Large probabilities of demand exceeding capacity were also found for the archetype structure for Case 2, where $\theta_R = V_{ne}$, and the median of the resistance function R shifted towards the load function S.

The probabilities of demand exceeding capacity in 50 years for the three design methodologies and cases are displayed in Figure 19-8. The maximum probabilities are also given in Table 19-6. The acceptance criterion for critical elements is less than 1% in 50 years. This acceptance criterion is stricter than the MCE criterion, and the criterion is not met for LATBSDC design for Cases 4, 6, and 7. The shape of the probabilities of demand exceeding capacity is similar for both acceptance criteria, with largest probabilities for Case 7, and Case 2 for the archetype structure, and lowest probabilities for Case 1.

It is concluded that both PEER/TBI and LATBSDC meet the acceptance criterion for MCE shaking. PEER/TBI results in more reliable shear walls, but assuming $\beta_R \leq 0.30$ and $\beta_S \leq 0.29$, LATBSDC meets all acceptance criteria. However, for $\beta > 0.30$ and $\beta > 0.29$, LATBSDC does not meet the acceptance criteria. Extensive research into shear capacity of shear walls provides reasonable confidence in the parameter estimates for β_R and β_S. Therefore, LATBSDC design with $\beta_{eff} = 1.50$ is recommended for design of shear walls.

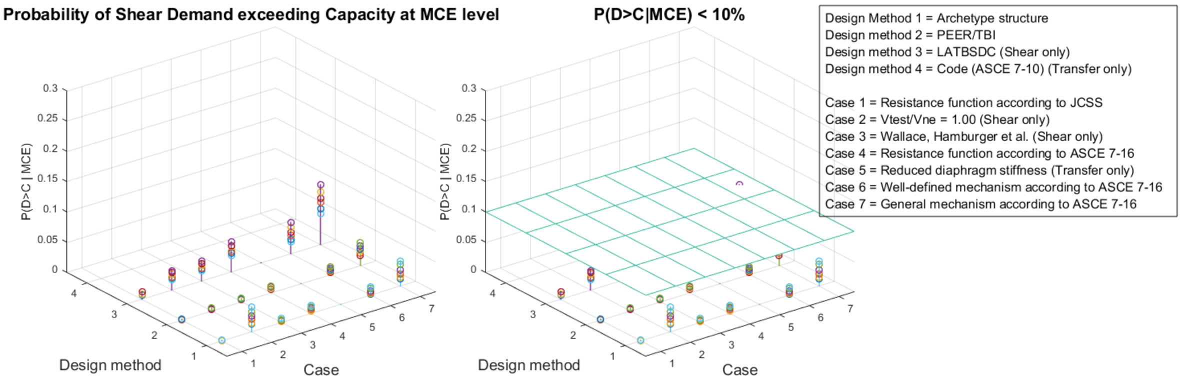

Figure 19-7: Probability of shear demand exceeding capacity at MCE level

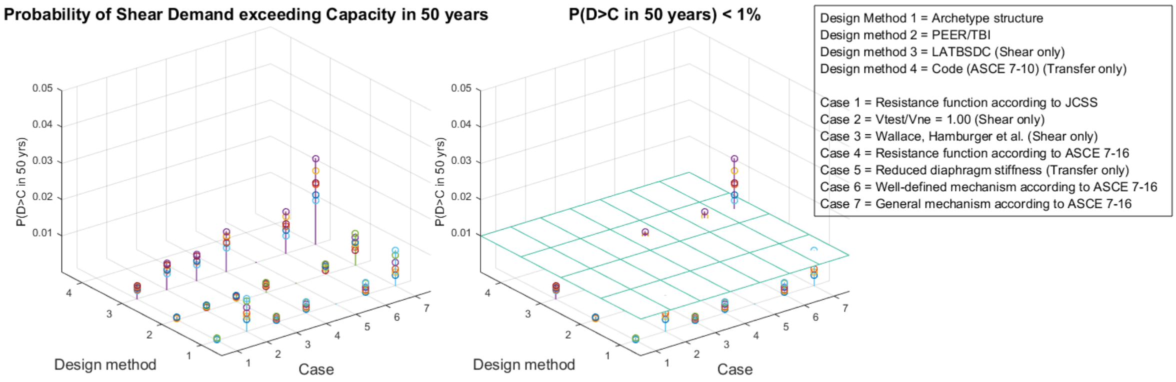

Figure 19-8: Probability of shear demand exceeding capacity in 50 years

	Archetype structure	PEER/TBI	LATBSDC
Case 1	0.059%	0.058%	0.364%
Case 2	0.907%	0.155%	0.728%
Case 3	0.170%	0.155%	0.728%
Case 4	0.314%	0.266%	1.103%
Case 5	-	-	-
Case 6	0.331%	0.282%	1.143%
Case 7	0.970%	0.864%	2.362%

Table 19-6: Maximum probability of demand exceeding capacity in 50 years for shear force

	Archetype structure	PEER/TBI	LATBSDC
Case 1	0.123%	0.126%	1.230%
Case 2	4.091%	0.531%	3.241%
Case 3	0.659%	0.531%	3.241%
Case 4	1.351%	1.134%	4.994%
Case 5	-	-	-
Case 6	1.431%	1.205%	5.170%
Case 7	4.181%	3.729%	9.896%

Table 19-7: Maximum probability of demand exceeding capacity given MCE for shear force

19-4-2 Reliability of distributors in transfer diaphragms

The probabilities of demand exceeding capacity given MCE shaking for two design methodologies and seven cases are given in Figure 19-9 and Table 19-8. The acceptance criterion for MCE shaking for ordinary elements is less than 25% probability of collapse given MCE shaking. For PEER/TBI design, the acceptance criterion for MCE shaking is met for all cases. The lowest probabilities were found for Case 1 and 5, the largest probabilities for demand exceeding capacity were found for Case 7 with $\beta_R = 0.37$ and $\beta_S = 0.46$. For ASCE 7-10, the acceptance criterion is not met for any of the considered cases. The lowest probabilities of demand exceeding capacity were found for Case 5, where the median θ_S of the load function S to account for reduced diaphragm stiffness resulting from ASCE 7-10 design where diaphragm thickness is governed by transfer forces. Therefore, Case 5 may present the most realistic estimate for ASCE 7-10 design. Still, the MCE criterion is not met for upper-bound ASCE 7-10 design.

The probabilities of demand exceeding capacity in 50 years for two design methodologies and seven cases are given in Figure 19-10 and Table 19-9. The acceptance criterion for ordinary elements was set at less than 2.5% probability of collapse in 50 years. This acceptance criterion is met for all but Case 7 for PEER/TBI design. ASCE 7-10 design does not meet the acceptance criterion for all cases. The shape of the probabilities of demand exceeding capacity for the different cases is similar for both acceptance criteria, with the largest probabilities of failure found for Case 7, and the lowest probabilities of failure found for Case 1 and 5.

It is concluded that PEER/TBI design of distributors meets the acceptance criteria for structural reliability for ordinary elements. ASCE 7-10 design of distributors results in unreliable design, even if reduced diaphragm stiffness is assumed. Therefore, PEER/TBI design with $\beta_{eff} = 1.50$ is recommended for design of distributors.

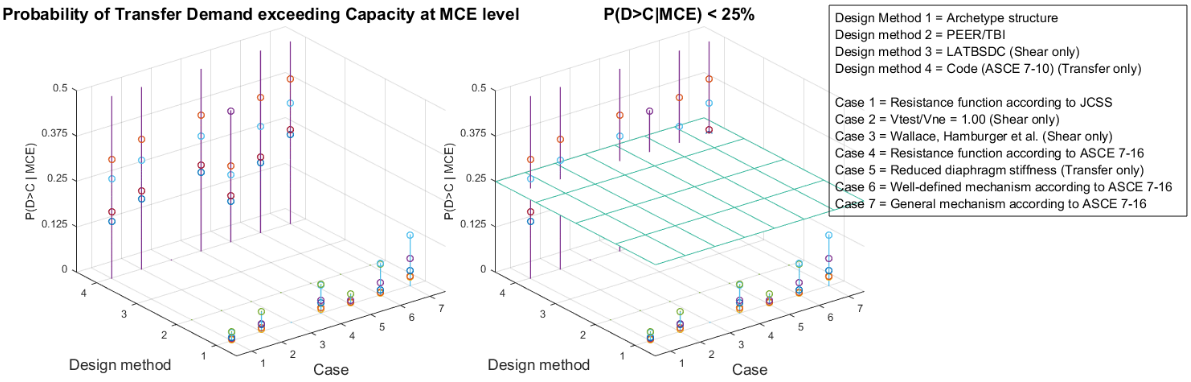

Figure 19-9: Probability of transfer demand exceeding capacity at MCE level

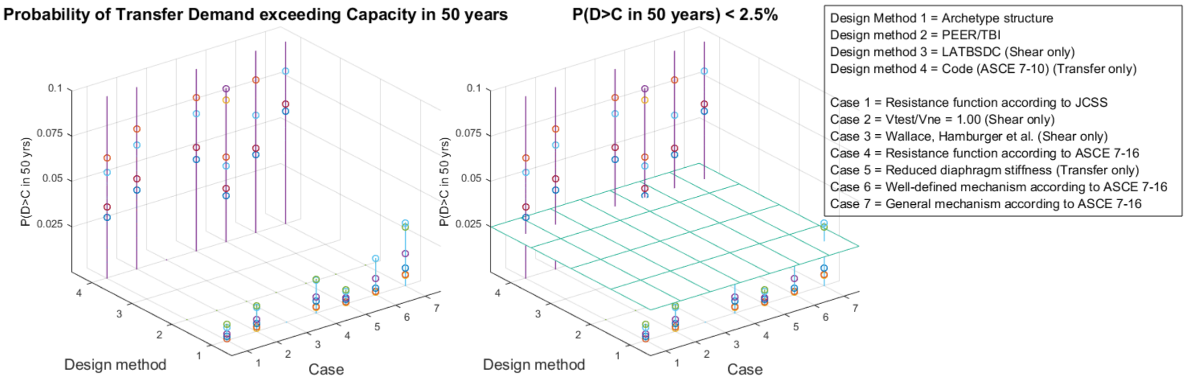

Figure 19-10: Probability of transfer demand exceeding capacity in 50 years

	PEER/TBI design	ASCE 7-10 design
Case 1	2.378%	57.164%
Case 2	5.512%	56.240%
Case 3	-	-
Case 4	7.866%	55.852%
Case 5	2.781%	36.062%
Case 6	8.632%	55.602%
Case 7	14.045%	54.238%

Table 19-8: Maximum probability of demand exceeding capacity given MCE for transfer force

	PEER/TBI design	ASCE 7-10 design
Case 1	0.888%	12.086%
Case 2	1.421%	13.300%
Case 3	-	-
Case 4	1.858%	14.074%
Case 5	0.765%	8.448%
Case 6	2.003%	14.313%
Case 7	3.471%	15.712%

Table 19-9: Maximum probability of demand exceeding capacity in 50 years for transfer force

Chapter 20

Recommendations for risk-consistent design of shear walls and distributors

20-1 Introduction

In Chapter 19, the probability of demand exceeding capacity was computed for seven discrete cases to evaluate the effect of assumptions for resistance function R and load function S on the structural reliability. For shear wall design, it was concluded that both PEER/TBI and LATBSDC meet the acceptance criteria for MCE shaking, and PEER/TBI results in more reliable shear walls. The difference between the PEER/TBI and LATBSDC design methodology is the required ratio between mean demand and capacity β_{eff}.

In Section 20-2 and 20-3, the influence of the ratio between the mean demand θ_S and θ_R on the probability of demand exceeding capacity is evaluated for the shear force and transfer force, respectively. In Section 20-4, the influence of the target spectrum on the required ratio β_{eff} for shear walls and distributors to meet the acceptance criteria is discussed. In Section 20-5, an alternative design method for preliminary design of distributors in transfer diaphragms based on ASCE 7-10 and MRSA is proposed. The accuracy of the tails of the distribution and computed probability of demand exceeding capacity is discussed in Section 20-6. The general applicability of the proposed framework for structural reliability is discussed in Section 20-7.

20-2 Required ratio between demand and capacity for shear in shear walls

The probability of demand exceeding capacity is compared to the ratio between the median demand θ_S and median capacity θ_R in Figures 20-1 and 20-2. The median demand is calculated from a suite of seven ground motions selected and scaled to match the Uniform Hazard Spectrum.

In Figure 20-1, the ratio θ_R/θ_S is compared to the acceptance criterion for MCE shaking, $P(\text{C}|\text{MCE}) \leq 10\%$. From Figure 20-1 follows that the LATBSDC ratio $\beta_{eff} = 1.5$ is sufficient for the upper-bound Case 7 to meet the acceptance criterion for MCE shaking. The acceptance criterion for probability of collapse in 50 years is more strict, $P(\text{D>C in 50 years}) \leq 1.0\%$. For the expected Case 3, $\beta_{eff} = 1.50$ is sufficient to meet the acceptance criterion. However, β_{eff} is insufficient to meet the acceptance criterion for more conservative assumptions for β_R and β_S. The required ratios for the expected Case 3, lower-bound case 1 and upper-bound case 7 are given in Table 20-1 for $P(\text{D>C}|\text{MCE})$ and $P(\text{D>C in 50 years})$.

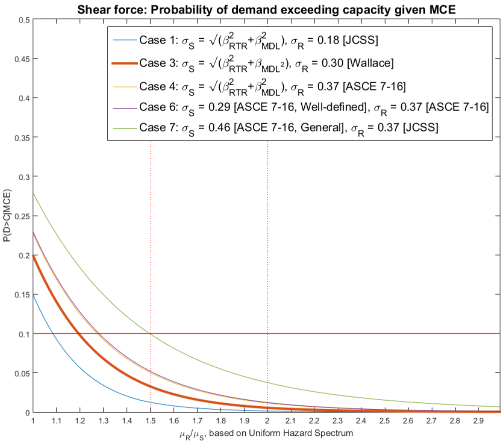

Figure 20-1: Probability of shear demand exceeding capacity given MCE, based on UHS

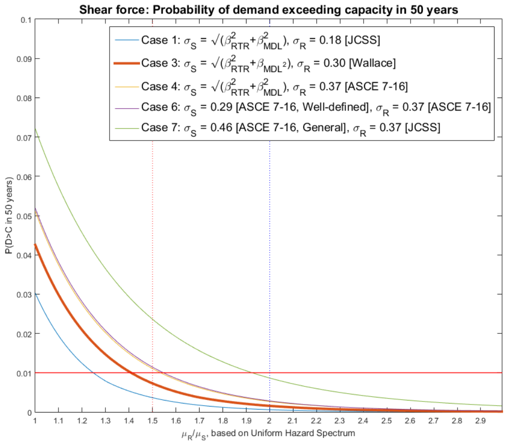

Figure 20-2: Probability of shear demand exceeding capacity in 50 years, based on UHS

		Shear force	
		P(D>C|MCE)	P(D>C in 50 years)
Expected required ratio	β_{eff}	1.19	1.41
Lower-bound ratio	β_{eff}	1.08	1.25
Upper-bound ratio	β_{eff}	1.49	1.92

Table 20-1: Required ratios β_{eff} for shear force based on UHS

20-3 Required ratio between demand and capacity for distributors in transfer diaphragms

The probability of demand exceeding capacity for distributors is compared to the ratio between the median demand θ_S and median capacity θ_R in Figures 20-3 and 20-4. The median demand is calculated from a suite of seven ground motions selected and scaled to match the Uniform Hazard Spectrum.

From Figures 20-3 and 20-4 follows that the ratio $\beta_{eff} = 1.50$ is sufficient to meet all acceptance criteria for ordinary elements for all considered cases. The required ratios for the expected Case 4, lower-bound Case 1 and upper-bound Case 7 are given in Figure 20-2.

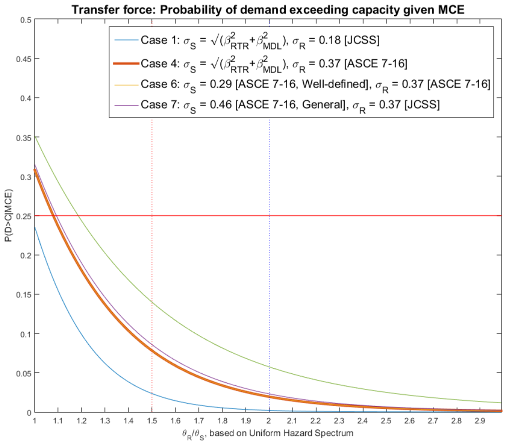

Figure 20-3: Probability of transfer demand exceeding capacity given MCE, based on UHS

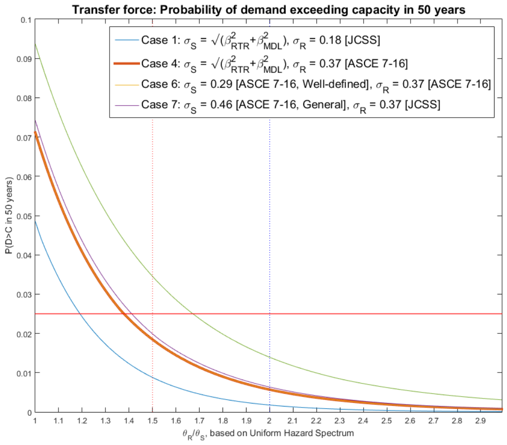

Figure 20-4: Probability of transfer demand exceeding capacity in 50 years, based on UHS

	Transfer force	
	P(D>C|MCE)	P(D>C in 50 years)
Expected required ratio β_{eff}	1.08	1.38
Lower-bound ratio β_{eff}	1.00	1.19
Upper-bound ratio β_{eff}	1.19	1.67

Table 20-2: Required ratios β_{eff} for transfer force based on UHS

20-4 Influence of target spectrum

20-4-1 Introduction

For PEER/TBI and LATBSDC design, the force demand was calculated with nonlinear time history analyses (NLTHAs). A suite of 7 ground motions was selected and scaled to match the uniform hazard spectrum (UHS). The mean of the force demand was multiplied by the dispersion factor β_u to determine the required capacity. UHS is uniform because every ordinate has an equal probability of being exceeded. As discussed in Section 8-2-2-1, it is unlikely that those spectral acceleration values at each period all occur within a single ground motion, especially for rare earthquake events. Hence, the UHS will generally be a conservative target spectrum.

The Conditional Mean Spectrum (CMS) was developed as an alternative target spectrum, addressing the limitation of the UHS by conditioning the spectrum on spectral acceleration of a single period. In the proposed document ASCE 7 Chapter 16 for Seismic Response History Analysis, the CMS is proposed as a new alternative to the UHS for response-history analysis procedure.

The CMS is essentially the same as the Conditional Spectrum, with the difference that the CMS does not take the variability in the response spectra at other periods than the conditioning period into account, as discussed in Section 8-2-2-2. Therefore, the expected mean force demand for alternative design using CMS is assumed to be equal to the mean force demand from the reliability analysis using the Conditional Spectrum at 2% in 50 years ground motion intensity. The effect of using CMS for calculation of force demand on the required ratio β_{eff} to meet the acceptance criteria will be evaluated for shear force in Section

20-4-2 Required ratio between demand and capacity for shear in shear walls with force demand calculated using CMS

The probability of demand exceeding capacity for shear force in shear walls is compared to the ratio θ_S/θ_R in Figures 20-5 and 20-6. The median demand was calculated from sets of ground motions selected and scaled to match the Conditional Spectrum.

From Figures 20-5 and 20-6 follows that the ratio $\beta_{eff} = 1.50$, as recommended by LATBSDC, is insufficient to meet the acceptance criteria. Ratio $\beta_{eff} = 2.00 - 2.10$ provides sufficient margin between the demand and capacity to meet the acceptance criteria.

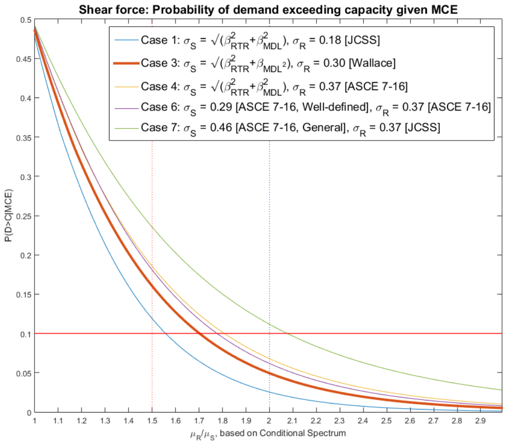

Figure 20-5: Probability of shear demand exceeding capacity given MCE, based on CMS

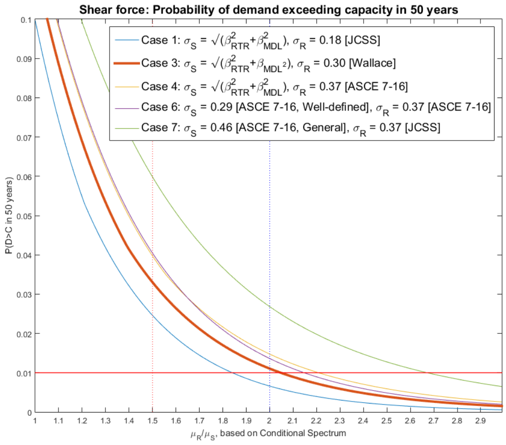

Figure 20-6: Probability of shear demand exceeding capacity in 50 years, based on CMS

	Shear force	
	P(D>C|MCE)	P(D>C in 50 years)
Expected required ratio β_{eff}	1.70	2.05
Lower-bound ratio β_{eff}	1.56	1.84
Upper-bound ratio β_{eff}	2.08	2.67

Table 20-3: Required ratios β_{eff} for shear force based on Conditional Spectrum

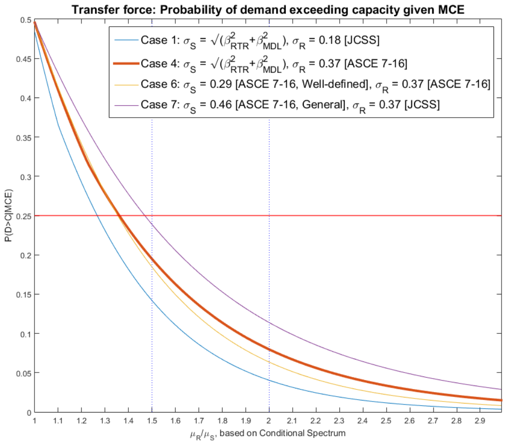

Figure 20-7: Probability of transfer demand exceeding capacity given MCE, based on CMS

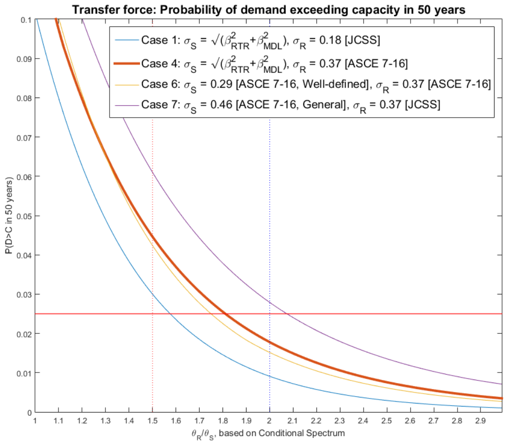

Figure 20-8: Probability of transfer demand exceeding capacity in 50 years, based on CMS

20-4-3 Required ratio between demand and capacity for distributors in transfer diaphragms with force demand calculated using CMS

The probability of demand exceeding capacity for distributors in transfer diaphragms is compared to the ratio θ_S/θ_R in Figures 20-7 and 20-8. The median demand was calculated from sets of ground motions selected and scaled to match the Conditional Spectrum.

From Figures 20-7 and 20-8 can be concluded that the recommended ratio $\beta_{eff} = 1.50$ is insufficient to meet the acceptance criterion for collapse in 50 years, but sufficient to meet the acceptance criterion given MCE shaking. Since the Code [ASCE 7-16, 2014] only specifies a design criterion for ordinary elements given MCE shaking, it is concluded that the specified ratio $\beta_{eff} = 1.50$ for distributors is sufficient to meet the acceptance criterion for all considered cases.

	Transfer force	
	P(D>C|MCE)	P(D>C in 50 years)
Expected required ratio β_{eff}	1.36	1.81
Lower-bound ratio β_{eff}	1.27	1.58
Upper-bound ratio β_{eff}	1.47	2.07

Table 20-4: Required ratios β_{eff} for transfer force based on Conditional Spectrum

20-4-4 Conclusion influence of target spectrum

The effect of the selected target spectrum on the ratio β_{eff} to meet the acceptance criteria for structural reliability was investigated. Nonlinear time history analyses with UHS as target spectrum gives larger force demands compared to analyses with ground motions scaled to the CMS. Therefore, the probability of demand exceeding capacity is larger for structures designed according to force demands calculated with ground motions scaled to the CMS.

For shear walls, the acceptance criteria for structural reliability are met for $\beta_{eff} = 2.00 - 2.10$. The required ratio $\beta_{eff} = 1.50$ per LATBSDC fails to meet the acceptance criteria. Therefore, the required ratio $\beta_{eff} = 2.00$ per PEER/TBI is recommended for shear walls designed with NLTHA with ground motions scaled to CMS. Alternatively, $V_e = 1.35V_{ne}$ could be assumed, with required shear capacity $V_{ne} \geq 1.50\bar{V}_{CMS}$. Per ASCE 7-16, UHS and CMS are interchangeable. It is recognized that developers of design codes prefer to use one factor β_{eff} for uniformity. For Codes allowing both UHS and CMS, $\beta_{eff} = 2.00$ is recommended.

For design of distributors, the acceptance criterion for MCE shaking for distributors for structural reliability is met for ratio $\beta_{eff} = 1.50$. Therefore, ratio $\beta_{eff} = 1.50$ is recommended for design of distributors in transfer diaphragms designed with NLTHA with ground motions scaled to CMS.

20-5 Alternative design method for distributors in transfer diaphragms based on MRSA

As concluded in Section 18-2-2, the current Code procedure is unsuitable to design distributors in transfer diaphragms. The ratio between the mean force demand from CMS and required capacity per ASCE 7-10 is $\beta_{eff} = 1.17$, and the probability of demand exceeding capacity is unacceptable, as shown in Figure 20-9.

Preliminary design is often done per ASCE 7-10, and the design is verified using NLTHA. For the expected Case 4, the minimum required capacity is $\beta_{eff} = 1.24$ for CMS. Design per ASCE 7-10 uses seismic performance factors R, I_e, and Ω_o and strength reduction factor ϕ to calculate the expected force demand. The combination of these factors reduces the force demand by a factor of 0.70, as displayed in Figure 14-2. For preliminary design, the required capacity of distributors is therefore recommended to be set equal to the unreduced upper-bound force demands, i.e. shear force in the basement walls. From Figure 20-9 follows that the probability of demand exceeding capacity is acceptable for design per ASCE 7-10 with MRSA using unreduced upper-bound basement wall shear to determine the required distributor capacity.

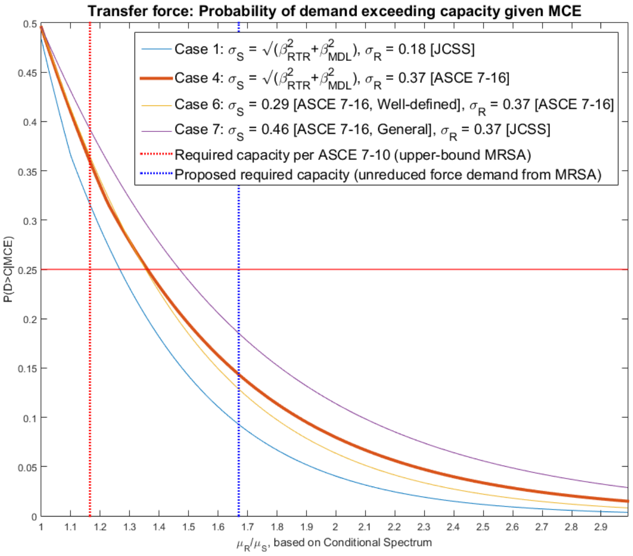

Figure 20-9: Probability of demand exceeding capacity given MCE for distributors designed per ASCE 7-10 (MRSA)

20-6 Tails of distribution

This section provides a brief discussion on the accuracy of tails of the load function S and resistance function R, which have the largest contribution to the limit state function Z. As discussed in the previous sections, the assumptions for the shape of the load function S and resistance function R, and consequently the shape of the tails of the distribution, have a significant contribution to the probability of demand exceeding capacity for a given intensity level and for the computed collapse fragility curves.

The probabilities of demand exceeding capacity can be computed at a large number of intensity levels to compute the corresponding collapse fragility curves. Alternatively, a large number of NLTHAs can be computed at a limited number of intensity levels. As the collapse fragility curves are assumed to be lognormal, only two points are needed to define the collapse fragility function, and these two points lead to a better estimation of the collapse fragility function [Miranda et al., 2014]. It is argued that this method can significantly reduce the margin of error with the same computational effort. Furthermore, Miranda et al. [Miranda et al., 2014] note that estimating the ordinates of the fragility function with less than twenty ground motions leads to relatively large errors. The level of error can be reduced by considering more ground motions.

Therefore, the structural reliability analysis was done with a limited number of ground motion intensity levels (RP975, RP2475, and RP9950). Sets of 40, 61, and 40 ground motions were used to evaluate the probability of demand exceeding capacity for the respective intensity levels. Deaggregation of mean annual frequency of collapse, see for example Figure 16-9, showed that spectral accelerations in the range between RP975 (S_a=0.1625 [%g]) and RP2475 (S_a=0.2243 [%g]) have the largest contribution to the hazard. Eads et al. [Eads et al., 2013] suggest to select IM levels for structural reliability analysis corresponding to the estimated 35% and 90% points on the cumulative collapse deaggregation plot. The selected IM levels approximately correspond to the suggested optimal IM levels, and therefore provide sufficient insight in the probability of demand exceeding capacity and the corresponding collapse fragility curves.

Moreover, the effects of varying the assumptions for the standard deviation of the load function S and resistance function R were evaluated in Chapter 19 and the previous sections. Therefore, the accuracy of the tails of the distribution and the sensitivity of the results to the variations in the shape of the distribution function have been taken into account. Hence, the presented range of probabilities of demand exceeding capacity are expected to accurately represent the actual range of structural reliability of the considered elements.

20-7 General applicability of proposed framework for structural reliability analysis

The probabilistic framework developed in this study sets an example for future structural reliability analyses. The developed framework could be used to evaluate the structural reliability of other force-controlled components of structures subject to earthquake loading. Moreover, the framework could be used to evaluate the reliability of structural components subject other types of loading.

The method can be applied to loading types for which limited data is available. From the structural reliability analysis follows that the ground motions intensities with a return period of 9950 years do not have the largest contribution to the seismic hazard. Lower intensity earthquakes have a larger contribution to the seismic hazard. As noted in Section 20-6, the probability of demand exceeding capacity only has to be evaluated at two intensity levels to compute collapse fragility curves.

The provided framework can be extended or additional assumptions can be made if parameter estimates are unknown. For example, record-to-record variability was explicitly calculated by selecting ground motions that both match the mean and variance of the corresponding target response spectrum. These ground motions were selected from a large database. If the database would have been limited, the mean response could have been calculated by selecting ground motions through spectral scaling and matching, and a conservative assumption could have been made to account for record-to-record variability. In the same manner, this study uses recommendations from literature to account for capacity uncertainty β_R and modelling uncertainty β_{MDL}. The framework could be extended to explicitly calculate those uncertainties.

Therefore, many parts of the structural reliability analysis exchangeable for more conservative estimates that require less computational effort or preliminary knowledge. An example is elastic modelling of transfer diaphragms and distributors. Transfer diaphragms and distributors are expected to possess some ductility. Implementing the ductility in the structural model would allow for yielding of these elements, which would reduce the force demands and therefore increase the computed reliability of the distributors. As the ductile behaviour of the transfer diaphragms is neglected, the computed force demand is larger and consequently the required capacity is larger to meet the acceptance criteria. The proposed framework therefore provides an upper-bound estimate of the structural reliability and increased computational effort could lead to more economical design.

Therefore, it can be concluded that the developed framework can be used for a large variety of engineering challenges. The framework could be used for elements for which all parameters affecting the structural reliability are known, but can also be used for structures for which limited data is available, as long as conservative assumptions are made to account for the unknowns.

Part VI

Conclusions and recommendations

Chapter 21

Conclusions

This study evaluated the structural reliability of seismic design methodologies for shear walls and distributors in transfer diaphragms in reinforced concrete shear wall buildings. The main conclusions from this study are summarized in this chapter. The objective of this study was to:

> *Provide insight in the reliability of current design methodologies and provide recommendations for risk-consistent design of specific force-controlled components in reinforced concrete shear wall buildings.*

A probabilistic framework was developed to evaluate the structural reliability of force-controlled components. The structural reliability of shear walls loaded in shear and designed according to PEER/TBI and LATBSDC has been evaluated. Furthermore, the reliability of distributors in transfer diaphragms designed according to ASCE 7-10 and alternative approaches has been computed. The conclusions regarding the structural reliability of current design methodologies, sensitivity of the analysis results to variations in stiffness, parameter estimates, and target spectra, and the recommended design provisions for risk-consistent design of force-controlled components are given in the following sections. First, the conclusions regarding the structural reliability of shear walls loaded in shear are discussed in Section 21-1. Subsequently, the conclusions regarding the structural reliability of distributors in transfer diaphragms are discussed in Section 21-2.

21-1 Structural reliability of shear walls loaded in shear

The conclusions regarding the structural reliability of shear walls loaded in shear will be summarized in this section. First, the conclusions regarding the reliability of shear walls designed according to PEER/TBI and LATBSDC will be given. Subsequently, the conclusions regarding the sensitivity of the computed reliability to stiffness variations, analysis assumptions, target spectra and nonlinear behaviour will be summarized. Finally, recommendations for risk-consistent design provisions of shear walls loaded in shear will be given.

21-1-1 Reliability of current design methodologies

The reliability of shear walls loaded in shear and designed according to PEER/TBI and LATBSDC has been evaluated. The acceptance criteria for structural reliability of critical elements, e.g. shear capacity of shear walls, were defined as less than 10% probability of demand exceeding capacity given MCE shaking and less than 1% probability of demand exceeding capacity in 50 years.

- The reliability of shear walls in the archetype structure, designed according to PEER/TBI and computed using expected parameter estimates for load and resistance function, met the acceptance criteria for structural reliability of critical elements.
- The reliability of shear walls increased for an increasing ratio between expected demand and required capacity β_{eff}.
- Shear walls loaded in shear and designed per PEER/TBI with $\beta_{eff} = 2.00$ met the acceptance criteria for structural reliability of critical elements, given expected parameter estimates for the load and resistance function.
- Shear walls loaded in shear and designed per LATBSDC with $\beta_{eff} = 1.50$ met the acceptance criteria for structural reliability of critical elements, given expected parameter estimates for load and resistance function.
- The computed reliability of shear walls loaded in shear is a conservative estimate. The probability of collapse given demand exceeding capacity is most likely less than 1.

21-1-2 Sensitivity of analysis results

The influence of stiffness variations of the podium and basement diaphragms and basement walls on the probability of demand exceeding capacity has been evaluated.

- Variations in diaphragm stiffness did not affect the mean shear force demand or variance of the load function for shear force in shear walls. The probability of demand exceeding capacity in shear walls was not altered by variations in diaphragm stiffness.

- Variations in basement wall stiffness did not affect the shear force demand in shear walls.

Furthermore, the influence of nonlinear stress-strain behaviour on the computed force demand and record-to-record variability has been evaluated.

- In general, nonlinear stress-strain behaviour saturated the maximum forces in the structures and reduced the observed record-to-record variability. Therefore, disregard of nonlinear stress-strain behaviour may result in overestimation of the probability of demand exceeding capacity.

Moreover, the sensitivity of parameter assumptions for the load function and resistance function on the predicted probability of demand exceeding capacity has been evaluated for six different cases.

- In general, increasing the median of the load function, decreasing the median of the resistance function, and increasing the standard deviation of the load function and resistance function increased the probability of demand exceeding capacity.
- Shear capacity design of shear walls per PEER/TBI met the acceptance criteria for all considered cases.
- Shear capacity design of shear walls per LATBSDC met the acceptance criterion for all considered cases given MCE shaking. LATBSDC methodology failed to meet the acceptance criterion for probability of collapse in 50 years for larger-than-expected cases.

Finally, the sensitivity of the computed probability of demand exceeding capacity to the selected target spectrum has been evaluated.

- In general, nonlinear time history analysis with the conservative Uniform Hazard Spectrum (UHS) as target spectrum resulted in larger force demands compared to analyses with ground motions scaled to the Conditional Mean Spectrum (CMS). Hence, the required capacity for structures designed with CMS as target spectrum was smaller and consequently the probability of demand exceeding capacity was larger.
- Shear wall design per LATBSDC with CMS and $\beta_{eff} = 1.50$ failed to meet the acceptance criteria.
- Shear wall design per PEER/TBI with CMS and $\beta_{eff} = 2.00$ provided sufficient structural reliability.

21-1-3 Recommendations for risk-consistent design of shear walls loaded in shear

Based on the structural reliability analysis and sensitivity analysis, the following recommendations for risk-consistent design of shear walls loaded in shear have been provided.

The acceptance criteria for structural reliability of ordinary elements, e.g. distributors in transfer diaphragms, were defined as less than 25% probability of demand exceeding capacity given MCE shaking and less than 2.5% probability of demand exceeding capacity in 50 years.

- As the parameter estimates for load and resistance function of shear walls have been verified by extensive research, LATBSDC design with $\beta_{eff} = 1.50$ is deemed acceptable for shear walls loaded in shear. Therefore, for design of shear walls with NLTHA using ground motions scaled to the Uniform Hazard Spectrum, ratio $\beta_{eff} = 1.50$ is recommended.
- For design of shear walls with NLTHA using ground motions scaled to the Conditional Mean Spectrum, the recommended ratio should be increased to $\beta_{eff} = 2.00$. Alternatively, equivalent reliability is also provided for $V_{ne} \geq \beta_{eff}\bar{V}_{CMS}$ with $\beta_{eff} = 1.50$ and assuming V_e=1.35V_{ne}.
- For design of shear walls with design codes for which use of UHS and CMS is interchangeable, such as ASCE 7-16, $\beta_{eff} = 2.00$ is recommended. Alternatively, equivalent reliability is also provided for $V_{ne} \geq \beta_{eff}\bar{V}_{CMS}$ with $\beta_{eff} = 1.50$ and assuming V_e=1.35V_{ne}.

21-2 Structural reliability of distributors in transfer diaphragms

The conclusions regarding the structural reliability of distributors in transfer diaphragms will be summarized in this section. First, the conclusions regarding the reliability of distributors designed according to ASCE 7-10 and PEER/TBI will be given. Subsequently, the conclusions regarding the sensitivity of the computed reliability to stiffness variations, analysis assumptions, and target spectra will be summarized. Finally, recommendations for risk-consistent design provisions of distributors in transfer diaphragms will be given.

21-2-1 Reliability of current design methodologies

The reliability of distributors in transfer diaphragms designed according to ASCE 7-10 and PEER/TBI has been evaluated.

- PEER/TBI design of distributors in transfer diaphragms met the acceptance criteria for structural reliability of ordinary elements, computed with $\beta_{eff} = 1.50$ and expected parameter estimates for load and resistance function. This also holds for LATBSDC design of distributors in transfer diaphragms.
- ASCE 7-10 design of distributors in transfer diaphragm failed to meet the acceptance criteria for structural reliability of ordinary elements, computed with expected reliability assumptions for distributors.
- The computed reliability of distributors in transfer diaphragms is a conservative estimate. Ductile behaviour of distributors, load transfer through columns, and out-of-plane shear stiffness of thick walls are likely to reduce the force demand in distributors and consequently increase the reliability.

21-2-2 Sensitivity of analysis results

The influence of stiffness variations on the force demand in the diaphragms has been evaluated.

- Variations in diaphragm stiffness affected the mean transfer force demand in distributors. The shear demand increased for increasing diaphragm stiffness. Variation in diaphragm stiffness increased both the mean and variance of the load function of the distributors. Therefore, consideration of the variation in diaphragm stiffness increased the probability of demand exceeding capacity of the distributors.
- Variations in basement wall stiffness did not affect the mean transfer force demand in distributors.

The sensitivity of parameter assumptions for the load function and resistance function on the predicted probability of demand exceeding capacity has been evaluated for six different cases.

- PEER/TBI and LATBSDC methodologies for design of distributors in transfer diaphragms met the acceptance criteria for structural reliability for ordinary elements for all considered cases given MCE shaking.
- ASCE 7-10 design of distributors results in unreliable design, even if reduced diaphragm stiffness is assumed.

The sensitivity of the computed probability of demand exceeding capacity to the selected target spectrum has been evaluated.

- The probability of demand exceeding capacity was larger for distributors designed with the Conditional Mean Spectrum.
- Design of distributors in transfer diaphragms per PEER/TBI with $\beta_{eff} = 1.50$ and the Conditional Mean Spectrum met the acceptance criteria for ordinary elements.

21-2-3 Recommendations for risk-consistent design

Based on the structural reliability analysis and sensitivity analysis, the following recommendations for risk-consistent design of distributors in transfer diaphragms have been provided.

- For preliminary design, an initial estimate of the required capacity of distributors can be made by requiring the capacity to be larger than the unreduced upper-bound force demands from MRSA, i.e. shear force in the basement walls.
- The current ASCE 7-10 methodology is discouraged for final design of distributors in transfer diaphragms.
- The PEER/TBI and LATBSDC design procedures with β_{eff}=1.50 provided sufficient reliability for design using ground motions scaled to the UHS and CMS. Furthermore, the PEER/TBI and LATBSDC design procedures met the acceptance criteria for all considered cases. Therefore, the alternative approaches with β_{eff} are recommended for design of distributors in transfer diaphragms.

Chapter 22

Recommendations

The following recommendations can be given based on the findings from this research. First, recommendations will be given for further research into the structural reliability of seismic design methodologies for shear walls and distributors in reinforced concrete structures. Subsequently, recommendations will be given for further research using the probabilistic framework proposed in this study.

Further research into structural reliability of shear walls and distributors

The following topics for further research are recommended for seismic design methodologies for shear walls and distributors in reinforced concrete structures:

- Establish new design provisions for risk-consistent design of distributors in transfer diaphragms per ASCE 7-10.
- Evaluate the effect of substituting the Uniform Hazard Spectrum with the Conditional Mean Spectrum on the reliability of structure and determine whether new design provisions are required to meet the acceptance criteria for structural reliability.
- Investigate the effect of soil-structure-interactions on the structural reliability of distributors in transfer diaphragms. Furthermore, additional research into the effects of stiffness variations of transfer diaphragms and basement walls is recommended.
- Evaluate the effect of varying the configuration of the archetype structure. This includes, but is not limited to, building height, diaphragm openings, ramps in basements connecting diaphragms at different levels, distance between basement walls and shear walls, dual systems and basement story height.
- Investigate the effect of multiple buildings sharing one basement.

Probabilistic framework

This work provides insight in the reliability of design current design methodologies and the influence of design criteria, design decisions and analysis assumptions on the structural reliability of force-controlled components. The proposed framework sets an example for reliability analysis of structural components. The proposed framework can be simplified or extended, in accordance with the available data and desired effort. Therefore, the proposed framework is recommended for future structural reliability analyses.

Bibliography

[Abdelnaby, 2012] Abdelnaby, A. E. (2012). *Multiple Earthquake Effects on Degrading Reinforced Concrete Structures*. PhD thesis.

[ACI 318-11, 2011] ACI 318-11 (2011). *Building code requirements for structural concrete.*

[ASCE 41-13, 2013] ASCE 41-13 (2013). *Seismic Evaluation and Retrofit of Existing Buildings.*

[ASCE 7-10, 2010] ASCE 7-10 (2010). Minimum Design Loads for Buildings and Other Structures. Technical Report ASCE/SEI 7-10, American Society of Civil Engineers.

[ASCE 7-16, 2014] ASCE 7-16 (2014). ASCE 7 Standards Committee - ASCE 7-16 Chpt. 16.4. Technical Report I.

[ATC 72-1, 2010] ATC 72-1 (2010). Modeling and Acceptance Criteria for Seismic Design and Analysis of Tall buildings. Technical report.

[Baker, 2014] Baker, J. W. (2014). Efficient analytical fragility function fitting using dynamic structural analysis. *Earthquake Spectra.*

[Barney et al., 1980] Barney, G., Shiu, K., Rabbat, B., Fiorato, A., Rssell, H., and Corley, W. (1980). Behavior of Coupling Beams under Load Reversals.

[Belarbi and Hsu, 1994] Belarbi, H. and Hsu, T. (1994). Constitutive laws of concrete in tension and reinforcing bars stiffened by concrete. *ACI Structural Journal*, 91(4):465--474.

[Chang and Mander, 1994] Chang, G. and Mander, J. (1994). Seismic energy based fatigue damage analysis of bridge columns: Part I - evaluation of seismic capacity. Technical report, State University of New York, Buffalo, New York.

[Chopra, 2014] Chopra, A. K. (2014). *Dynamics of Structures.* Earthquake Engineering Research Institute, 4th edition.

[Cur-instituut, 2000] Cur-instituut (2000). Kansen in de civiele techniek Deel 1 : probabilistisch ontwerpen in theorie. pages 1--240.

[Deierlein et al., 2010] Deierlein, G. G., Reinhorn, A. M., and Willford, M. R. (2010). Nonlinear Structural Analysis for Seismic Design. *NEHRP Seismic Design Technical Brief No. 4.*

[Eads et al., 2013] Eads, L., Miranda, E., Krawinkler, H., and Lignos, D. G. (2013). An efficient method for estimating the collapse risk of structures in seismic regions. *Earthquake Engineering & Structural Dynamics*, 42(1):25--41.

[FEMA 356, 2000] FEMA 356 (2000). Prestandard and Commentary for the Seismic Rehabilitation of Building. *Rehabilitation*, (November).

[FEMA P695, 2009] FEMA P695 (2009). Quantification of Building Seismic Performance Factors. Technical Report June, Federal Emergency Management Agency.

[Filippou et al., 1983] Filippou, F., Popov, E., and Bertero, V. V. (1983). Effects of Bond Deterioration on Hysteretic Behavior of Reinforced Concrete Joints. Technical report, University of California, Berkeley, CA.

[Fischinger et al., 1992] Fischinger, M., Vidic, T., and Fajfar, P. (1992). Nonlinear Seismic Analysis of Structural Walls Using the Multiple-Vertical-Line-Element Mode.

[Galano and Vignoli, 2000] Galano, L. and Vignoli, A. (2000). Seismic behavior of short coupling beams with different reinforcement layouts. *ACI Structural Journal*, 97(6):876--885.

[Ghodsi and Ruiz, 2009] Ghodsi, T. and Ruiz, J. A. F. (2009). Pacific earthquake engineering research/seismic safety commission tall building design case study 2. Technical report.

[Gogus, 2010] Gogus, A. (2010). *Structural wall systems - nonlinear modeling and collapse assessment of shear walls and slab-column frames.* PhD thesis.

[Haselton and Deierlein, 2007] Haselton, C. and Deierlein, G. G. (2007). Assessing seismic collapse safety of modern reinforced concrete moment frame buildings. Technical report, Pacific Earthquake Engineering Research Center, Berkeley, CA.

[Jangid, 2014] Jangid, R. (2014). *Introduction to Earthquake Engineering.* National Programme on Technology Enhanced Learning (NPTEL).

[Jayaram et al., 2011] Jayaram, N., Lin, T., and Baker, J. W. (2011). A Computationally Efficient Ground-Motion Selection Algorithm for Matching a Target Response Spectrum Mean and Variance. *Earthquake Spectra*, 27(3):797--815.

[JCSS, 2000] JCSS (2000). Probabilistic Model Code (concrete). pages 1--5.

[LATBSDC, 2014] LATBSDC (2014). *An Alternative Procedure For Seismic Analysis and Design of Tall Buildings Located in the Los Angeles Region*. Los Angeles, CA.

[Liel and Deierlein, 2008] Liel, A. and Deierlein, G. G. (2008). Assessing the collapse risk of California's existing reinforced concrete frame structures: Metrics for seismic safety decisions. Technical report, Stanford University, Stanford, CA.

[Liel et al., 2007] Liel, A., Haselton, C., Deierlein, G. G., and Baker, J. W. (2007). Assessing the Seismic Collapse Risk of Reinforced Concrete Frame Structures, Including the Effects of Modeling Uncertainties. page 12.

[Lin et al., 2012] Lin, T., Harmsen, S., Baker, J. W., and Luco, N. (2012). âĂIJConditional Spectrum Computation Incorporating Multiple Causal Earthquakes and Ground Motion Prediction Models. *Bulletin of the Seismological Society of America*, 103(2a).

[Lin et al., 2013] Lin, T., Haselton, C., and Baker, J. W. (2013). Conditional spectrum-based ground motion selection. Part I: Hazard consistency for risk-based assessments. *Earthquake Engineering & Structural Dynamics*, 41(11):1549--1568.

[Luco et al., 2007] Luco, N., Ellingwood, B. R., Hamburger, R. O., Hooper, J. D., Kimball, J. K., and Kircher, C. a. (2007). Risk-Targeted versus Current Seismic Design Maps for the Conterminous United States. *Structural Engineering Association of California 2007 Convention Proceedings*, pages 1--13.

[Lunne et al., 1997] Lunne, T., Robertson, P., and Powell, J. (1997). Cone Penetration Testing in Geotechnical Practice.

[MacKay-Lyons, 2013] MacKay-Lyons, R. (2013). *Performance-Based Design of Rc Coupled Wall High-Rise Buildings With Viscoelastic Coupling Dampers*. PhD thesis.

[Mander, J.B.; Priestley, M.J.N., Park, 1988] Mander, J.B.; Priestley, M.J.N., Park, R. (1988). Theoretical Stress-Strain Model for Confined Concrete.

[Menegotto and Pinto, 1973] Menegotto, M. and Pinto, P. . (1973). Method of analysis of cyclically loaded RC plane frames including changes in geometry and non-elastic behavior of elements under normal force and bending. *Preliminary Report IABSE, vol 13.e.*

[Miranda et al., 2014] Miranda, E., Eads, L., Krawinkler, H., and Lignos, D. (2014). Efficient Collapse Risk Assessment for Performance-Based Earthquake Engineering. In *Tenth U.S. National Conference on Earthquake Engineering*, Anchorage, AK.

[Moehle et al., 2010] Moehle, J. P., Hooper, J. D., Kelly, D. J., and Meyer, T. R. (2010). Seismic Design of Cast-In-Place Concrete Diaphragms, Chords, and Collectors. *NEHRP Seismic Design Technical Brief No. 3.*

[Naish, 2010] Naish, D. (2010). *Testing and Modeling of Reinforced Concrete Coupling Beams*. PhD thesis.

[Naish et al., 2009] Naish, D., Wallace, J. W., Fry, J. A., and Klemencic, R. (2009). Experimental Evaluation and Analytical Modeling of ACI 318-05 / 08 Reinforced Concrete Coupling Beams Subjected to Reversed Cyclic Loading.

[Naish et al., 2010] Naish, D., Wallace, J. W., Fry, J. A., and Klemencic, R. (2010). Modeling of Diagonally Reinforced Concrete Coupling Beams. *5th International Conference on Earthquake Engineering (5ICEE)*, pages 4--8.

[Nakaki, 2000] Nakaki, S. D. (2000). Design Guidelines for Precast and Cast-In-Place Concrete Diaphragms.

[Napier and Abell, 2014] Napier, J. and Abell, M. (2014). No Title.

[NEHRP Consultants Joint Venture, 2012] NEHRP Consultants Joint Venture (2012). Soil-Structure Interaction for Building Structures. Technical report.

[Oesterle et al., 1984] Oesterle, R., Aristizabal-Ocha, J., Fiorato, A., Russell, H., and Corley, W. (1984). Web Crushing of Reinforced Concrete Structural Walls. *ACI Journal*, 81(22):231--241.

[Orakcal et al., 2006] Orakcal, K., Massone, L. M., and Wallace, J. W. (2006). Analytical modeling of reinforced concrete walls for predicting flexural and coupled-shear-flexural responses. *October*, (October).

[Orakcal et al., 2009] Orakcal, K., Massone, L. M., and Wallace, J. W. (2009). Shear strength of lightly reinforced wall piers and spandrels. *ACI Structural Journal*, 106(4):455--465.

[Orakcal and Wallace, 2004] Orakcal, K. and Wallace, J. W. (2004). Modelling of slender reinforced concrete walls. *13th World Conference on Earthquake Engineering*, 18(1):141--143.

[Orakcal et al., 2004] Orakcal, K., Wallace, J. W., and Conte, J. P. (2004). Flexural Modeling of Reinforced Concrete Walls. *ACI Structural Journal*, 101(5):688--698.

[Pais and Kausel, 1988] Pais, A. and Kausel, E. (1988). Approximate formulas for dynamic stiffnesses of rigid foundations. *Soil Dynamics and Earthquake Engineering*, 7(2):213--227.

[Paulay and Priestley, 1992] Paulay, T. and Priestley, N. (1992). *Seismic design of reinforced concrete and masonry buildings*.

[Paulay, T.; Binney,] Paulay, T.; Binney, J. Diagonally Reinforced Coupling Beams of Shear Walls.

[PEER Task 12 Group, 2011] PEER Task 12 Group (2011). PEER Case Studies of the Seismic Performance of Tall Buildings Designed by Alternative Means. Technical Report July.

[PEER/TBI, 2010] PEER/TBI (2010). Guidelines for Performance-Based Seismic Design of Tall Buildings. Technical report, Pacific Earthquake Engineering Research Center, Berkeley, CA.

[Perform 3D User Guide, 2006] Perform 3D User Guide (2006). Nonlinear Analysis and Performance Assessment for 3D Structures. Technical Report August.

[Powell, 2007] Powell, G. H. (2007). PERFORM 3D Detailed example of a tall shear wall building-Nonlinear Modeling, Analysis and Performance Assessment for Earthquake Loads. *Computers & Structures Inc, Berkeley.*

[Powell, 2013] Powell, G. H. (2013). Modeling of coupling beams in shear walls.

[Rad and Adebar, 2006] Rad, B. R. and Adebar, P. (2006). Shear Demand on High-Rise Concrete Walls: Influence of Diaphragms Below-Grade. *Journal of Structural Engineering.*

[Rad and Adebar, 2008] Rad, B. R. and Adebar, P. (2008). Dynamic Shear Amplification in High-Rise Concrete Walls; Effect of Multiple Flexural Hinges and Shear Cracking. *Journal of Structural Engineering.*

[Rad and Adebar, 2009] Rad, B. R. and Adebar, P. (2009). Seismic Design of High-Rise Concrete Walls: Reverse Shear due to Diaphragms below Flexural Hinge. *Journal of Structural Engineering.*

[Salas, 2008] Salas, M. (2008). *Modelling of tall reinforced concrete wall buildings.* PhD thesis, University of California, Los Angeles.

[SAP2000 Analysis Reference Manual, 2009] SAP2000 Analysis Reference Manual (2009). CSI Analysis Reference Manual. (April).

[Vulcano et al., 1988] Vulcano, A., Bertero, V. V., and Colotti, V. (1988). Analytical Modeling of R/C Structural Walls. *Proceedings of Ninth World Conference on Earthquake Engineering.*

[Wallace, 2007] Wallace, J. W. (2007). Modelling Issues for Tall Reinforced Concrete Core Wall Buildings. *Geotechnical, Geological and Earthquake Engineering*, 17:279--307.

[Wallace, 2012] Wallace, J. W. (2012). Behavior, design, and modeling of structural walls and coupling beams - Lessons from recent laboratory tests and earthquakes. *International Journal of Concrete Structures and Materials*, 6(1):3--18.

[Wallace et al., 2013] Wallace, J. W., Eeri, M., Tran, T., Segura, C., Hamburger, R. O., and Moehle, J. P. (2013). Shear Design of Reinforced Concrete Structural Walls for Tall Buildings.

[Wood, 1989] Wood, S. (1989). Minimum Tensile Reinforcement Requirements in Walls. *ACI Structural Journal*, 86(5):582--591.

[Yassin, 1994] Yassin, M. H. M. (1994). *Nonlinear analysis of prestressed concrete structures under monotonic and cyclic loads.* PhD thesis, University of California.